



UNIVERSITÀ  
DEGLI STUDI  
DI PADOVA

UNIVERSITA' DEGLI STUDI DI PADOVA

Dipartimento di Ingegneria Industriale DII

Dipartimento di Tecnica e Gestione dei Sistemi Industriali DTG

Corso di Laurea Magistrale in Ingegneria Meccanica

Notch sensitivity in a 3D woven E-glass/epoxy composite investigated by using Digital Image Correlation

Relatore: Chiar.mo Prof. Marino Quaresimin

Relatore Estero: Prof. Stephen Louis Ogin

Laureando: Alberto Trevisan 1104935

Anno Accademico 2016/2017





*To my parents, my family  
and my friends*



# Abstract

In this work, notch sensitivity behaviour of a 3D woven composite is analysed with the help of Digital Image Correlation, this, together with the fatigue behaviour, is one of the main concerns about composite materials and materials in general. To investigate this, the material architecture was firstly characterized with the use of optical microscopies to measure the internal parameters and to check the presence of defects. The DIC technology was also tested comparing the results given by virtual strain gauges (i.e. averaging the DIC strains over rectangular areas) with the ones of traditional strain gauges, the results of virtual strain gauges of assorted sizes were also related to the fabric architecture (i.e. the composite unit-cell). After that, several quasi-static tests were done, all along warp direction in tension, the focus was initially on the relationship between the superficial strain pattern detected by the DIC and the composite architecture. In this context, was also explained the formation of a transverse patten of alternated lines of high and low strains through the Strain Magnification Factor theory. Then, the normalized ultimate tensile strength was plotted against the notch size, comparing the results with the notch insensitivity line, this was done for various manufacturing techniques and data taken from literature were compared with the experimental results. Was found that 3D woven composites present a notch insensitivity behaviour, similar for specimens manufactured using VARTM and Wet lay-up technique, this was also verified for different thicknesses. 3D woven composites present in general a closer behaviour to the notch insensitivity than 2D composites, but must be remembered that this can vary depending on the lay-up. The own made laminates were studied in terms of fibre volume fraction and mechanical properties and the results were compared to other works present in the bibliography. Using DIC results, I have tried to explain the notch insensitivity behaviour of 3D woven composites finding a characteristic damaging mode. To do so, the results of multiple tests were discussed, focusing particularly on the relation between damage, final failure and resin rich regions between weft tows. To better understand that, the strains around the hole in the loading direction were plotted in a polar graph, their shape was also compared with 2D woven composite and aluminium specimens. As last thing, the damage development near the hole in plain specimens and in notched ones was investigated, this was

possible stopping the test at the predetermined stage and taking microscopies of the cut specimen using optical and scanning electron microscopies. Was found that the same phases of damage can be found in the two cases, moreover the damage progression in a quasi-static test is similar to one that can be found in fatigue. Matrix cracks do not appear just in resin rich regions, even for a notched specimen, since the weft tow edges represents a preferential spot for damage formation. In any case, resin channels and in general the inherently material inhomogeneity represent some factors that highly influence the response of the material and its notch sensitivity.





## Table of Contents

Abstract.....	V
Introduction.....	XV
Chapter 1 Literature review.....	1
1.1 Introduction.....	1
1.2 Types of composites.....	1
1.2.1. 2D woven fabrics.....	3
1.2.2. 3D reinforced composites.....	7
1.2.3. Braiding.....	8
1.2.4. Knitting.....	10
1.2.5. Stitching.....	12
1.2.6. Z-pinning.....	13
1.2.7. Non-crimp fabrics.....	14
1.3 3D non-crimp woven composites.....	15
1.3.1. Through-thickness angle interlock and layer-to-layer interlock.....	18
1.3.2. Orthogonal woven architecture.....	19
1.3.3. Weaving process for 3D orthogonal composites.....	21
1.3.4. Microstructure of 3D woven composites.....	24
1.3.5. Static mechanical properties of 3D orthogonal woven composites.....	28
1.3.5.1. Influence of the z-yarns volume fraction over the static properties	28
1.3.5.2. Quasi-static tensile properties of 3D woven.....	30
1.3.5.3. Quasi-static damage evolution.....	34
1.4 Strength reduction in notched 3D woven composites.....	36
1.5 Digital Image Correlation.....	41
1.5.1. Introduction.....	41
1.5.2. The correspondence problem.....	42

1.5.3.	Speckle pattern.....	42
1.5.4.	System calibration.....	44
1.5.5.	Basic principles of 2D Digital Image Correlation for in-plane displacements 45	
1.5.6.	Basic principles of 3D Digital Image Correlation.....	54
1.6	Concluding remarks.....	54
Chapter 2	Experimental methods.....	57
2.1	Introduction.....	57
2.2	Specimen Manufacture.....	57
2.2.1.	Material properties.....	57
2.2.2.	Wet lay-up manufacturing technique.....	58
2.2.3.	Fibre volume fraction calculation.....	64
2.2.4.	Cutting of the specimen and end-tabbing.....	66
2.2.5.	Strain gauging.....	67
2.3	Quasi-static tensile tests.....	68
2.4	Digital Image Correlation.....	69
2.4.1.	Camera and software system.....	69
2.4.2.	Specimen preparation.....	70
2.4.3.	Camera set-up.....	73
2.4.4.	System calibration.....	75
2.5	Microscopies.....	77
2.5.1.	Specimen preparation.....	77
2.5.2.	Optical microscope.....	81
2.5.3.	Scanning electron microscope.....	81
2.6	Concluding remarks.....	83
Chapter 3	Microstructure measurements.....	85



3.1	Introduction .....	85
3.2	Material structural parameters .....	85
3.3	Defects inside the composite .....	92
3.4	Concluding remarks .....	95
Chapter 4 Virtual strain gauge investigation.....		97
4.1	Introduction .....	97
4.2	Comparison between the DIC results and the composite unit-cell .....	97
4.3	Concluding remarks .....	107
Chapter 5 Relation between DIC pattern and internal geometry of the composite		109
5.1	Introduction .....	109
5.2	Relation between DIC results and z-binders .....	109
5.3	Relation between DIC, weft tows and transverse lines formation.....	114
5.4	Strain Magnification Factor (SMF) .....	114
5.4.1	Experimental results .....	115
5.4.2	Idealized model.....	118
5.5	Concluding remarks .....	123
Chapter 6 Notch sensitivity investigation .....		125
6.1	Introduction .....	125
6.2	Notch sensitivity for VARTM specimens.....	125
6.3	Notch sensitivity for Wet lay-up specimens.....	127
6.3.1	Fiber volume fraction calculation.....	127
6.3.2	Quasi-static tensile tests.....	129
6.4	Digital Image Correlation results discussion .....	136
6.4.1	Plain specimen.....	136
6.4.2	2.5mm hole .....	140
6.4.3	5mm hole .....	142

6.4.4	10mm hole .....	146
6.5	Strain mapping around holes using DIC.....	148
6.5.1	Test program and specimen preparation .....	148
6.5.2	3D woven composite with a 2.5mm hole.....	149
6.5.3	3D woven composite with a 5mm hole .....	151
6.5.4	3D woven composite with a 7.5mm hole.....	153
6.6	Comparison of 3D composite strain mapping with a 2D composite and an aluminium specimen .....	155
6.6.1	2D composite specimen with a 5mm hole.....	155
6.6.2	Aluminium specimen with a 5mm hole.....	161
6.7	Concluding remarks .....	164
Chapter 7	Damage evolution investigation.....	167
7.1	Introduction.....	167
7.2	Damage investigation at 0.7% strain in a plain specimen.....	168
7.3	Damage investigation before failure in a plain specimen .....	171
7.4	Damage investigation around a 5mm hole before failure .....	177
7.4.1	Specimen 1.....	178
7.4.2	Specimen 2.....	179
7.5	Concluding remarks .....	182
Chapter 8	Conclusions and further work.....	185
Appendix 1	Wet lay-up manufacturing progress .....	191
Appendix 2	Quasi-static tensile tests.....	197
Appendix 3	Fibre density and tow area measures.....	199
Appendix 4	Numerical plane simulation to verify the SMF idealized model.....	201
References	.....	205
Acknowledgments	.....	209





# Introduction

Composites are a class of materials that is becoming more and more widespread because of the advantages that they can offer with respect to traditional ones. One of the main advantages of composite material are the high specific properties, since they present high stiffness and strength together with lightness, this because different materials are combined together giving birth to a material that has intermediate properties. So, industry have found in these materials the perfect answer for high-performance applications. The most used composite materials are 2D laminates of fibre reinforced polymers manufactured using ply-by-ply method, this is a labour-intensive technique but it permits to obtain very high in-plane properties and to tailor the response to specific application. Some examples of applications are: the aerospace sector, naval (boats hulls), military, automotive, wind turbines. Another important advantage of these materials is the important level of crashworthiness that can be reached adding these materials into a system, creating a specific structure to absorb energy, this is for example very used in the aerospace industry and it is becoming widespread also in the automotive. Nevertheless, these materials present also some drawbacks, for example delamination is very common in 2D laminates since through-thickness properties are very low with respect to the in-planes ones and given just by the resin between the plies, another one is the poor drapability that forces to separately mould the various parts and then join them together to create complex shapes. Laminates of 2D plies have also minimal impact damage properties, because of the poor through-thickness ones. To resolve these problems, through-thickness reinforcements were added and among all the results the most promising results came from 3D composite, where one part of the in-plane fibres are deviated in the z-direction. These gives a very high resistance to delamination, which is no more a damage mechanism that can bring the composite to failure, giving also enhanced impact properties. A 3D fabric is also easier to handle, complex parts can be moulded at a single time and because of the architecture it is faster to infuse a 3D composite than a 2D. The type of 3D composite under analysis, developed by the company 3TEX, have the important peculiarity of being a non-crimp fabric, which has better in-plane properties than 2D woven, since the yarns are straight, without interlacing like a stuck of unidirectional yarns at  $0^\circ$  and  $90^\circ$ . This is

a quite new material and despite the extensive use that composite materials have nowadays, 3D composites are not so widespread. One of the main concerns about composite materials is about fatigue properties, damage characterization and notch sensitivity. This work focuses on the latter problem, since other works have already been done about fatigue, while less has been done about notch sensitivity. This work investigates the notch sensitivity behaviour of 3D non-crimp orthogonal woven composites using Digital Image Correlation. This method is a non-contact solution to calculate the strains on the material surface using a set of cameras, a speckle pattern must be sprayed on the sample surface and then the software can calculate the displacement of a point, inside a subset area, with respect to the initial one, thus obtaining the local strain. This technique can provide both reliable full-field and local results, it is then suited to investigate the overall behaviour of a material. In this context, this work is one of the firsts that try to combine the information provided by the DIC to explain the notch insensitivity behaviour of the composite, finding a characteristic damage. Parallel to this, an analysis about the reliability of the DIC was done comparing it with electrical resistance strain gauges and FEM analyses. At the end a damage progression analysis in quasi-static tensile tests was done using optical and scanning electron microscopies.







# Chapter 1

## Literature review

### 1.1 Introduction

This chapter will describe the theoretical background of the topics that will be part of this work. In the first part, a classification of composites materials will be presented, then the focus will be about 3D composites, describing the diverse types, the manufacturing processes, advantages and drawbacks of each category. After that, 3D non-crimp woven composites will be extensively treated, describing 3D orthogonal woven composites in particular. This part will talk about their classification, their microstructure, the particular waving process that leads to this, the most common defects that can be found and the static mechanical properties of this category of materials. Then, the other topics that are part of this work are presented, a section will focus on the behaviour of notched composites, describing the outcomes of several works about 3D composites with notches. Later, the Digital Image Correlation basic principles are exposed, together with the mathematical background at the basis of this method. The investigation of notch sensitivity in 3D woven composites by using Digital Image Correlation represents the peculiarity of this work, since a little has been done in this direction to explain notch insensitivity of 3D woven composites, throughout a damage model.

### 1.2 Types of composites

Fiber reinforced composites is a class of materials that has emerged for its relevant properties in term of light-weight, specific stiffness, strength, fatigue resistance and corrosion resistance in comparison with classical metallic materials as steel or light alloys. So, their use is particularly appreciated when weight-saving is one of the project drivers. A primary form of composite is realized by different layers of uniaxial continuous fibers placed one over the other in a predetermined angular sequence, which is called ply-by-ply lay-up and forms a 2D laminated preform. For a better handling was introduced 2D waved fabrics, which is essentially formed by two interlacing fibers, called warp and weft, one over the

other forming a 2D sheet. This kind of material, presents also a good drapability in addition to the easier manual handling previously mentioned and it can be formed even in thick layers. The principal drawback of this class of 2D materials is the labour-intensive manufacturing required in the production processes, since it is required to cut and accurately place every ply before consolidating the laminate with the resin. Another important disadvantage is the lack of through-thickness resistance, due to the fact that in the thickness direction there is not a reinforcing structure and the only contribution is given by the matrix. The lack of through-thickness fibers means that in the manufacturing the plies could slip one over the other causing the misalignment of the fibres orientation, which is a serious drawback for the overall properties of the laminate. To partially resolve these problems was introduced the 3D reinforced woven composites, in which a part of the in-plane fibers is deviated and waved in the z-direction creating the through the thickness reinforcement.

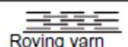
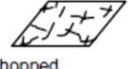
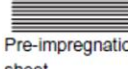

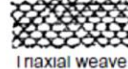
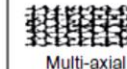
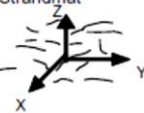

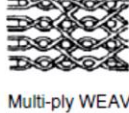



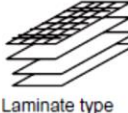
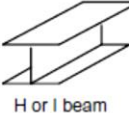
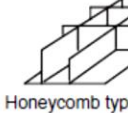
In Table 1.1 can be seen a classification of the various types of composites, as described before. The first category is composed of discontinuous fibers without a precise orientation, which makes them not suited for structural applications. The second category is constituted by the classical unidirectional plies, with the highest levels of fibers linearity and that gives to it the better in-plane properties but it has the drawback of inter-lamina and the intra-lamina weakness. The third category is composed by the 2D woven, which still presents the problem of the inter-lamina strength. The latter however presents better properties in terms of drapability than the UD ply, which need to be produced in separate parts and then joined together (by co-curing, adhesives or mechanical fastening), since they cannot be produced in complex shapes. Finally, the fourth category is composed by composites with reinforcement in all the three-dimensions, forming a spatial entanglement that gives better inter-lamina properties and against delamination than the previous types of composite.

*Table 1.1: Classifications of fiber composites [1].*

<i>Type</i>	<i>Reinforcement system</i>	<i>Textile construction</i>	<i>Fiber length</i>	<i>Fiber orientation</i>	<i>Fiber entanglement</i>
<i>1</i>	<i>Discrete</i>	<i>Chopped fibers</i>	<i>Discontinuous</i>	<i>Uncontrolled</i>	<i>None</i>
<i>2</i>	<i>Linear</i>	<i>Filament yarn</i>	<i>Continuous</i>	<i>Linear</i>	<i>None</i>
<i>3</i>	<i>Laminar</i>	<i>Simple fabric</i>	<i>Continuous</i>	<i>Planar</i>	<i>Planar</i>
<i>4</i>	<i>Integrated</i>	<i>Advanced fabric</i>	<i>Continuous</i>	<i>3D</i>	<i>3D</i>

Considering the composite dimensions, the fibers architecture and their direction, the various types of composite materials can be classified in the following way, according to Table 1.2:

Table 1.2: Composites classification [1].

AXIS Dimension		Non-axial	Mono-axial	Biaxial	Triaxial	Multi-axial
1D			 Roving yarn			
2D		 Chopped	 Pre-impregnation sheet	 Plane weave	 1 raxial weave	 Multi-axial
3D	Linear element	 Strandmat	 3D braid	 Multi-ply WEAVE	 Triaxial 3D weave	 Multi-axial 3D weave
	Plane element	 Laminated structure	 Laminate type	 H or I beam	 Honeycomb type	

### 1.2.1. 2D woven fabrics

Composites called 2D woven are produced using roughly the same techniques used to produce common tissues, which are around from thousands of years. They are the most common composites used today, and, as has been said, they are composed by warp yarns, also called ends, and by weft yarns, called picks. The manufacturing of these fabrics is fast, so it is economical with respect to the 3D waves, but they present an inherent high level of interlacing, also called waviness, of the fibers and that drops the mechanical properties with respect to UD laminates. Basically, the warp yarns are fed into the machine in  $0^\circ$  direction, which is the machine direction, and then the weft tows are inserted, lifting the proper warp tows. This operation is the one that controls the architecture of the 2D fabric. The lifting mechanism selects which yarns to be lifted, creating a space through which the weft yarns can pass, they are inserted at the right angle with respect to the warp tows, that is  $90^\circ$ . The yarns can be inserted through mechanical devices, using for example a shuttle as an old method, or using high-speed methods like through a long, slender arm (rapier), with high-pressure air or water. This weaving procedure creates a lot of damage in the yarns, especially if they are advanced fibers, so inherently brittle. This damage is caused because the yarns must pass through the heddles to be lifted up and down at every insertion, causing abrasion. This is one of the reasons, with

the yarns crimp, that affects and drops down the properties of this composites. The lifting sequence, and so the pattern created by the warp and weft tows, controls the properties of the resulting fabric, above all: drapability, tensile properties, fiber volume fraction. The important result of this traditional waving method is that yarns can be inserted only in  $0^\circ$  or  $90^\circ$  direction, and this is another one of the disadvantages of this technique. A scheme of a traditional weaving machine is depicted in Figure 1.1, where can be noticed the presence of the shuttle, carrying the weft yarns.

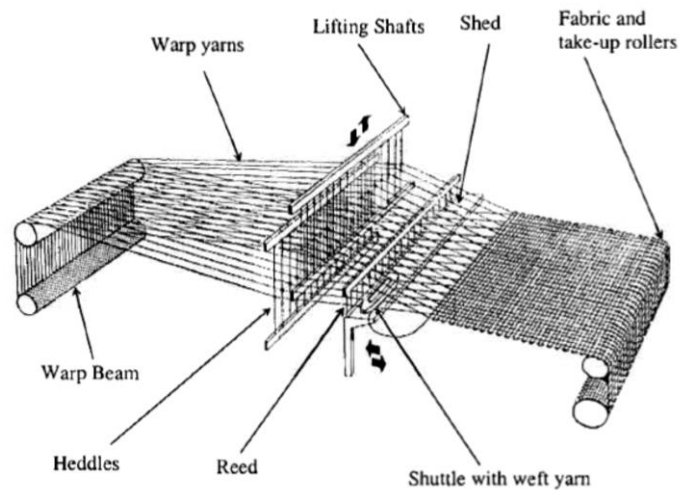


Figure 1.1: Loom example for traditional waving.

The waving process is usually divided in the following main parts which are also depicted in Figure 1.2 [2]:

- i. Shedding: lifting of the chosen warp tows (formation of an open channel) for the insertion of the filling yarns to form the desired pattern.
- ii. Filling insertion: weft tows are introduced in the open channel.
- iii. Beat-up: packing of the weft tows to the fabric using a comb-like device, called reed.
- iv. Take-up: the fabric is advanced by a series of rollers to replicate the process.

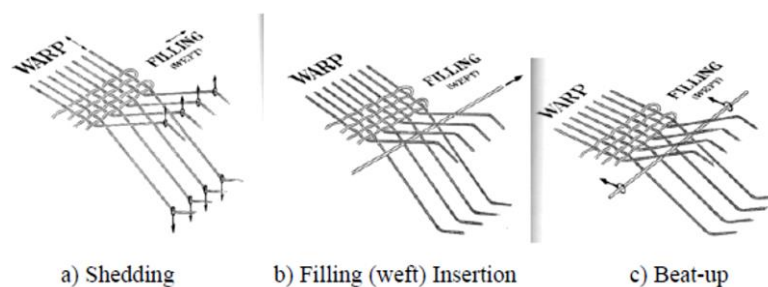


Figure 1.2: Waving process steps.

The different ways of combining the constitutive fibers can result in different outcomes which is visualized in different wave patterns. The final composites can have properties which can be the combination of the constituents or substantially different from the individual ones. The major types of 2D weave are the following:

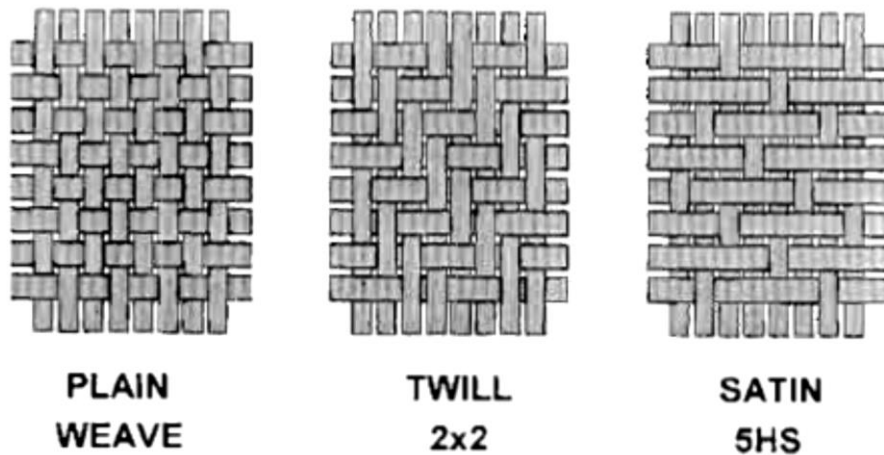
Plain weave: it is the simplest fabric and is obtained simply lifting and lowering alternatively a warp tow across one weft yarn. So, one end passes under one pick and then over another one and so on. It forms a strong and hardwearing cloth.

Twill weave: it is a fabric that reproduces itself after 3 or more ends and picks and produces diagonal lines on the face of the composite, where derives the name. It gives less intersections and a more open construction than the plain weave fabric. The smallest twill is generated by the repetition of 3 ends x 3 picks, there is no theoretical upper limit to this, but it must respect the manufacturability of the fabric. The twill weave is determined by a number, for example 2/1, which identifies the number of ends that pass over the picks, in this case an end will pass over two picks and then under one. So, the basic combinations of this pattern are four. Twill weave can also be made with the same number of ends and picks passing over and under each other, like: 2/2 or 3/3 twills. The resulting fabric is strong and has a great drapability.

Satin - Sateen weave: satins is a warp-faced weave and it is also called “warp satin”, they have usually more warp than weft density. Sateens are generally referred as “weft-sateen” and are weft faced, they have a higher density of weft than warp tows. They are used to produce a surface without twill diagonal lines and the first ones are more common because is cheaper to wove a fabric with less weft tows than warp ones. In order to avoid the twill lines, both satin and sateen waves must respect some rules. The weaving pattern must be as random as possible and they must interlace one time in every repeat. The steps that must be avoided are:

- One or one less than the repeat because it will form a twill or a plain weave.
- Ends and picks in the repeat must not have the same number and share a common factor, to make the yarns interlace.

So, the interlacements are never adjacent, the smallest possible weave number is 5 for either weave and cannot be constructed fabric with weave number of 6, 9, 11, 13, 14 and 15.



*Figure 1.3: Examples of 2D woven fabrics.*

As previously said, this type of composites has low strength and elastic modulus in the through-thickness direction, since their mechanical properties in this direction relies on the properties of the resin matrix and of the fibre-resin interface. A proof of that can be seen in Figure 1.4 and Figure 1.5, where can be seen that the properties in z-directions are approximately 10% of the in-plane ones and so they cannot be used in structures that must support high inter-lamina shear loads or through-thickness loads [3]. Another problem related to that is the poor impact damage properties and easy delamination, caused by the lack of a z-reinforcement. The latter one is the most common and difficult to defeat failure mode in these materials [2]. This loss of mechanical properties is often counterbalanced with a thickness increase in the design stage, that over-engineering causes an increase in costs, weight and time. Other problem related with these woven composites are that they present anisotropic properties, poor in-plane shear resistance, difficulties in handling and manufacturing because is required the positioning of every ply, one over the other [3].

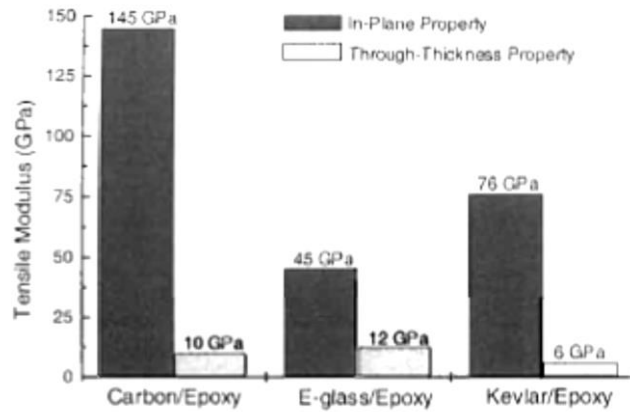


Figure 1.4: In-plane and through-thickness modulus comparison of a generic 2D composite.

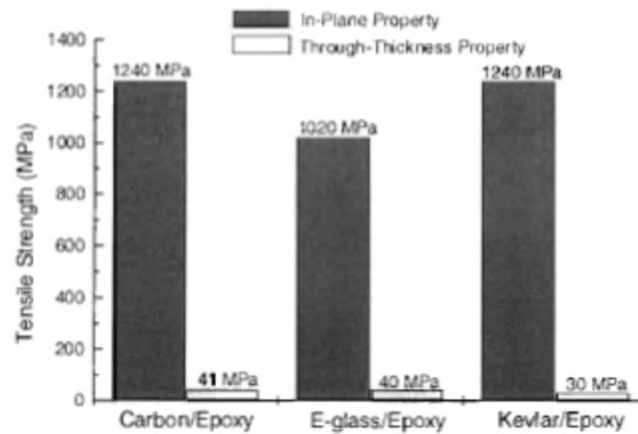


Figure 1.5: Figure : In-plane and through-thickness strength comparison of a generic 2D composite.

### 1.2.2. 3D reinforced composites

3D composites have been developed to improve the 2D woven composites lack of mechanical properties. As said, the major improvements are in reduction of manufacturing costs since it is avoided the labour intensive manually lay-up of the plies, increase of through-thickness properties (stiffness, strength and fatigue resistance), impact damage resistance and resistance to delamination (improve of interlaminar fracture toughness), avoiding the need to use prepreg that must be preserved in refrigeration facilities. Also, the prepregs have a low drapability, so they cannot be moulded in complex shapes but they must be produced in different pieces and then joined. 3D reinforced composites can be made using different techniques, the two major ways to do this are:

- 1) Adding some z-reinforcement in the through-thickness direction
- 2) Re-directing some of the primary yarns in the secondary direction

The most utilized techniques are: insertion of short rods in the thickness of the conventional laminate also called z-pinned reinforcements, using special weaving techniques like braiding, stitching and knitting, or using 3D weaving. The first category before mentioned gathers: stitching and z-pinning, while the second: 3D braiding, knitting and 3D weaving.

### 1.2.3. Braiding

Braiding is the first manufacturing technique used to produce 3D composites. It was firstly used in the late '60s to produce innovative rocket motor parts for hot temperatures in substitution of alloy parts, with the purpose of weight reduction, archiving weight savings of 30%-50%. They were also used in airplane brakes for elevated temperature purposes. It has good drapability, torsional mechanical properties and low presence of defects [3]. It can be distinguished several types of braiding, the majors are: two-step braiding, four-step braiding (with the subtype of the multi-step braiding) and multi-layer braiding. All these techniques involve a deep interlacing of the tows along an axis.

2D braiding: this technique is carried out with the use of a set of coupled counter-rotational yarn carriers that rotate around a circular frame. During the process, every yarn passes from one gear to the next. The shapes that comes from this procedure are usually flat or tubular fabrics and it can be also performed on a mandrel to produce intricated preforms. The preforms shapes can vary in cross section, vary dimensions in their lengths, have holes or attachment points incorporated saving extra-steps and improving the mechanical properties. Braiding, unlike all the other systems to produce composites, can produce fabrics with fibers at  $0^\circ$  and at  $45^\circ$  or at other angles, with the exception of fibers at  $90^\circ$  for intrinsic manufacturing reasons. This technique has the drawback that it cannot easily produce thick structures and for this reason was introduced the following technique that is the four-step braiding. The two steps of this method, from where it is called, are the following, in the first one the yarn carriers alternately rotate in one diagonal direction while the mandarin remains still, in the second step they invert their moving direction.

Four-step 3D braiding: in this method is required a flat bad that combines the yarns. It is called four-step since four distinct stages are required for the manufacturing, between



each step the yarns are mechanically packed, like the beat-up stage in the classical weaving, to consolidate the resulting fabric. For this method, it is utilized a flat bed of yarns and columns of yarn carriers, additional yarn carriers depending on the shape to be produced. This method takes four motions of rows and columns to produce the final preform. This method is characterized by the fact the all the yarns are lying at different angles with respect to the axial main direction and, also, the through-thickness direction, as can be seen in Figure 1.6 (b). The mechanical properties of the product can be chosen changing the angles of the yarns in three-directions.

Two-step 3D braiding: unlike the previous method, in this one there are various yarns fixed in the axial direction and a smaller number braided at a different angle. The resulting structure is generally constituted by some axial yarns connected by other angled through-thickness yarns, as depicted in Figure 1.6 (a). It should be noted that, the quantity of axial and interlacing yarns can be chosen to suite the particular application. The two steps consist in the two movements of the yarn carriers through the structure formed by the axial yarns. It can forms very intricated shapes and does not requires the beat-up stage differently from the four-step process.

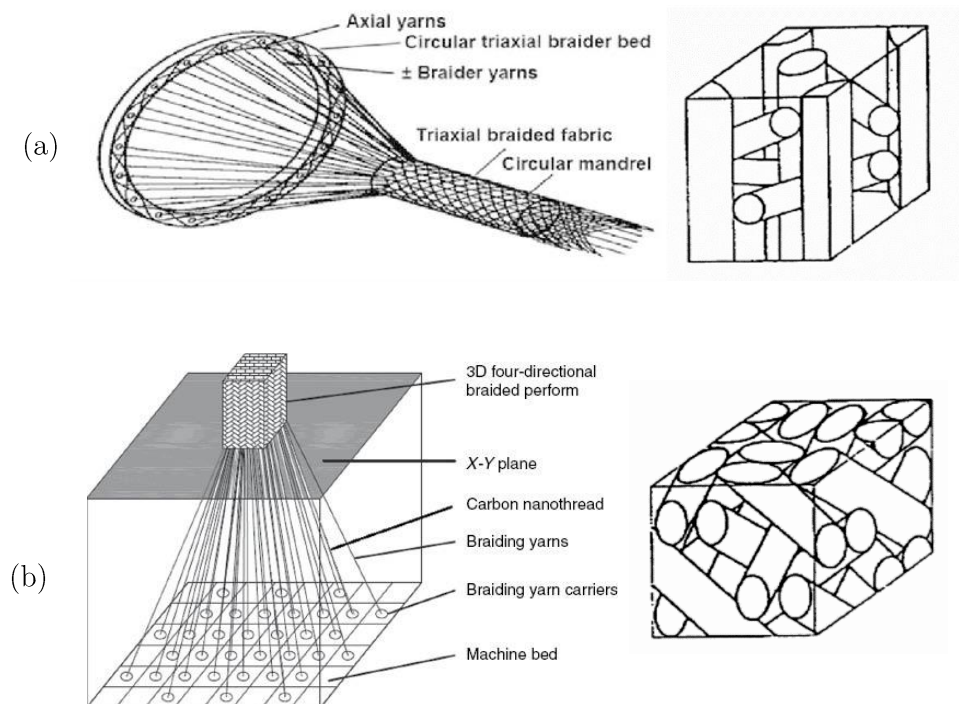


Figure 1.6: Example of the braiding techniques, (a) two-step 3D braiding and (b) four-step 3D braiding with their resulting fabric structures.

In both methods, holes and inserts can be braided in the structure increasing the mechanical properties, with respect to the machined ones. It can be used different types of fibers: glass, carbon, aramid, ceramic or metal.

The main advantages of composites produced with braiding over 2D woven are [4]:

- Possibility to produce near-net-shape preforms.
- Automated production.
- Higher delamination and impact resistance, due to the high interlacement.
- Higher crashworthiness properties.
- Less sensitive to notches.

The disadvantages concerning this method are [4]:

- The size of the preform is controlled by the size of the machine.
- Long set-up times.
- Slow and expensive machines.
- Little investigation of some mechanical properties.
- Lower stiffness and strength than 2D laminates (most of the twos are off-axis with the load and presents a high level of crimping).
- Lack of predictive models for strength and fatigue.
- Complex failure mechanisms with respect to the 2D laminates because they depend on a wide multitude of factors.
- The mechanical properties are strongly affected by the conditions of the edges.
- Uses confined to long and slender structures.

#### 1.2.4. Knitting

This class of 3D composites comprehend the least understood and used of all the processes generally utilized. Can be distinguished two different processes of knitting: weft knitting and warp kitting, both of them can be produced on standard knitting machines with the use of carbon or other classes of fibers. In warp knitting, several yarns are fed in the machine in the main axial direction and each yarn forms a series of knits loops in the production direction. Otherwise, in weft knitting, only one yarn is inserted at 90° with respect to the production direction and it forms a line of knits in the width of fabric.



Figure 1.7: (a) weft knitting and (b) warp knitting.

The production method is carried out with the use of a needle bed (in circular or flat configuration) that creates the knit loops through the previously made knit loops. In weft knitting the yarn carrier draws the fibers through the needles as it travels across the width of the needle bed. In warp knitting, every knitting needle has an individual supply of yarns. The standard knitting methods can produce 2D fabrics, however with the use of many needle beds, also 3D fabrics, made of multiple layers, can be produced. The resulting product presents a high fabrics curvature level, which causes a loss in the mechanical properties. Moreover, compressive properties are greatly affected by the aforementioned characteristic. However, this high interlacing level causes high level of impact damage resistance and damage tolerance, it also provides high levels of deformability and thus it is suitable to produce complex-shape components for non-structural applications.

The main advantages of 3D knitting composites over 2D laminates are [4]:

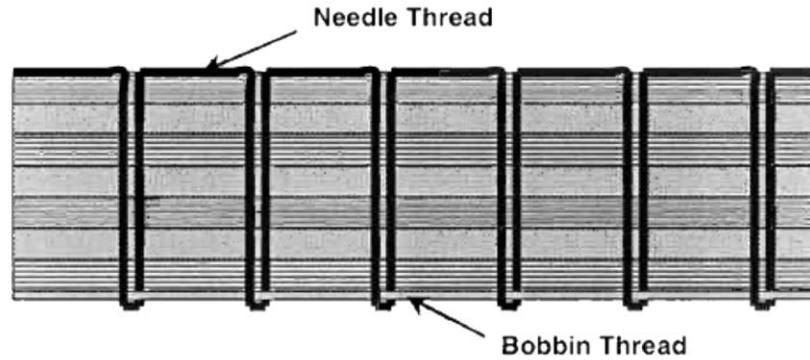
- Better formability because of their enhanced drapability.
- Possibility of producing near-net-shape preforms.
- Lower specific density.
- Higher impact damage resistance and crash worthiness.

The disadvantages are otherwise:

- 3D knitting machines are still under development.
- It is difficult to create thick preforms.
- Crimping and breakage of the in-plane fabrics.
- Lower in-plane stiffness and strength.
- Failure modes not completely characterized.

### 1.2.5. Stitching

This is the simplest one of the various manufacturing techniques to produce 3D composite materials and it can be done with a small investment. It consists in sewing high tensile fibers like glass, carbon or Kevlar, using a needle in the z-direction, through a stack of uncured prepreg or dry fabric 2D plies. Aramid yarns are the most commonly used in stitched composites as they are more resistant in handling than glass or carbon fibers and presents high toughness. Must be said that, this type of material presents the drawback of the easiness in absorbing moisture, this fact accelerates several times the speed of environmental degradation of the structures. They also present the difficulty in binding with some type of resin matrix. Glass and carbon do not have this problem but it is more difficult to use them for stitching. The main problem, however, remains the fact that the insertion of the z-binders causes the breakage and the distortion of some in-plane fibers, this damage causes a reduction of the properties of the material, approximately with a reduction in strength, Young's modulus and fatigue resistance of 10-20% [4]. This is also caused by the formation of resin rich channels which generates stress concentration and becomes a preferential sport for damage formation. So, it is preferable to stitch uncured prepreps to minimize the caused damage. Another limitation to this method is represented by the thickness of the specimen to be stitched, which is correlated to the capability of the needle to penetrate the fabric layers. The most recent machines can perform the required task only from one side, on the preform as it is on a table, thus simplifying the manufacturing process. A grate advantage of this method is the use of standard 2D fabrics in the lay-up, so it is possible to tailor the properties for the required application. It can also be put only in so specific areas to reinforce them, as at the edges of the composite laminate. Another main application for this method is in joining different parts, since stitched joints presents high strength, in some cases even higher than with the use of metal inserts. A lot of research was driven in this field, mostly by aircraft manufacturers in order to improve the knowledge for the application in aircraft joints, this to reduce the use of mechanical fasteners because the first are lighter and provide a more uniform stress state. The problem of the accelerated environmental degradation is the main drawback that limits the use of this method in certain application, like in marine ones. Another problem is related to the sewing machine that limits the dimensions of the stitched preform, since large preforms are not easily stitched. This method, as the following, involves another manufacturing step and it is so time and money consuming.



*Figure 1.8: Section of a stitched composite.*

Summarizing, the principal advantages of this technique are:

- Improvement in handling the preforms.
- Higher impact damage resistance.
- Higher delamination resistance and fracture toughness.
- High joint strength.

The limitations are, on the other hand:

- Limitation in width and thickness of the preforms.
- Impossibility to stitch complex shapes.
- Degradation of in-plane properties.
- Easy environmental degradation of the joining structures.
- It requires one more manufacturing passage.

### 1.2.6. Z-pinning

This method is an alternative method to stitching and consists in incorporating in the structure some short rigid pins, through the stack of the 2D plies. One of the methods utilized to insert these pins is to place the procured fibers in a thermoplastic matrix positioned upon the stack of the plies or dry fabrics, inside a vacuum bag. During the manufacturing process, the thermoplastic foam will collapse because of pressure and temperature and the z-pins, forced by the vacuum, will be inserted into the prepreg. This procedure can be carried out in a standard autoclave or using, at room temperature, ultrasounds that heat up a local region around the pins. The in-plane properties go down as the volume fraction of the z-pinnings increase, but the damage created by this technique to the yarns is less compared to others and also there is less fibers crimping. Some

problems that may arise with this method are the misalignment of the in-plane fibers around the pins, caused by the need of these to create a space for their self, so the in-plane fibers are distorted and pushed aside, around these regions are also present some resin pockets in both the sides of the pins. These resin regions, generated by the pins, create some tunnels that passes from one side to the other of the laminate. As noted for the previous method, also this one involves an additional manufacturing step which leads to time and money increase.

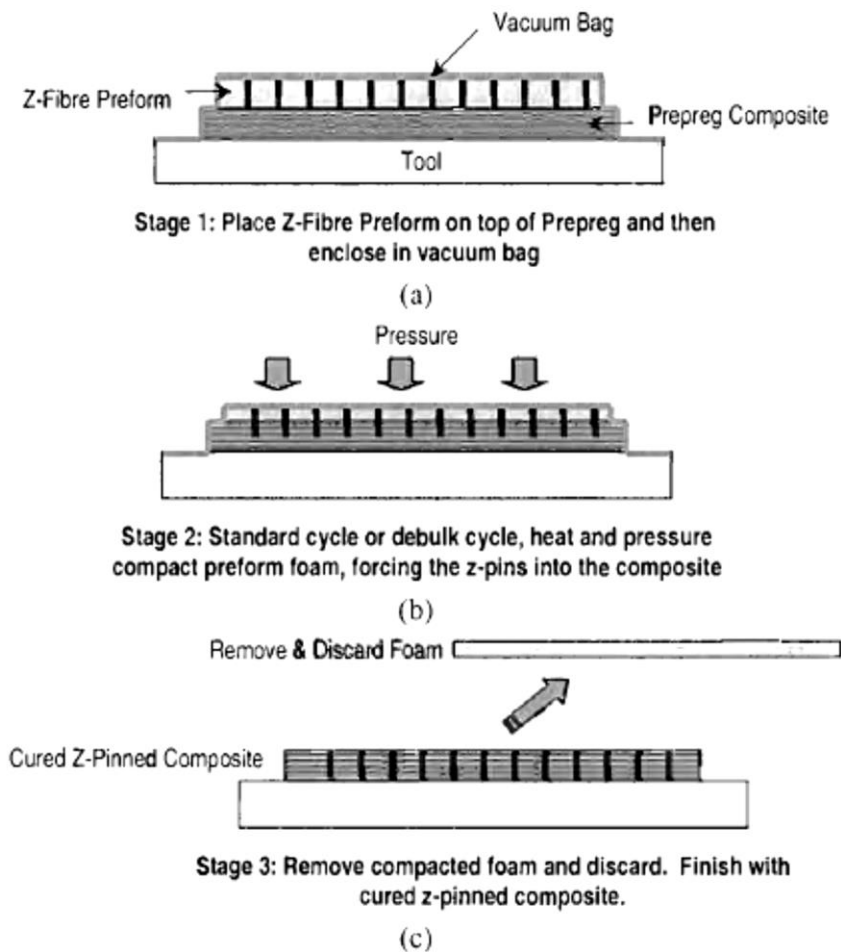


Figure 1.9: Z-pinning insertion using the autoclave method.

### 1.2.7. Non-crimp fabrics

This is a method that combines aspects of weaving and knitting, it can be utilized with the most common types of fibers as, glass, carbon and aramid. The material utilized as joining material is usually polyester yarns. The machines used for this method forms knit loops outside the layers, so it does not damage the laminate. The lay-ups that can be

utilized are all the most common as,  $90^\circ$ ,  $45^\circ$ ,  $0^\circ$ , since the process is very flexible. The limitations are on the total thickness, the order of the lay-up (in some types of machine, since outside can be preferable to have  $0^\circ$  plies) and the order of the stations to be linked in the length. This technique can be described as a fast method, since it can reach high production volumes and it can operate with large materials width. NCF are widespread because of their higher in-plane properties than using 2D woven fabrics, one other advantage is the easiness of manufacturing since is avoided the lay-up process. These structures, however, do not presents improvements in the out of plane properties or in the impact resistance since it is utilized as z-binder not a structural fiber. Non-crimp fabrics are usually used in high performance sectors as, aeronautics, yachts and wind turbines.

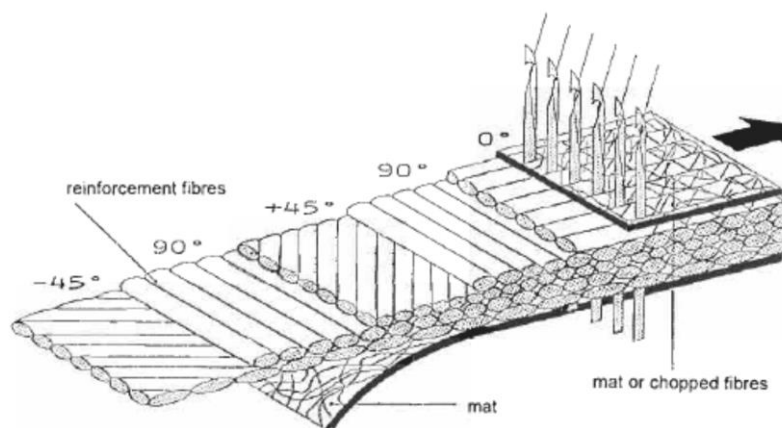


Figure 1.10: Schematics of the process to create an NCF composite.

### 1.3 3D non-crimp woven composites

This method consists in a multi-layer weaving of yarns. The main difference with the traditional weaving is the need to feed the waving loom with different layers of warp yarns (i.e. yarns in the longitudinal direction) and this can comport high set-up times for the machines. The machines that can produce this type of material can be some modified traditional looms, as the Jacquard looms, where are inserted multiple needle eyes in the lifting mechanism that permits the use of different layers of warp yarns, or special developed machines, as the ones owned by 3TEX. Utilizing the traditional looms to create the 3D structure, damage is inserted in the yarns as for the weaving of the 2D fabrics. It was found that there is a loss between 30% and 50% of the initial yarn strength due to the abrasion caused in the weaving process, according to paper [5]. Since there are different

layers of weft yarns (i.e. yarns in the transversal direction, also referred as filling yarns or picks), different sheds (i.e. passages for the insertion of the weft yarns) are created, through this can be controlled the insertion sequence of weft tows and so the resulting pattern. The third type of yarns in this material, the binding yarns in z-direction, can be inserted either in the warp or in the weft direction and their path through the thickness can be controlled by the lifting sequence, obtaining different categories of 3D woven composites. In every type of geometry, the resulting effect of the out-of-plane reinforcement is also an induced waviness of the in-plane fibers (varying a lot for the specific configuration) and a reduction of their volume fraction, reducing so the mechanical properties. Must be said that for all the categories that can be created, only architectures containing just  $0^\circ$  and  $90^\circ$  in-plane yarns are possible, as for the traditional weaving, the z-binders although can be oriented at different angles choosing the interlock sequence. This is a main limitation looking at the shear and torsional properties.

3D composites were first developed in the '70s to replace some expensive structures subjected to high thermal stresses made in light alloys, like airplanes brakes for aeronautical companies. The research in this field remained still until the '80s when there was a renewed interest to resolve the problems encountered with the traditional 2D laminates, above all, expensive manufacturing processes and problem during the maintenance or during general work for accidental damages due to object hitting the fuselage, caused again by the low impact-resistance properties.

As for other types of 3D composites, also 3D woven provides better through-thickness properties (i.e. transverse strength, fracture toughness), virtually suppressing delamination and improve impact and ballistic resistance. On the other hand, it is necessary to make a trade-off between these properties and the in-plane ones, since the latter are degraded with the improve of the first. Some disadvantages related to the use of these materials are: lack in mechanical characterization data, problems for joining different thick structures, lack of universally accepted and approved mathematical models and tools. The most important advantages of the 3D woven composites are:

- Possibility to produce component via near-net-shape manufacturing, also for complex shape components.
- The previous point can reduce the overall production expenses, reducing the various manufacturing steps and the material wastage, making the production of these composites less expensive and simpler.



- The percentage of the different yarns can be tailored to suite in the best way the application needed. As an example, can be chosen the percentage of the z-binder to improve the out of plane properties, even if their proportion is usually less than 5% and almost never over 10%.
- Possibility to produce hybrid woven composites using together different types of materials, which is one of the fields where the research on these materials is focusing today.
- Like all the aforementioned 3D composites, they present higher impact damage resistance, through- thickness properties and delamination tolerance. It has been reported that the impact energy to initiate damage in 3D woven is up to 60% greater than in 2D carbon-bismaleimide composites, also the mode I interlaminar toughness was reported to be ~ 6-20 times higher than UD carbon-epoxy laminates [4].
- They can present higher strain-to-failure values.

The main problems related to them are, on the other hand:

- Impossibility to produce 3D composites with different in-plane yarn orientation except for  $0^\circ$  and  $90^\circ$ , this causes low shear characteristics and so they are not suited for main torsional loads. Another result of this are the anisotropic properties that they present which is a limitation for their extensive use in the aircraft sector.
- Low characterization of the failure mechanisms and of all the properties, specifically for all the various types of geometries that can be produced and analysing also the hybrid yarns. This still does not permit to create the optimized structures as in-plane and in z-direction properties for a specific design.
- The in-plane properties of the 3D woven are similar to 2D UD laminates regarding the stiffness, but inferior for tension and compression strength.

Some applications where 3D non-crimp woven composites are used are, aerospace components mainly subjected to bending loading and with limited torsion (some parts of leading and trailing edges of the wings), beams and floors in trains, ferries and trucks; they can also be utilized in civil infrastructures or medical prosthesis. Another field should be the use as energy absorbers and crash members. Another particular application could be the use as container for heavy carriage in substitution of metallic containers to reduce the weight of the tare, making it more cost efficient.

The three possible types of 3D woven composites are here listed:

- Orthogonal woven

- Through-thickness angle interlock
- Layer-to-layer angle interlock

This does not divide the three categories by process or machine used, even if 3D orthogonal wave can be done on specific machines with a different process.

In the following paragraphs, these structures will be briefly discussed.

### 1.3.1. Through-thickness angle interlock and layer-to-layer interlock

Through-thickness angle interlock fabrics are made of straight weft yarns interlaced by the warp yarns that pass through the thickness, waving in a diagonal direction. If the interlacing comprehends each layer of the structure, then it is called layer-to-layer interlock. There can also be straight warp yarns added, with still the presence of the angled binders. It is important to notice that angle-interlock present low values of shear modulus, in particular if the binding fibers are constituted only by warp yarns, because the only shear resistance in this case is provided by the friction that is exerted at the upper and lower faces. This produces otherwise a good drapability that provides a good formability for spherical or complex shapes.

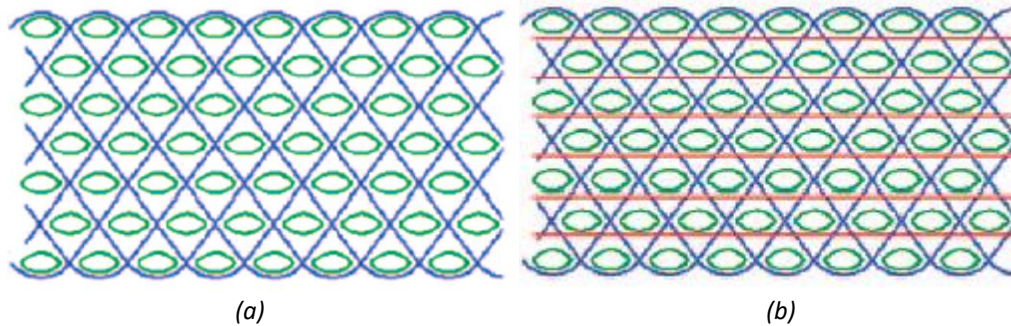


Figure 1.11: (a) Through-thickness interlock, (b) Warp yarns added

For the layer-to-layer interlock, every layer is visible since it is separated by the other through a layer of weaving fibers. The stitching fibers can pass from any layer to another, but they are supposed not to change the pattern of the in-plane yarns. Usually, for more stable fabrics, the rule of making the binding yarn pass on adjacent layers is followed, one above and one under. This structure, for its intrinsic nature, has a high level of crimping, since even the inside layers are weaved by the binding layers, differently from the through-thickness or for the orthogonal wave where only the external layers experience high levels of crimping. This gives to this type of 3D composite a lower in-plane

Young's modulus. Even in this case, like for through-thickness interlock, straight yarns in the warp or weft direction can be added to increase the tensile modulus in the fibres direction. Yarns inserted through the thickness add only for a little part their contribution to the overall stiffness and strength in the in-plane direction.

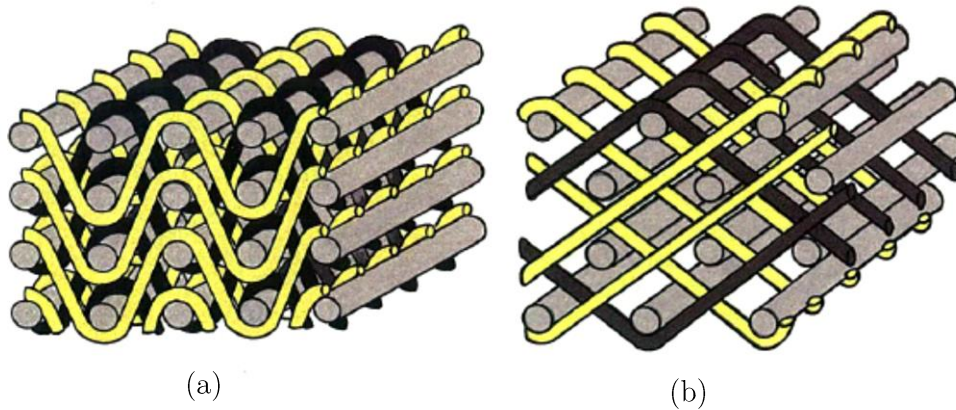


Figure 1.12: Representation of 3D interlock weave; (a) angle interlock 3D weave and (b) warp interlock 3D weave.

### 1.3.2. Orthogonal woven architecture

These types of structures are often produced using the machines developed in the late '80s and early '90s at the North Carolina State University by Dr. Mansour Mohamed et al. This invention led to the US patent for this technology, which is now a property of the company 3TEX with the name of 3WAVE.

The peculiarity of this type of 3D woven is the fact that z-binders passes vertically the whole composite thickness any two weft yarns between the top and the bottom, interconnecting all the weft and warp yarns. Total thickness is indicated by the total number of warp and weft layers. The number of the warp layers can be normally expressed by:

$$\text{weft yarn layers} = \text{warp yarn layers} + 1 \quad (1.1)$$

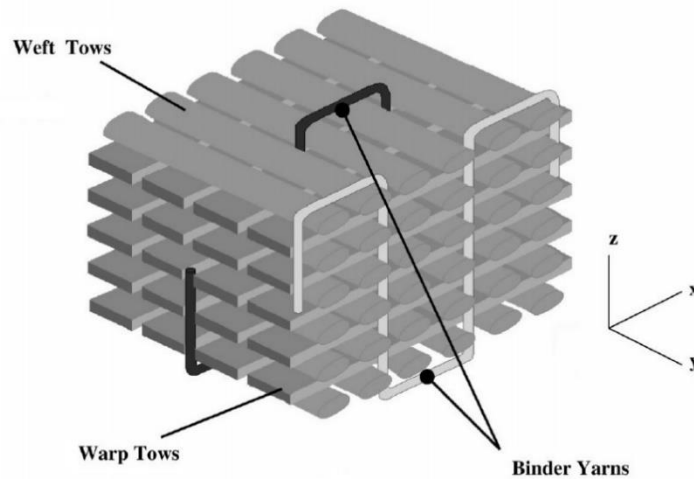


Figure 1.13: Schematic representation of a 3D orthogonal fabrics.

Two different types of orthogonal woven fabrics can be seen, depending on the binding-yarns geometry; there can be one or two sets of z-binders, the first are the most common orthogonal wave, the second are less common and addressed as enhanced orthogonal structures, because of the two sets of opposite-traveling binders, as can be seen in the next picture. The binding yarns do not add any sensible contribution to stiffness and strength in the in-plane direction, instead they contribute mainly to the properties in the out of plane direction.

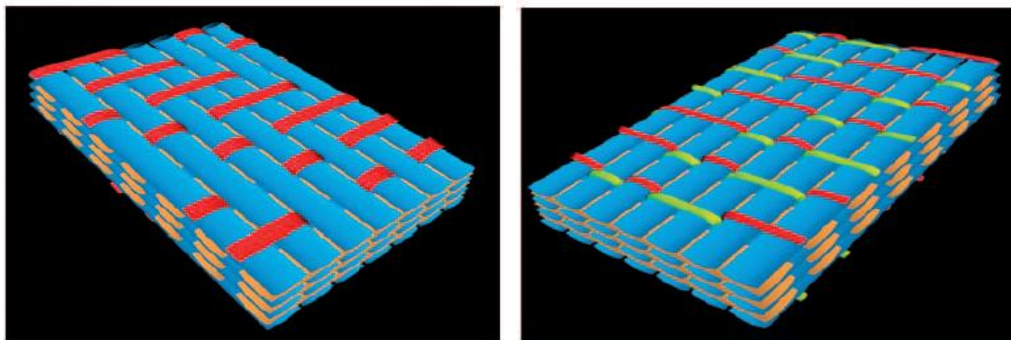


Figure 1.14: On the left the ordinary orthogonal wave, on the right the so called enhanced orthogonal wave.

The main advantages of this technique, developed by 3TEX, are:

- Warp and weft tows do not interlace themselves, giving an approximately zero-crimp structure, since both runs straight.
- Insertion of all the weft tows in series between two z-harness motions carried by a special system through the warp tows at every cycle.

- The possibility to produce hybrid systems using different types of fibers and with different architectures, by means of special system for the through-thickness insertion of the z-yarns.
- The weft and warp yarns do not pass through the harness frame so the method induces low damage on the yarns. Only the z-binders must pass through the harness system, so through the heddles of the weaving machine, to be moved up and down. This permits to these machines to work with brittle fibers as graphite, ceramic or optical fibers [6].
- All the weft and warp yarns remain basically straight, giving to them the name of non-crimp fabric, so they are supposed to have a lower downgrade of the in-plane properties with respect to 2D woven composites.
- Faster and cheaper manufacturing process since one layer of 3D composite replaces multiple layers of 2D fabrics, giving the same thickness.

Another improvement related to produced geometry and so to the straightness of the in-plane yarns, to the single layer architecture and to the poor presence of defects, is the faster propagation of the resin in this fabric produced by 3TEX than in common 2D woven fabrics. Due to the low presence of defects and the well-defined structure, this type of 3D woven provides a repetitive grid with open channels for the flow of the resin. With the superposition of single layers of 2D woven, some parts can nest together and interfere with the infusion process. The benefits of the faster resin flow are that larger fabrics can be infused in the same time (i.e. there is more time for the resin to flow) or can be utilized a more viscous resin with the advantage that the resin can be less heated during the infusion to make it thinner [6]. The time saving factors can be thus summarized:

- Faster and so cheaper infusion process
- Avoid the manual lay-up of the plies (avoiding the misalignments and defects that can arise at this point)

### 1.3.3. Weaving process for 3D orthogonal composites

In this chapter, it will be presented the peculiar method utilized to produce the material, which is analysed in this thesis that is the one developed by 3TEX, trying to present the differences from other manufacturing methods and its drawbacks in producing 3D woven.

Traditional weaving machines were studied to produce 2D fabrics with high productivity, some modified machines can also produce 3D fabrics but doing this one layer every time

and this reduced a lot their speed. The main drawback with the use of these machines is the damaged imparted to the fibers, because every yarn needs to pass through the heddles, which are moved up and down every cycle, or to be in contact with some moving parts. This continuous contact between the fibers and the heddles and between fibers and fibers produces abrasion in the yarns and their strength results greatly affected by this, thus limiting the possible speed of the machines. They also provide higher levels of crimping with respect to the weaving process by 3TEX.

3TEX has created, at North Carolina State University, a new type of specialized weaving machine to produce at high speed and with low levels of crimping 3D fabrics, even for thick composites. Its speed derives from the fact that it is an inherently 3D method, so the structures is not built as the result of the different 2D plies junction, instead it derives from a simultaneous insertion of multiple weft yarns at a time, so a unit of thick composites is formed at each weaving cycle. The resulting machine has therefore nothing in common with the classical equipment for the traditional weaving. Since during the production process this new type of machine is very gentle with the fibers and induces in them approximately zero-crimp, hybridization with the use of different types of fibers is very easy and every yarn type and every layer can be modified individually. Moreover, the types of material that can be used for the z-yarns are: glass, carbon, ceramic, Kevlar, polyester and also stainless steel or other metallic alloys. Also, optical fibers can be wired as z-yarns in order to be used as strain sensors for the material itself or for the bonded joint. All the weft and warp yarns do not need to pass through the heddles, but only the z-binders needs to pass through them in order to be moved up and down to create the interlaced structure, so only in the latter is inserted a degree of damage. Moreover, even the size of each yarn can be modified, using for example different sizes for the z-binders in different composites. The peculiar simultaneous insertion of the fill yarns permits to reach a high level of productivity, even at low speed and so the greatest advantage there is when producing thick composites.

The different stages, presented in the 3TEX patent for their new weaving method to produce 3D fabric in a fast way are presented below [7]:

Stage 1: the z-harness for the z-binders and all the harness for the warp yarns are positioned up, while the heddle Z2 is positioned down to create an open passage for the insertion of the weft yarns. These are placed with the use of a mechanical rapier and then

they are cut, forming the first layer of the 3D woven fabric. At the end is performed the beat-up stage by the component number 18.

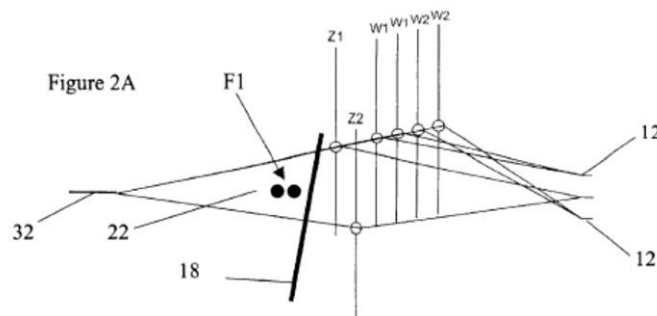


Figure 1.15: First stage of the 3TEX weaving method.

Stage 2: for the introduction of the second layer, out of three, the Z2 and W1 harness are positioned down and the harness W2 remains up for the insertion of the second layer of y-direction filling yarns F2. Also in this case the last event of this stage is the beat-up part by the component 18.

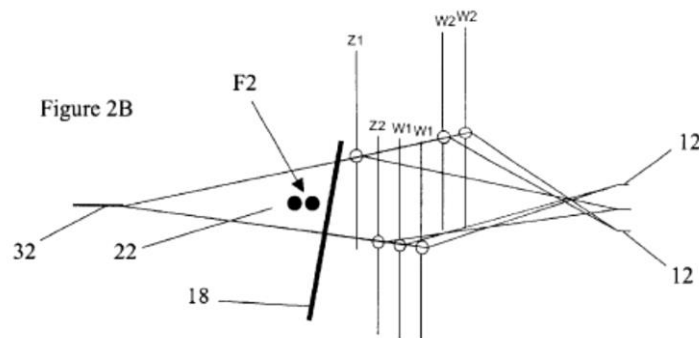


Figure 1.16: Second stage of the 3TEX weaving method.

Stage 3: the harness for the z-binders are still in the same position but now all the harness for the x-direction fibers are down for the insertion of the top later of the y-yarns F3, then beat-up occurs.

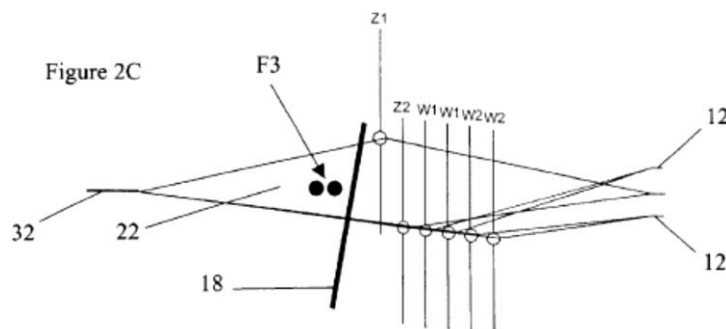
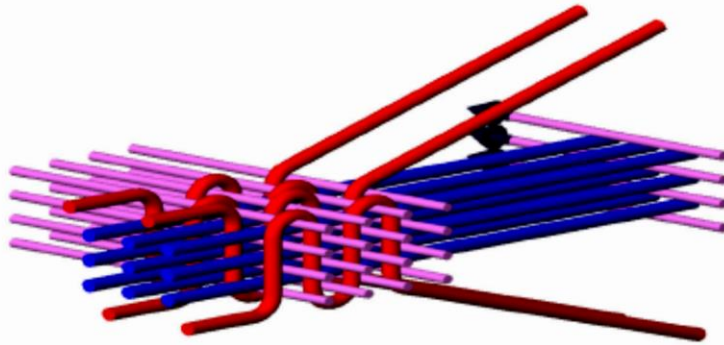


Figure 1.17: Third stage of the 3TEX weaving method.

Take-up is the next stage, where the x-yarns are advanced by adjusting the rotational roll, advancing the structure until one cycle is completed. For the next cycle, the passages start again with the x-direction warp yarns in the same position but inverting the position of the z-binders in order to produce the wavy structure of the binder, to cross each other from top to bottom surface. The following steps for the new weft yarns insertion starts again from the latest stage of the previous cycle. All the x-direction harnesses are still down, but now the z-binder has been inserted in the structure. So, now the weft yarns can be inserted again. The following stages happen in the reverse order as the ones showed before. A representation of the 3TEX process is depicted in the next picture, Figure 1.18, where is visible the weft yarns insertion while the z-binders are kept in opposite direction to create their weave pattern.



*Figure 1.18: Representation of the yarn positioning from 3TEX.*

This new technique permits to create a fabric with low defects and low internal waviness and this permits to have comparable in-plane properties with the 2D weave laminates and superior compared to the through-thickness interlock, since the latter presents higher levels of crimping and a lower shear modulus, this will be widely explained in the next chapters.

#### 1.3.4. Microstructure of 3D woven composites

The innovative weaving method developed by 3TEX have improved some of the drawbacks that were caused by weaving 3D fabrics. These defects, as was before mentioned, cause the loss of in-plane, impact and, in a lower way, also through-thickness properties.



In this chapter, the most common defects that are present in 3D non-crimp woven composites are presented and also the different results of the weaving processes with the use of the standard modified looms or the 3TEX ones.

The following kind of defects could be seen with the use of an optical or scanning electron microscope, in particular when the 3D fabric is produced with the use of an electronic Jacquard loom:

- *Z-binder crimping*: even if theoretically z-binders path should be orthogonal to the in-plane fibers, practically the z-yarns presents a wavy profile since during the weaving process it is necessary to apply a tensile load to the fibers that causes the different final shape. When 3D non-crimp orthogonal composite is manufactured with the use of a 3TEX machine, the z-binders still presents a wavy shape but less enhanced than for the same composite made, as an example, on modified Jacquard looms.

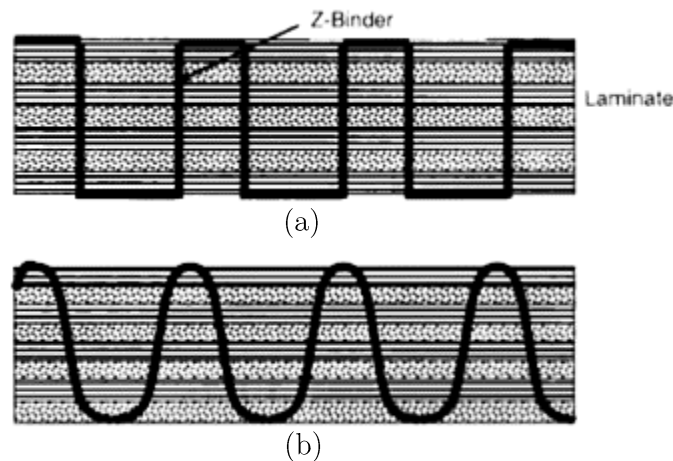


Figure 1.19: Ideal (a) and real (b) z-binder profiles for 3D non-crimp orthogonal fabrics.

- *Polymer-rich regions*: these regions are formed nearby every z-binders and polymer channels are formed in the region where the z-yarns present the sinusoidal shape, dividing the in-plane weft yarns. The first kind of polymer-rich region is depicted in Figure 1.20 and it is due to the fact that the warp yarns are widened to make space to the z-yarns. During the infusion, the resin fills these regions that have a gap between the yarns, forming two polymer channels aside of every z-binder viewing the composite from the top. Other two polymer-rich channels are formed above and under the z-binder, viewing it from the side. It is important to notice that increasing the z-yarns volume content, these channels raise and so, the mechanical properties goes down as will be seen in the next chapter.

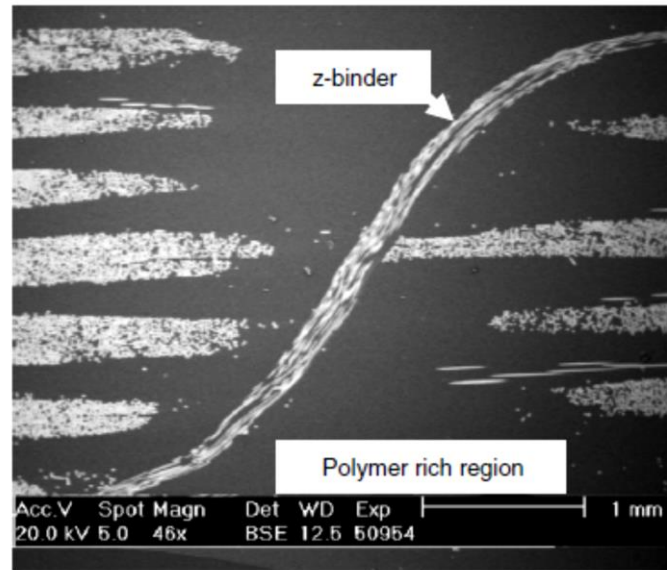


Figure 1.20: Lateral profile of a z-binder taken from a scanning electron microscope, showing the sinisodal shape. The resin rich regions between the weft tows are also visible.

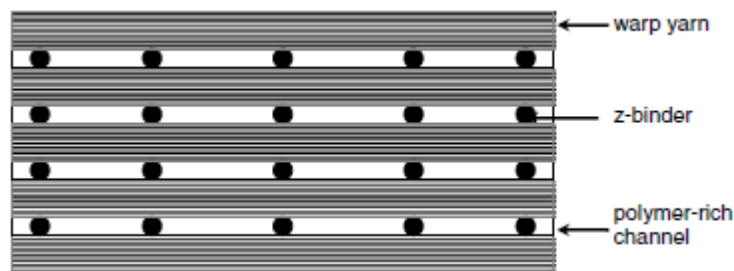
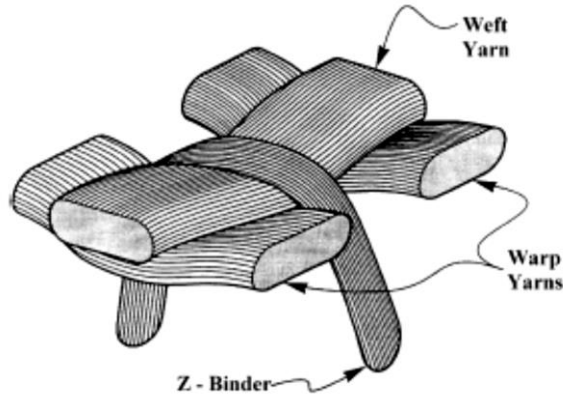


Figure 1.21: Vertical view of a section, showing the polymer-rich channels in the space where the z-binders are.

- *Damage of z-binders*: when the z-fibers are woven, they must be lifted up and down passing through the heddles, with a great downgrade of the tensile properties, above all the strength, whereas the stiffness is not so affected. When passing through the eyes, abrasion is generated to the fibers and they are constrained to change direction, being bent. These actions on such a brittle material cause microcracks that are very dangerous. When the fabric is weaved using a modified 2D loom, abrasion is also caused in the in-plane yarns because they slide against moving parts of the machinery. The overall downgrade of the tensile properties can be of 30% or even more.
- *Fibre crimp*: undulation of the yarns can be seen in the 3D composites with some differences, in 3D woven composites made with the use of modified 2D looms also the internal yarns can be seen having a wavy pattern, on the contrary using the 3TEX's machines only the external weft tows presents a wavy pattern. This region is the zone where the z-binders overcome the weft tows creating the so-called z-

crowns, creating various indentation spots. In traditional weaving machines, the misalignment from the in-plane straightness can be between  $5^\circ$  and  $10^\circ$  or even more [3]. This fact is a major source of mechanical properties downgrade for the composite, since they are greatly affected by the misalignment, even of few degrees. This crimping creates also regions of high fibres content since the yarns are pushed and packed, and this leads to the creation of polymer-rich areas in between.



*Figure 1.22: Schematics of a 3D orthogonal woven external section, where it is represented the indentation generated by the z-binder on the weft yarns.*

The term non-crimp fibers is used for the composite made using the 3TEX machines since it was proven that the deviations that are present in the in-plane fibers are not due to the weaving process but to the fabric handling and the manufacturing process, because when the fabric is cut and placed it is bent and during the vacuum infusion, the bag compresses and interacts with the dry fabric. This causes the creation of indentations, more specifically on the surface areas and on the z-crowns, which are due to the tension applied to the yarns during the weaving process to keep them taut.

- *Voids*: air bubbles and defects usually are concentrated in the resin channels and near the z-binders. These defects are caused by the air bubbles that are still present in the resin even after the degassing process or by air intrusion during the infusion, which is to be avoided.

At the end, can be said that using different weaving techniques and so different machines, leads to different results in terms of fibers architecture and this influences also the resulting mechanical properties.

### 1.3.5. Static mechanical properties of 3D orthogonal woven composites

#### 1.3.5.1. Influence of the z-yarns volume fraction over the static properties

As described in paper [6], there are three principal factors that influences the in-plane properties:

1. Fiber volume fraction.
2. Fiber distribution along the three principal directions.
3. Fibers waviness.

An interesting study, reported in the same paper mentioned before, was conducted to investigate how the z-binders size affects the properties of the composite in the three different directions. The first easy conclusion is that, as the z-yarns size increases, the spacing between the in-plane fibers increases as well and for very thin z-yarns the fabric is more similar to a common cross-ply laminate.

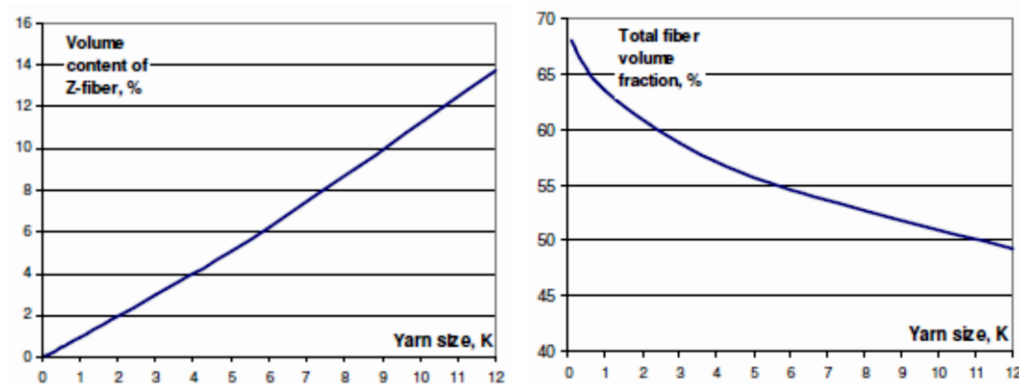


Figure 1.23: variation of the z-yarns volume fraction (left) and total volume fraction (right) as a function of the yarn size

The difference that can be seen in Figure 1.23 is that the volume content of the z-binders increases as the yarn size goes up with an almost linear curve, on the other hand, the total fiber volume fraction decreases not with a linear function, especially for small yarn sizes.

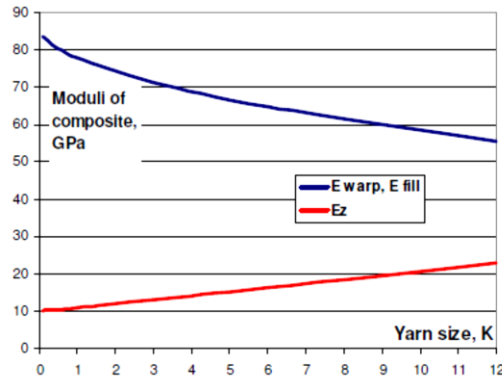


Figure 1.24: In-planes and through-thickness moduli variation as function of z-yarn size.

In the figure above it is clear the trade-off that must be exerted between the in-plane properties and the properties in the z-direction. These data are extrapolated by predictions, that can be validated by tensile tests in warp and weft direction, but not in the through-thickness one because the small thickness does not allow to grip the specimen. As the yarn size increases, and so the z-yarn volume fraction, also the Young's modulus in this direction rises. On the contrary, the in-plane properties go down, as the Young's moduli in the warp and weft directions decrease in similar ways, sharply for small yarn sizes and in a similar way to the total fiber volume fraction. The loss of Young's modulus in the weft direction is usually slightly more pronounced than in the warp, probably for a wavier pattern or a lower volume fraction in this direction.

Regarding the through-thickness reinforcement, its properties can be modified changing the fiber fraction in this direction. This operation can also be done in the other two directions, tailoring the fiber volume fraction in weft and warp direction to the desired application, changing their relative percentage. As a rule, the fiber percentage in the z-direction should lead to failure initiation at the same time as for the in-plane fibers, this to have an optimized structure without excess of strength when it is not required, to make so, the volume fraction in each direction should be the exact amount required. From this point of view, the 3D fabrics can lead to a more optimized structure in all the three-dimensional space properties, instead of a laminate that exerts higher in plane properties but delaminates easily with a properties loss, before leading to the fiber failure. In 3D fabrics, this requirement can be resolved with the use of through-thickness reinforcement, giving a suited structure for triaxial loads. Up to now, there is still no approved and verified model to guide through this process, so the z-fibers percentage is decided by the producer based on its previous experience. Generally, 3TEX produces its fabrics with an

average z-fibers percentage around 5%, but it can vary from a material to the other. Usually this percentage is enough to avoid delamination and it is also too much for this application, since to avoid delamination is required a little percentage, around 2%. Rudov and Mouritz quoted from Guénon's work that a z-binder percentage of 1% can already improve the interlaminar toughness of 10 times [8]. The latter value is still too much considering just the fracture toughness, as some works have pointed out, since the strength level reached is higher than the one required for the most common load cases. This high level of through-thickness strength also provides better response for impact, ballistic or explosion damages, this characteristic is so much enhanced with respect to common 2D composites that 3D woven are eligible to be used in protective armours.

The best way to characterize the properties in the z-direction and to evaluate the influence of the z-yarns on the composite properties is to determine the interlaminar toughness or the strain energy release rate, that can be determined by standard tests where a preformed crack is then propagated. Without the presence of z-direction fibers, between the layers there are planes of only resin through which is easy for the cracks to propagate, leading to delamination. With 3D composites, otherwise, the presence of the fibers in the z-directions slows down the crack growth since it has to brake the matrix and also these fibers to propagate, sometimes is also present the bridging mechanism, which is another dissipative mechanism that makes more difficult the crack propagation. This permits to achieve higher values for  $G_{IC}$  and  $K_{IC}$ , sometime higher than 20 times (in paper [6] is reported that when the crack involved the z-binders the values of  $G_{IC}$  increased at 40-50 times the initial value for the propagation in the pure matrix).

#### 1.3.5.2. Quasi-static tensile properties of 3D woven

Several studies have been conducted to analyse the properties of 3D non-crimp woven and to compare them to common 2D woven laminate or other categories of 3D composites. The first key factor to obtain meaningful results is to compare samples of different material types with the same total fibers volume fraction and the same thickness. Moreover, to have significant results also the same resin type, the same constitutive fibers type, the same manufacturing procedure and equipment must be used to create the different composite varieties under investigation. The performances of 3D orthogonal woven have substantial differences compared to 3D angle interlock, the latter shows lower in-plane stiffness and strength, even lower than 2D woven laminate, due to the fact that the internal geometry is markedly crimped. As a comparison, M. H. Mohamed and A. E. Bogdanovich

in the paper [2] has produced their samples manufacturing the 2D laminate with the prepreg technique and the 3D woven with a combined use of resin infusion under vacuum and consolidation in an autoclave, obtaining similar fiber volume fraction around 50% for every type of material. Here are reported the results as a ratio of 3D orthogonal and angle interlock properties over 2D weave laminate and as the ratio between orthogonal over angle interlock:

*Table 1.3: Comparative study of different types of 3D composites [2]*

<i>Material</i>	<i>E+ warp</i>	<i>E+ weft</i>	<i>UTS+ warp</i>	<i>UTS+ weft</i>	<i>UTS- warp</i>	<i>UTS- weft</i>
<i>3Dinter / 2D</i>	<i>0.74</i>	<i>0.88</i>	<i>0.67</i>	<i>0.62</i>	<i>0.56</i>	<i>0.74</i>
<i>3Dorth / 2D</i>	<i>1.11</i>	<i>0.95</i>	<i>1.10</i>	<i>1.02</i>	<i>1.06</i>	<i>0.99</i>
<i>3Dorth / 3Dinter</i>	<i>1.50</i>	<i>1.08</i>	<i>1.64</i>	<i>1.64</i>	<i>1.89</i>	<i>1.34</i>

Can be seen that the properties of the angle interlock composites are lower than 2D laminate or 3D orthogonal because in 3D angle interlock all inner weft and warp yarns presents an inherent waviness which is not present in 3D orthogonal where only the surface weft yarns present a wavy pattern induced by the interlacing with the z-yarns. On the other hand, the in-plane properties of the 3D woven orthogonal are comparable with the one of the 2D weave, resulting sometimes higher but with the advantage of the avoided delamination. Table 1.3 demonstrates that it is necessary to make a distinction between the different types of 3D woven because their properties can be very different due to the internal architecture of the yarns.

In paper [9], Carvelli et al. compared a 3D woven composite and a 2D wave laminate obtaining similar results to the ones presented in the previous section. The first one is a 3D non-crimp orthogonal weave produced by 3TEX called 3D-96, the second one is a 4 layers 2D plain weave fabric made of E-glass.

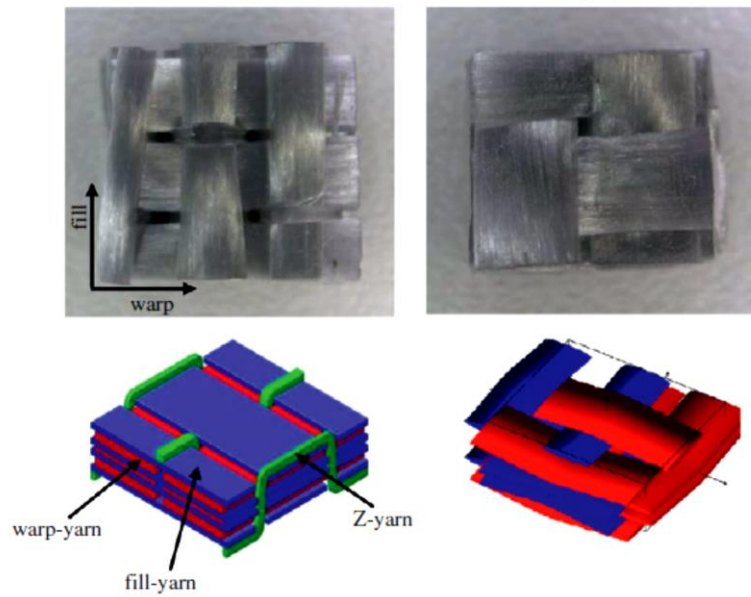


Figure 1.25: 3D orthogonal weave (left) and 2D plain wave (right).

The results are presented in the following table:

Table 1.4 : Average data with standard deviation from quasi-static mechanical tests [9].

Material	$E$ [GPa]	Ultimate Stress [MPa]	Ultimate Strain [%]
3D warp	$26.34 \pm 0.63$	$540 \pm 20$	$2.92 \pm 0.05$
3D weft	$26.39 \pm 0.76$	$441 \pm 26$	$2.41 \pm 0.13$
2D plain wave	$24.68 \pm 1.51$	$427 \pm 23$	$2.45 \pm 0.18$
3D warp / 2D	1.07	1.26	1.19
3D weft / 2D	1.07	1.03	0.98

As the previous research has pointed out, the Young's moduli in warp and weft directions are pretty close and substantially comparable with the ones of 2D laminate. Otherwise, the values of the final tensile strength are much more higher and this tendency can be seen in both the researches. In paper [9] was also reported that the fiber volume fraction was slightly inferior for 3D composite than for 2D laminate, so the uncrimped structure of the 3D woven not only compensate this but also gives better in-plane properties than their counterpart. A difference between this paper and the previous is also present since the ultimate tensile values are less high and can be noticed a significant difference between the values in weft and warp direction. The same tendency is present for the ultimate strain. The authors have explained this for two main reasons: the inferior crimping in the 3D woven from 3TEX and the lower yarn damage caused by the different manufacturing method developed.



In another work, S. V. Lomov, A. E. Bohdanovich et al. [5] tested two different types of E-glass 3D orthogonal woven and one stack of 2D fabrics made by four plies of E-glass fibers, similarly to the previous research. The two types of 3D orthogonal wave are made by vacuum infusion using two types of 3TEX, one is called 3D-96 (i.e. 96 oz/yd<sup>2</sup> preform) and the other 3D-78 (i.e. 78 oz/yd<sup>2</sup> preform) with lower areal weight and thickness. Otherwise, 3D-96 and 2D laminate have the same areal weight, close thickness and total fiber volume fraction. Also in this case, they have been manufactured using the same equipment and process, in the same laboratory and they were also tested in the same lab.

*Table 1.5: Results of the tensile tests reported in [5].*

<i>Material</i>	<i>Direction</i>	<i>E [GPa]</i>	<i>E (50%Vf)</i>	<i>ν</i>	<i>UTS (MPa)</i>	<i>UTS (50% Vf)</i>	<i>Ultimate strain (%)</i>
<i>3D-96</i>	<i>Warp</i>	$24.3 \pm 1.2$	$24.6 \pm 1.2$	<i>0.143</i>	$429 \pm 34$	$435 \pm 34$	$2.74 \pm 0.29$
	<i>Weft</i>	$25.1 \pm 2.3$	$25.5 \pm 2.3$	<i>0.128</i>	$486 \pm 5$	$493 \pm 5$	$3.33 \pm 0.27$
	<i>Bias</i>	$12.9 \pm 0.5$	-	<i>0.508</i>	$124 \pm 5$	-	$14.1 \pm 0.4$
<i>3D-78</i>	<i>Warp</i>	$23.0 \pm 2.5$	$24.2 \pm 2.6$	<i>0.115</i>	$423 \pm 29$	$446 \pm 29$	$2.96 \pm 0.51$
	<i>Weft</i>	$23.0 \pm 2.5$	$25.7 \pm 1.6$	<i>0.149</i>	$427 \pm 8$	$450 \pm 8$	$3.14 \pm 0.44$
	<i>Bias</i>	$13.4 \pm 0.8$	-	<i>0.861</i>	$118 \pm 14$	-	$14.3 \pm 1.0$
<i>2D</i>	<i>Warp/Weft</i>	$26.0 \pm 1.5$	$24.8 \pm 1.5$	<i>0.207</i>	$413 \pm 4$	$394 \pm 4$	$2.38 \pm 0.02$
	<i>Bias</i>	$12.2 \pm 0.4$	-	<i>0.666</i>	$109 \pm 6$	-	$9.7 \pm 0.4$

The results are reported for warp, weft and bias directions, which corresponds to  $\pm 45^\circ$ . Are also presented the values after being scaled for 50% total fiber volume fraction, with this procedure the results are no more affected by the differences due to the different total fiber volume between the different composites. Comparing the in-plane Young's moduli for the three materials after being scaled can be seen that there are not significant differences between them. Authors reported that the differences before the scaling are due to: differences in fiber content between warp and weft direction and, of course, different total volume fraction. Otherwise, the in-plane Poisson's ration is greater for 2D woven than for 3D composites. The tests in bias direction, for what concerns the Young's modulus, produced every time a result roughly half than the values in warp and fill direction, but the results in bias direction are similar for all the materials. Difference can although be seen in ultimate stress and strain, a noticeable difference can be seen between the ultimate stresses of 3D-96 and of 2D, particularly in weft direction, where a difference of 25.1% is registered after scaling, where the 2D composite have lower ultimate stress. Also, the ultimate stresses in bias direction show the similar tendency, ultimate stress in bias direction are higher for 3D-96 than for 3D-78 and significantly more than for 2D laminate, this latter difference is about 13.8%. A significant difference can be seen also for the

ultimate strain, where these values for 3D composites in weft direction are higher than in warp, and significantly higher than for 2D, with a 40% difference. Even in the case of the values for the ultimate strain in the bias direction, they show a marked difference between 3D composite and 2D, with a difference around 45%. 2D composite presents also the disadvantage that the threshold points where the damage starts, and so where losses in stiffness (visible in the stress strain curve) can arise, happens earlier than for 3D-78 and 3D-96, in both the principal directions, weft and warp. From all these works, can be seen that 3D orthogonal woven composites present advantages over other types of 3D composites, like 3D angle interlock, and over 2D laminates. These advantages can be seen for higher ultimate strength and strain and for later damage development, in both warp and fill directions. The authors of the paper [5] explained this difference between 2D and 3D orthogonal composites regarding the earlier damage initiation of the first category for the following reasons:

- 2D fabrics presents yarn crimping, on the other hand 3D orthogonal presents for all warp and most of weft yarns approximately zero-crimping. The crimping causes an out-of-plane deformation when the material is loaded in either the two in-plane directions. This causes shear stresses in z-direction that affect the matrix and the internal yarns, this adds another stress to the tensile loading, creating multiaxial stress state, which makes easier to reach the damage initiation.
- Lower damage imparted during the production process of the 3D orthogonal fabrics.
- Absence of delamination, and in part for longitudinal splitting, in 3D orthogonal composites which causes in 2D woven a pre-failure damage that alters the stress field.

#### 1.3.5.3. Quasi-static damage evolution

##### *Initial stage*

Minor damage starts already after few cycles, but with some peculiarities. When 3D-96 composites are loaded in the warp direction (i.e. z-binders parallel to the warp yarns), damage starts in a region near the so-called z-crowns. This term identifies the specific region where the z-binders passes over the weft yarns at the surface, this region creates a stress concentration when a load is applied in the x-direction and the z-binders creates a notch on the weft yarns that lay underneath. Furthermore, it was experimentally proved that micro-cracks easily generate in this region and they are oriented across the z-yarns, corresponding to matrix cracks that arises at the interface between z-binders and the

matrix. It is important to notice that this is, as usual in composites, a progressive damage related with the stochastic distribution of defects in the material. The aforementioned behaviour is typical of the 3D-96 fabrics, in 3D-78 this kind of damage is not so common and usually they present transverse cracks. This kind of damage usually starts later than micro-cracks around z-crowns and also later than transverse cracks in 2D composites. When a 3D-96 composite is loaded in the weft direction some transverse cracks in warp direction appear in the regions near the z-crowns, inside the warp yarns or at the boundary between weft yarns and the matrix. In 3D-78, the crack that arises when a load is applied in the weft direction seems not to be related with the z-crowns but they are still located in the warp yarns. As was said previously, 3D composites seem to be less affected by transverse cracking at the early stages of the damage with respect to 2D plain weave.

#### *Intermediate stage*

When the loading increases, if this is applied in the warp direction other cracks to the ones near the z-crowns appear in the transverse direction of 3D-96 composites. The micro-cracks before mentioned grow but remaining of a limited length and other cracks generates through all over the sample. When a 3D-96 composite is loaded in the weft direction, the already present transverse cracks near the z-crowns grow, remaining limited by two adjacent yarns. In 3D-78 loaded in weft direction, transverse cracks in warp direction keep growing.

#### *Final stage*

When the load reaches a level near the final failure, for 3D-96 composite loaded in warp direction, the cracks originated by the z-crowns created debonding regions and the transverse cracks located in the weft yarns are now very dense, but the warp yarns are still quite intact. When they are loaded in the weft direction, the transverse cracks are now very dense and there are also cracks in the z-yarns, especially in the region near the z-crowns and interfacial cracks appear. At the late stages cracks in fill direction lead to the breakage of the weft yarns. 3D-78 composites are, on the other hand, severely affected by transverse cracks. [10]

A similar behaviour can be seen for damage progression during fatigue, which recounts the stages mentioned for static loading, as can be seen in Baiocchi's (2013) and Novello's (2014) Master's Theses, cited in the bibliography.

## 1.4 Strength reduction in notched 3D woven composites

Asses the behaviour of the material with the presence of holes is important because, although joining methods like adhesive bonding or stitching are gaining more and more space, still there will be the need of mechanical fastening to bond highly loaded regions. The presence of a notch in a plate has two principal effects, which also modify the stress field in the component near the notch itself:

- i. Reduces the cross-section area
- ii. Concentrates the stresses around the hole

These two effects are always present together but the response of the material can vary if it is sensitive or insensitive to the presence of a notch. The full notch sensitivity is defined when the stress on the component undergoes the following relation:

$$\frac{\sigma_{notch}^g}{\sigma_{plain}} = \frac{1}{K_{tg}} (< 1) \quad (1.2)$$

Where  $\sigma_{notch}^g$  is the gross strength of the notched specimen,  $\sigma_{plain}$  is the strength of the pristine material and  $K_{tg}$  is the stress intensity factor defined on the gross section.

On the contrary, the notch insensitivity is defined by the relation:

$$\frac{\sigma_{notch}^g}{\sigma_{plain}} = 1 - \frac{a}{w} \quad (1.3)$$

Where this time  $a$  is the net specimen length counting the hole and  $w$  is the total length of the component without the hole.

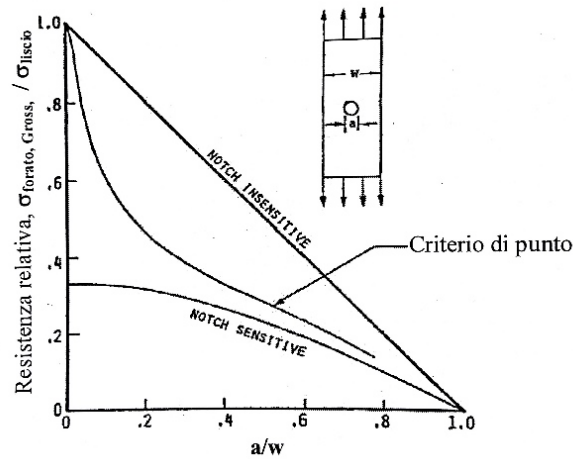


Figure 1.26: Strength reduction in a composite plate for notch sensitivity or notch insensitivity. It is visible the hole size effect for big hole sizes for unidirectional laminates, they presents a notch insensitivity behaviour for small hole sizes, while for big hole size their behaviour is closer to the notch sensitivity.

The value of the stress intensity factor can be described considering the material a whole equivalent anisotropic infinite plate, accounting for the stress in the principal direction, for a plate with a hole, as follows:

$$K_T^\infty = 1 + \sqrt{2 \left( \sqrt{\frac{E_{11}}{E_{22}} - \nu_{12}} \right) + \frac{E_{11}}{G_{12}}} \quad (1.4)$$

Which is equal to 3 for an isotropic material. For a 3D woven composite, as was previously presented, the in-plane properties are very similar, thus  $E_{11}$  and  $E_{22}$  are considered equal.

Small work was done on the notch properties of 3D woven composites since most of the work was done about the tensile and fatigue behaviour of un-notched specimens. So, most of the work that can be found about this topic refers to diverse types of materials, as orthogonal hybrid composites, orthogonal glass composites made with traditional looms and so on. In a recent paper, Muñoz et al. [11] tested in tension until failure hybrid carbon-glass composites made as a layered structure, the first four layers made of glass, the bottom four made of carbon fibers and an hybrid layer made of glass and carbon was placed in the middle, with polyethylene z-binders was tested. The panel was manufactured by vacuum infusion using the material from 3TEX, which is a hybrid orthogonal woven composite, infused with epoxy-resin. The specimens were tested with a central hole of two different diameters and the peak strains was recorded using the digital image correlation technique. The results show that there is not a significant difference between the failure

strength of the notched and un-notched specimens, which is reported by the fact that the failure points are on a line when they are plotted as a function of the hole size over the specimen width, as can be seen in Figure 1.27.

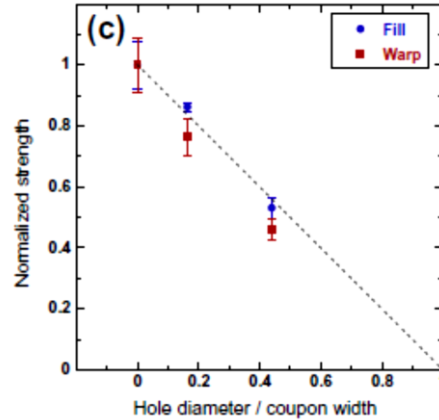


Figure 1.27: Notch sensitivity behaviour of the hybrid carbon-glass 3D woven composite, the notch insensitivity is represented by the dotted line. [11]

The picture above shows that the specimens failure points are quite aligned to the line of the notch insensitivity, since on this line the only source of strength reduction is the reduction in the specimen width. Thus, can be said that this type of material under investigation is quite insensitive to the presence of notches and that the stress intensification around the hole does not influence the failure of the composite. This characteristic was attributed to the generation of damage and debonding during the test which leads to a reduction of the stress intensification around the damage site, which in this case is the hole.

In another paper, Dai, Cunningham et al. [12] have investigated the presence of open holes during quasi-static tests for orthogonal and angle-interlock specimens. Even this time, full-field strains have been recorded using the DIC method. The material used in this research are a 3D orthogonal woven and a through-thickness angle interlock, both produced with the use of a traditional loom. For the quasi-static tests, two-hole sizes were analysed as in the previous paper and the results obtained are here presented:

Table 1.6: Quasi static opne-hole test results.

Material	$\Phi$ (mm)	Notched strength (MPa)	Un-notched strength (MPa)
3D orthogonal	4.1	1145.71	1358
	12.5	1093.98	

<b>3D angle interlock</b>	<b>4.1</b>	<b>1265.01</b>	<b>1280.99</b>
	<b>12.5</b>	<b>1201.87</b>	

The notch strength refers to the net stress calculated on the specimen area considering the hole. It can be seen a reduction in strength which is anyway not so high, both the composites present a higher reduction for the larger hole but the difference is also in this case small. The trough-thickness angle interlock composite presents better response regarding the notched properties degradation, with a reduction of the properties less than 10% for both the hole size, while the orthogonal wove composite presents a reduction around 18% from the un-notched properties. So, even in this case it is confirmed that the presence of a hole or a notch as a little influence on the ultimate tensile strength of 3D woven composites. Even in this case the presence of damage induced by the presence of the hole is responsible of the unsensitivity to the damage. The damage progression shows that around the hole edge there is a formation of longitudinal cracks (splitting), after that there is also the formation of a debonding region and the formation of transverse matrix cracks from the resin channels. All these phenomena generate a stress relaxation around the stress intensifier which creates a notch unsensitivity in the material. It is also clear that the material is not sensitive to the notch size.

Lijun Qin, Zhongwei Zhang et al. [13] studied the notch effect in a 3D woven composite made of carbon fibres reinforcing a carbon matrix. The investigation was carried out using the DIC technique to address the full-field strains and different hole configurations were tested to analyse the reciprocal influence of multiple holes. The holes were cut using wire-electrode cutting on 140x25mm samples with aluminium end tabs. During the strain measurement, sub-pixel technique was used applying the Newton-Raphson algorithm, using a CCD camera with 256 grey levels and a resolution of 1624x1236 pixels. Performing this strain analysis is also possible to obtain the stresses using the Hook's law. In the paper is defined a measure which is the Notch Strength Ratio (NSR), defined as:

$$NSR = \frac{\sigma_{notched}^n}{\sigma_{plain}^n} \quad (1.5)$$

Where the  $\sigma_{plain}^n$  is the strength of the un-notched specimen and so of the pristine material, while the  $\sigma_{notched}^n$  is the net strength of the notched material. The NSR can assume the following values: if  $NSR > 1$  the material is defined as notch strengthening material, which is an impossible condition, if the  $NSR = 1$  the material is notch insensitive and if

the  $NSR < 1$  the material is notch sensitive and it is defined as notch weakening material. It was found in this research that the NSR is close to one for different hole configurations. It was also found that the concentrated strains do not increase linearly but near the failure is visible a nonlinear behaviour, which can be explained with a redistribution mechanism that makes the stress on the section more similar before final failure. This phenomenon can be the result of the shear bands formation. The presence of the local nonlinear behaviour determines a higher strain which is again caused by the shear damage because the shear strength in 3D composites is low, this anyway does not affect the overall behaviour which remains unaffected by the presence of the notches.

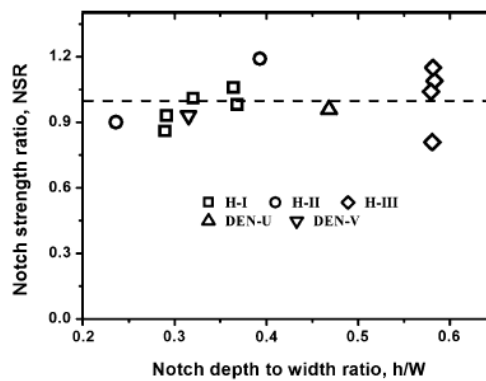


Figure 1.28: Results of the notch sensitivity investigation with different holes sets.

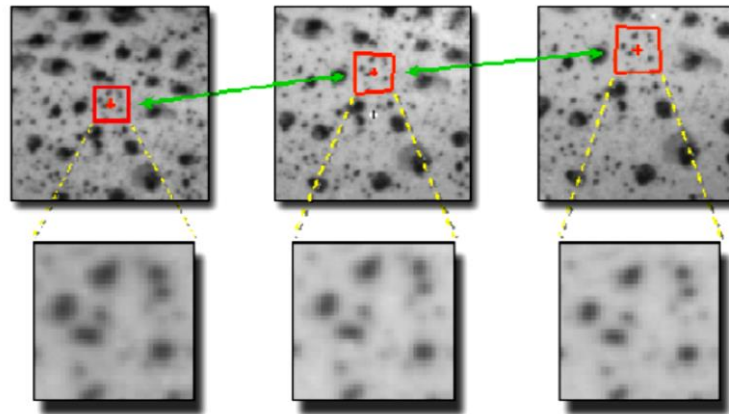
In Figure 1.28 the point H-I identify the presence of one hole, H-II the presence of two adjacent holes in the transverse direction to the loading direction, H-III three holes in a triangular pattern, while DEN-U a double square-notched geometry and DEN-V two v-shaped notches. The presence of different holes creates a multiaxial stress state that can affect the behaviour of the notched material, in any case can be seen that the NSR is always near to one, which represents that the 3D woven composite is insensitive to notches and this characteristic is independent from the material, the notch configuration and notch depth. Thus, the strength of a plate is function only of the minimum net area and at the end the specimen can be considered as unnotched just counting the net area of the specimen [13].



## 1.5 Digital Image Correlation

### 1.5.1. Introduction

Digital Image correlation, also called DIC, is a new and growing technique to investigate strain and displacement in a material. There are many advantages of this technique over the common methods, the main are: the simplicity of the measurement, the possibility to analyse large specimens or structures which is translated into full-field measurements, the possibility to use it in an outdoor environment, the fact that it is a cheap technique and that it does not require any contact with the object, so it is non-intrusive. It can be defined as an optical method that tracks groups of pixels, register and process them in order to measure the surface displacement and build a strain map comparing the images at different stages.



*Figure 1.29: Tracking of a pixels subset during the deformation.*

Using a single camera set-up, only in-plane displacements can be measured. Otherwise, using a multiple camera set-up, usually with 2 cameras, also out of plane displacements can be measured creating a three-dimensional map. Since it is a non-intrusive method that requires a simple system, it can be used in many different applications such as, displacement measurements of high temperature objects, submerged structures, measurements at a microscope, to identify the strain field at a crack tip or for dynamic analyses [14]. It must be pointed out that the resolution required for these applications can be very different, since for point measurements required in engineering must be much higher than in full-field applications. The overall procedure to apply the DIC technique can be divided in three main steps: specimen preparation, system set-up and calibration [15].

Compared to other techniques, Digital Image Correlation is simpler to use, with a faster set-up time and cost effective compared to other classical methods like laser shearography or interferometry, since they require a precise set-up and a protect environment because they have strict stability requirements, so it cannot be performed outdoor and it limits the environment of application. It can also produce full-field results with a good accuracy, in contrast with strain gauges that gives only point results. Another advantage over the strain gauging technique is that DIC is a contactless technique, so it can be performed also at micro level and, in any case, it does not affect the material response because an external object is placed on the specimen under measurement. Moreover, it is a cheap technique since it can be performed also with commercial cameras, better if they are without zoom lenses but with fixed lenses in order to avoid lens distortions.

### 1.5.2. The correspondence problem

The Digital Image Correlation method is based on the acquisition of different images at various times, which means at different deformation stages in the material, this to identify the pixel displacement, map and compare them to extract the strains in the material using an algorithm. If it is used a set of two cameras, two different images are produced and they must be matched for every single pixel. The problem arises when trying to match a single pixel with another one in two subsequent images. Because a single image is acquired as a matrix of grey values, each one is a pixel, the same grey level can be found in many different pixels all over the image, so a correspondence investigation of this type cannot be performed since it would lead to wrong and useless results. The former is referred as the aperture problem, which is a special case of the general problem called correspondence problem. To resolve the former problem a larger area of neighbour pixels must be considered (also called subset or window) to compare and match the levels of grey between the two, however there are some cases in which this problem remains, for example when we consider a grid-shaped image, it must be enlarged to a much higher scale to resolve it. This problem is resolved with the use of a random texture placed on the surface of the specimen, avoiding in this way the grid-like structure but some problems must still be present, as it will be described more in detail later [16].

### 1.5.3. Speckle pattern

To avoid the correspondence problem, it must be used a speckle pattern made of little dots since it introduces some properties that permits to find a unique correspondence in

two images. The key characteristics, that the applied pattern must have to be a random pattern, are [17]:

- Uniformity
- Non-repetitiveness
- Isotropy
- High contrast
- Adherence

If all these characteristics are met, can be said that the pattern is random, since it does not present an oriented structure.

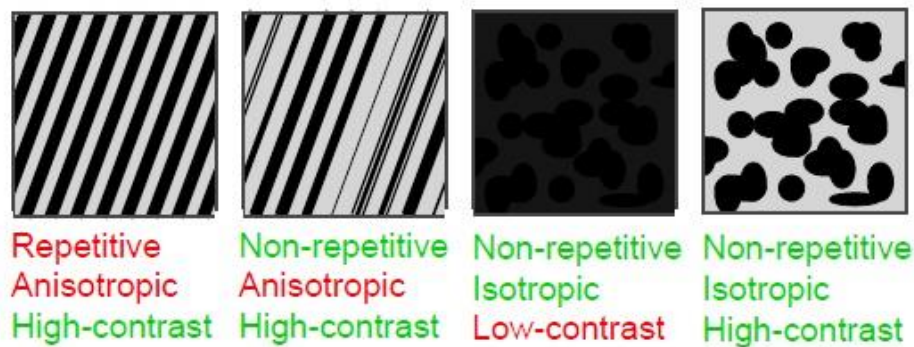


Figure 1.30: Comparison of different types of patterns that could be used in the DIC technique.

To apply this pattern numerous and diverse ways exist, the choice for one instead of another depends on the size of the material to be tested, the operator preference who will do the test and the level of resolution that is required. Some of the techniques that can be used are: spray painting, ink painting (with the use of a thin pen), lithography, vapor deposition, dry sponge application, toothbrush technique, stencils, printing and adhesives. The important thing for the pattern is that it must deform as the material without reinforcing and changing the response of the material during the test. It also must maintain the properties under the testing conditions, for example for what concerns temperature, humidity and deformations. For what concerns the pattern optimization it must not presents reflections, so the best option is to use a white background with black dots over it, better if they are not dense, since a too fine pattern will lead not to reliable results, approximately three to five pixels per speckle. On the other hand, big paint speckles must be avoided since it is required a sufficient density to achieve maximum spatial resolution. Thus, can be said that if the pattern is too large must be used a larger subset to identify the random patter, otherwise the subset will be entirely over a uniform black speckle or

on a white region, which will not allow to have a correspondence. To avoid this must be used a large subset, renouncing to the spatial resolution. If the patten used is too small, the camera can have difficulties to identify the pattern, which is called the aliasing effect, because the camera lacks in resolution. The result is that the specimen will not appear to move smoothly. Another drawback of the fine patterns is that it is easy for the camera to get out of focus [18]. Good speckle patterns should be 3-4 pixels as size, to avoid either the case of a pattern too big or too small. Sometimes it is required to paint also the rough surface of the object, as was said, with a white background to provide a better contrast. Since the software just sees a contrasting pattern made of different grey levels, it is not important the colour of the speckle pattern, so a white background with black speckles works as well as white spackles on black. In most cases, it is not required a particular lightning and the natural light is sufficient to obtain satisfactory results.

#### 1.5.4. System calibration

To effectively use this method, it must undergo the calibration procedure, which is a shape measurement process during which various images of a calibration target are taken in different positions. To fulfil the calibration, two requirements must be respected, the calibration target must not deform during the procedure and a distance between two points of the target must be known. The entire procedure is made to calibrate the camera parameters such as: focal length, distortion, misalignment of a camera, the relative position of each camera when two or more cameras are used and so on. The set-up of all these parameters is made at the same time measuring the dimension and position of a calibration target. The calibration procedure consists in taking multiple images, usually fifteen or more, of a flat target where a triad of points is placed among a grid of dots and where a distance between two points of interest is precisely known to determine the target absolute dimensions, to do so, the target must be hold at the same distance as the specimen that must be tested. The different images must be taken at different orientation to create a set of different views. The target used is a coded one, which means that the software can automatically extract the calibration function by means of a dots pattern. The calibration procedure is also needed to calibrate the distortions that are induced by the optics, which are small at the focal centre and becomes larger at the boundaries, they are described by polynomial equations function of the distance from the image centre [17]. To accurately calibrate these distortions, the grid in the target must cover all the view of the camera.

The parameters that are calibrated can be divided in two categories: Intrinsic and extrinsic. Intrinsic parameters are specific of a camera and are: focal length, aspect ratio, sensor centre, and they change if it is changed the position of the lenses, aperture or focus. Extrinsic parameters are those who defines the relationship between the two cameras, they are the displacements in the three directions and the three angles between the two cameras. They move if the cameras are moved or rotated in one of the direction. The calibration of all the parameters is made at the same time.

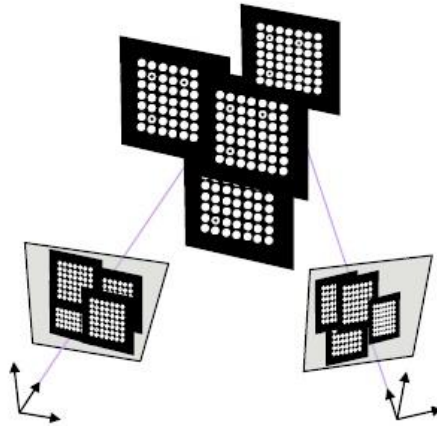


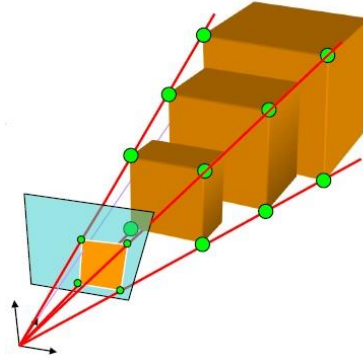
Figure 1.31: Image acquisition at different angles to calibrate the system.

### 1.5.5. Basic principles of 2D Digital Image Correlation for in-plane displacements

In this chapter will be presented only the in-plane displacement and strain investigation, for doing this only a mono-camera system is needed, so it will not be addressed the problem of a three-dimensional measurement for out-of-plane displacements which requires a set of multiple cameras, moreover with this set-up is possible only the investigation of plane specimens. This choice is made to present the mathematical basis of the Digital Image Correlation method in a simple formulation.

An important fact about the use of a single camera is that the system in this configuration is not capable to capture the relative position of an object in the space, as for a cyclopean view. So, it is not possible to distinguish between a deformation or a movement in the camera direction, for example a deformation with a gain in volume is equivalent to a movement toward the camera as is depicted in Figure 1.32. As a consequence, during the

whole measurement, must be assumed that the object remains at a constant distance from the camera, parallel to it and with a planar surface.



*Figure 1.32: Schematics of a monocular apparatus, where is indistinguishable if an object is deforming or moving into space in the camera direction.*

In this configuration, if all these requirements are matched, can be used an algorithm to identify the displacement vector of every pixel through the matching of a neighbourhood of pixels between two deformed images that maximizes a similarity function. This aggregate of neighbouring pixel is called subset or window. To determine the displacement vector, the grey levels of the subset of interest must be tracked, searching for an area with the same grey levels over two images. For this reason, the surface must present a random pattern in order to identify in a unique way every subset of pixel. The correlation function that must be applied to resolve this method and find the deformation vector can be of the following types:

$$C(x, y, x^*, y^*) = \frac{\sum F(x, y) \cdot G(x^*, y^*)}{\sqrt{\sum F(x, y)^2 \cdot G(x^*, y^*)^2}} \quad (1.6)$$

Where the summation is made over the subset, F indicates the grey levels at (x, y) coordinates before the deformation, G the grey levels after the deformation in the deformed position  $x^*, y^*$  [14]. When a maximum value is reached for this coefficient C, as is shown in Figure 1.33, the matching subset position after the deformation is known. So, the procedure is to change the subset position until a maximum value is reached, the position of the displacement vector of the pixel under investigation is then around the position of the subset centre. This because in most of the cases the deformation is not an integer value of a pixel, so the position of the new deformed pixel can be at a discrete position

around the subset centre, in these cases is needed a subpixel investigation with interpolation.

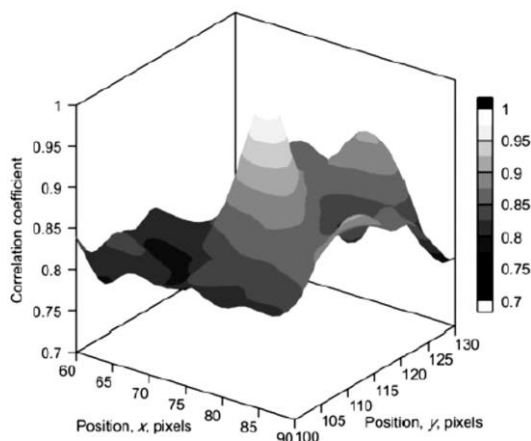


Figure 1.33: Correlation coefficient distribution over a region of the deformed image.

Another equation that can be used for the correlation function is the following:

$$C(x, y, u, v) = \sum_{i, j = -\frac{n}{2}}^{\frac{n}{2}} (I(x+i, y+i) - I^*(x+i+u, y+i+v))^2 \quad (1.7)$$

Where  $I$  is the grey level distribution before the deformation,  $I^*$  is the distribution after the deformation, and the summation is made over the subset starting from the centre. In this case, the position of the deformed pixel is known when the correlation function reaches the lowest value, hypothetically zero. At this point must be pointed out that the images are always altered by some noise, the light may change during the test and the pattern during the deformation that stretches it can slightly change colour, all these factors can affect and modify the grey levels between the two images that will lead to a correlation coefficient different from the theoretical one and can, in some unlucky cases, get to mismatches of the subsets [17].



Figure 1.34: Visualization of the subset in the undeformed image and in the one after the deformation.

Thus, if there is not deformation of the subset the position of the central pixel after deformation  $(x^*, y^*)$  can be described as just the result of a rigid motion, as:

$$\begin{aligned} x^* &= x + u_x \\ y^* &= y + u_y \end{aligned} \tag{1.8}$$

Where  $u_x$  and  $u_y$  are the displacement components from the undeformed position  $(x, y)$ . Otherwise, the subset does not remain undeformed but changes from a square initial shape to a deformed one like a parallelogram, it is so necessary to model this deformation (known as subset shape function) to find the actual displacement vector. If the subset is sufficiently small, as it should be, the deformations inside the subset are also small and so the deformation gradient can be considered uniform. The previous equations, considering also the subset deformation, can be now written as:

$$\begin{aligned} x^* &= x + u_x + \frac{\partial u_x}{\partial x} \Delta x + \frac{\partial u_x}{\partial y} \Delta y \\ y^* &= y + u_y + \frac{\partial u_y}{\partial x} \Delta x + \frac{\partial u_y}{\partial y} \Delta y \end{aligned} \tag{1.9}$$

Where  $\Delta x$  and  $\Delta y$  denotes the distances from the subset centre to a position of a point  $x, y$  inside the subset, as is shown in the following picture.



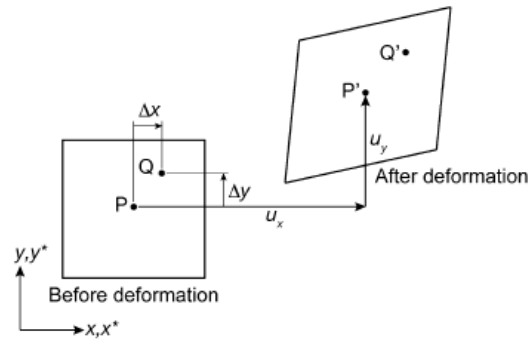


Figure 1.35: Subset deformation with change of shape from a squared one to a parallelogram.

As was said in the introduction, it is usually needed the use of a subpixel technique to identify the correct subpixel centre since the generally the displacements do not correspond to integer pixels. To do so, can be used a function that approximate the distribution of the correlation coefficients or can be used a grey-level interpolation technique. It is preferred this one since it can give better results and it allows to take into account the subset deformation. Another problem is that when the subset deforms, the position of the pixel in the subset locates now between the camera pixel, so an interpolation of the grey levels at the neighbouring pixels must be done either for a subset deformation or for a general displacement, to do so are used bilinear or bicubic functions.

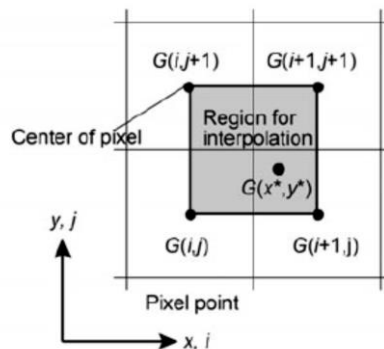


Figure 1.36: Graphical visualization of the pixel interpolation area.

The grey level of every pixel is the average value of the light intensity over the pixel area and it is regarded to be the value at the centre of the pixel. The grey level in a position between the pixels can be found using a bilinear interpolation function:

$$G(x^*, y^*) = a_{11}x'y' + a_{10}x' + a_{01}y' + a_{00} \quad (1.10)$$

Where  $x', y'$  are the position of the pixels from the reference point, that is the centre of the region under investigation. The coefficients are determined solving the system of equations that is made considering the grey values at the edges of the region which are the neighbouring pixels:

$$\begin{aligned} a_{11} + a_{10} + a_{01} + a_{00} &= G(i + 1, j + 1) \\ a_{10} + a_{00} &= G(i + 1, j) \\ a_{01} + a_{00} &= G(i, j + 1) \\ a_{00} &= G(i, j) \end{aligned} \quad (1.11)$$

To obtain the interpolation using a bicubic interpolation function, the grey levels of the sixteen neighbouring pixels are considered.

In the following paragraph, the mathematical principles that goes from deformations into the material to the strains found by the DIC algorithm.

Considering a system as the one presented in Figure 1.35, considering a PQ segment with components  $(dx, dy, dz)$ , it is supposed to be small even after the deformation with components  $(dx^*, dy^*, dz^*)$ . After the deformation, the points P and Q moves to the position  $P^*$  and  $Q^*$ , described as:

$$\begin{aligned} P^* &= x^*, y^*, z^* = (x + u(P), y + v(P), z + w(P)) \\ Q^* &= x^* + dx^*, y^* + dy^*, z^* + dz^* = (x + u Q + dx^*, y + v Q + dy^*, z + w Q + dz^*) \end{aligned} \quad (1.12)$$

The length of the segment between the points  $P^*$  and  $Q^*$  can be wrote as:

$$\begin{aligned} P^*Q^* &= dx^*, dy^*, dz^* \\ &= (u Q - u P + dx, v Q - v P + dy, w Q - w P + dz) \end{aligned} \quad (1.13)$$

Using a Taylor's linear pension series around the point P it is possible to obtain:

$$\begin{aligned} u Q - u P &\approx \frac{\partial u}{\partial x} dx + \frac{\partial u}{\partial y} dy + \frac{\partial u}{\partial z} dz \\ v Q - v P &\approx \frac{\partial v}{\partial x} dx + \frac{\partial v}{\partial y} dy + \frac{\partial v}{\partial z} dz \\ w Q - w(P) &\approx \frac{\partial w}{\partial x} dx + \frac{\partial w}{\partial y} dy + \frac{\partial w}{\partial z} dz \end{aligned} \quad (1.14)$$

And so, the deformed segment components between the points  $P^*$  and  $Q^*$  are:

$$dx^* \approx \left(1 + \frac{\partial u}{\partial x}\right) dx + \frac{\partial u}{\partial y} dy + \frac{\partial u}{\partial z} dz \quad (1.15)$$

$$\begin{aligned}
dy^* &\approx \frac{\partial v}{\partial x} dx + \left(1 + \frac{\partial v}{\partial y}\right) dy + \frac{\partial v}{\partial z} dz \\
dz^* &\approx \frac{\partial w}{\partial x} dx + \frac{\partial w}{\partial y} dy + \left(1 + \frac{\partial w}{\partial z}\right) dz
\end{aligned}$$

From these equations can be derived the strain equations. Considering that the initial segment has no components except for the one in x direction, so can be written  $dz = dy = 0$ . The strain can be calculated as:

$$\varepsilon_{xx} = \frac{|P^*Q^*| - |PQ|}{|PQ|} = \frac{\partial u}{\partial x} + \frac{1}{2} \left[ \left(\frac{\partial u}{\partial x}\right)^2 + \left(\frac{\partial v}{\partial x}\right)^2 + \left(\frac{\partial w}{\partial x}\right)^2 \right] \quad (1.16)$$

At the end, considering just in plane deformations and neglecting the out of plane ones, using just the monocular 2-D DIC, the strains have the following form:

$$\begin{aligned}
\varepsilon_{xx} &\cong \frac{\partial u}{\partial x} + \frac{1}{2} \left[ \left(\frac{\partial u}{\partial x}\right)^2 + \left(\frac{\partial v}{\partial x}\right)^2 \right] \\
\varepsilon_{yy} &\cong \frac{\partial v}{\partial y} + \frac{1}{2} \left[ \left(\frac{\partial u}{\partial y}\right)^2 + \left(\frac{\partial v}{\partial y}\right)^2 \right] \\
\varepsilon_{xy} &\cong \frac{1}{2} \left( \frac{\partial u}{\partial y} + \frac{\partial v}{\partial x} \right) + \frac{1}{2} \left[ \left(\frac{\partial u}{\partial x} \cdot \frac{\partial u}{\partial y}\right) + \left(\frac{\partial v}{\partial x} \cdot \frac{\partial v}{\partial y}\right) \right]
\end{aligned} \quad (1.17)$$

Now, will be considered the procedure to apply these mathematical concepts to derive the strains applying a numerical analysis for the DIC. Considering a pixel and its intensity value inside the subset, which is deformed from a position  $P$  to  $P^*$ , the intensity values are:

$$\begin{aligned}
f P &= f(x, y) \\
f^* P^* &= f^*[x + u P, y + v P]
\end{aligned} \quad (1.18)$$

The same thing can be done for the point  $Q$ , which is at a position  $x + dx, y + dy$  from the point  $P$ .

$$\begin{aligned}
f Q &= f(x + dx, y + dy) \\
f^* Q^* &= f^*(x + dx + u Q, y + dy + v Q)
\end{aligned} \quad (1.19)$$

At this point some assumptions must be made, the first one is that the intensity pattern changes during the deformation are negligible, so can be written:

$$f Q = f^* Q^* = f(x + dx + u Q, y + dy + v Q) \quad (1.20)$$

The same for the previous point  $P$ .

The second assumption is that the deformations are small, so can be used a Taylor's linear expansion, at the end can be written that the position of the point  $Q^*$  is:

$$Q^* = x + u P + dx^*, y + v P + dy^* \quad (1.21)$$

$$= \left( x + u P + \frac{\partial u}{\partial x} dx + \frac{\partial u}{\partial y} dy + dx, y + v P + \frac{\partial v}{\partial x} dx + \frac{\partial v}{\partial y} dy + dy \right)$$

Finally, the expression for the intensity level of the deformed point  $Q^*$  is:

$$f^* Q^* = f \left( x + u P + \frac{\partial u}{\partial x} P dx + \frac{\partial u}{\partial y} (P) dy + dx, y + v P + \frac{\partial v}{\partial x} (P) dx + \frac{\partial v}{\partial y} (P) dy + dy \right) \quad (1.22)$$

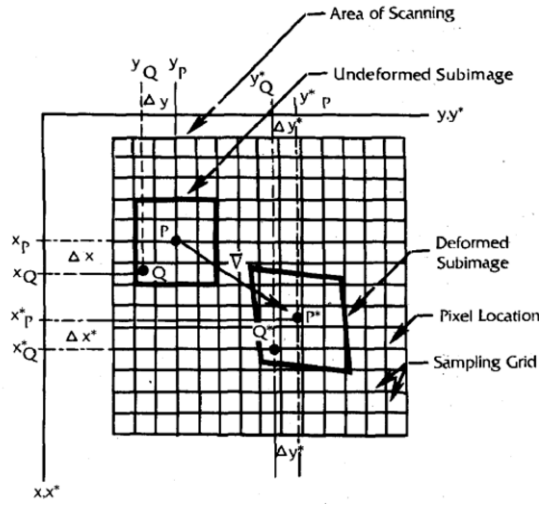


Figure 1.37: Subset deformation with change of shape from a squared one to a parallelogram

So, the position and the intensity level (i.e. the grey level) of a point are a function both of its displacement and of the displacement gradient and to define the position of a point in the subset must be known the position of the central point P and the derivative terms. It is clear now that also the correlation coefficient C is a function of the displacement gradients so the equation must be adjusted. Now the research for the maximum value of the correlation coefficient is carried out using the following formula:

$$C \left( u, v, \frac{\partial u}{\partial x}, \frac{\partial u}{\partial y}, \frac{\partial v}{\partial x}, \frac{\partial v}{\partial y} \right) =$$

$$= \frac{\sum_{\Delta M} f(x, y) \cdot f \left( x + u + \frac{\partial u}{\partial x} dx + \frac{\partial u}{\partial y} dy, y + v + \frac{\partial v}{\partial x} dx + \frac{\partial v}{\partial y} dy \right)}{\sqrt{\sum_{\Delta M} [f(x, y)]^2 \cdot \sum_{\Delta M^*} [f \left( x + u + \frac{\partial u}{\partial x} dx + \frac{\partial u}{\partial y} dy, y + v + \frac{\partial v}{\partial x} dx + \frac{\partial v}{\partial y} dy \right)]^2}} \quad (1.23)$$

Where  $\Delta M$  is the subset in the undeformed image and  $\Delta M^*$  is the subset in the deformed one. The procedure is the following, the first step is to compare the grey level in the subsets before and after the deformation with the correlation coefficient as it would move with only a rigid motion without distortion. This is the first approximation of the central point of translation, giving a first iteration for the vector  $(u, v)$ . Then, the previous values are maintained fixed and the derivatives are made vary to maximize the deformation terms. The first iteration values are then reduced to find a best correlation for the displacement vector, adjourning the values of  $(u, v)$ , after that also the deformation terms are updated until the difference of values between on iteration and the other is lower than a determined value.

Since now the displacements of the specimen are known, the strains can be measured differentiating the displacements around the point of interest on the surface. The displacements contain some errors that, after the differentiation, will greatly affect the resulting strains. So, other methods have been developed to obtain better results. The easiest thing is to approximate the displacements in a local area with the least-squares method. So, a function that approximate the displacements over an area is created and then it is derived to obtain the strains. Since the strains are defined in the tangential plane of the surface, the displacements are defined as a planar surface:

$$\begin{aligned} u_x &= a_x x + b_x y + c_x \\ u_y &= a_y x + b_y y + c_y \end{aligned} \quad (1.24)$$

So, as it has been said, the strains are then obtained differentiating the displacements expressed in the previous equations:

$$\begin{aligned} \varepsilon_x &= \frac{\partial u_x}{\partial x} = a_x \\ \varepsilon_y &= \frac{\partial u_y}{\partial y} = b_y \\ \gamma_{xy} &= \frac{\partial u_x}{\partial y} + \frac{\partial u_y}{\partial x} = a_y + b_x \end{aligned} \quad (1.25)$$

Better and smoother results are obtained if the field over the displacements are computed is very large, but must be said that this dimension is related to the resolution of the strain field that is needed. This procedure is then repeated over the whole image to obtain the full-field strains.

### 1.5.6. Basic principles of 3D Digital Image Correlation

With this technique, 3-D objects can be investigated and not only planar ones, so can be assessed any type of shape with also out of plane movements, keeping all the advantages of the previous one. To perceive a three-dimensional view of the environment, a binocular view, as the human one, is needed so, a set of two cameras is used. This is obtained by matching the two captured images, which permits to resolve the three-dimensional structure of the object and of the environment. This procedure is called stereo-triangulation and it requires a correlation between two optical rays that must be seen in the same coordinate system, to do this a calibration procedure is needed.

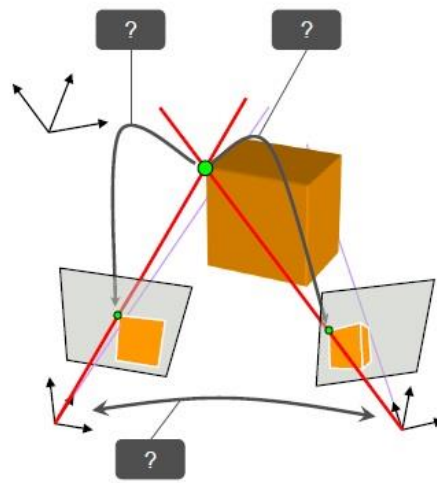


Figure 1.38: Stereo-triangulation of an object edge.

The calibration procedure was already explained and it can be described as a shape measurement of the target, where the different images that comes from the cameras are matched in various positions, adjusting also the internal distortions.

## 1.6 Concluding remarks

In this chapter, an overview of fibre reinforced polymer composites was presented with a deep characterization of the several types of 3D reinforced composites. Was proven that through the newer weaving techniques, it is now possible to produce 3D composites with a non-crimp structure with comparable or better properties than 2D. Major researches have involved the characterization of quasi-static and fatigue properties of this class of materials, as was extensively presented inside the chapter, while less was done about

notch sensitivity. Nevertheless, was proven by many studies that 3D composites present an enhanced notch insensitivity behaviour but none of them answer the question about why this happens. This work tries to investigate this problem with the use of Digital Image Correlation, this full-field method to calculate the strains on the surface of a material under testing is here described. The theoretical background and the basic mathematical principles on which the method is based are also exposed for a better understanding of the way it works. The problem of the notched behaviour of this material will be investigated analysing the strains on the tested specimens in particular around the hole to detect a characteristic mechanism that differentiate 3D composites from 2D ones.





# Chapter 2

## Experimental methods

### 2.1 Introduction

In this chapter, the material properties and its manufacturing method are exposed in detail. After that, all the activities connected with the specimens testing are presented, such as the fibre volume fraction calculation, the specimen cutting, end-tabling and strain gauging; quasi-static tests procedure is then described, presenting also the equipment used. In a second part, the complete equipment used is analysed and all the activities related to the use of the DIC are described, starting from the specimen preparation with the application of the speckle pattern, passing through the system set-up and finishing with the system calibration via software. At the end, the procedure needed to take microscopies of the specimens is reported, describing the passages to mount the cut samples inside the resin and then the grinding and polishing operations. Finally, the machines used to take the microscopies are presented and their operation is briefly described.

### 2.2 Specimen Manufacture

#### 2.2.1. Material properties

The material used in this work is a thin 3D orthogonal woven fabric produced by the company 3TEX Inc. called with the commercial name of 3WEAVE, it is also called 3D-96 because of its areal density, which is 96.6 oz/yd<sup>2</sup>, where it derives its name. The main characteristics of this product, according to what the producer declare, are reported in the following tables:

*Table 2.1: Geometrical properties of the 3D-96 from 3TEX.*

<b>Area weight</b>	<b>96.6 oz/yd<sup>2</sup></b>	<b>3.28 kg/m<sup>2</sup></b>
<b>Thickness</b>	<b>0.10 in</b>	<b>2.54 mm</b>
<b>Material</b>	<b>Hybron 2022 silane sized E-glass</b>	

Table 2.2: Yarn properties of the 3D-96 from 3TEX.

Characteristic	Warp direction	Weft direction	Z-yarns
Yarn type	E-glass roving	E-glass roving	E-glass roving
Weight (%)	47.6	48.5	3.9
N° layers	3	4	/
Areal density ( $g/m^2$ )	3255		
Insertion density	2.76 ends/cm	2.64 picks/cm	2.76 ends/cm
Yarns (tex)	Top and bottom: 2275	1470	1800
	Middle layers: 1100		

All the layers and the yarns are made by PPG Fiber Glass made of E-glass fibers called Hybon 2022, which is suitable for the use with polyester, vinyl ester or epoxy resin and for its good abrasion resistance, wet out and general properties is recommended for the use with filament winding and woven. The fabric is a 3D orthogonal woven, where the straight warp and weft yarns are weaved by through-thickness z-yarns, more precisely it is made of 7 layers, 3 warps and 4 weft layers in attendance to the usual configuration for orthogonal woven fabrics. More in detail, in the previous table the properties of the 3D-96 concerning the tows density are also reported, according to paper [9]. Must be highlighted that Tex is a unit that represents the linear mass of fibers and it is defined as the mass in grams per km,  $[\frac{g}{km}]$ .

### 2.2.2. Wet lay-up manufacturing technique

The manufacturing method used to produce the material for the specimen is the wet layup technique. This is a simple and fast technique which does not require a sophisticated apparatus, but still permits to manufacture materials with satisfactory properties. The first step for this procedure is cutting the dry fabric in the required size, for this project was used the standard size of  $31cm \times 31cm$ . After that, the three parts, which the resin is made, are weighted and mixed together. The three components are respectively: for the epoxy resin the choice is an Epoxy resin 300, the curing agent, also called hardener, is a Sigma-Aldrich menthyl nadic anhydride MNA and as accelerator Ancamine K61B. The ratio between the different parts, in terms of weight is the following: 100 parts of epoxy resin, 60 parts of hardener and 4 parts of accelerator. The weight of every component used to infuse the fabric with the dimensions previously reported is here reported in the table below:

Table 2.3: Resin components weights for the wet lay-up process.

Component	Epoxy resin	Hardener	Accelerator
Weight (g)	200	120	8

The various parts are put into a clean baker starting from the accelerator, then the curing agent and at the end the epoxy resin.



*Figure 2.1: (a) the fabric is first cut from the roll using a pizza-cutter, (b) the three components of the resin are here depicted.*

After that, the mixture is stirred until the strips that are formed inside the material, due to the presence of different components, are not visible anymore, this procedure must be conducted slowly in order to avoid that the resin incorporates air. The best choice for this operation is to carry out it inside a fume cupboard to avoid any risk of inhaling the toxic fumes from the mixture. The stirring procedure must be done for at least 15 minutes to be sure that the mixture is homogeneous. To make this procedure easier, the baker was placed inside a metal bowl with hot water inside, this procedure permits to have a less viscous resin, which is easier to mix and pour. The resin is then placed inside a vacuum over for the degasation at a temperature of  $60^{\circ}$  and at  $-1$  bar. In this operation, air bubbles inside the resin are released and will form a foam on the surface of the mixture, caused by the raising of the bubbles. The degasation process is meant to be concluded when there is no more foam on the surface, must be said that even after this step some air is stuck inside the mixture, so it is not possible to remove completely all of it. The degassing procedure of the resin must take from forty-five to one hour to be concluded.

## Experimental methods

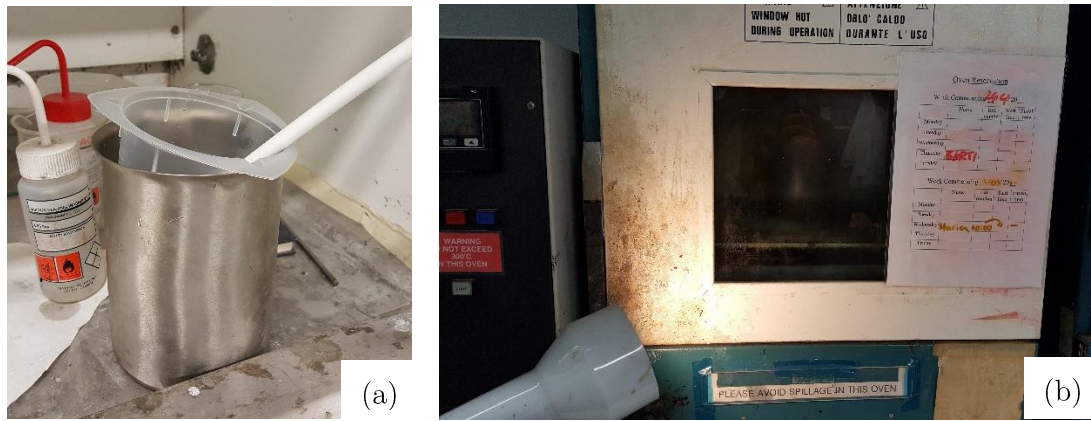


Figure 2.2: (a) the resin is stirred in a metal baker containing hot water for at least 10 min, (b) then it is degassed for an hour at -1 bar.

Then, the plastic structure to sustain and contain the fabric is joined with the use of screws, the dimensions of this structure are  $37 \times 37 \text{ cm}$  as external side of the square and approximately  $33 \times 33 \text{ cm}$  as inside side. At the bottom of it, the whole perimeter is covered with a plastic sealant, from the company General Sealant, in order to stitch to it a Melinex layer that permits to place over it the fabric for the infusion and to contain the spillage of the resin in excess from the composite during the following step of the process.

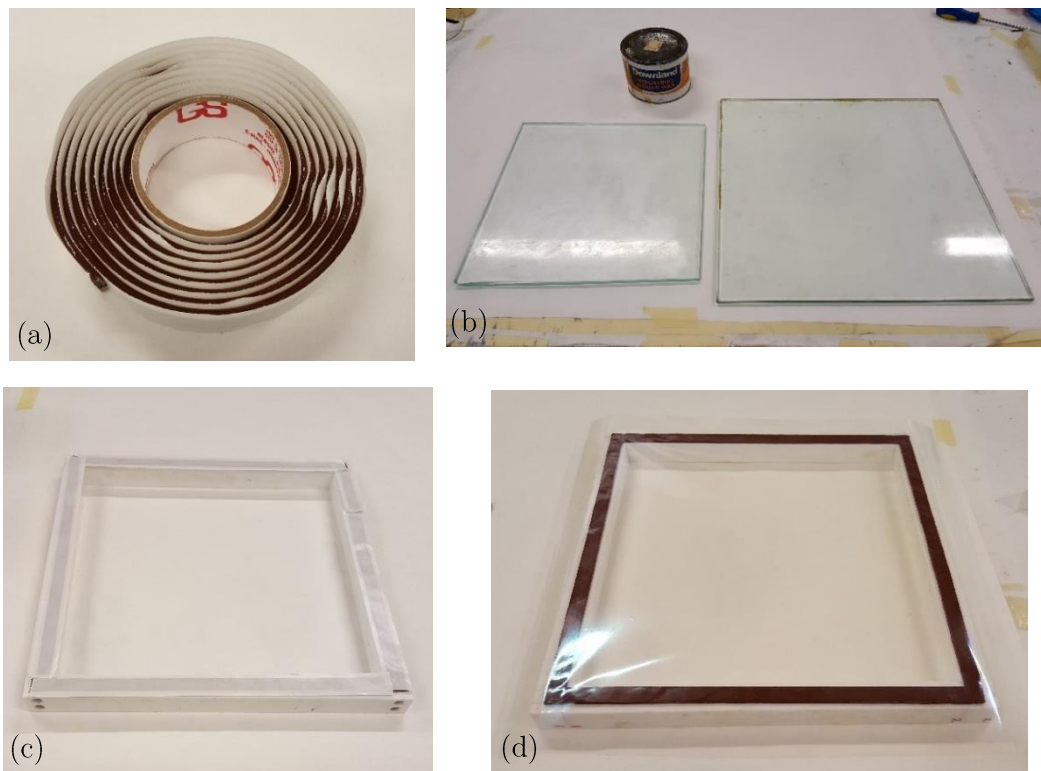


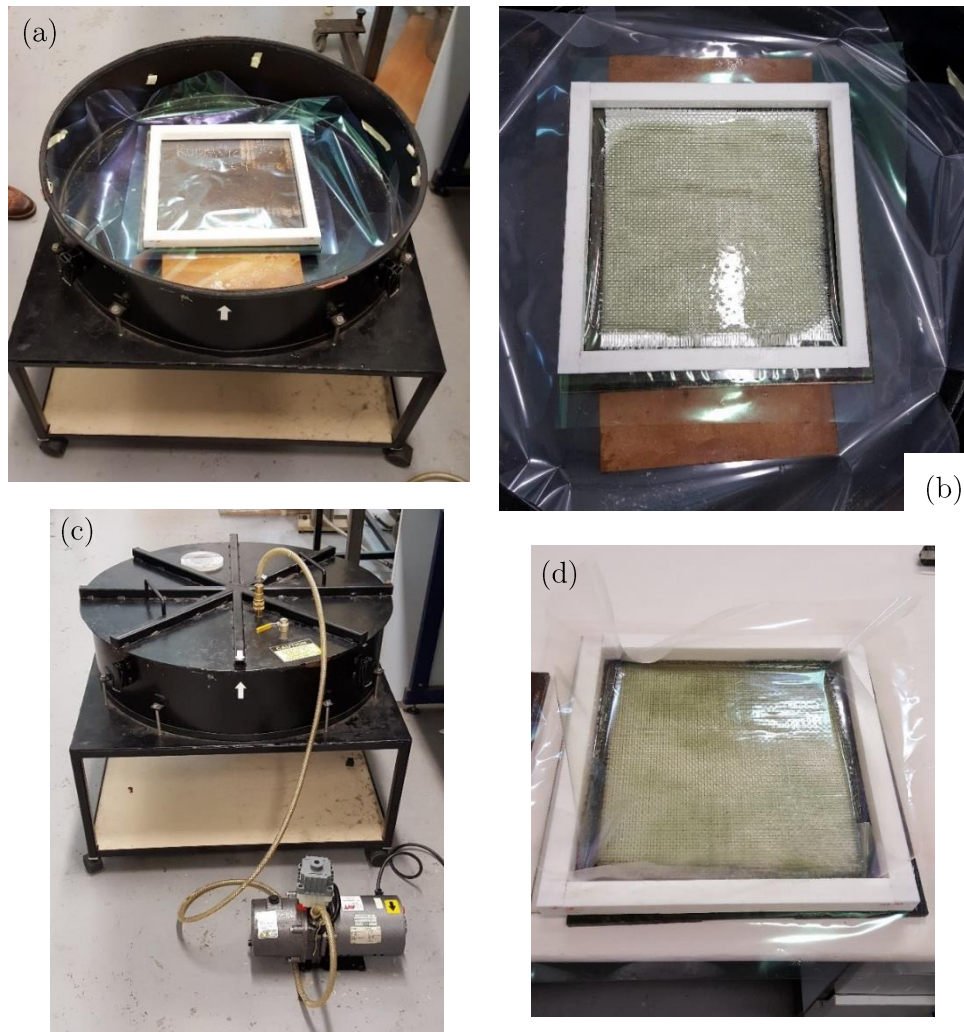
Figure 2.3: (a) Plastic sealant used to contain the resin excess, (b) glass lates which need to be covered by a wax layer, (c) containing structure with the plastic sealant applied, (d) a layer of melinex is placed on the structure inside of which will be put the cloth.

At this point, the supporting and heating structures were prepared. First of all, two glass plates of different measures are then polished from the previous old wax on the surface with the use of a razor and some tissue and a newer layer of industrial wax is placed using some tissue to distribute it with circular movements. This layer of wax has the function to prevent that the plastic layer to stick to the glass plate and so make it easier the removing. After that, both the larger glass plate and two metallic plate where put inside a hoven to reach the temperature of 100 °C and left inside it thill a homogenous temperature is reached. This device has the function to maintain the resin and, as an extent, the entire system heated for a longer time, in this way the resin will be less thick making easier the impregnation process inside the vacuum box. Then, the sustaining structure is placed over the glass plate with the wax, which is placed over two metallic plate and the dry fabric is so placed inside it and the resin poured trying to distribute it in the most homogeneous way. This set was then placed inside a vacuum chamber at -1 bar to let the resin infuse and wet all the fabric, using the vacuum to remove all the air trapped inside the cloth during the impregnation, to do this the composite is let inside the chamber for at least 1 hour. During this period, the remining air trapped inside the resin is also pulled out. It is important to notice that the arrows of the vacuum box edge should be aligned to have a perfect sealing of the lid, otherwise there would be some leakages and some air would continue to enter inside, lowering the depression inside. To open again the vacuum box a valve must be opened to let the external air came inside again, this procedure must be done very slowly, otherwise a lot of air would come into the composite and inside the fibers again, giving as a result a poor finishing with a lot of voids and open channels on the surface.



*Figure 2.4: (a) glass and metal plate heated inside the oven, (b) beker with the resin at the end of the degassing process.*





*Figure 2.5: (a) the structure is placed inside the vacuum box as first thing, (b) the cloth is placed inside it and the resin is poured homogenously, (c) the vacuum box is closed and the vacuum pump is linked, (d) when the infusion process is ended a layer of Melinex is placed at the top and the air trapped under it is removed with a piece of plastic.*

The final stage is to extract the structure, then a layer of Melinex is placed over the composite and the excess of resin and the air that is still trapped are pulled out mechanically with the use of a plastic spatula. When it is believed to have arrived at a good result, the composite is then ready to be placed inside the oven for the curing process, before that a smaller squared glass plate of 30 cm as side is put over the composite. The whole set-up is so heated and a set of weights is placed over it during the whole time, four weights of 40 lbs and one weight of 44 lbs, which gives a total weight of 92.52 kg. Considering the area of the small plate, this weight generates a pressure of 10.08 kPa on it. The curing cycle used is the standard one for this kind of resin in this university, which is composed by three steps, reaching the maximum temperature of 100 °C:

- Heat up with a slope of 2.5 °C per minute.
- Maintaining the maximum temperature of 100 °C for 3 hours.
- Cool down till room temperature with a rate of 2.5 °C per minute.



Figure 2.6: Composite inside the oven during the curing cycle with the weights on top.

The next image shows graphically the curing cycle, described above.

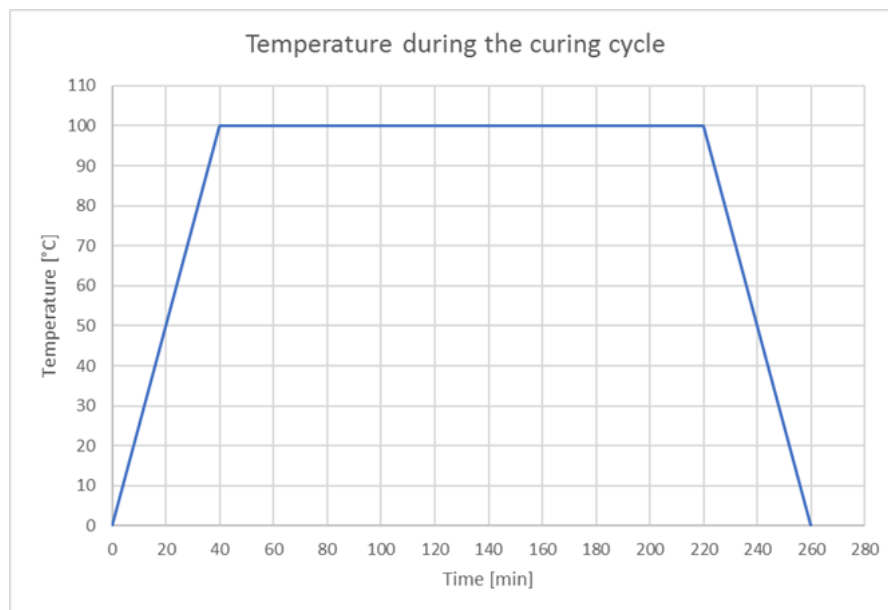


Figure 2.7: Scheme of the curing cycle.

The advantages of this technique are:

- Easy processing.
- Low capital investments, good for low-volume production and prototypes.

## Experimental methods

- Possibility to use a large variety of resins and fibres.
- High fiber content (but lower than Pre-Preg process).

The disadvantages are on the contrary the following:

- Labour intensive method.
- Hazardous situations can be possible since it is a process worked with hands.
- The result depends on the operator skills and practice.
- It is an open moulding process so it can be not suitable for environmental reasons.
- For a better infusion, the resin needs to be less viscous since its worked by hands.

### 2.2.3. Fibre volume fraction calculation

To be sure about the valuable properties of the own made laminates, the fibre volume fraction was calculated to have an idea of the voids content inside the composite and to be able to compare the result of the fibre volume fraction calculation with the data in literature. The technique used was the burn-off method, it involves heating up the composite until a temperature where the matrix burns and it is dissolved in fumes, while the fibres remain stable and unaffected. Initially, five composite samples were cut from the two laminates made. The position of these was randomly chosen along the laminate width, while all these were cut in the same strip considering the length. The best choice should be to pick the samples randomly over all the surface to have a more representative distribution of the data, in this case was preferred not to sacrifice one specimen for this calculation so, the samples were taken from the spare cuts. The samples were cut with the side roughly of  $20\text{mm} \times 20\text{mm}$ . Then the measure of each side and the thickness were taken to obtain the specimen volume. To put the specimen inside the oven some cup with their lid must be used, so their weight must be measured in obtain in a further step the specimens and fibres alone weight.





Figure 2.8: On the right can be seen the cups with the lid, inside them there are the samples and can be also seen the balance used. On the left there is the the furnace with the suction system for the fumes.

At this point the specimens can be put inside the oven to melt and burn the resin, the temperature at which this process take place is around 600 - 615 °C, the oven is programmed to reach this temperature and maintain it for three hours to be sure that all the resin is burnt, then it cools down until room temperature. The crucibles with inside just the fibers have been then weighted again, the final volume fraction can be calculated as follow, knowing the densities of the various parts:

$$V_f = \frac{V_{fibers}}{V_{fibers} + V_{matrix}} = \frac{\frac{m_{fibres}}{\rho_{fibers}}}{\frac{m_{fibres}}{\rho_{fibers}} + \frac{m_{matrix}}{\rho_{matrix}}} \quad (2.1)$$

To find the fibres density was considered the density of the E-glass, to calculate the one of the matrix must be accounted the different densities of the parts that compose the matrix, they are reported in the next table:

Table 2.4: Densities of the epoxy resin components.

Density		
Fibers	2,57	g/cm3
Epoxy	1,16	kg/L
Hardener	1,232	g/mL
Accelerator	0,97	g/mL
matrix	1,182	g/mL

Where for the density of the fibers was considered the density of the pure E-glass, which is equal to  $2.57 \text{ g/cm}^3$ , because the material with which they are made is PPG Hybron 2022 E-glass. The density of the matrix was calculated counting each density with its proportion inside the mixture, the quantity of epoxy resin was 100, the one for hardener is 60 and for the accelerator is 4, as reported in the previous chapter. The final density is  $1.182 \text{ g/mL}$  which is the same as  $\text{g/cm}^3$ .

#### 2.2.4. Cutting of the specimen and end-tabbing

The laminate obtained from the manufacturing procedure has then been cut with the help of a water-cooled diamond saw in different coupons, getting rid of the external parts which cannot be used for their rough finishing. Before this operation, the external plastic frame must be opened, removing all the polyester sheet (Melinex) from the top and the bottom of the laminate, giving attention not to ruin the finishing of the surface. The specimen measures are the following: *Length* = 230 mm, *Width* = 25 mm, *Thickness*  $\approx$  2.53 mm, as can be seen in the next image. These measures conform to the standard as given in ASTM “*Standard test method for tensile properties of polymer matrix composite materials*” (D 3039/D 3039M), particularly for balanced and symmetric fabrics.

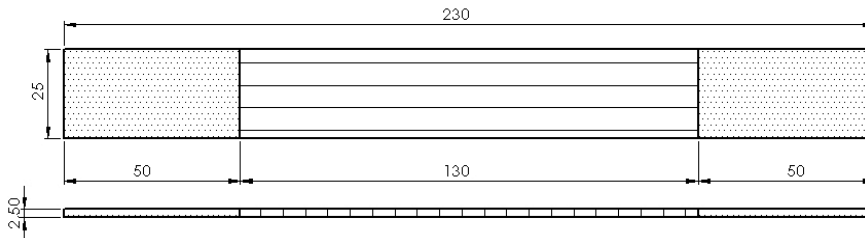
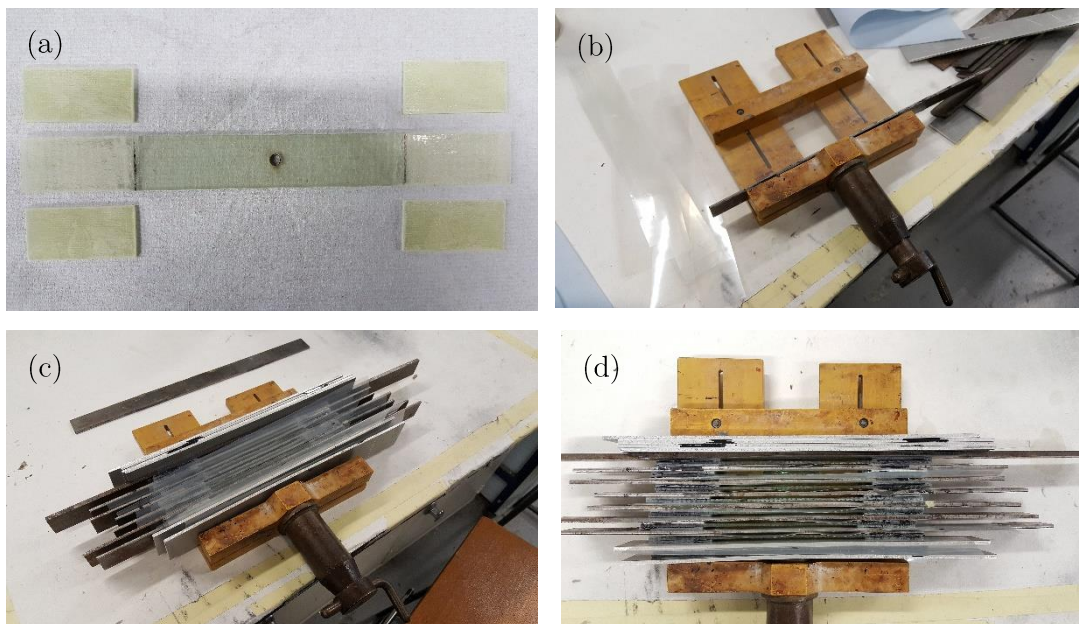


Figure 2.9: Specimen geometry cut in the warp direction.

All the specimens were cut in warp direction, using the same length.

Three standard hole dimensions were chosen and for each of them three specimens were made for the testing:  $\emptyset = 2.5 \text{ mm}, 5 \text{ mm}, 10 \text{ mm}$ . In a second investigation, the bigger hole size was replaced by a  $\phi = 7.5 \text{ mm}$  as hole size. This choice was made to avoid the presence of the edge effect, which would affect the stress field near the hole if it is too close to the specimen edge, other nine tests have been done again. The end-tabbing was carried out in order to reinforce the specimen ends, to avoid that the grips damage the specimen and to permit a smoother load transfer. To do so, the first passage is to cut four

end-tabs for every specimen from a plate of material using the diamond-saw, the dimensions of the end tabs are as wide the same of the specimen and as length 50 mm. Then, the end-tabs can be sanded using sandpaper on one side and the specimens on each side, this to have a rough surface where the glue can attach better. After this, the powder is removed from the surface using some tissue and methanol. At this point the bicomponent glue can be placed on the end-tabs, which are then attached to the coupons, then they are stacked in the clamp alternating one metal plate between two coupons. On each side of the metal layer and on the inferior clamp surface are also placed some Melinex strips for the glue leakages. Finally, the clamp can be tightened and leaved for at least 24 hours for the glue to harden.

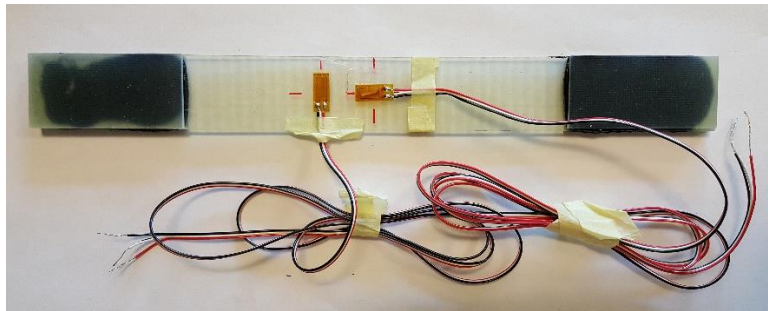


*Figure 2.10: The end tabbing procedure is here reported. a) the surface of both the specimen and the tabs are scratched with sandpaper, b) some Melinex strips are placed on the bottom of the clamp and between every specimen and the metal plates, c) the clamp is then tightened, d) upper view of the specimens in the clamp.*

### 2.2.5. Strain gauging

To verify the results of the DIC technique, strain gauges were put on the specimens to compare the strains coming from the two methods. The procedure that must be followed to apply the strain gauges is this, first some lines must be drawn where is intended to place the gauge to align it properly. Then, the surface is scratched using a glass fibre pen to make the surface rough enough for a better adhesion of the glue, the powder that is generated is polished with cotton wool buds wetted with methanol, scraping the surface

always in the same direction to remove the dirt. Then, the strain gauge is taken out from the protective envelope and removed using a piece of tape to stick it. At this point, the strain gauge is positioned on the chosen spot, aligning it with the lines previously drawn, attaching the tape to the specimen surface. An edge of the tape is lifted carrying with itself also the strain gauge and a drop of glue is put beneath it, the gauge is then repositioned and a pressure is applied over it with the thumb while the glue is hardening, after a while the tape can be removed. Now, the attention can be paid to the wire, the plastic edges can be removed and each metallic part is soldered, from the gauge side the white and black cables are joined, while at the other side the three cables are kept separated. Then, the gauge platelet, where the wires will be attached, is scratched using the soldering iron to remove the plastic film which covers it. Subsequently, the wires are kept in place using a paper tape strip and the edges are soldered to the gauge with two little drops of melted metal. As a last thing, the resistance of the gauge is tested to check if everything was done properly, it should result around  $123 - 125 \Omega$  after a correct procedure.



*Figure 2.11: Final result of the strain gauging procedure. Two gauges are placed, one of them for the Poisson's ratio measurement.*

## 2.3 Quasi-static tensile tests

All the tests were performed as uniaxial quasi-static tensile tests on a servo hydraulic machine, which is the Instron 5982, provided with a 100kN load cell. The machine was set to apply to the sample 1 mm/min displacement. During some experiment, the sample was equipped with one or more strain gauges in order to collect more points than the strain data given by the DIC analysis and in an easier way, in order to plot the stress-strain curve of the specimen. Must be said that this measure is affected by the damage that appends under the gauge surface, so the two curves, the one given by the strain gauge measurement and the one given by the DIC technique, could present some differences where the damage is formed because the second one represents an average on a

bigger area, depending on the size of the rectangle chosen to calculate the average strain, so less affected by the local effects. The samples were measured before the test considering the specimen width and thickness, as an average between three measures along the length, so it was possible to calculate the stresses inside the material knowing the cross-sectional area. The load data acquisition provided by the machine was set to collect one data every 0.1 seconds, the data was acquired using the software provided with the Instron machine which is called Instron Bluehill. The machine is equipped with a digital display and the results given are already in the digital format, moreover also the load desired can be adjusted directly using the screen commands, the same for the measure of the instant load without any kind of intermediate operation. The strain measures, coming from the strain gauges, were recorded using an external Micro Measurements 7000 data logger and another laptop computer.

Some tests were conducted stopping the machine when the strain value reached a predetermined value analysed using strain gauges, chosen because related to the damage formation inside the material. So, some tests were stopped when the first extensive damage appears or before final failure. Other tests were stopped to analyse the damage development around the notch, so also in this case the test was stopped before final failure, taking into account the load to failure registered from other tests.

## 2.4 Digital Image Correlation

### 2.4.1. Camera and software system

The apparatus used is composed by two Allied vision technologies - Manta G917B cameras, one Hedler DX15 lamp and one tripod by Manfrotto. The software used is the VIC-3D provided by the company correlated solutions. The software was set to collect on set of data, which is equivalent to capturing one image, every 6 seconds.

The subset size is the area where the software makes the calculation, creating a grid all over the specimen, and its size is dependent on the speckle pattern, the option used in most of the calculations made in this work is  $27 \times 27$  pixels. This because the speckle pattern used was optimized for this specimen size and never changed.

The step size is defined, on the contrary, as the distance in pixels between each position for the calculation, in this work is set to be 7 pixels. So, it is tracked an area of  $27 \times 27$  pixels for every 7 pixels. It is important to notice that the step size is usually  $\frac{1}{4}$  of the size of the subset. For every subset is collected one data point, which is placed in the subset centre. This leads to a problem near the edges because the closes point that can be tracked is one half of the subset size from the edge, this problem related to the DIC is called edge effect. So, near the edges and holes there will be some areas that are not possible to analyse, as will be seen. To analyse also the edges, it is necessary to use smaller subsets, which means using a smaller speckle pattern.

### 2.4.2. Specimen preparation

As it was said, it is necessary to apply a random pattern on the surface of the specimen to apply this technique, this is a very important step in the process since it affects directly the results and it can be not so easy as it seems. To do so was used the spray painting technique. This one is the most common one and it is suited for intermediate size components, so this method cannot be used if the DIC wants to be used with microscopic resolution or on large scale structures, the suitable dimensions for this technique are between 25 *mm* and 1.25 *m*. One issue related to the painting application is that it is applied directly on the specimen surface, so this must not be chemically altered by the painting itself.

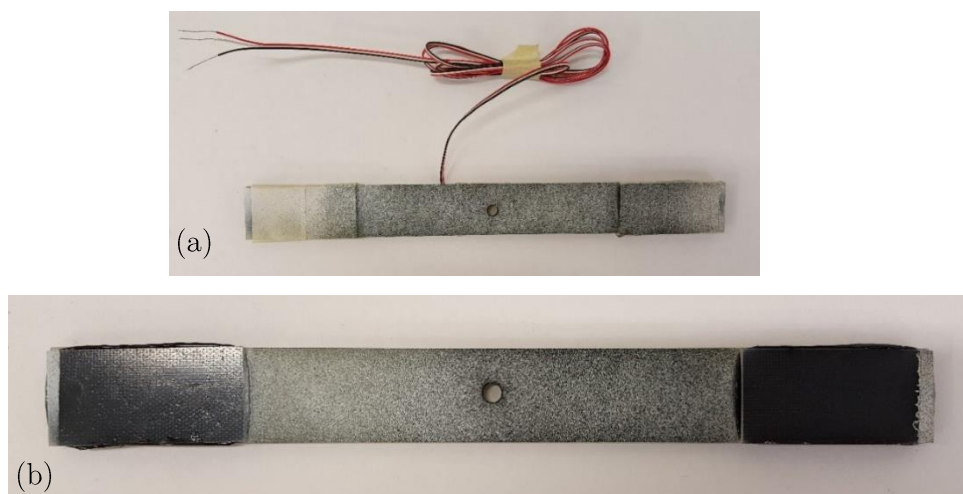
The first thing to do is to apply a uniform white paint on one surface of the specimen, this should be as thin as possible without hardened drops on it, which can change the surface shape leading to problems in the next steps. When the paint is dry, a speckle pattern can be applied, to do so several fast passages with the spray can are made, making care that the begin and the end of every pass are made outside the specimen in order to avoid that some spots completely full of painting arose. The distance between the spray can and the specimen must be selected accurately because it affects the size of the drops of painting, which must be calibrated for the specimen since the resolution needed is directly correlated with them. Also, the velocity of every pass is a variable that must be taken into account, if it is too slow some darker areas will appear which will create some inhomogeneities inside the same area treated.



*Note:* A useful tip is that, if a darker area is created, this can be fixed spraying a pass of white paint over it, which will cover again part of the black speckles recreating the homogeneous speckle density of black dots.



*Figure 2.12: (a) Working environment with fumes cupboard, (b) specimen after the application of the white background, (c) spray painting of the black speckle pattern*



*Figure 2.13: Specimens after the application of the speckle pattern, (a) specimen with strain gauge and with the paper covers to protect the end tabs, (b) final result with the end tabs visible for a specimen with the same hole size without the strain gauge.*

## Experimental methods

To check the uniformity and the effectiveness of the speckle pattern to be used in the image correlation must be used a tool provided inside the software Vic-Snap, which is called “sigma plot”. It gives to the user a visual representation of the worthiness of the image in terms of confidence interval for the matching ability of every pixel on the area of interest, when a pixel is coloured in purple, it means that the image is good, if it is red that there are some problems with it. These problems can be due to the spackle pattern or to the focus of the image, in the first case the speckle pattern cannot have enough contrast or definition, otherwise it can be too thick or too thin for the size of the specimen under analysis, the second case can be seen when the image is out of focus [15].

The scale of values represents the error that is arising during the matching of one pixel between the images given by the cameras, so the areas pictured with pink are the ones with the lower errors and ideally all the specimen should be of this colour.

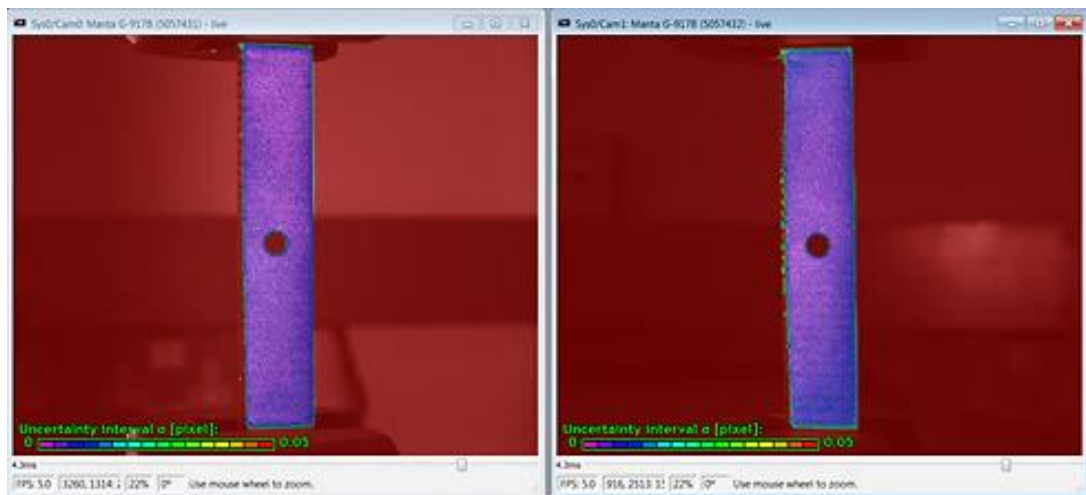
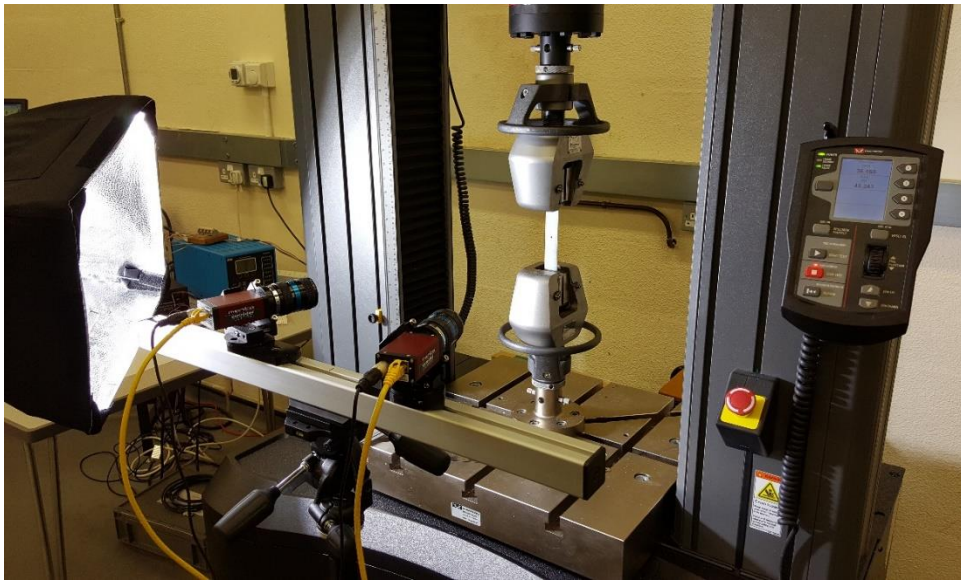


Figure 2.14: Sigma-plot of the two cameras during a preparation phase for the test.



### 2.4.3. Camera set-up



*Figure 2.15: Digital Image Correlation system during a tensile test.*

When the testing machine and the specimen are placed, the camera and the tripod can be positioned taking care about its distance from the specimen and the height, the cameras are not provided with a zoom to avoid the presence of distortions caused by the zoom itself, so the position of the tripod must be manually adjusted to make the specimen fit the entire field of view, which also depends on the size of the lenses. The specimen must fit the entire image without cutting some parts of it, if the specimen covers an area of the image too small, a lower special resolution will be the result, which is obviously to avoid. Even the tripod height must be adjusted in order to align the image centre with the specimen centre, to do so a grid can be visualized through the software. The tripod must be checked to make sure that it is parallel with the ground in every point (i.e. in the midway point and at the edges), the distance between the tripod and the machine must be the same at the two edges, so with the use of a meter it should be measured to verify it. At this point, the initial set-up of the cameras must be changed to adjust both the angles of pitch and yaw. The angle between the two cameras must be symmetric and it must be between  $15^\circ$  and  $45^\circ$  to have satisfactory results, angles under  $10^\circ$  and over  $60^\circ$  does not give usable results. It is important that the two cameras have different orientation because in this way from the different orientation between the two images can be reconstructed the out of plane displacements, otherwise if the angle between the cameras is too large there will be some problems caused by the distortions, if the angle is too little

the camera cannot recognise the difference between the two images, which will give problems to calculate the out of plane displacements, as if the two images were two 2D images. A light is placed near the specimen to improve the contrast of the image, because the natural light of the laboratory is not enough to reach satisfactory results.

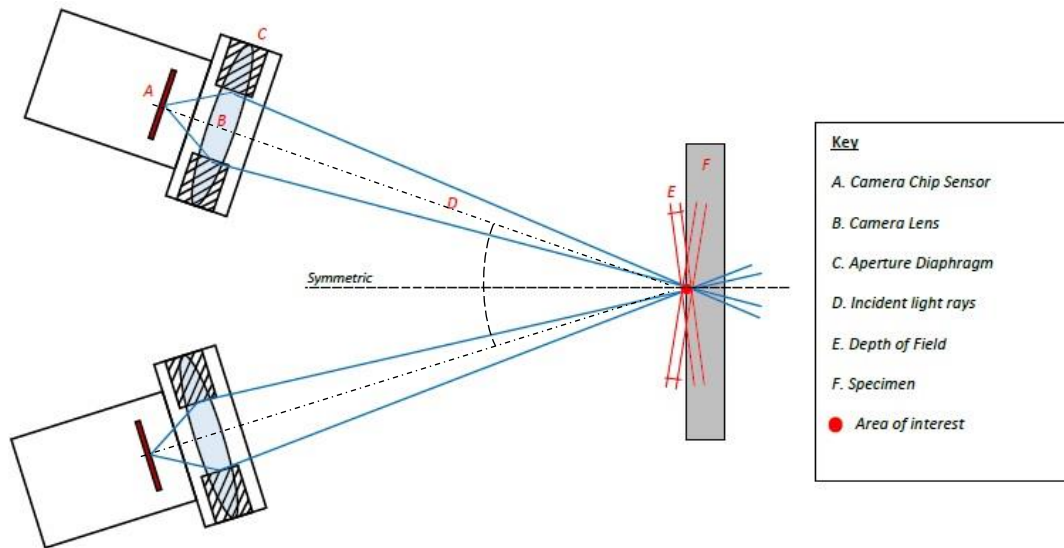


Figure 2.16: Overall set-up of a Digital Image Correlation system as the one used in the present work [15].

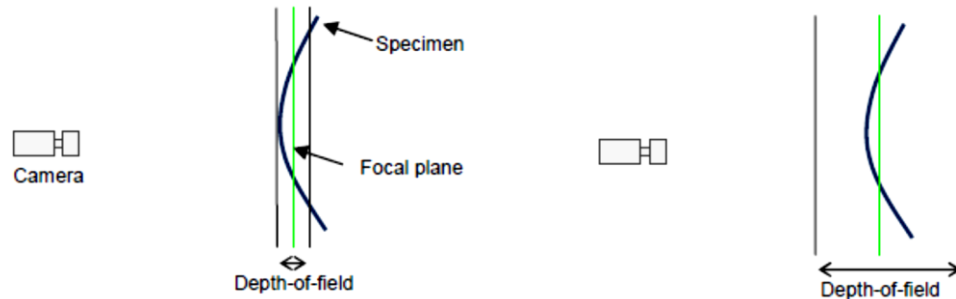
The parameters that can be adjusted in our cameras are:

- Focus, controlled by the focal ring, controls the distance where images are sharp.
- Aperture, which controls the diaphragm aperture and the quantity of light that comes on the sensor. It is also called f-number, which is indicated on the lens ring, a higher f-number corresponds to a lower aperture and a lower DOF (i.e. the range where the image is sharp).
- Exposure time, which is the time that the sensor gathers light for each image, a higher exposure time makes the image brighter but it is not suitable for fast movements.

The set-up procedure can be divided in different steps:

1. In the first step is to check that all the image is in focus and that the centre of the field of view is actually on the specimen plane. To do so, the aperture of the camera is opened till its limit so the diaphragm is now fully open and the quantity of light that comes inside the camera is the maximum, having a brighter image. This operation is made because, doing this, the depth of field (DOF) is reduced and adjusting the focus can be made sure that the specimen is really on focus. The depth of field is defined as the zone or the range of distance where a picture

has an acceptable sharpness, the other regions will otherwise appear blurry. When the diaphragm is fully open, the pixels of the image will result all red because the saturation is at its maximum, thus one pixel cannot be distinguished from another.



*Figure 2.17: In the right image can be seen the effect of the aperture of the diaphragm, focusing the image with a small DOF permits to center the focal plane correctly on the midplane of the object. After closing the aperture, the focal plane remains in its position but the other parameters are taken back to the values for the test.*

2. To have again a detailed image the exposure time, defined as the time that the camera gathers light for every image, which is also the inverse of the frame rate, must be reduced to a very low value. Doing so, the camera will take pictures faster so the quantity of light that is gathered by every image with all the diaphragm open is lower, permitting to have again a contrasted image without the predominant saturation, so again the image is composed by pixel of different grey levels without red pixels.
3. At this point, the focus of the camera can be adjusted using the focal rings on the camera objective.
4. The last step is to return to the original settings for the aperture and exposure time, which are the ones that will be used for the whole test.

#### 2.4.4. System calibration

This procedure is done to make the system recognise the relative position of one camera to another. During this procedure and the entire test, the specimen must be completely visible by both cameras to collect effective data. The procedure can be divided in different steps:

1. The first step is to select the proper calibrated board for the specimen under test. The image size, where to apply the DIC, is selected on the specimen size, so to effectively calibrate the entire area a board that can cover the entire field of view must be chosen. A calibrated board is a square where a grid of dots is printed

which are recognisable by the software, moreover three special dots are printed on it, which represents a triad that is the actual set of points that are taken in consideration during the calibration. So, if the grid is too large for the field of view, the calibration can be still carried on successfully as long as the triad is visible by the cameras, as shown in the next image. If the board is too small, there might be some problems for the software to track the points and it would be difficult to calibrate the entire field of view, unless more images are used.

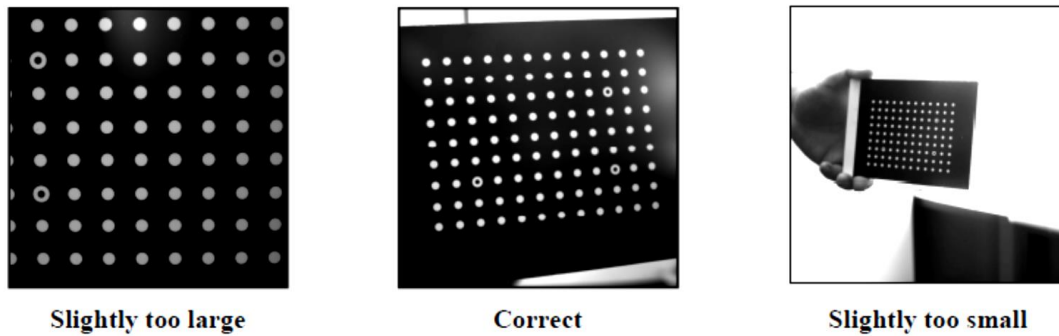
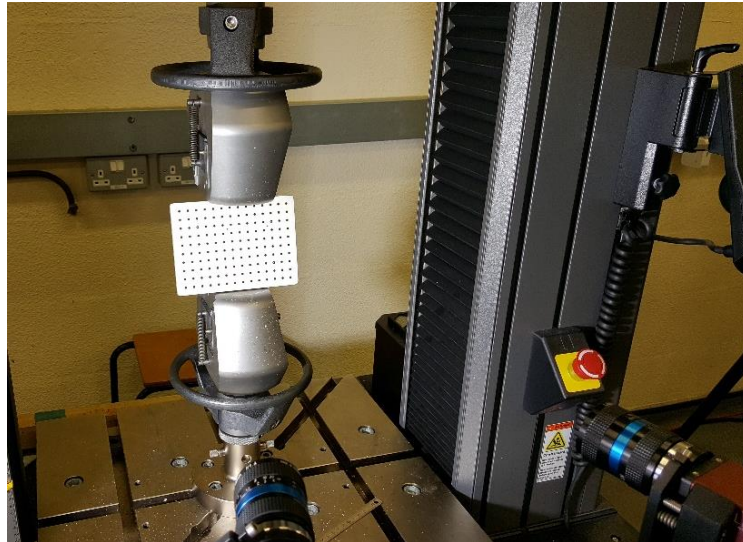


Figure 2.18: This picture show the different configurations that can be seen during the calibration of a DIC system.

2. The next step is to place the board on the machine at the same distance as the specimen, the best choice is to take off the specimen and place the board directly where it should be the coupon. If this it is not possible, the board can be placed in front of the specimen, taking care that the board touches the specimen in every picture during the calibration. Even if the calibration does not refer to a specific plane in the field of view, when the board is placed in front of the specimen must be taken care that the depth of field is large enough to have sharp images of the board in every position.
3. After that, a series of images must be taken moving the board at each image, rotating it in different planes. The minimum number of images necessary to successfully calibrate the system is twenty but a higher number is required because some of them will be discarded during the calibration process. At the end of the calibration process done by the software, a score is given to each image and an overall score to the calibration is also printed on the screen, each score represents the error or better the standard deviation. Some of the images with a bad score, usually coloured in red, must be deleted to lower the final error and if the overall score (called “standard deviation of residuals for all views”) is roughly less than 0.05, the result of the calibration can be considered acceptable.



*Figure 2.19: Digital Image Correlation system under calibration.*

## 2.5 Microscopies

### 2.5.1. Specimen preparation

To obtain some results from the optical microscope or from the scanning electron one, it is necessary to properly prepare the samples. The first operation is to cut the specimens in some strips, roughly of about one-centimetre length around the area of interest, to do so was used a handsaw taking care to have a straight cut, to be more precise two lines was drawn with the use of a marker.



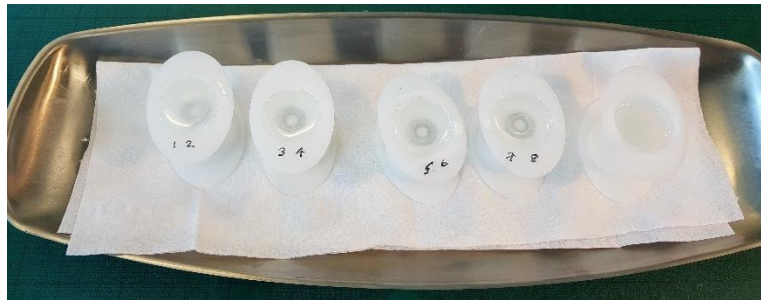
*Figure 2.20: Specimen cutting using an hand saw.*

The next step is to place the cut samples inside the resin in order to make easier the polishing and grinding processes. To make so, the samples where mounted in some plastic carriers to keep them straight and vertical when the resin will be poured. The process



## Experimental methods

requires to put them inside some cylinders closed at the bottom with a cap, inside these cylinders were put the epoxy resin, which is a prepared kit by Strueurs made of fifteen volume parts of epoxy resin and two volume parts of hardener, which is triethylenetetramine, this kit is called EpoFix Kit. The fifteen millilitres and the two millilitres parts are required for each cup. A part of this resin was mixed with aluminium powder to make the background brighter for a better view during the microscopy. The mixture of the two components must be stirred for at least two minutes inside a bowl placed into hot water to make the process easier. Then it is left to rest for one minute to make the bubble come to the surface. After this it is finally possible to pour the resin inside the plastic cylinder inside which there is the composite sample, firstly is poured the resin mixed with the aluminium since the face of the specimen that wants to be analysed is downfacing and after the pure resin. To prevent the composite to float a bolt is placed over it while the resin is curing. The curing of the resin happens at room temperature and it takes twelve hours to be completed.



*Figure 2.21: This image shows the prepared samples where it also visible the blot to prevent the composite samples to float.*

When this process is completed the cylinder made of resin can be removed from the plastic container, removing the lid. On the upper face of the resin sample can be put the ID number using a hand engraver directly on the resin. At this point can start the most important part of the process which is the polishing process of the composite surfaces. As can be seen this process involved four resin samples inside which were mounted two composite specimens. The first part of this process is the rectification of the cylinder faces, it was conducted on a Struers LabPol-21 using a sandpaper P240 and water as lubricant provided directly by the machine. This first passage was just to make the outer surface flat, which is relevant during the use of the microscope, so a very coarse sandpaper was used. After this passage, the specimens have been polished passing very gently some tissue soaked with water on the surface, starting from the edges and then passing on the inner

surface taking care to change the part of tissue used, in order to avoid getting dirty again the surface. Before this process, some diluted soap was sprayed over the surface to polish better the grinded surface. Before and after the cleaning with the soap the surface was washed with water under the tap. After this, some isopropanol was put on the surface and then dried using a hairdryer to remove the last dirty remaining and make the surface completely dry.



Figure 2.22: Struers LabPol-21 machine.

After this, the specimen was grinded with a thinner sandpaper using a ATM Sapphire 520, all the specimens were mounted at the same time since the machine can operate six specimens together. The procedures used, on all the samples, are explained in the following tables:

Table 2.5: Grinding schedule.

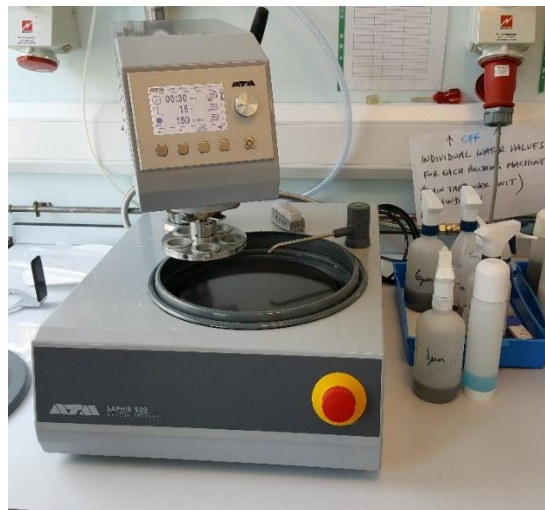
<b>Grinding</b>	<b>1</b>	<b>2</b>	<b>3</b>	<b>4</b>
Disc	Abrasive paper	Abrasive paper	Abrasive paper	Abrasive paper
Grinding media	SiC	SiC	SiC	SiC
Grain size	600 / 800	1200	2500	4000
Lubrican	water	water	water	water
Pressure [N/sample]	15	15	15	15
Speed [rpm]	300	300	300	300
Time [s] [min]	As required	As required	2 x 30s	2 x 30s

Table 2.6: Polishing schedule.

<b>Polishing</b>	<b>1</b>	<b>2</b>
Disc/Cloth	MD-DUR	MD-DUR
Grinding media	Diamond	Diamond
Grain size	3 $\mu\text{m}$	1 $\mu\text{m}$
Lubrican	Blue	Blue
Pressure [N/sample]	15	15
Speed [rpm]	150	150
Time [s] [min]	5 min	5 min

## Experimental methods

Between two different passages, the same cleaning procedure previously described was adopted, in order to remove the dirty from the surface for the next step. The polishing procedure mainly differs from the grinding one because while in the first the grinding media is represented by the sandpaper, in the second one the media is composed by diamond particles, which must be sprayed on the rotating disc. So, every minute two spay of diamond suspension was added on the rotating cloth and every fifteen seconds two spay of blue lubricant were also spayed on the surface, the same process repeated during the whole five minutes. Before starting the test, when the plate was rotating while the samples were already not positioned, the cloth was wetted with the lubricant and some spray of diamond suspension was also added. In the grinding operation, water was used as lubricant which is provided by the machine in this case, even this time before starting the process the sandpaper was wetted with water making the disc spinning to facilitate the operation. The machine used during the grinding and polishing operation is depicted in the next picture:



*Figure 2.23: The ATM Sapphire 520 machine is here depicted, at the right can be seen also the diamond suspension and the blu lubricant.*



## 2.5.2. Optical microscope

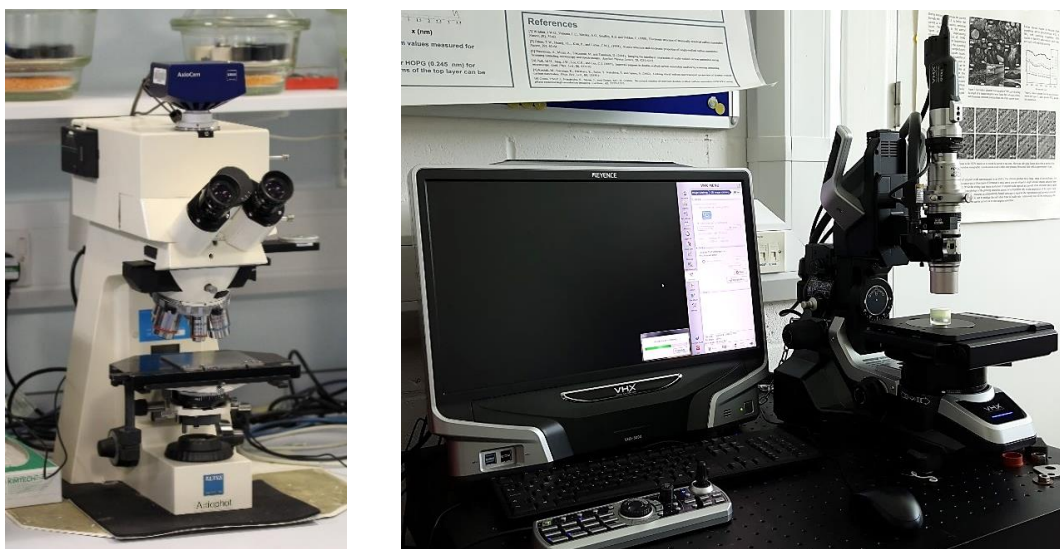


Figure 2.24: On the right a Zeiss AxioPhot and on the left a Keyence VHX-5000 optical microscope.

Most of the images taken during this work have been captured using optical microscopes. The microscopes used are a Zeiss AxioPhot and a Keyence VHX-500. The first one is a manual microscope while the second one is an automated one. So, for taking singles images have been used the first one, the second has been used when was necessary to stitch a lot of pictures together. This operation is automatically done by the one from Keyence, moving the base every time of the same distance following a spiral path. To do this operation on the manual one it is necessary to do a postprocessing work using an external software, overlapping manually the different images previously taken.

## 2.5.3. Scanning electron microscope

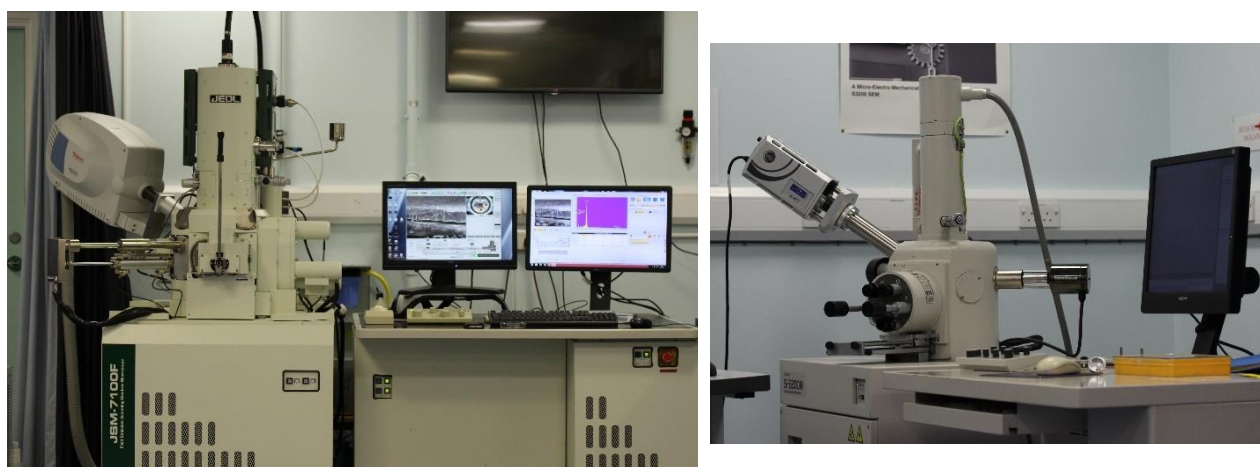


Figure 2.25: On the right a Jeol JBM-7100F and on the left an Hitachi S-3200N scanning electron microscope.

To collect images with high magnification, higher than the one that can be obtained using an optical microscope, or to have well focused images with not perfectly flat samples, was used the scanning electron microscope. The microscope resolution is inversely proportional to the wavelength of the used medium. In optical microscopes, photons are used to scan the sample surface and a series of lenses to magnify the image, so the main limitation to the resolving power of an optical microscope is light wavelength, which does not permit to resolve to different objects closer than  $200nm$ , improvements in lens permit to arrive at  $100nm$  nowadays, still lower than the resolution that can be obtained with electron microscopies. In SEM microscopies, an electrons beam is shot on the sample surface, here it interacts with the material producing secondary electrons and other radiations, that are collected and analysed to produce an image. The resolving power of this microscope, analysing secondary electrons emitted from the surface, can arrive at  $1nm$ . The electrons are generated from a tungsten filament cathode and then are focused by a series of condenser lenses. The beam is controlled in the x and y planes by the deflection coils and after that, hits the sample surface generating a reflection of the primary electrons and the emission of secondary electrons which are captured by a detector that converts these inputs into electric signals, for each point on the screen. To be used in this type of microscope, the sample was subjected to the same grinding and polishing steps as for the other samples. In this case the sample must be analysed under vacuum, if not the electrons would interact with the air molecules and it must be grounded, otherwise it will accumulate electrostatic charges and this would disturb the image acquisition. For this reason, a strip of copper is placed between the sample and the metallic holder. The surface must be also gold coated to enhance the outgoing signal.

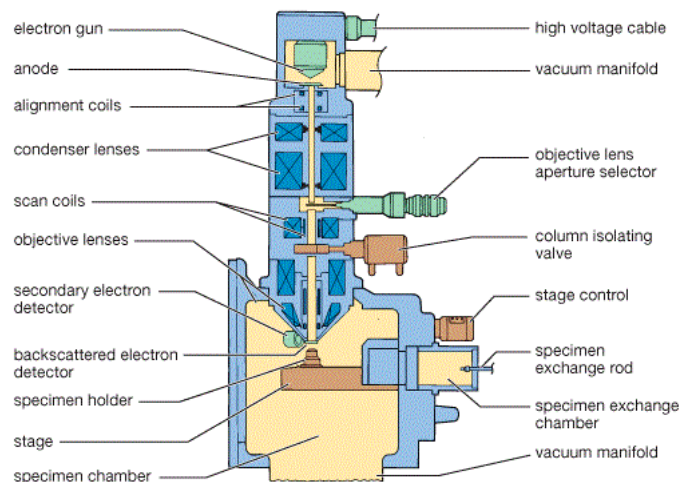


Figure 2.26: A typical scanning electron microscope architecture.

## 2.6 Concluding remarks

In this chapter, the details of all the methodologies used in this work have been explained. The manufacturing technique is given with an elevated level of detail and for further insights it is possible to see Appendix 1. The procedure needed to collect data using the DIC has also been presented, providing an insight on all the steps and the most critical aspects. Also, the specimen preparation for quasi-static tensile tests and fibre volume fraction calculation were described, as the procedure to collect microscopic images with a rough explanation of their operation. In this chapter was tried to give, with all the limitations that are inherently related with this, all the information needed to reproduce the experimental results discussed in this work.



# Chapter 3

## Microstructure measurements

### 3.1 Introduction

To properly analyse the material, its structural parameters are measured using microscopy images of untested specimens, this to characterise the elementary cell of the material. Its internal structure, with its peculiarities, is also studied. This study is important because all the work will deal with the material internal structure and the damage development related to this one. In a second part, the damage visible at the optical microscope, regarding defects that arise during the manufacturing and that are not directly related with the fabric architecture (these defects were described in §1.3.4), are presented.

### 3.2 Material structural parameters

As was already said, this type of 3D woven composite called 3D-96 is composed by three layer of warp tows and four layers of weft tows, which are binder by z-yarns that goes in an orthogonal direction to them for all the thickness, each of them going in the opposite verse with respect to the other two nearby. What was described previously is better explained by the following image where in blue are warp-yarns, in red weft-yarns and in green z-binders. Can be seen that the fibers form different layers one over the other at  $90^\circ$  between them but they never interlace and are kept together by the z-binders. This characteristic is of key importance in the manufacturing of this product, giving less crimping to the fibers, and it distinguish this fabric from a 2D woven composite, which on the contrary presents interlacements between the yarns of the same layer.

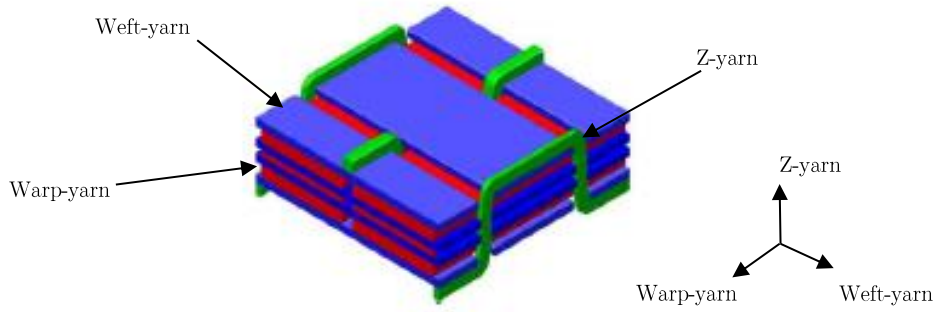


Figure 3.1: Schematics of a 3D-96 fabric, the different yarns terminology and directions are explained.

The internal architecture of the composite can be described cutting it in different planes and watching it from an orthogonal direction to the cut. In the following images, the notation reported for the planes will be used. Plane A-A describes a plane passing through the midline of a warp tow, plane B-B cutting the composite along a z-binder, so both these two represent the structure in the warp direction. Plane C-C on the contrary represents a cut on the weft tow midline and it describes the internal architecture in a direction, which is orthogonal to the previous one. The convention described before is visually depicted in the next image.

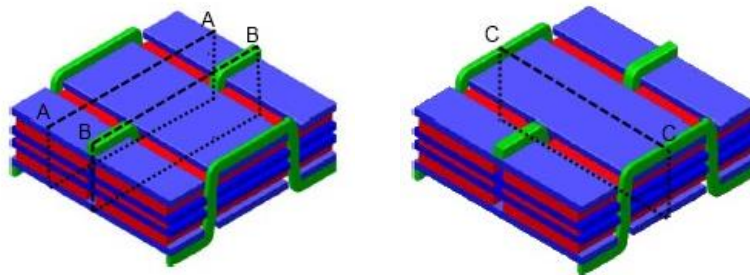


Figure 3.2: Section plane convention to describe the composite architecture.

In the next images, the composite architecture is represented and the internal parameters, which characterize the material and define its unit-cell, are also measured. The following two images show the same view taken from two different parallel planes respectively plane A-A and B-B, in these the distance between weft tows was measured. The first image is taken cutting the fibres in a plane that passes through the z-binders, while the second image is taken in a plane that passes in the middle of a warp bundle. In the first image, this statement can be verified because the 3 warp yarns, characteristic of the 3D-96, are quite not visible, as it should be, because where the z-binders passes, the warp yarns are

not present, thus creating some resin channels near the z-binders. On the contrary, in the second image the z-binders are not visible because this time we are on the plane of the warp tows. Comparing the measures, can be seen that there is a variability of the results due to the fact that the yarns can move when are dry during the handling and also during the manufacturing, so this consideration is not something new and this is something that must be taken into account for every measure. However, it can be seen as for the other case, which will be analysed further on, that there is good agreement between the theoretical results provided by the manufacturer and the measures made during this work, considering the unavoidable scatter of the data. To make this measurement, the approximate centre of the weft tow was found and the distance in pixel between them was compared with the number of pixels that define the scale bar reported in every picture. As was said, in the measure of the weft tows there is a variability of the data and this can be seen in the next two images.

The following image also shows a complete wavelength for the z-binder, which represents a unit-cell dimension, so the measure reported in figure is half the measure of the unit-cell in this direction. It is also possible to see the characteristic z-binders shape, which should be theoretically straight and orthogonal to the other fibers, but in reality, they are shaped as an S, following a sinusoidal path, instead a squared one. This, as was previously said, is generated because the fibers must be tightened during the manufacturing applying to the them a tensile load in order to weave them, making them deviate from the theoretical path. This changes also the shape of the weft tows, that becomes rounded in the proximity of the z-crowns. The last thing causes also the weft tows to be thicker at the z-binder edge because their length is lowered by the binders' constraint imposed. Another effect of this, is that the weft tows are distanced one to another and this creates some superficial resin pockets alternated to the weft tows. As was said, in the next image, cutting the composite along the B-B plane, it is possible to see the absence of the warp tows. This generates the presence of resin channels between one warp yarn and the other where the z-binders run, so between on warp yarn and the other there must be space for the z-binders and in the left spaces the resin will be filled in during the impregnation. Looking at this image, it is possible to see that the structure of a 3D non-crimp fabric is similar to the one of a 2D composite, it is made of straight yarns at  $90^\circ$  between each other without the presence of crimping as in 2D woven fabrics. In a 3D woven, the non-

interlacing yarns are kept together by the presence of the z-binders, which generate crimping in the superficial yarns where they must turn over the weft tows. For these reasons, a 3D composite presents better properties than a 2D woven, because it presents a lower level of crimping, even if its in-plane properties are lower than the ones of a unidirectional composite.

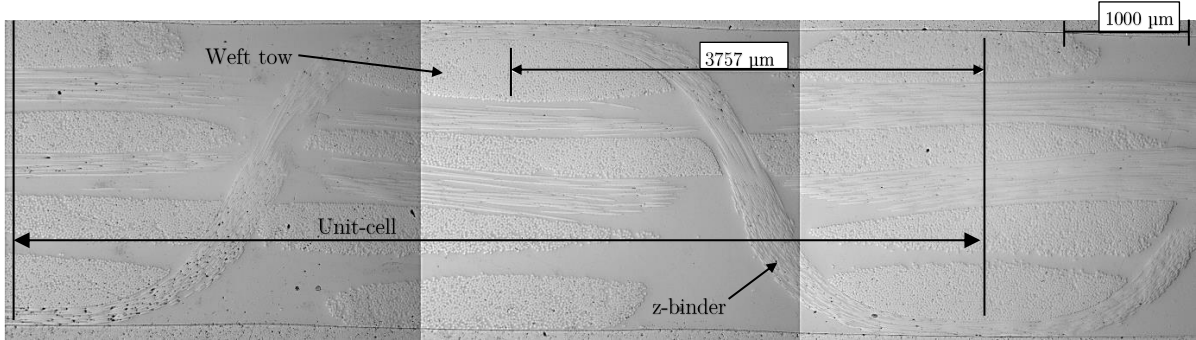


Figure 3.3: Weft tows distance (B-B plane).

The next image shows a similar view to the previous one but in this case, it is taken from a parallel plane, which is in this case the A-A plane, passing in the middle of the warp tows. Thus, in this case is not possible to see a z-binder but can be seen in the same image warp and weft tows and are also visible the superficial resin pockets that are positioned between the weft tows. It also visible how the internal layer in the warp yarns is much thinner than the external two, this will be described again in the following part. Also in this view is visible that the weft tows have a different shape from the one expected, which is sinusoidal shaped because of the z-binders. It must be noted that also the internal yarns are constrained to a different shape form the squared one that can be expected, this witness how the z-binders modify and affect the whole geometry.

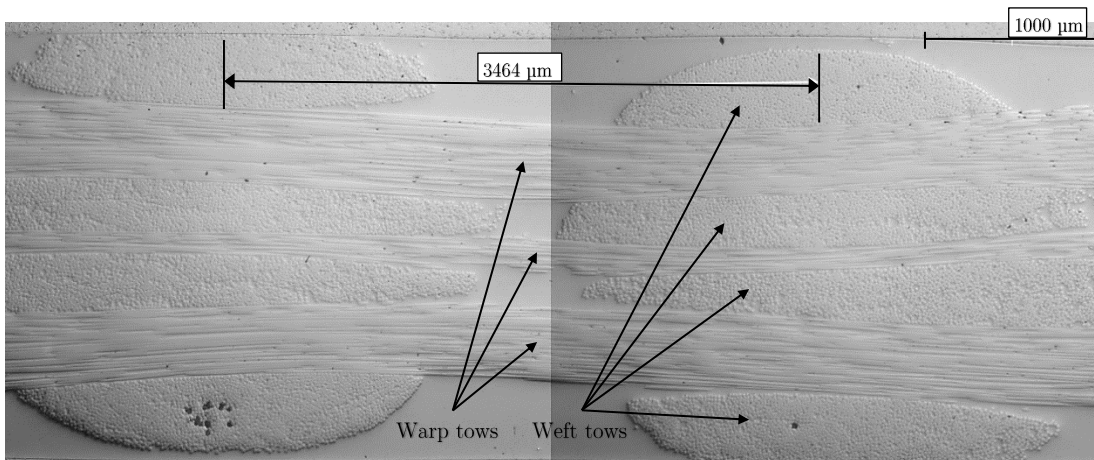
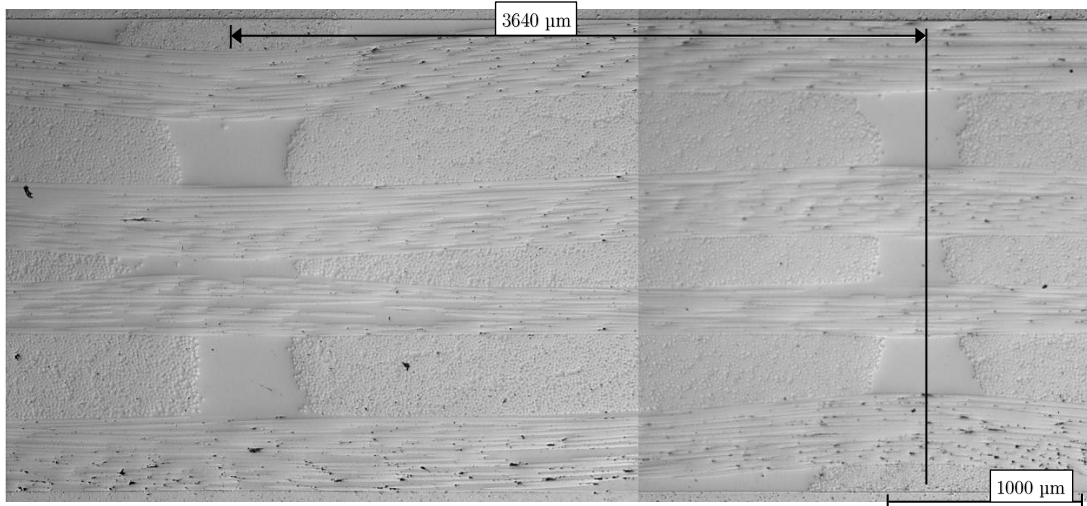


Figure 3.4: Weft tows distance (A-A plane).

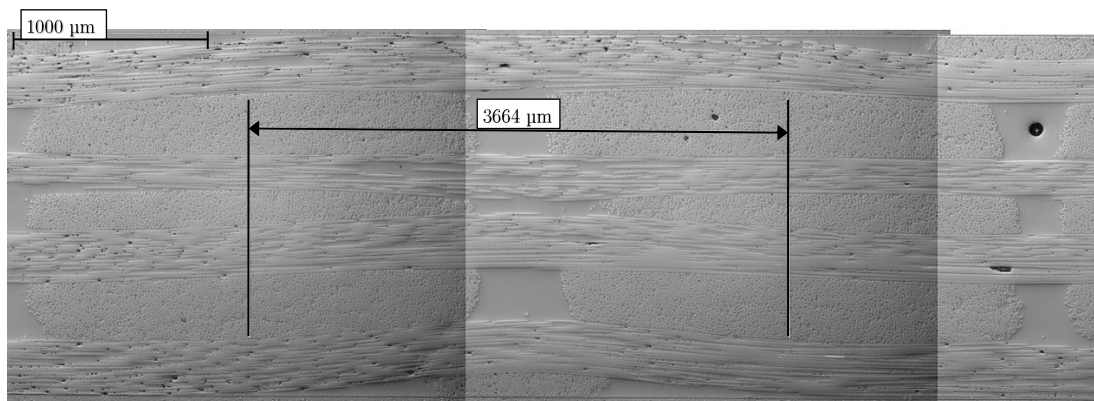


In the next image is represented the distance between two consecutive z-binders, this view is made cutting the warp tows in a direction parallel to the weft tows, in the region called z-crown. Can be seen that in this case the distance measured is quite similar with the one reported in literature.



*Figure 3.5: Z-binders distance (C-C plane).*

Picture 3.6 reports the distance between two consecutive warp tows. Even in this case the distance is taken in a plane passing through the so-called z-crowns, so a plane passing through them and parallel to the weft tows. In fact, in the next picture can be seen three yarns which are the warp tows and four yarns, which are the weft tows. Also in this case, there is a good agreement between the result in this investigation and the theoretical one.



*Figure 3.6: Weft tows distance (C-C plane).*

In the next table, the theoretical parameters describing the internal geometry are compared with the ones obtained from the measured made in the previous image:

Table 3.1 : Micostructural parameters comparison of the yarn distances (theoretical values from [9]).

	Theoretical distance [mm]	Experimental distance [mm]
Warp	3.6	~ 3.66
Weft	3.8	~ 3.76
Z-yarns	3.6	~ 3.64

Can be seen that the results are quite similar between the theoretical and the experimental ones, this result is important because knowing the internal parameters permits to understand the measures of the unit-cell of the material, which is the characteristic unit that defines its geometry.

A wavelength of a z-yarn has the following theoretical value, which is double than the distance between two adjacent weft tows, and it is:

$$z - \text{yarns wavelength} = \frac{10}{2.64} \cdot 2 = 7.58 \text{ mm}$$

So, this measure is the distance that defines the repetition of a sub-unit and it defines the length of the unit-cell in the warp direction.

Table 3.2 : Linear density of the yarns [9].

	Warp	Weft	Z-yarns
Tex	Top and bottom: 2275	1470	1800
	Middle layers: 1100		

The yarn diameter can be calculated using the following formula:

$$\phi = \sqrt{\frac{\text{tex} \cdot 10^{-6}}{\rho \cdot 7.854}} \quad (3.1)$$

Where  $\rho$  is the density of the material, calculated as  $[\frac{g}{mm^3}]$  and the tex is defined as  $[\frac{g}{km}]$ .

From this formula and from the data provided by the literature can be seen that the weft yarns present same diameter and so the same thickness in the various images, as can be seen in the next pictures. The differences between the measures are due to the fact that the fibres are not perfectly aligned inside the composite so the image plane cuts the fibers in different positions. The same thing can be seen in Picture 3.8, where in this case the composite is cut on a plane passing through the length of a z-binder and not perpendicular to them. In this image only the weft tows are visible, while in the place of the warp tows

there are resin channels, this to make space for the passage of the z-binders. The theoretical values for the yarns diameter are,  $269 \mu\text{m}$  regarding the weft tows, while  $298 \mu\text{m}$  for the z-yarns. A certain degree of variability is present as must be expected but the data are still close to the theoretical ones.

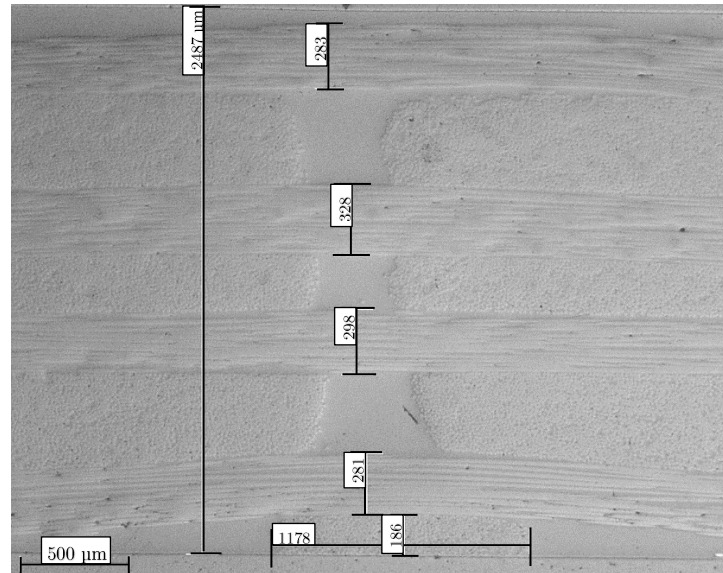


Figure 3.7: Weft tows thickness with z-yarn measures (C-C plane).

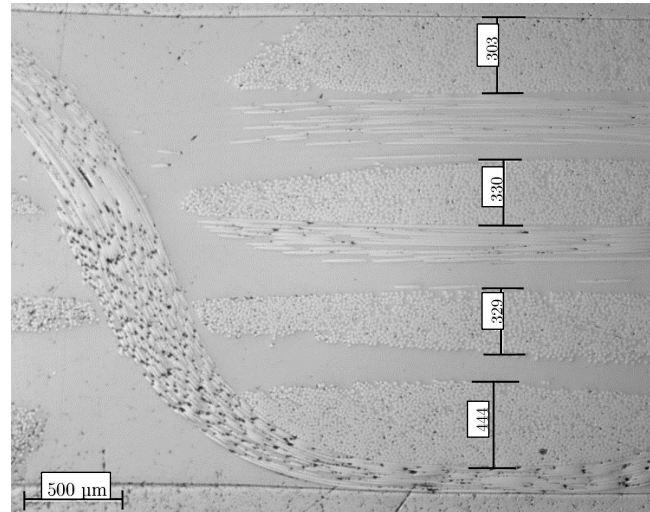


Figure 3.8: Weft tows thickness (B-B plane).

In the following image can be seen that while the weft tows have approximately the same thickness for all the yarns, as declared in literature, the warp town presents a different thickness and so a different diameter between the two external tows and the internal one. Theoretically, the internal layer should have half the thickness of the external one and this is confirmed in Figure 3.9, where it can be seen that the internal

war layer is much thinner than the other two. The theoretical values calculated using the formula for the diameter previously seen are  $335 \mu m$  for the external yarns and  $233 \mu m$  for the internal one. So, it can be seen that there is a clear difference between the literature data and the measures in the following picture. This is because the yarn width is not bounded but can vary and so also the thickness and the diameter can vary as a consequence. Other possible causes are that the cutting plane does not pass exactly on the centre and so this can lead to differences, another one is the possible misalignment between one yarn and another inside the composite.

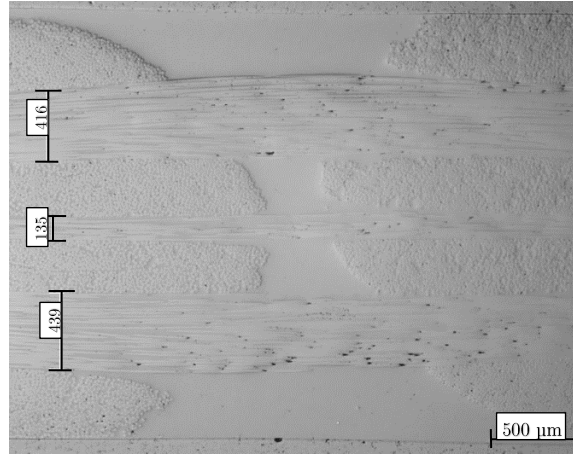


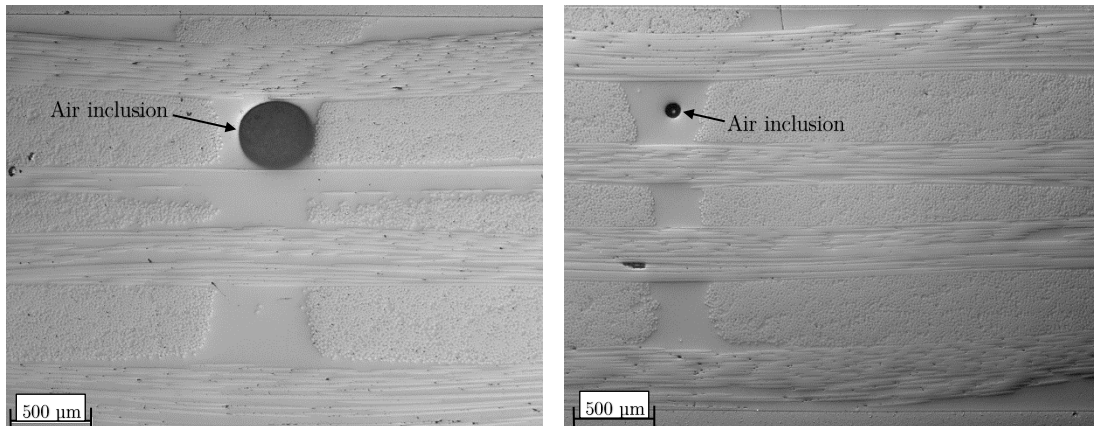
Figure 3.9: Warp tows thickness (A-A plane).

### 3.3 Defects inside the composite

From the previous images can be seen that inside the composite are present various defects, in literature and other works have been described for example air inclusions, unfused areas inside the yarns, matrix cracks and micro-delamination. These observations made using the optical microscope are important to properly characterize the material and identify the possible areas where a damage may start during the tests.

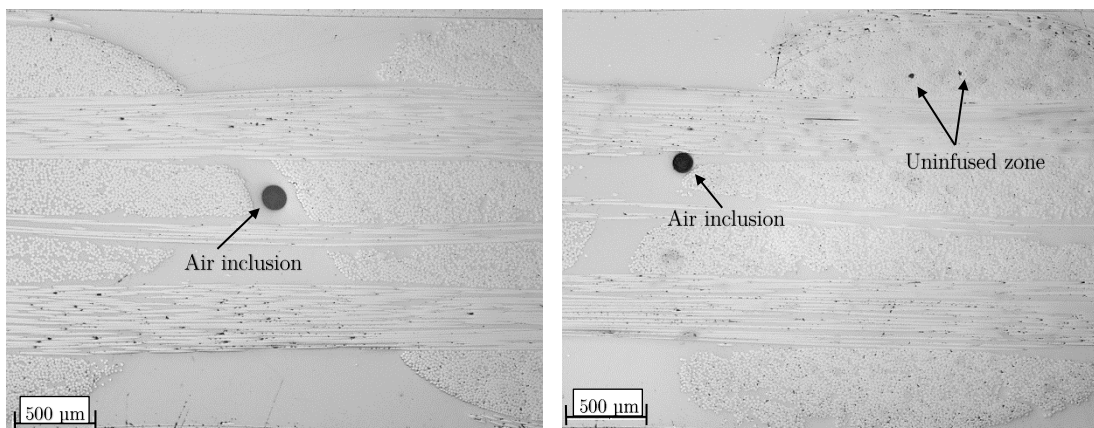
It is visible from these images but also from a visual inspection of the composite that there is a presence of air bubbles trapped inside the structure. This is the result of the wet lay-up manufacturing technique applied to this kind of fabric. This technique is simple and very effective but it is more suited for 2D fabric manufacturing, since it is easier to take out the air when the plies are put one over the other. When this method is used with a 3D composite, during the infusion is not possible to take off all the air that is trapped inside the fabric, especially in some spots. The position where it is very likely to find the voids caused by the air trapped inside are under the z-binder edges, an area called z-

crowns, as can be seen in the next pictures. The following pictures represents a view of the composite cut along a weft tow where the z-binder is at its edge. Can be seen that there is the presence of voids inside the resin pocket under the z-binder. This is a very usual spot since it can be seen, watching the full laminate, that there are bubble lines where the z-binders are positioned.



*Figure 3.10: Air inclusion examples in a 3D-96 composite.*

Another spot where it is very likely to find air bubbles are on the matrix pockets between one weft yarn and another. So, in the next pictures are shown cuts along a plane parallel to the z-binders but inside a warp yarn. Can be seen that some air is trapped between the yarns since it is a spot where it is not so easy to take off the bubbles because they are blocked by the adjacent yarns.



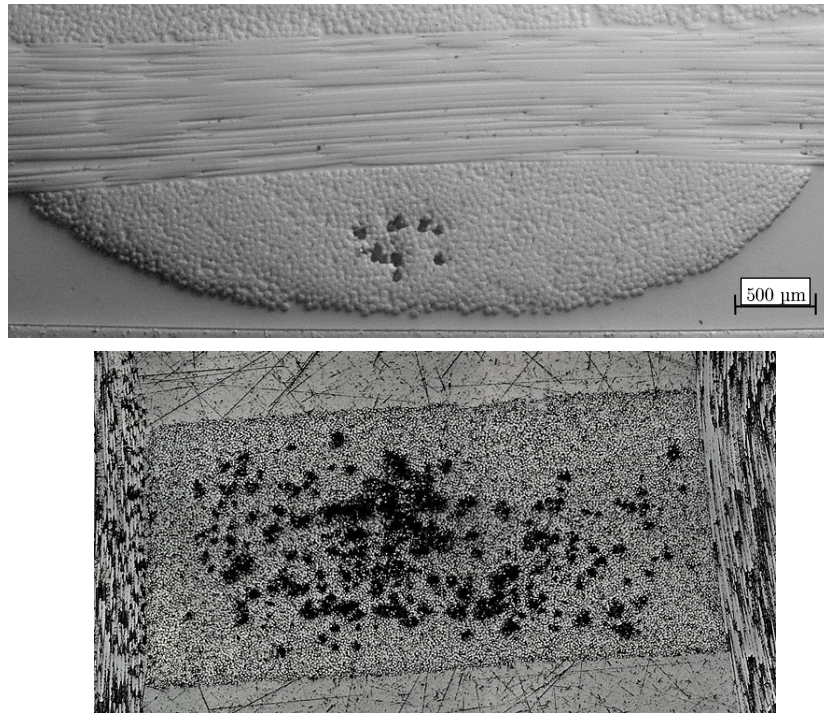
*Figure 3.11: Other defect examples in a 3D-96 composite.*

The cause for these trapped bubbles must be searched during the manufacturing. Some of these bubbles can be already present inside the resin, but this is a very unlikely situation because the resin was degassed at  $-1 \text{ bar}$  for one hour, which should be enough to pull out all the air inside it. The major cause that generates the air trapped is to be searched in the pouring of the air, since this is a 3D woven fabric it is not possible to extract the air once the resin is poured. So, when the resin is poured on it, must be just waited that the resin impregnates the fabric because of gravity, while in a 2D composite it is possible to manually remove the air using a spatula during the lay-up. During the impregnation, it is very likely that some air remains trapped between the yarns. Some of this air, especially the one that is trapped at the bottom of the composite, can be pulled out before the curing using a plastic spatula, but not all the bubbles can be pulled out during this procedure, in fact the bubbles that are imprisoned under the z-crowns cannot be removed using this method. As was previously said during the manufacturing part, to prevent the formation of these bubbles inside the composite is important to slowly release the valve after the infusion inside the vacuum chamber, otherwise a lot of air would be trapped inside. To get rid of this problem the manufacturing process must be changed, using instead of the wet lay-up the VARTM technique, which can pull out all the air thanks to the different resin infusion mechanism.

The unfused areas inside the yarns are visible as dark spots as in the upper picture in Figure 3.12, which is the result of the presence of some areas without the presence of resin inside the yarns but with air trapped around the fibers. This defect is visible from a macroscopic point of view, looking directly with the eyes at the laminate, as what seems to be scratches inside the composite. This defect is not so common for this type of composite while it is very common on the thicker one as will be shown now. In the next image are visible two examples of unfused areas inside the composite, the first one referring to the thin woven composite called 3D-96, the second one to a thick one called 3D-739, both cut along a direction parallel to the warp fibers. If in the first case the presence of small voids is something natural using the wet lay-up technique but their presence is limited, in the second example is showed a very poorly infused composite. This is because the fabric used was so thick that even using a vacuum assisted technique the result was not good. The problem was the time required to infuse all the fabric and the density of the resin during the process. It goes without saying that this type of defects, as any other



defect, is something that should be avoided, so second example of composite results not suitable for practical applications.



*Figure 3.12: Unfused areas examples in a 3D-96 composite (upper image) and in a thick 3D composite (lower image).*

Another type of defect, which has been mentioned in the previous works from Baiocchi (2013) and Novello (2014), is the presence of cracks between adjacent yarns or inside them, which have been called micro-delaminations. The first ones have been spotted between the z-crowns and the weft tows, while the second ones inside the yarns along a direction parallel the warp tows. The reason for the formation of these defects has been addressed to be the thermal shrinkage caused during the curing. Further details can be found in Novello's dissertation. These defects were not seen in the composites analysed with the optical microscope in this work, even if the manufacturing technique used and the curing cycle were the same. An explanation for this different behaviour is not possible to make and so we will just limit to mention it, as a matter of facts.

### 3.4 Concluding remarks

In this chapter, the fabric architecture was described and the unit cell dimensions were found by means of optical microscope measurements, showing a good agreement between the experimental results and the data found in literature (provided by the manufacturer).

This results it is very important because will be used in the following chapters, with the use of DIC. An inherently scatter of data was found, caused by the yarn movements during the impregnation or fabric handling. The tow geometry, the presence of resin reach channels and pockets, both influenced by the presence of the z-binders was discussed and the consequences explained. Other defects not related to the fabric architecture but to the manufacturing process, such as air inclusions and uninfused areas, are here discussed presenting the most common spots where they can be found and the reasons that generate them.



# Chapter 4

## Virtual strain gauge investigation

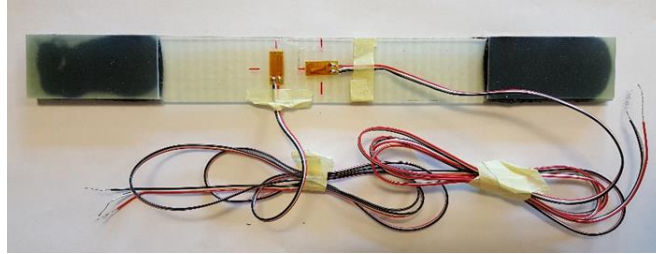
### 4.1 Introduction

In this chapter, the relation between the strain measures obtained using the strain gauge are compared with the measure obtained with the use of the DIC. The DIC measures are taken as the average over an area, which is each time related to the size of the composite unit cell. So, the unit cell is taken as a reference and each time the various DIC measures are compared with the average strain on the overall specimen, which is considered to be the true value. This is to identify the minimum areal value from which the strain measures present reliable values, with a low scatter considering various positions. This because the strain measures are highly affected by the material inhomogeneities, related to the fabric architecture, so using smaller and smaller areas where to average the strain, the measure will be more affected by this phenomenon. On the other hand, the same procedure will be done using an area multiple of the unit cell to see the differences with the other measures. At the end, the aims of this investigation are: compare the result of the DIC with the one from the strain gauge to prove that the DIC is an effective method to calculate the strain and find the smallest area where the average strain is still representative of the overall sample behaviour.

### 4.2 Comparison between the DIC results and the composite unit-cell

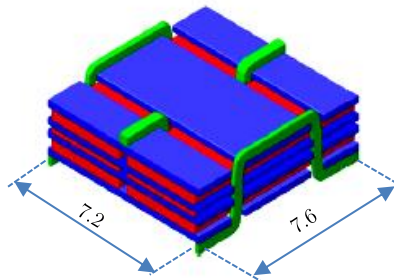
The first operation made on the plain specimens of the preliminary testing was to analyse the DIC results and compare them to the information given by the strain gauge to verify their reliability. To correlate the results given by the strain gauge with the ones given by the Digital Image Correlation, a study of the average strains on a rectangular area over the second plain specimen, provided with the strain gauge, was conducted. The strain

gauges were positioned as can be seen in Figure 4.1, the specimen used, as said, is a plain one, so there are not problems related to the positioning of the gauges far from stress concentrations, in order to have reliable results, also to calculate the mechanical properties of the composite as Young's modulus and Poisson's ratio.



*Figure 4.1: Strain gauges set-up used in these tests.*

The strains analysed are always the ones in the longitudinal direction, called  $\epsilon_{yy}$ , which is also the direction of the applied load. The study was done to find when it is possible to have accurate strain results on one area depending on its size. So, three areal size was taken as reference, considering as a model the area of the geometrical unit-cell of the composite, which is defined as the smallest volume containing the fundamental geometry that repeating itself composes the material. An image of the cell unit for the 3D fabric called 3D-96 is shown below with its in-plane measures:



*Figure 4.2: Schematics of a theoretical 3D-96 unit-cell (measures in millimeters).*

The in-plane measures of the unit-cell were also repeated in the DIC software comparing the specimen width in the picture with the ration between the real specimen width and the unit-cell width, which in this case is the distance between two z-binders. The measures that were taken into account for this study were the theoretical ones reported in paper [9]. The procedure adopted was initially done to find the ratio between the real specimen width and the theoretical unit-cell width. After that, the number of pixels of the specimen width in the picture was calculated and then the ratio before calculated was multiplied

for the specimen width in the picture to have the final measure wanted of the unit-cell width in the picture. This procedure was adopted because the two images produced by the two different cameras are not aligned with the specimen but are affected by a parallax error, since the two cameras forms an angle with the specimen to permits the stereo view. Knowing the unit-cell width measure affected by the parallax it is possible also to have a rough measure of the other measure of the unit-cell.

$$\text{Specimen width} = 24.96 \text{ mm} \approx 25 \text{ mm} \rightarrow \frac{7.2\text{mm}}{25\text{mm}} = 0.288 ; \frac{7.6\text{mm}}{7.2\text{mm}} = 1.05$$

*DIC specimen width = 425 pixel  $\rightarrow$  unit cell: width  $\approx$  122 pixel ; length  $\approx$  132 pixel*

This procedure is not the correct one to obtain the measures of the unit-cell length since the length measure is not affected by the parallax error. In any case, since the DIC technique analyse just one part on the specimen, the image was zoomed to the central specimen area, moreover a part of the specimen is hidden inside the clamps, so it is not possible to calculate the number of pixels of the whole specimen length to obtain the measure of the unit-cell length. Must be said that for the validation of the strains is not compulsory the use of a precise areal size, so this measure is just indicative and approximately equal to the unit-cell inside the composite, which must be said that is also slightly variable from place to place.

Five area measure was taken as first attempt, these areas were placed randomly on the surface, as can be seen in the next pictures. Must be pointed out that is visible a relation between the area used and the pattern composed by the purple dots in the second image, which can be related to the pattern of the z-binders' edges. This is also representative of the unit-cell pattern in the composite. It is also visible, as was said, that the various areas were not placed compulsory over the various cell.

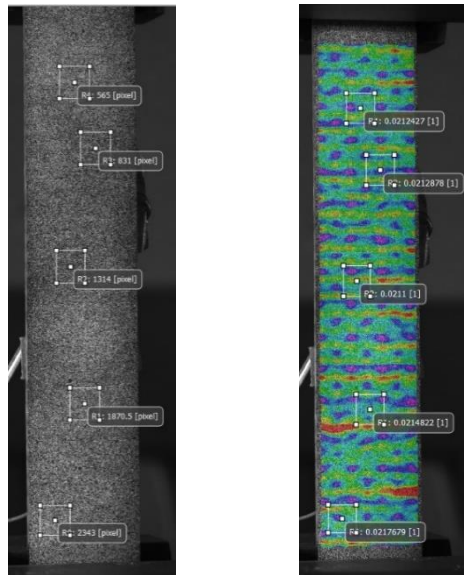


Figure 4.3: On the left is depicted the position of the 5 areas considered over the speckle pattern, on the right the same image over the strain plot before failure.

The test was conducted on the plain specimen provided with the strain gauges, so a comparison of the results given by the different measures of the average strain on the different areas and the value given by the axial strain gauges is provided. The plot reported below provides in the x-axis the value of the strain average on the whole specimen while in the y-axis is reported the strain value for the areal size under investigation. So, as much one curve is near the line at  $45^\circ$ , which represents the curve of the average strain vs the average, it provides better reliable information, not affected by local effects.

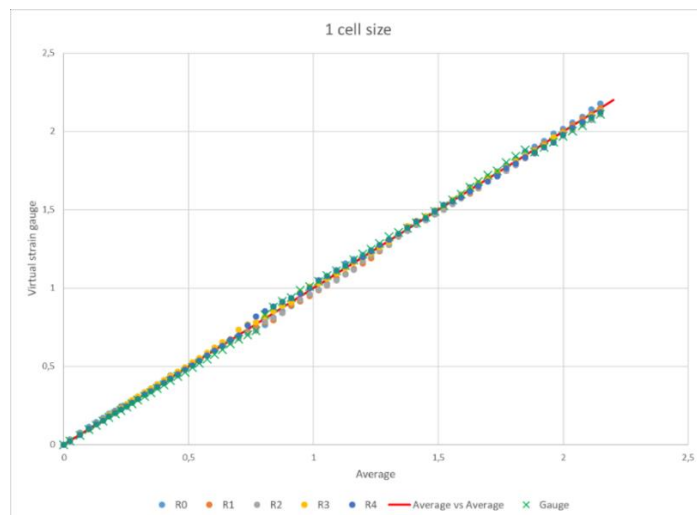
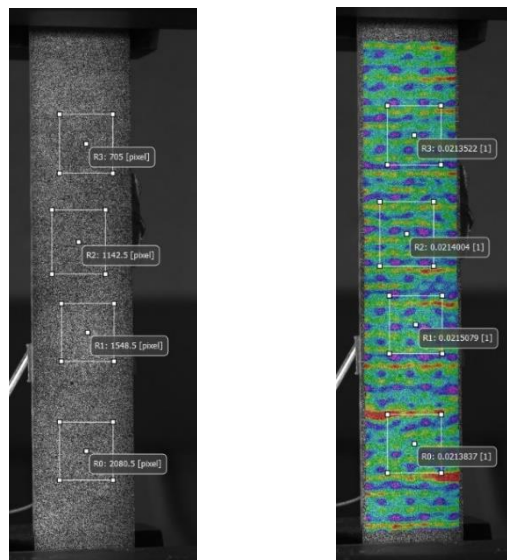


Figure 4.4: Plot of the strain values for every image during the quasi-static tensile test and comparison with the values given by the gauge.

It is possible to see that the various measures are in good agreement, so it can be said that there is no difference between the use of a strain gauge and DIC. Moreover, the different measures on the areas do not show a significant difference between them.

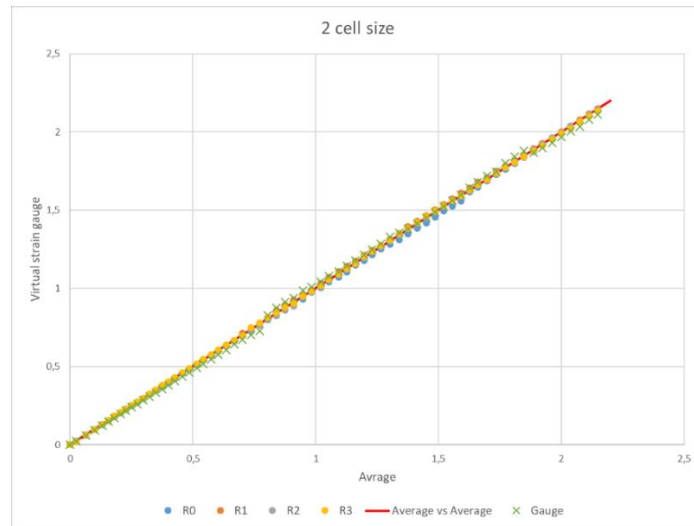
So, after this investigation it is possible to confirm that the results provided by the DIC investigation give an effective measure of the strain on the material as the one given by the strain gauge. It is also verified that all the procedure followed before the test, concerning the specimen preparation, camera set-up and system calibration was correctly done, moreover can be said that the speckle patten used is correct for this kind of test and specimen size.

To verify if the values given by this areal size are sufficiently good, the same operation conducted before was repeated doubling the measures of the rectangles sides, so, considering this time 4 cell at each time but this time instead of 5 measures only 4 average values were considered.



*Figure 4.5: On the left is depicted the position of the 4 areas considered over the speckle pattern, on the right the same image over the strain plot before failure.*

## Virtual strain gauge investigation



*Figure 4.6: Plot of the strain values for every image during the quasi-static tensile test and comparison with the values given by the gauge.*

In this case can be seen that the results from the DIC and the one using the strain gauge are very close and can be added that the results obtained before and the ones obtained doubling the sides are very close. So, can be assumed that the value of the strain is already sufficiently good using one unit-cell areal size. It also important to notice that the average values do not change drastically when a crack is considered inside the area. This can be seen more in detail in the next investigation.

To be sure of the strain values and see the possible differences that may appear, an area size obtained tripling each side was considered, as shown below:

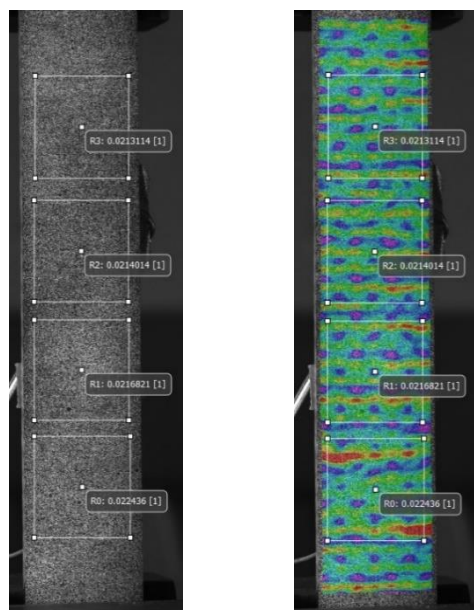


Figure 4.7: On the left is depicted the position of the 4 areas considered over the speckle pattern, on the right the same image over the strain plot before failure.

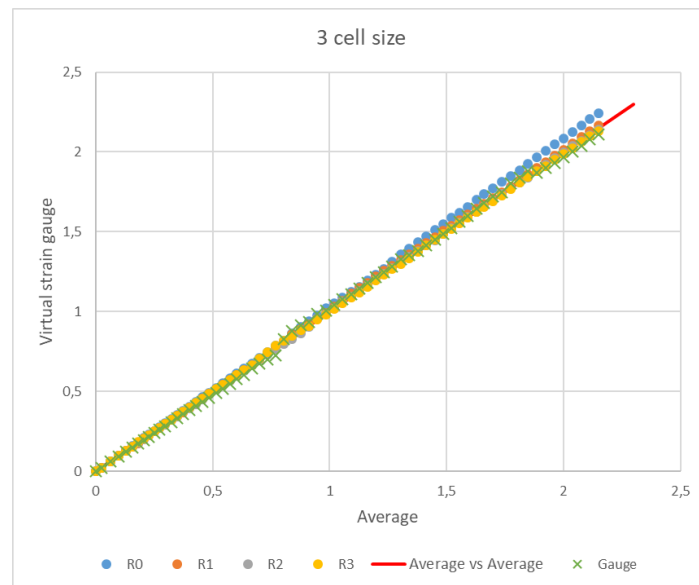


Figure 4.8: Plot of the strain values for every image during the quasi-static tensile test and comparison with the values given by the gauge.

In this case can be seen that the measures are still not so different from the one made with the strain gauge, but it is visible how in one area is concentrated the formation of the failure cracks and these changes the value of the average strain making it higher than in the other areas.

To identify the limit of the smallest area that gives reliable results in terms of strain distribution, the same investigation done for the other cases before was done this time taking into account smaller rectangular areas. So, areas with the sides half of the unit-cell and a quarter of the unit-cell side were analysed and the results are discussed in the next part. Placing five areas randomly on the surface and analysing the average strain inside the areas can be seen, as shown in Picture 4.9, that in the first linear part, before that the damage starts to happen, the results are very close between the different areas and close to the right one, even if the strain concentrations on the resin channels starts to make the results diverge. When the damage begins to happen, around 0.6 – 0.7% strain, the average strains inside the areas begins to be very different and this depend for the presence of strain intensification under them caused by the presence of damage and their position over the structure. So, the different response depends on the area position with

respect to the strain patten induced by the composite architecture and on the presence of damage.

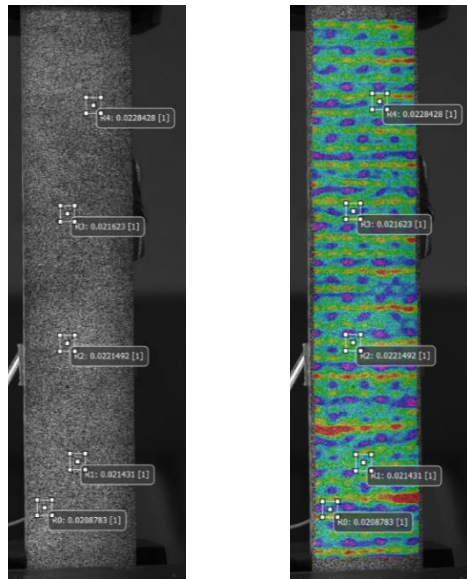


Figure 4.9: Rectangles position over the specimen, half of the unit cell side size were used.

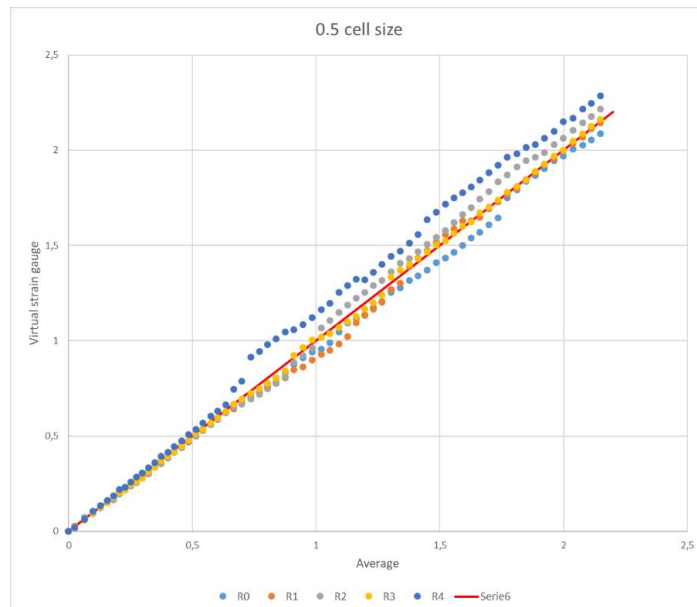


Figure 4.10: Strains for the five half-sided areas comaperd with the average one.

Accounting this time for an area with each side respectively a quarter of the unit-cell ones, the results obtained this time starts to be different since the initial part of the curve, before the damage begins to start, so even in the initial region some differences between the curves can be noticed. This is due to the smaller area, which captures almost only a



punctual part of the composite, so the results are highly affected by the position with respect to the pattern because the average made on the area this time is almost a punctual information and depending if the rectangle is on a resin pocket, on a weft tow or on a z-crown the result will be different since the early stage. This tendency is amplified in the damage area as it is to be expected.

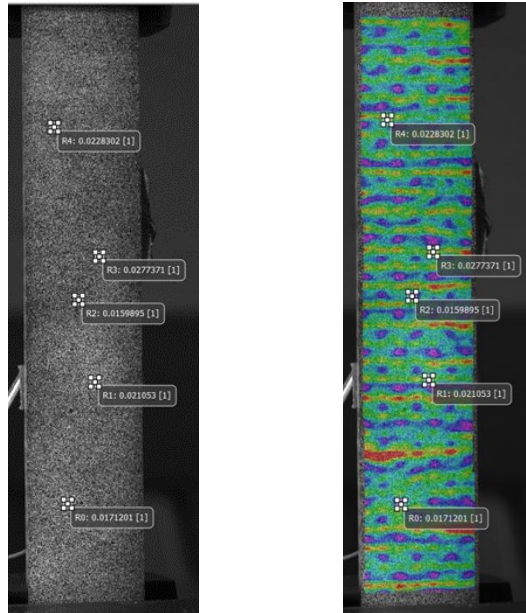


Figure 4.11: Rectangles position over the specimen, a quarter of the unit cell side size were used.

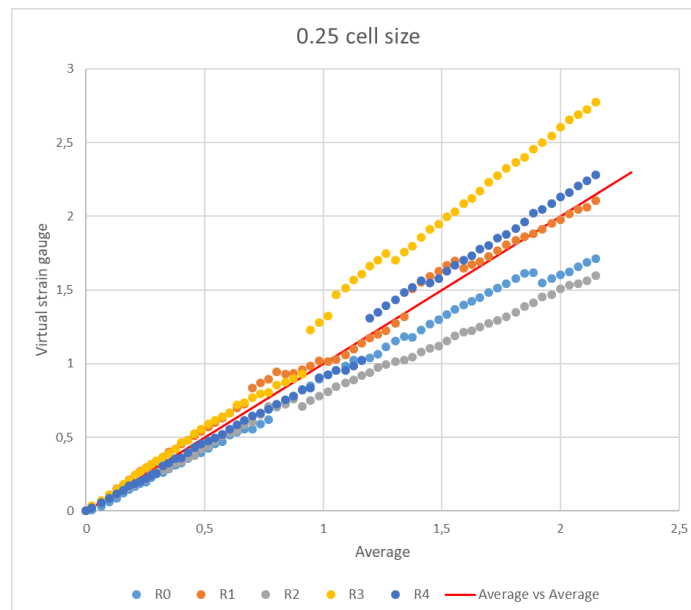


Figure 4.12: Strains for the five quarter-sided areas compared with the average one.

Concluding, the values of the average strain over the area during some pictures taken as reference is plotted in the following tables:

*Table 4.1: Average strain values taken at different stages during the test for one cell-sides virtual strain gauge.*

1 cell side							
Pic	R0	R1	R2	R3	R4	Ave	StDev
20	0,548	0,541	0,533	0,553	0,536	0,542	0,007
40	1,239	1,189	1,207	1,224	1,235	1,219	0,019
60	1,986	1,960	1,933	1,961	1,929	1,954	0,021

*Table 4.2: Average strain values taken at different stages during the test for two cell-sides virtual strain gauge.*

2 cell side						
Pic	R0	R1	R2	R3	Ave	StDev
20	0,543	0,539	0,547	0,541	0,542	0,003
40	1,244	1,234	1,236	1,214	1,232	0,011
60	1,962	1,964	1,955	1,956	1,959	0,004

*Table 4.3: Average strain values taken at different stages during the test for three cell-sides virtual strain gauge.*

3 cell side						
Pic	R0	R1	R2	R3	Ave	StDev
20	0,553	0,541	0,538	0,544	0,544	0,005
40	1,269	1,256	1,236	1,230	1,248	0,016
60	2,046	1,975	1,961	1,950	1,983	0,038

It is visible that the values are more or less compatible and the differences are to be searched in the presence of more or less cracks inside the area taken as reference. In any case, it was proven that the strain values are already good taking just one unit-cell as reference area. Moreover, taking larger areas, it is possible to have more possibility to fully include a formed crack, which will change the value of the strain. So, can be said that the size of the area taken to calculate the strains is not so important to obtain true values. Comparing the results of the previous tables with the ones for smaller areas, can be seen that although the average results are still quite in agreement with the previous ones, the variability of this results are much higher than before, as can be seen from the dispersion of the points in the following tables. This again is because the averaging area is so small that the results are highly influenced by its position on the composite surface.

Thus, considering a restricted area the average is no more representative of the overall strain and behaviour and the results are so affected by a large scatter.

*Table 4.4: Average strain values taken at different stages during the test for a virtual strain gauge with half a unit-cell side.*

0.5 cell side							
Pic	R0	R1	R2	R3	R4	Ave	StDev
20	0,528	0,534	0,529	0,536	0,569	0,539	0,015
40	1,175	1,165	1,291	1,200	1,358	1,238	0,075
60	1,945	1,959	2,029	1,970	2,099	2,000	0,057

*Table 4.5: Average strain values taken at different stages during the test for a virtual strain gauge with a quarter unit-cell side.*

0.25 cell side							
Pic	R0	R1	R2	R3	R4	Ave	StDev
20	0,453	0,602	0,476	0,617	0,497	0,529	0,067
40	1,064	1,198	0,974	1,700	1,346	1,257	0,255
60	1,580	1,952	1,469	2,546	2,086	1,927	0,384

### 4.3 Concluding remarks

In this chapter was verified that the DIC offers reliable results, comparable with the ones offered by the strain gauges, for the average strains over an area, offering also the possibility to have full-field information and being a faster testing method compared to the strain gauges. Considering one unit-cell size as averaging area, it is visible that the results are quite good compared to the overall average strain and the same it is using multiples of the cell size, as expected, even if it is still present the problem related with the presence of the final failure damage inside the area considered, which gives different results for the final part of the strain graph. Using smaller areas, the data scatter grows while the measures average remains similar to the overall strain for statistical reasons. So, it can be said that one cell size is the smallest area where it is possible to have reliable results for the average strains randomly placing it on the specimen, while using smaller areas the strain values are influenced by the position of the area with the respect to the composite architecture and to the damage that is developed underneath. Moreover, the damage starting from 0.7% strain seems to be the most important factor that affects the results

Virtual strain gauge investigation

since in the first part of the stress-strain curve the data overlap the line of the overall specimen strain.

# Chapter 5

## Relation between DIC pattern and internal geometry of the composite

### 5.1 Introduction

The relation between the DIC superficial pattern, visible throughout the test, and the internal architecture of the composite is here studied. Particularly, it is possible to appreciate the formation of a transverse lines pattern, where high strain lines are spaced by low strain lines, this phenomenon it is more visible at the beginning of the test. In a later stage of the test, the formation of low strain circular spots on the surface is more visible. The correlation of the DIC information with the composite architecture is made by using different techniques and it is important to properly understand the DIC results. Later, a simple model is proposed to verify the DIC results about the transverse lines formation, the model used is based on the Strain Magnification Factor model developed to explain the strain magnification at micro-level between fibers and matrix surrounding them. This model in this case is adapted to a 2D problem, a correction factor is then applied to correct the model and make it agree with the experimental results.

### 5.2 Relation between DIC results and z-binders

The correspondence between the strain pattern that can be visualized in DIC images and the position of the z-binders inside the composite will be investigated.

To correlate the pattern revealed by the DIC with the internal geometry several microscopies have been taken and stitched together to recreate the whole width of the specimen. The samples have been taken near the fracture surface, approximately where it ended the part damaged by the failure. The images have been taken using an optical microscope with a 2.5x objective. Starting from the failure point, which is visible in the DIC image, and counting the number of weft tows inside the composite was possible to find the position where it was cut the specimen in the DIC images. Knowing the number of weft tows to be counted was possible because they are visible in the failed specimen, so they

have been directly counted. It is so visible that the pattern formed by the purple dots can be related to the one formed by the z-binders passing over the weft tows in the region called z-crowns. As a matter of facts, where the purple spots are located, there is also a line of low strains that link them and between these lines, other of higher strains. These differences can be associated with the alternation of weft tows and superficial resin channels between them, so the higher strain transversal lines are related to the resin channels and the lower strains with the weft tows, since higher strains are related to a lower modulus and vice versa. The proof of this will be discussed later on, in the next chapter. Looking at the next images, can be seen that the pattern of transversal lines made of regions of high strains and low strains is recognisable since the initial stages of the test because the difference in modulus between the glass yarns and the matrix is so high that the composite at a local level starts behaving in a different way very early. On the contrary, the formation of the circular spots where the z-crowns are located happens in a second time, at higher strain levels. This can be explained with the fact that the z-binders, when the composite is tensioned, correspond to an area with higher modulus with respect to the surroundings. This because the fibers inside the z-yarns are aligned in the warp direction, while the yarns near them are aligned in the transverse direction. So, also considering that the z-binders are inclined because of their nature, they have a higher modulus because they are tensioned in the fibers direction. Can be also said that, they exert a compression action on the weft tows underneath, so at higher strains they locally pinch and restrain the composite.

To prove that the purple spots are effectively caused by the z-binders, their distance was measured using the stitched image of the composite width, comparing it with the results given by the DIC. Calculating the distance between the spots in the X direction and dividing it by the whole specimen width measured in pixels inside the DIC image, we obtain the following results, which can be also seen in Figure 5.1, together with the DIC result. The same procedure was conducted on the microscopies in order to compare the ratio between the z-binders distance and the whole width in the DIC images and the microscopies, the calculation is here reported:

*Table 5.1: Z-binders distance calculated in the DIC image and in the optical microscopy considering the specimen in Figure .*

	<i>DIC</i>	<i>Microscopy</i>
<i>Specimen width [pixels]</i>	<i>502</i>	<i>9690</i>
<i>z-binders distance [pixels]</i>	<i>139</i>	<i>2868</i>

<i>Ratio</i>	$139/502 \cong 0.28$	$2868/9690 \cong 0.29$
--------------	----------------------	------------------------

So, it is visible that the two ratios between the two pictures of z-binders taken in the same plane are quite similar, can be assumed that the two information, coming from the DIC during the test and the microscopy of the width taken in a section near the final failure, gives the same kind of result. Moreover, can be seen from the two different pictures in Figure 5.1 and Figure 5.2, that is also present a pattern of four spots followed by three spots and so on, which is also visible in the two images for the z-binders succession. Seven z-binders are contained in the composite section, four that goes on one side and three on the other, as it is visible comparing the two images. So, there it is another proof that the purple spots come from the alternation of the z-crowns on the composite surface.

The confirmation that the transverse lines that alternatively forms on the DIC results is not completely done and their related pattern is still just assumed, so a possible interpretation is just suggested here. So, after having performed this preliminary investigation and having seen the pattern formed, a further investigation will be needed to prove that these lines are related to the alternans of weft tows and resin channels, which will be performed in the next chapter.

Relation between DIC pattern and internal architecture

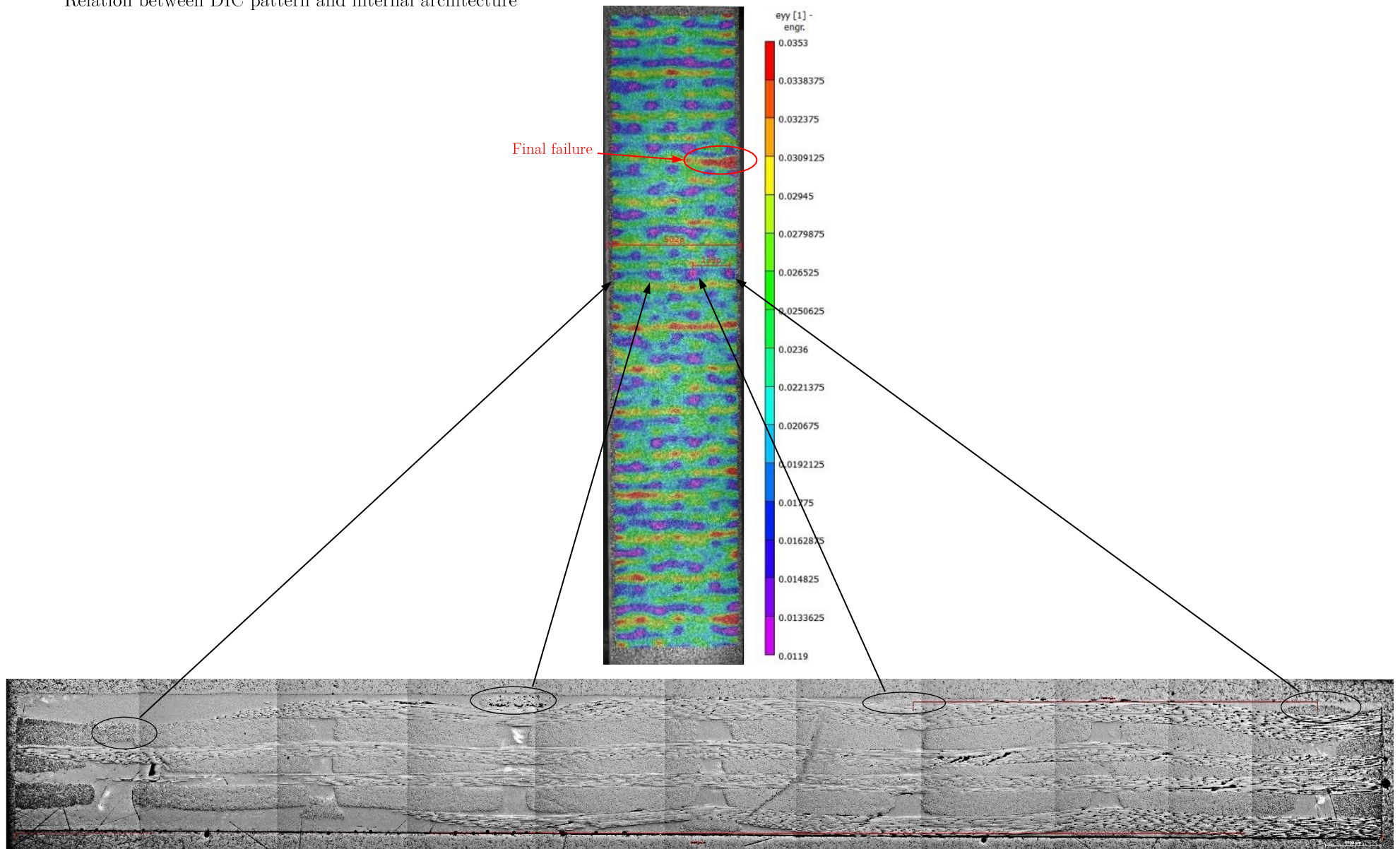


Figure 5.1: Correlation between DIC results and optical microscopy concerning the z-binders (Plain no gauge - Specimen 1).



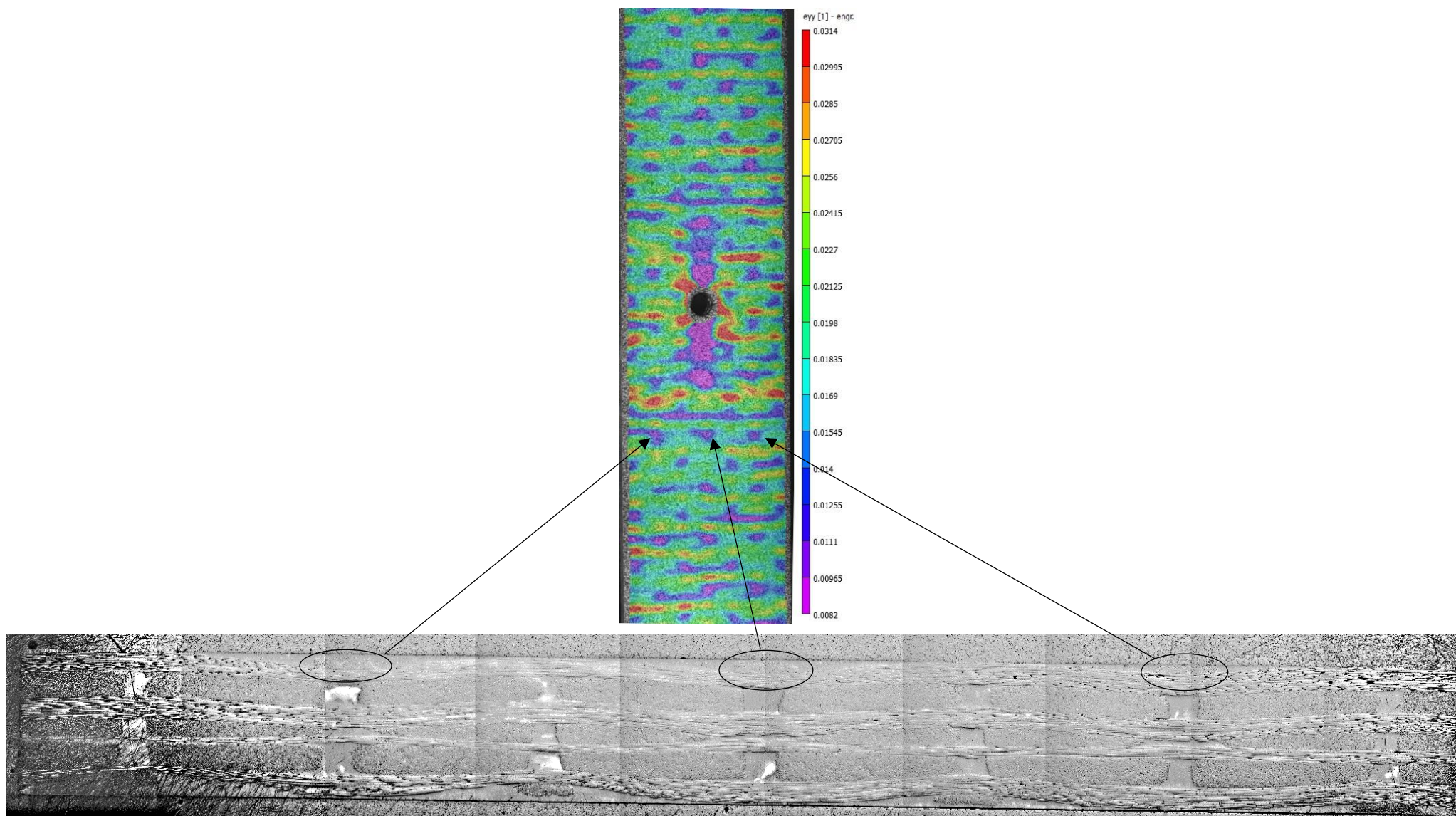
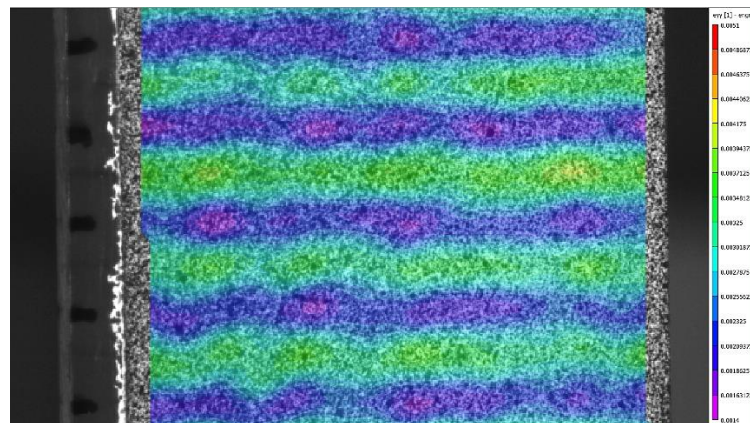


Figure 5.2: Correlation between DIC results and optical microscopy concerning the z-binders (2.5mm - spec 3).

### 5.3 Relation between DIC, weft tows and transverse lines formation

To directly prove that the transverse lines with low strains are formed in correspondence of the weft tows, while the higher strains are present in the resin superficial channels, a direct investigation was performed. To do so, in the second round of tests, an edge of the specimen was not painted with the speckle pattern but the internal geometry was kept visible. A mark was put in correspondence of the middle line of the weft tows, this to permit during the test to compare the position of the DIC pattern with the composite architecture. The tested revealed, as was expected that the higher strains are placed in correspondence of the resin channels while the lower in the weft tows. This is again caused by a properties mismatch between the two superficial constituents, since the weft tows in the transverse direction still have a higher modulus than the matrix. This causes a different strain distribution, which is linearly related to the difference in modulus of the constituents and their width.



*Figure 5.3: Transversal strain pattern shown in the early stages of the quasi-static test where is visible the relation between weft tows and low strains.*

### 5.4 Strain Magnification Factor (SMF)

In the following paragraph will be answered the question about the reason for the formation of the transverse lines and a simplified model is proposed to verify the assumptions made.

### 5.4.1 Experimental results

As can be seen in the next picture, to experimentally analyse the strain distribution between resin channels and weft tows, a line of point equally distanced was created and for each point a strain value was extracted. The result of this operation can be seen in the graph below where the distribution is plotted with the average value of the strains on the overall specimen. The two graphs in Figure 5.5 are taken at the same points but at two different average strain levels. This causes also a movement of the points with respect to the structure because the points position is fixed while the composite underneath is tensioned during the test. From the graph, the maximum strain points can be extracted, as shown in Table 5.2. These points will be used to calculate the experimental value of the Strain Magnification Factor, which will be later compared with the one calculated from the idealized model.

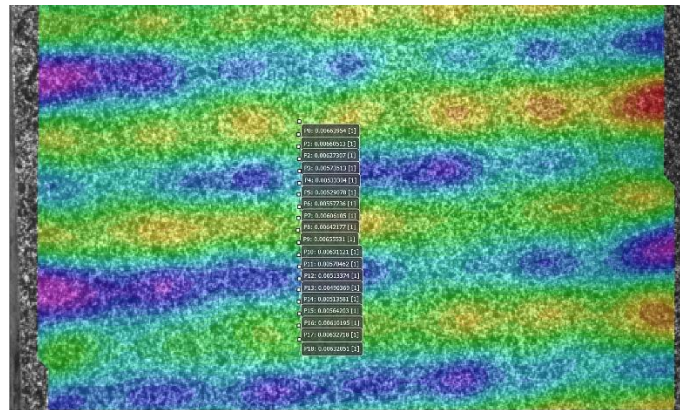
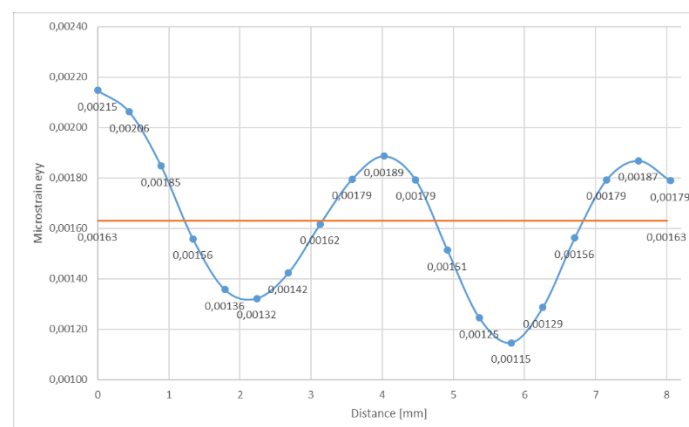


Figure 5.4: Positions of the the points where the punctual strains are extracted (Plain specimen 1).



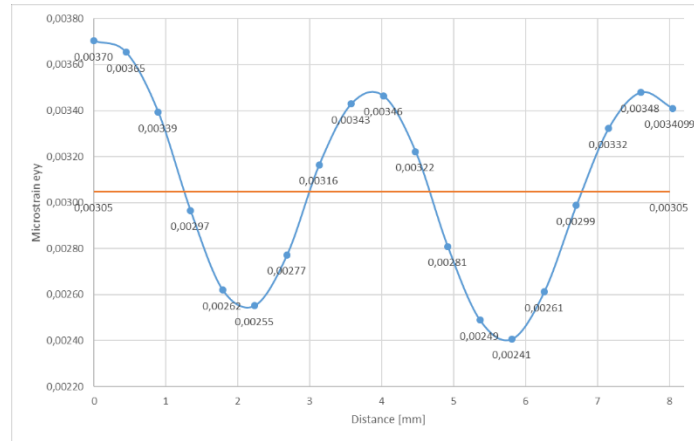


Figure 5.5: Strain distribution at two different average strain levels (Plain specimen 1).

In the next table are reported the values for the points at the two average strain levels, with their average value and standard deviation.

Table 5.2: Strain Magnification factor calculation for the first specimen.

Strain level [ $\mu$ strain]	Average strain $\epsilon_{yy} = 0.00305$			Average strain $\epsilon_{yy} = 0.00163$		
Point	Point 1	Point 2	Point 3	Point 1	Point 2	Point 3
Microstrain	0,003704	0,003480	0,003485	0,002147	0,001886	0,001868
SMF	1,2152	1,1416	1,1432	1,3178	1,1577	1,1467
Average	1,1870					
StDev	0,0637					

The same procedure, that was done for the previous specimen, is now reproduced on another specimen to extract more experimental points and have a better statistical characterization for the experimental value of the SMF. So, from a line of points the strain values are extracted and the graphs of their distribution at two average levels are shown in the following.

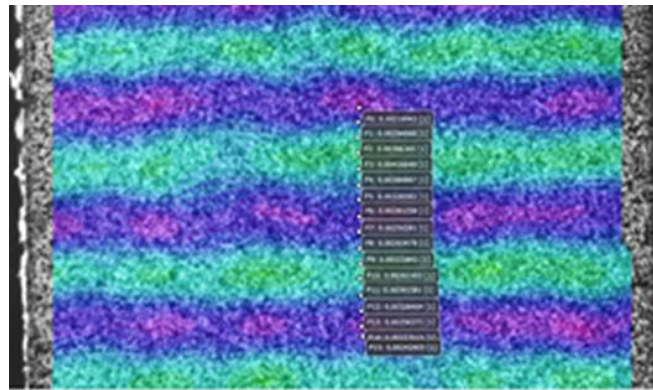


Figure 5.6: Positions of the the points where the punctual strains are extracted (Specimen 2.5 mm hole).



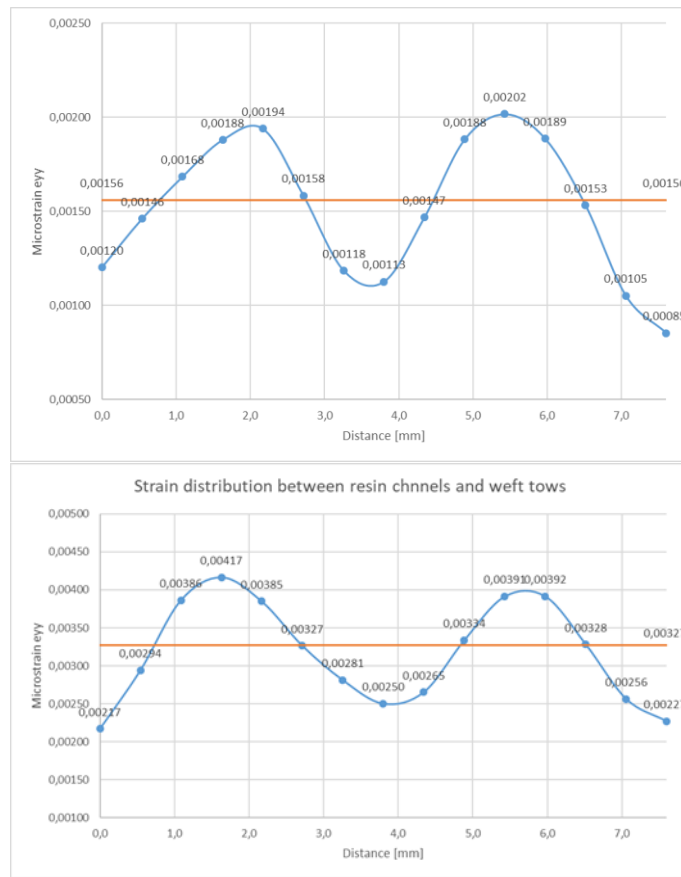


Figure 5.7: Strain distribution at two different average strain levels (Specimen 2.5 mm hole).

Here the values of the maximum point strain are reported and also the Strain Magnification Factor values, calculated as the ratio between the peak value and the average strain on the specimen, can be seen.

Table 5.3: Strain Magnification factor calculation for the first specimen.

Strain level [ $\mu$ strain]	Average strain $\epsilon_{yy} = 0.00305$		Average strain $\epsilon_{yy} = 0.00156$	
	Point 1	Point 2	Point 1	Point 2
Microstrain	0,00417	0,00417	0,00202	0,00196
SMF	1,2752	1,2232	1,2933	1,2573
Average	1,2623			
StDev	0,0259			

All the values of the SMF calculated for the two specimens are then averaged to obtain the experimental value for the Strain Magnification Factor, which is here reported:

$$SMF_{experimental} = \frac{\epsilon_{peak}}{\epsilon_{yy}} = 1,22 \pm 0,06 \quad (5.1)$$

### 5.4.2 Idealized model

In this chapter, an idealized model for the Strain Magnification Factor will be compared to the experimental results obtained in the previous paragraph. As was said, the difference in the strains between the weft tows and the resin channels is generated by the Young's modulus difference in the loading direction. So, the first thing to do is to characterize the Young's modulus of the material.

To experimentally do so, the first thing is to find out the fiber volume fraction value inside a single yarn, this because to obtain the value of the transverse modulus for the weft tows, it is necessary to know their fiber volume fraction value. This calculation was done experimentally, as a first step the fiber diameter value was obtained taking some random measures on different microscopic images, an example of this can be seen in Figure 5.8. The result is here reported:

$$\phi_{fiber} = 18.84 \pm 2.05 \quad (5.2)$$

To evaluate the fiber volume fraction, the measures of three different squared area have been taken, then the number of fibers inside have been counted and this was multiplied for the fiber diameter previously obtained. In the next figure can be seen an example of the microscopy taken to count the number of fibers inside the reference area. The pictures were taken using a 10x objective on the Zeiss Axiophot optical microscope.

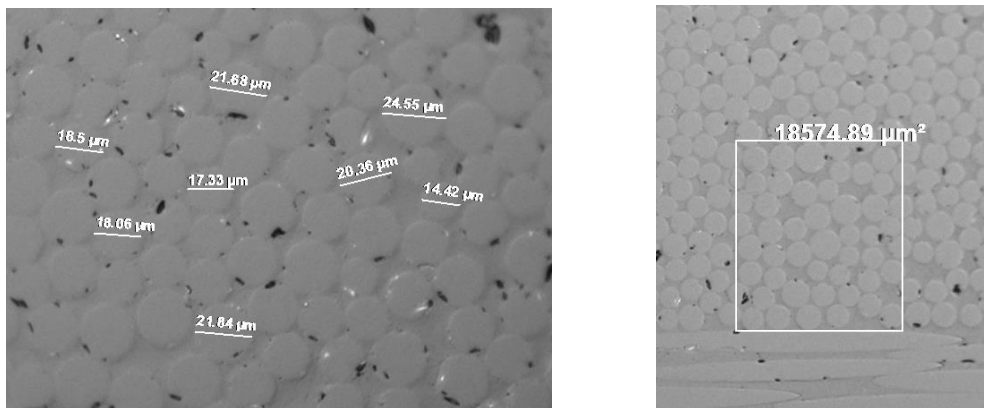


Figure 5.8: Example of fiber diameters and rectangular area to calculate the fiber volume fraction.

The resulting values from this calculation are reported in the next table with the fiber volume fraction obtained in each case.

Table 5.4: Strain Magnification factor calculation for the second specimen.

Sample	1	2	3
Total area [ $\mu\text{m}^2$ ]	18574.89	19307.92	17342.29
Fiber number	47.5	53.75	40.75
Fibers area [ $\mu\text{m}^2$ ]	14922.56	16886.06	10369.61
Vf [%]	0.713	0.776	0.655

The final average value with its standard deviation is then:

$$V_f \approx 0.72\% \pm 0.05 \quad (5.3)$$

This value is quite high considering that usually the fiber volume fraction is around 65-70%, with a theoretical maximum value of 90.7% for a hexagonal distribution as the one visible in the pictures, the value here reported can be justified with the fact that the fibers in the weft tows under a z-binder are more packed than in other sites for the compressive action of the binders, that tends to squeeze them because of the wavy shape that they assume.

It is now possible to calculate the transverse modulus for a yarn using the classical rule of mixture in the transverse direction, which is here reported:

$$\frac{1}{E_T} = \frac{V_f}{E_f} + \frac{1 - V_f}{E_m} \quad (5.4)$$

Where the value for the fibers modulus is  $E_f = 76 \text{ GPa}$  and for the matrix  $E_m = 4 \text{ GPa}$ .

Applying the previous formula with the fiber volume fraction experimentally calculated and the Young's moduli for fibers and matrix, the result is this:

$$E_T = 11.875 \text{ GPa} \approx 12 \text{ GPa} \quad (5.5)$$

The result obtained is considered to be sufficiently good in comparison to what was expected, for a better characterization the Halpin-Tsai rule can be applied, remembering that this equation was formulated for unidirectional lamina.

The Strain Magnification Factor fundamental equation is here reported, which is valid for well-bonded fibers:

$$\begin{cases} \bar{\epsilon}_y = \left(\frac{s}{s+2l}\right) \epsilon_m + \left(\frac{2l}{s+2l}\right) \epsilon_f \\ \sigma_f = \sigma_m \rightarrow \frac{\epsilon_f}{\epsilon_m} = \frac{\sigma_f}{\sigma_m} \cdot \frac{E_m}{E_f} = \frac{E_m}{E_f} \end{cases} \quad (5.6)$$

From this formula can be seen that the strain is not divided in the same way between fibers and matrix, this because of the difference in modulus between the two materials. So, the strains are redistributed due to the Young's moduli ratio and the length of the material considered. The theory was proposed to explain the strain magnification inside a composite at a microlevel between fibers and matrix, as can be seen in the next figure.

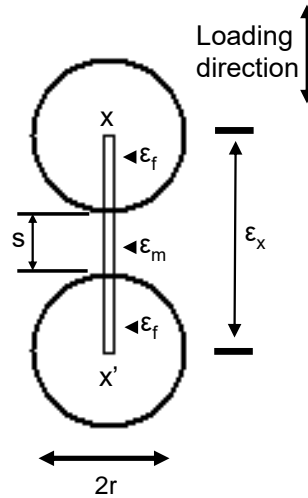
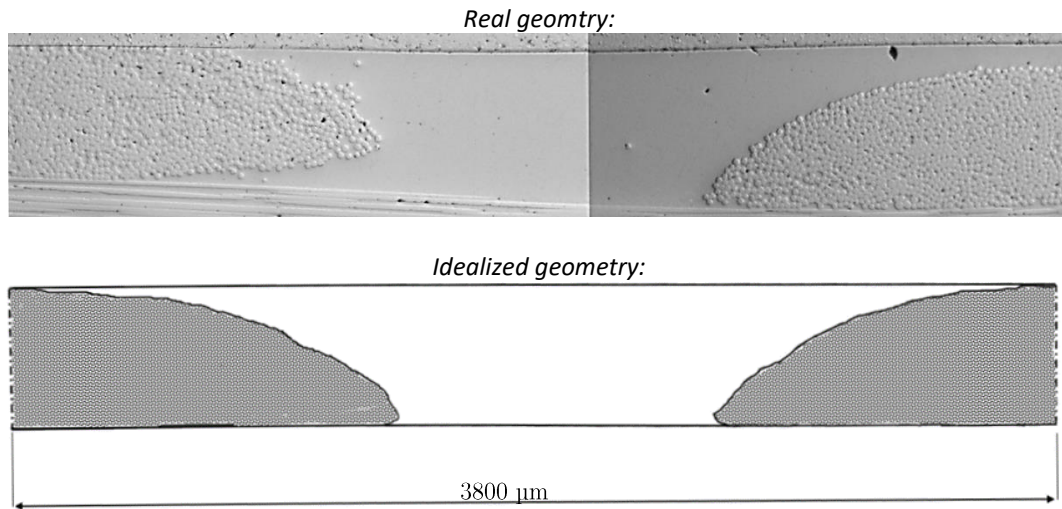


Figure 5.9: Usual method of estimation of Strain Magnification Factor in the classical theory.

In this work, the same formulation is readapted considering the composite at a higher level, that is the one considering the whole yarns. The SMF theory starts considering the length of the middle line that passes through the centres of the fibers, so it is a one-dimensional problem. The problem that we are dealing with it is two dimensional since must be considered the weft tows shape, which is irregular as can be seen in Figure 5.10. The tows are not always touching the surface but a resin gap can sometimes exist, this is caused by the presence of the z-binders that deform the fabric geometry. The geometry is not always perfectly rounded and sometimes dispersed fibers near the tow are present. A more defined shape is present when a z-binder is passing nearby, compacting the structure, while generating the resin gap, this can be noticed comparing the two tow shapes in the following figure. The one on the right is bounded by the presence of a z-binder passing near the cutting plane, while the other on the left is kept free do deform and so presents a less regular shape. For the entire procedure, the tows have been considered with a



symmetric shape and touching the surface, so the fact that some tows presents a resin gap is here ignored. Also, the distance between the middle points of the tows is always considered as the theoretical one, while in most of the cases the tows are shifted.



*Figure 5.10: Comparison between the internal geometry of the woven composite and the idealized one.*

As first thing, the semi-area of four different tows is calculated considering the envelope of the fibers. This procedure was adopted because the tow shape cannot be easily approximated with a mathematical equation, for example a parabola. The area calculation was possible using the program AxioVision 4.9.1, with which is possible to post-process the photos taken with the optical microscope. An example of this can be seen in the next picture, Figure 5.11, and the measures of the different areas are reported in Table 5.5. At this point, to come back to a one-dimensional problem, the geometry was idealized finding the rectangular area equal to the one of the original tow. To do so, the same height was considered starting from the surface until the first warp fibre. Doing this was possible to get the measure of the length of the major side, which is the measure that will be used to calculate the Strain Magnification Factor, this measure was named  $l$ .

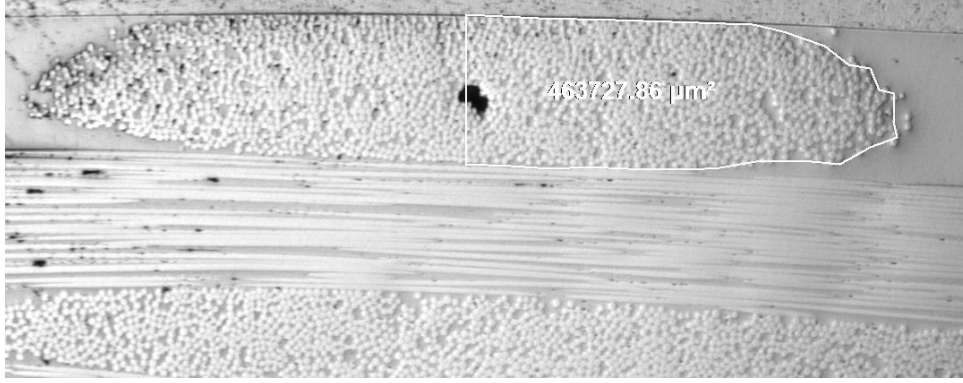


Figure 5.11: Semi-area calculation in a weft tow (Area 4).

The formula used to calculate the Strain Magnification Factor, directly obtained from the fundamental equation is here reported:

$$SMF = \frac{\epsilon_m}{\epsilon_{yy}} = \frac{1}{1 + \frac{2l \cdot \left(\frac{E_m}{E_f} - 1\right)}{s + 2l}} \quad (5.7)$$

From the next picture can be seen that the length between the two rectangular areas is called  $s$  and is idealized as having only resin, while the two semi-areas obtained are called  $l$  and are simplified as having the transverse modulus of the tows that was calculated at the beginning. The total length  $s + 2l$  is the theoretical one, which is  $3800 \mu m$ .

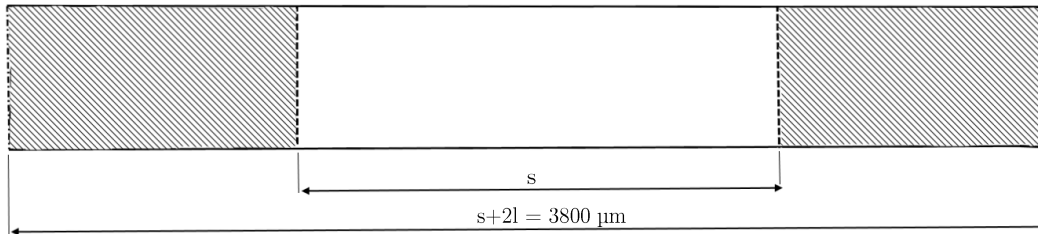


Figure 5.12: Simplified geometry used with equivalent tow area.

At this point, for every length  $l$  was calculated the strain magnification factor and it was compared with the statistical one obtained from the DIC investigation. Thus, a correction factor was added to every measure to adjust the result from the idealized model to the experimental one, so it was possible to have a correct model starting from the approximated one:

$$\alpha = \frac{SMF_{idealized}}{SMF_{experimental}} \quad (5.8)$$

Table 5.5: Claculation of the correction factor for the idealized model.

	Area [ $\mu\text{m}^2$ ]	$h$ [ $\mu\text{m}$ ]	$l$ [ $\mu\text{m}$ ]	SMF	$\alpha$
Area 1	406845.88	528.0	770.5	1.373	0.89
Area 2	421460.77	484.4	870.0	1.443	0.81
Area 3	483482.20	466.5	1036.4	1.577	0.77
Area 4	463727.87	430.6	1076.9	1.613	0.76

The weft tows theoretical length to obtain the result of the SMF obtained from the experimental investigation is here reported:

$$l_{th} = 503.17 \mu\text{m} \quad (5.9)$$

This value is obtained imposing in the SMF formula the experimental value obtained from the DIC investigation, which is  $1,22 \pm 0,06$ .

The average value for the correction factor  $\alpha$  obtained averaging the four different measures, shown in Table 5.5, with their standard deviation is:

$$\alpha = 0.81 \pm 0.05 \quad (5.10)$$

This correction factor considers the approximation made regarding the tow rounded geometry, the differences between each tow and their imperfections, load transfer between fibers and matrix.

## 5.5 Concluding remarks

At the beginning, must be said that using the DIC it is possible to obtain both quantitative local results in one point and full-field measurements, which allows to understand the strain flow on a large area and around a notch. Thus, using this technique it is possible to obtain precise results on a very small scale, for example near a stress concentrator, but it is also possible to analyse the behaviour of a structure all at once. These range of possibilities are not contemplated by the use a strain gauge, which remains a local investigation that average the strain on a certain surface represented by the grid area.

In this chapter was proven that the presence of weft tows and resin gaps between them creates a superficial strain pattern made of high and low strains alternated transverse lines, due to the difference of properties between the constituents. The same it is visible for the z-binders, which creates a dotted pattern in correspondence of the z-crowns. This again because the z-binders represents, at the surface, a constituent of higher modulus

compared to the weft tows beneath, because the fibers are aligned in the loading direction, while the weft tows are aligned in the transverse one. So, the z-crown regions have lower strains compared to the weft tows and polymer rich regions surrounding them.

An analysis of the Strain Magnification Factor, experimentally calculated point results using the DIC, was performed. To do so, the fiber volume fraction and the Young's modulus of the weft tows was obtained using microscopy investigation. This result was compared to the one analytically calculated using a simplified Strain magnification model. This model was also verified using a FE model (see Appendix 4) using a schematised and simplified weft tow profile, was proven that the FE model gives a SMF value that is in between the analytical and experimental one, even if this model is inherently so simplified that cannot be representative of the real 3D composite but just of the simplified analytical Strain Magnification model. A correction factor was introduced to correct the results from the model to the experimental value obtained. Finally, an average value with its standard deviation was obtained to make the analytical model coherent with the experimental results.

# Chapter 6

## Notch sensitivity investigation

### 6.1 Introduction

Notch sensitivity, together with fatigue properties, are two of the main concerns about composite materials, in this chapter this topic is discussed. In the first part, the samples residual strength obtained from quasi-static tensile tests is plotted over the ratio between hole size and specimen width, which is the classical plot for the notch sensitivity. The tests are done on samples obtained from Vacuum Assisted Resin Transfer Moulding and Wet lay-up laminates, they are compared with other data of 3D and 2D woven composites, all the tests are done from specimens cut along warp direction. For the laminates obtained with the wet lay-up technique, which are the ones own made, a fiber volume fraction calculation is performed together with a characterization of the static mechanical properties, these results are compared with other found in literature. Was found that this particular type of composite presents an enhanced notch insensitivity, with better properties than 2D woven ones. Fiber volume fraction and mechanical properties are found to be in good agreement with the results of other works. To understand the notch insensitivity behaviour, the strain pattern on the specimen's surface, and in particular around the hole is investigated, to understand the type of damage characteristic of this material and propose a damage model. For this reason, strain maps around the hole are plotted for different hole sizes and at various positions with respect to the internal architecture; these are also compared to the strain around a 5mm hole for an aluminium and a 2D woven specimen.

### 6.2 Notch sensitivity for VARTM specimens

To understand the material behaviour, the potentialities of the use of the DIC and the problematics related to this, a series of preliminary tests have been made. The material used for these tests is still a 3D-96 glass cloth from 3TEX impregnated using epoxy resin but in this specific case it was manufactured using the VARTM technology, which gives

a composite with less voids, defects and a slightly higher fibre volume fraction. All the specimens presented in this chapter have been analysed along the warp direction. At the beginning of the chapter, the data for the notched strength will be presented in a graph pointing out the notch insensitivity of the material. Then, the results from the DIC investigation will be presented and discussed and, at the end, some conclusions and peculiarities which will be explained in the rest of this work are introduced.

Using a spare laminate made using the Vacuum Assisted Resin Transfer Moulding (VARTM), eight specimens have been tested as reported in the following table. Two of them were unnotched and the other six were notched with a hole of three assorted sizes in the centre, two with a  $\varnothing 2.5 \text{ mm}$  hole, two with  $\varnothing 5 \text{ mm}$  and two with  $\varnothing 10 \text{ mm}$ . The load data recorded by the machine were plotted dividing the maximum load, reached at the failure, by the gross area of the specimen. The measured parameters for the width and the thickness of every sample are reported in the table below, with their uncertainties and the final value for the area with its uncertainty.

*Table 6.1: Results of the preliminary investigation on eight samples under quasi-static tensile test.*

<b>VARTM</b>	<i>a/w</i>	<i>UTS [MPa]</i>	<i>W [mm]</i>	<i>t [mm]</i>	<i>A [mm<sup>2</sup>]</i>	<i>l w (±) (95%)</i>	<i>l t (±) (95%)</i>	<i>l A (±) (95%)</i>
<i>Plain - no gauge</i>	/	410.46	24.89	2.54	63.30	0.06	0.05	1.31
<i>Plain - gauge</i>	/	414.04	24.96	2.48	61.91	0.15	0.02	0.88
<i>2.5mm - spec 2</i>	0.1	340.10	25.01	2.49	62.35	0.08	0.02	0.78
<i>2.5mm - spec 3</i>	0.1	377.56	24.89	2.49	62.07	0.20	0.02	1.09
<i>5mm - no gauge</i>	0.2	330.968	24.91	2.52	62.68	0.16	0.03	1.18
<i>5mm - gauge</i>	0.2	292.48	25.07	2.52	63.25	0.18	0.05	1.74
<i>10mm - spec 5</i>	0.4	203.52	24.92	2.51	62.56	0.08	0.02	0.71
<i>10mm - spec 6</i>	0.4	221.96	25.00	2.54	63.57	0.04	0.12	3.16

As it can be seen from Figure 6.1, data are distributed along the line of notch insensitivity, coloured in orange. Along this line, the strength reduction considers only the area reduction due to the presence of the hole and it can be described with the following equation, which was previously introduced in §1.4.

$$\frac{\sigma_{notch}^g}{\sigma_{plain}} = 1 - \frac{a}{w} \quad (6.1)$$

Where  $a$  defines the hole diameter and  $w$  the overall specimen width.

Composites are generally more sensitive to notches for big holes and less sensitive for small holes, this tendency is also here proved for 3D non-crimp woven composites since it seems that data are closer to the notch insensitivity line for 0.1 and 0.2 ratio and less for 0.4. In any case, the number of data analysed in this first part are not sufficient to make a meaningful statistical analysis, so it must be taken as an introductory work which can highlight some tendencies of the material behaviour. Anyway, these tests are already enough to highlight that the material expresses a noticeable notch insensitivity behaviour.

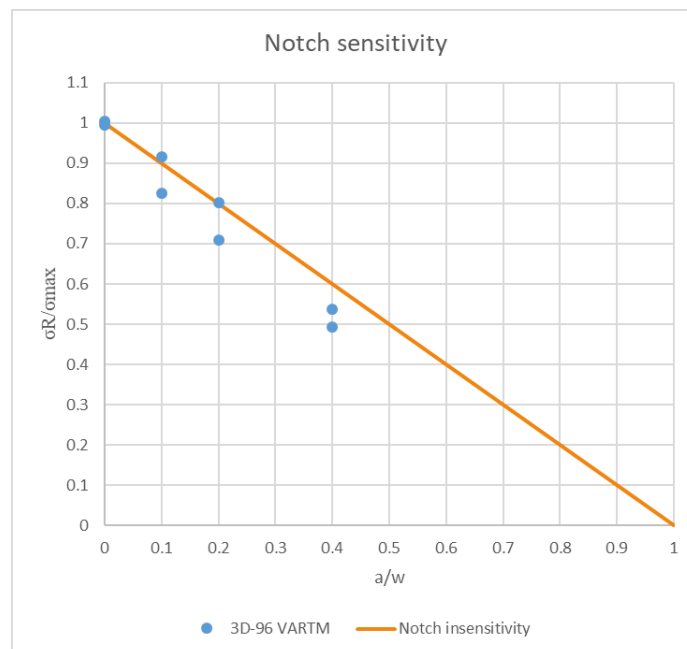


Figure 6.1: Plot of normalised residual strength against normalised hole; the solid line shows the predicted response assuming notch insensitivity (VARTM).

## 6.3 Notch sensitivity for Wet lay-up specimens

### 6.3.1 Fiber volume fraction calculation

To verify the quality of the own made laminates with the ones present in literature was performed the burn-off technique, which as result gives the fibre volume fraction expressed in percentage. This information indirectly gives a measure of the voids content and the resin percentage inside the composite, so if the resulting fibre volume fraction is high also

the composite properties will be high and so the infusion product goodness. The densities of the single parts that form the composite are listed in the following table, as previously described the matrix is composed by three different constituents with different densities, to account the final density, each part ratio in the mixture was considered. The final matrix density obtained is  $1.182 \text{ g/mL}$ , while for the fibre density was used the E-glass density, which is  $2.57 \text{ g/cm}^3$ .

*Table 6.2: Densities and ratio of the mixture components, with the final density value for the matrix.*

Density			Ratio
Epoxy	1.16	kg/L	100
Hardener	1.232	g/mL	60
Accelerator	0.97	g/mL	4
Matrix	1.182	g/mL	
Fibers	2.57	g/cm <sup>3</sup>	

The results obtained for the first laminate are reported in the following table, where are reported the measures of the weight for the crucible with the lid and the crucible and lid with the specimen inside, before and after the execution of the test. Considering that at the end of the test are present inside the crucible just fibres, it is possible to know also the matrix volume present before the test, subtracting the weight of the fibers from the weight of the specimen before the test, which can be known subtracting the weight of crucible plus specimen and the weight of the crucible alone, also before the test.

*Table 6.3: Burn-off measurements on the first laminate with the resulting average fiber volume fraction and its standard deviation.*

<b>Before bur-off</b>	Specimen 1	Specimen 2	Specimen 3	Specimen 4	Specimen 5		
cup [g]	46.157	48.093	45.652	46.0835	51.281		
cup+specimen [g]	48.222	49.935	47.508	47.938	53.176		
specimen [g]	2.065	1.842	1.856	1.8545	1.895		
<b>After burn-off</b>	Specimen 1	Specimen 2	Specimen 3	Specimen 4	Specimen 5		
Cup+specimen [g]	47.475	49.322	46.820	47.272	52.622		
fibers [g]	1.318	1.229	1.168	1.189	1.341		
matrix [g]	0.747	0.614	0.688	0.666	0.554		
						Aver	StDev
$V_f$	0.45	0.48	0.44	0.45	0.53	0.469	0.032



The results of the test on the second laminate are presented in the next section:

*Table 6.4: Burn-off measurements on the second laminate with the resulting average fiber volume fraction and its standard deviation.*

<b>Before burn-off</b>	<i>Specimen 1</i>	<i>Specimen 2</i>	<i>Specimen 3</i>	<i>Specimen 4</i>	<i>Specimen 5</i>		
<i>cup [g]</i>	46.157	48.093	45.653	46.083	51.281		
<i>cup+specimen [g]</i>	48.241	50.128	47.665	48.118	53.335		
<i>specimen [g]</i>	2.084	2.035	2.012	2.035	2.054		
<b>After burn-off</b>	<i>Specimen 1</i>	<i>Specimen 2</i>	<i>Specimen 3</i>	<i>Specimen 4</i>	<i>Specimen 5</i>		
<i>cup+specimen [g]</i>	47.54	49.42	46.931	47.477	52.63		
<i>fibers [g]</i>	1.383	1.327	1.278	1.394	1.349		
<i>matrix [g]</i>	0.701	0.708	0.734	0.641	0.705		
						<b>Aver</b>	<b>StDev</b>
<b><i>v<sub>f</sub></i></b>	<b>0.48</b>	<b>0.46</b>	<b>0.44</b>	<b>0.50</b>	<b>0.47</b>	<b>0.470</b>	<b>0.018</b>

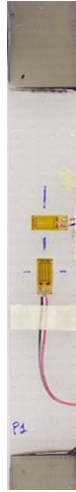
The resulting average volume fraction for the two specimens is:

$$V_{f_{average}} = 0.47 \quad (6.2)$$

This result still represents an excellent value for this type of technique, considering that it is wet lay-up, even if some points of percentage more could be reached refining the process. Comparing this result with the ones in literature can be seen that using the Vacuum Assisted Resin Transver Moulding (VARTM) process it is possible to reach higher fiber volume fractions. In paper [9], it is reported that the fiber volume fraction (%) obtained is 53.22%, while Lomov and Bogdanovich in paper [5] report that using also in this case the VARM technique, the fibre volume fraction obtained for a 3D-96 composite is 48.9%. The latter value is closer to the one obtained in this work that can be so accepted for our pursuits.

### 6.3.2 Quasi-static tensile tests

Three plain specimens have been tested to failure in order to characterize the material in terms of Young's modulus, Poisson's ratio and to obtain a precise value for the un-notched strength until failure.



*Figure 6.2: A plane specimen, tested to characterize the material with the presence of two strain gauges, is here presented.*

Here it is presented a classical stress-strain curve obtained from a tensile test in warp direction for this type of 3D woven composite. In the first part, the composite has a linear response, where it is calculated the Young's modulus of the composite, calculated between 0.1% and 0.3% strain. The first damage starts to appear around 0.3% of strain, where the curve starts to have a slight decrease in slope because there is the formation of non-visible damage, until it reaches the value of 0.7% where there is a huge increase of damage density. In fact, in this stage there is the formation of transversal matrix cracks, as was shown in the previous chapter. After this point the curve assumes a non-regular pattern with a continuous slope loss, which represents a Young's modulus decrease, until the material reaches the final failure around 2.6%-2.7% strain percentage.

The damage occurs firstly in the resin gaps between the weft tows, as will be discussed more in detail later, during the tests there is an increase of the damage density in the spots aforementioned, with also the formation of cracks inside the weft tows starting from the surface and near the z-crowns. These damage causes local micro-delamination around the fibers and tows, but in this type of material there is not the presence of actual delamination as in 2D composites. The stress concentration caused by the cracks lead to the breakage of the fibers aligned in the loading direction (i.e. warp tows) and to final failure.

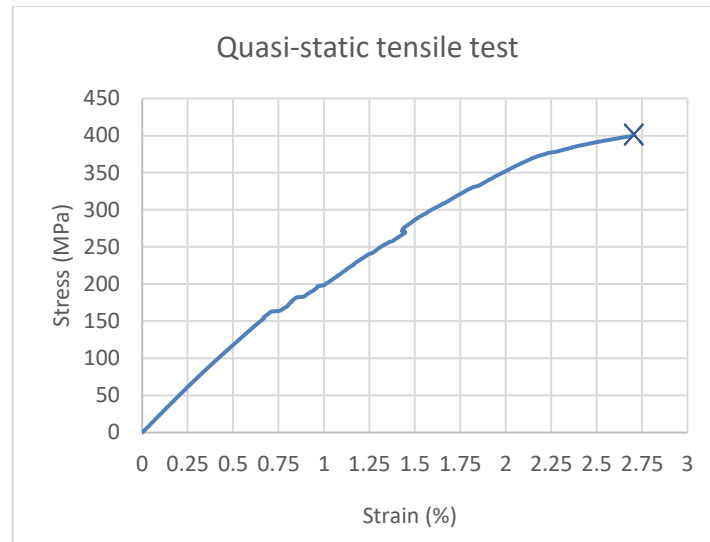


Figure 6.3: Example of a quasi-static tensile test until failure for a specimen loaded in warp direction.

In the table below are reported the results of the tensile tests done in this second part, with their average values and the standard deviation obtained. The strains are captured using two strain gauges, one in the longitudinal and one in the transverse direction, in the range between 0.1% and 0.3% strains. So, for the Young's modulus the value was calculated finding the tangent line to the curve passing through the origin. For the Poisson's ratio, the values were calculated as  $\nu = -\left(\frac{\epsilon_y}{\epsilon_x}\right)$  in the interval mentioned before for  $\epsilon_x$ , considering the results of the two strain gauges and then the results were averaged.

Table 6.5: Mechanical properties for 3D.96 composite.

	$E$ [GPa]	$\nu$	UTS [kN]	$\sigma_R$ [MPa]	$\epsilon_R$ (%)
Plain 1	24.53	-0.135	29.55	461.03	2.692
Plain 2	26.28	-0.126	28.14	436.73	2.373
Plain 3	24.53	-0.125	27.11	416,26	2.735
Average	25.11	-0.128	28.27	438.01	2.60
Standard deviation	0.825	0.005	0.999	18.301	0.161

In the next table, the results of the major composite properties are listed and compared with other works results, the composite analysed by Lomov was made using the VARTM technique, which gives better properties to the composite, while in Novello's work the composite used was made using the same wet lay-up infusion technique, as in this work. Can be se that the results for the Young's modulus are close to each other, while these is a difference for the Poisson's ratio, in any case the value proposed by Lomov has such a high standard deviation that it is not so meaningful. Talking about the Ultimate Tensile Strength, the results obtained in this work are quite close to the one found in Lomov's

paper, while the difference from Novello's work it's hard to explain and can be addressed to the statistic. The same consideration can be done for the Ultimate Tensile Strain, looking at this parameter can be said that the final failure is near the failure point of the E-glass fibers, which is around 2.6%, so can be said that the results are in good agreement with the value of the fibers ultimate strength.

*Table 6.6: Mechanical properties comparison between test result obtained in this work and literature data.*

	$E$ [GPa]	$\nu$	$\sigma_R$ [MPa]	$\epsilon_R$ (%)
<i>This work</i>	$25.11 \pm 0.825$	$-0.128 \pm 0.005$	$438.01 \pm 18.301$	$2.60 \pm 0.161$
<i>Lomov et al.</i>	$24.3 \pm 1.2$	$-0.143 \pm 0.159$	$429 \pm 34$	$2.74 \pm 0.29$
<i>Novello (2014)</i>	$26.2 \pm 1.3$	/	$470 \pm 34$	$2.54 \pm 0.33$

Nine notched specimens with a central hole of three assorted sizes, 2.5mm, 5mm and 7.5mm hole diameter, have been tested till failure to make a statistical analysis of the notch sensitivity. As was said, all these tests were performed on wet lay-up specimens and represents a further investigation to the one previously done with the use of a VARTM laminate. In this case 3 tests for each hole size were made, an accurate statistical investigation cannot be made even in this case but a general characterization of the material behaviour is still possible.

*Table 6.7: Quasi-static tensile test results for wet lay-up specimens.*

<b>Wet lay-up</b>		$a/w$	UTS [MPa]	$t$ [mm]	$w$ [mm]	$A$ [mm <sup>2</sup> ]	$l/w$ ( $\pm$ ) (95%)	$l/t$ ( $\pm$ ) (95%)	$lA$ ( $\pm$ ) (95%)
2.5mm	<i>Specimen 1</i>	0,1	325,33	2,65	24,98	66,291	0.21	0.03	1.34
	<i>Specimen 2</i>	0,1	325,92	2,56	24,95	63,961	0.13	0.03	1.11
	<i>Specimen 3</i>	0,1	331,99	2,61	24,92	64,972	0.12	0.03	1.08
5mm	<i>Specimen 4</i>	0,2	329,98	2,50	24,73	61,913	0.23	0.03	1.33
	<i>Specimen 5</i>	0,2	313,66	2,44	24,61	59,96	0.55	0.02	1.92
	<i>Specimen 6</i>	0,2	274,63	2,53	24,92	62,96	0.10	0.01	0.55
7.5mm	<i>Specimen 7</i>	0,3	276,39	2,39	24,48	58,59	0.23	0.05	1.80
	<i>Specimen 8</i>	0,3	244,08	2,33	24,85	57,82	0.12	0.06	1.82
	<i>Specimen 9</i>	0,3	237,59	2,63	25,03	65,82	0.26	0.04	1.57
Plain	<i>Plain 1</i>	/	461,03	2,52	25,40	64,10	0.06	0.05	1.45
	<i>Plain 2</i>	/	436,73	2,58	24,94	64,43	0.04	0.07	1.87
	<i>Plain 3</i>	/	416,26	2,61	24,96	65,14	0.07	0.04	1.20

In Figure 6.4, the notch sensitivity diagram obtained from these tests is plotted. It is visible a difference for 0.1 ratio, in this case the results are lower than the ones for VARTM specimens, which are closer to the notch insensitivity line. A clear answer for

this difference cannot be done, but the small number of samples analysed, especially for the first series of tests, cannot give a full understanding of the problem.

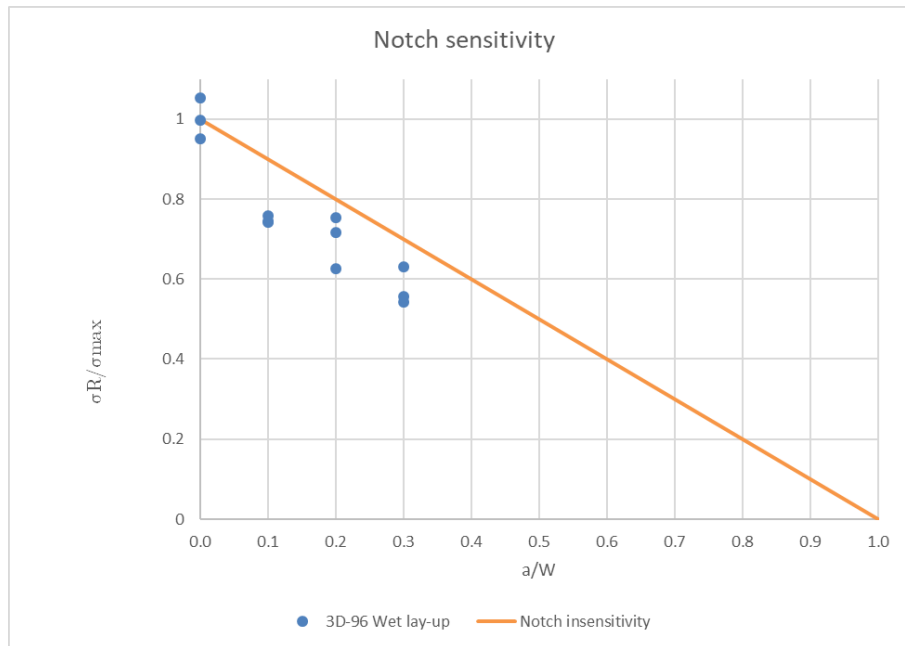


Figure 6.4: Plot of normalised residual strength against normalised hole; the solid line shows the predicted response assuming notch insensitivity (Wet lay-up).

In the next section, the results of the tests on a seven layers 3D woven, done in this work, and on a five layers composite presented by Farik (2015), reported in the table below, will be compared. The manufacturing method used for the 3D-78 was the same as the one in this work and the ratio between the resin components was also the same. The laminate was cut into specimens of 25mm wide and 230mm long, as the ones in the present work. It is possible to see that the results are in good agreement and there is an inconsistency just for the values of 0.1  $a/w$  ratio. These values are more similar to the results obtained with the 3D-96 manufactured with the VARTM technique, it is then possible to assume that there are not differences between the two types of composites and the difference that is visible at 0.1 ratio is due to the statistic. It is also clear that the notch properties of the material are not affected by the composite thickness, as it is for the tensile properties, this can be also seen in paper [10]. The 3D-78 is 25% less thick than the 3D-96, since the first one has two plies less.

Table 6.8: Tests results presented by Farik (2015) on a five layers 3D woven composite.

3D-78 "Farik"	a/w	UTS [MPa]
Plain	/	443

2.5mm	0.1	354
	0.1	374
	0.1	412
5mm	0.2	304
	0.2	285
	0.2	340
10mm	0.4	235
	0.4	213
	0.4	239

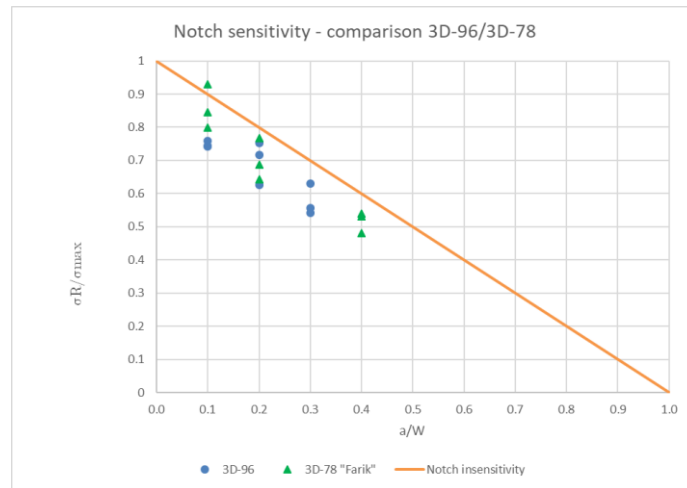


Figure 6.5: Plot of normalised residual strength against normalised hole for the tests on a 3D-96 and a 3D-76 woven composite both manufactured using the wet lay-up technique; the solid line shows the predicted response assuming notch insensitivity

The last comparison that will be made is the between 3D woven composite and the 2D discussed in paper [19]. In this work, quasi-isotropic notched laminates are tested in tension, the material used is made of eight layers symmetric stuck of 2D woven fabric, precisely the eight-harness satin weave presented this lay-up  $[0/90/+45/-45/-45/+45/90/0]$  and was manufactures using an in-house wet lay-up method. It is important to be noticed that the fiber volume fraction measured with a gravimetric matrix burn-off technique resulted to be 0.4, this value is lower than the one observed in this work and in other presented in §6.3.1. Must be said that the total thickness is lower than the one of the 3D composite here analysed. The specimens have the same measures as the ones tested in this work, 230m long and 50mm wide with 50x25 mm end tabs. In the next table, the results of the investigation made by Belmonte (2001) are summarized, for each result a minimum of 5 samples were tested. Can be noted that the laminate with  $0^\circ$  ply on the surface have a higher strength than the ones with  $90^\circ$  plies.

Table 6.9: Experimental results for the strenght of the notched specimens with their standard deviation.

2D 8-harness satin "Belmonte"	a/w	Lay-up	UTS [MPa]
Plain	/	(0/90/±45)s	291
2.5mm notch	0.1	(90/0/±45)s	168.5 ± 0.5
		(0/90/±45)s	183.9 ± 4.3
5mm notch	0.2	(90/0/±45)s	141.0 ± 2.0
		(0/90/±45)s	150.7 ± 4.0
7.5mm notch	0.3	(90/0/±45)s	102.5 ± 0.5
		(0/90/±45)s	111.5 ± 1.7

This lay-up gives intermediate properties between the ones with a higher matrix dominated behaviour and the ones with a fiber dominated, probably more similar to the matrix dominated. In particular, a lay-up with just [45] plies would be closer notch the notch insensitivity line, while one with just [0] would have an enhanced notch sensitivity.

From the final comparison between the data collected in this work and the results from Belmonte (2001), it is visible that 3D woven composites have a behaviour closer to the notch insensitivity with respect to the 2D woven. This result is interesting because this type of 3D composite presents straight yarns without crimping, thus like a [0/90]<sub>s</sub> lay-up of 2D plies, but with the presence of reinforcing yarns in the z-direction. So, it would have a behaviour intermediate between the matrix and fibre dominated, while it is visible that it is comparable to a matrix dominated one, having a lower notch sensitivity than the laminate presented by Belmonte with the presence of layer at 45°.

This different behaviour can be related to the different damage development and the fabric architecture. In 2D woven composites is present the development of splitting and delamination in the late stage of the specimen life, which cannot be seen in 3D composites. On the other hand, in 3D woven the damage development is not localized just to the hole tip but it spreads along the resin channels and on a wide range around the hole. This characteristic will be discussed in the next sections of this chapter. Must be pointed out that the different notch sensitivity can be affected by the different thickness and the fiber volume fraction, which is significantly lower than in the 3D composite analysed in this work (0.4% for 2D analysed in Belmonte's work and 0.47% for the 3D in this work). This discrepancy can affect the damage development around the hole, even if must be said that the normalized values in the notch sensitivity graph should be no more affected by this problem.

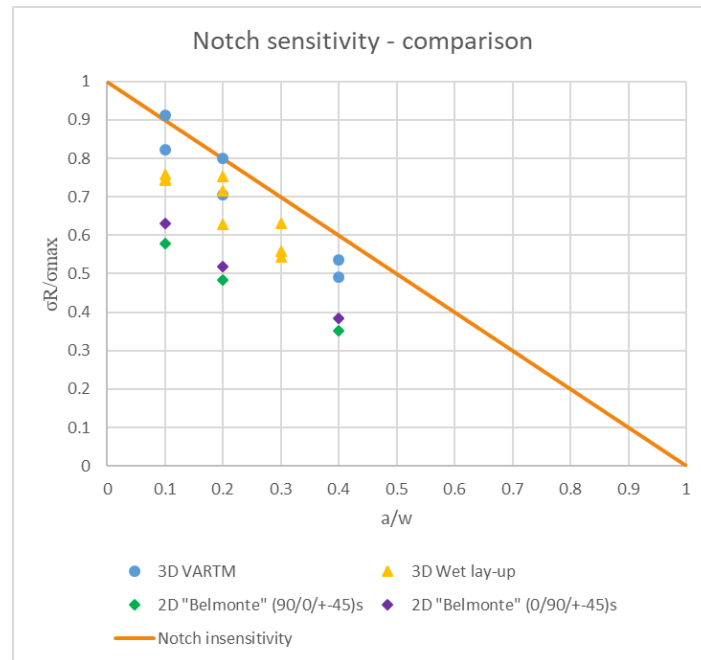


Figure 6.6: Notch sensitivity comparison between the 3D-96 composite analysed in this work and a 2D composite presented in literature [19].

## 6.4 Digital Image Correlation results discussion

Over every specimen tested before, a speckle pattern was sprayed and a DIC investigation of the strain distribution was performed. In the following part of the chapter a discussion of the results will be done, introducing some preliminary consideration about the material behaviour.

### 6.4.1 Plain specimen

In the next picture, a series of images taken at regular times is depicted with the load active on the specimen when the picture was taken and the related average strain on the overall specimen. Using the DIC technique, an image was acquired every 6 seconds, starting from zero load till failure, in this way it is also possible to derive interesting conclusions about the failure mechanism and damage progression during the entire test and predict the area where the failure will happen. From the first two pictures can be seen the formation of a regular pattern made of strips which is correlated to the regular alternation of weft yarns and resin rich regions on the surface. Can also be noted further on the formation of transverse cracks, which are represented by the red strips in the second pictures in Figure 6.7, which are pointed out by some red crosses. These cracks form probably in the resin rich superficial channels between two contiguous weft tows and can



be noted how their length grows almost instantaneously along the whole specimen width. This process goes on until there is a saturation of the cracks all over the length, as can be seen in the third picture. Then another pattern starts to appear, where some spots characterized by low strain values are surrounded by a diffuse background of higher strain, intermitted again by some strips of high strain, where the transverse cracks are located. The purple spots visible in the last two images, as was proven in §5, are related to the presence of z-crows, which are the superficial edges of the z-binders. These fibres represent an area of higher modulus, with respect both to the resin and to the weft tows surrounding them. So, the strains are preferentially redirected to the surrounding areas, which have higher displacements. Final failure starts at the edge of the specimen, in the area highlighted by the red circle in the last image. The failure started in this region probably because of the presence of a defect induced in the manufacturing, which was a wide-open surface channel. In any case, can be said that usually the final failure starts at the specimen edges caused by the well-known edge effect, which generates a stress intensification at the free-edges. The warp yarns then started to fail in this region related to the highest strains in the resin rich region between the weft tows and between two z-crows, suggesting a correlation between final failure of weft tows and strains in the adjacent resin regions in the matrix.

In the second plain specimen (Figure 6.8), the same characteristic stages can be seen, with the formation of a strips pattern, the progressive formation of transverse cracks, the damage accumulation in the resin rich region, the formation of the characteristic pattern made of purple spots corresponding to the z-binders and the final failure in the area with the highest strains at a free-edge. Must be pointed out that the failure in the second test, differently from the first one, happen near the gripping region. This is very common since the load induced in the material to grip it and the presence of the discontinuous geometry caused by the presence of the end-tabs, modify the stress distribution in this region.

Notch sensitivity investigation

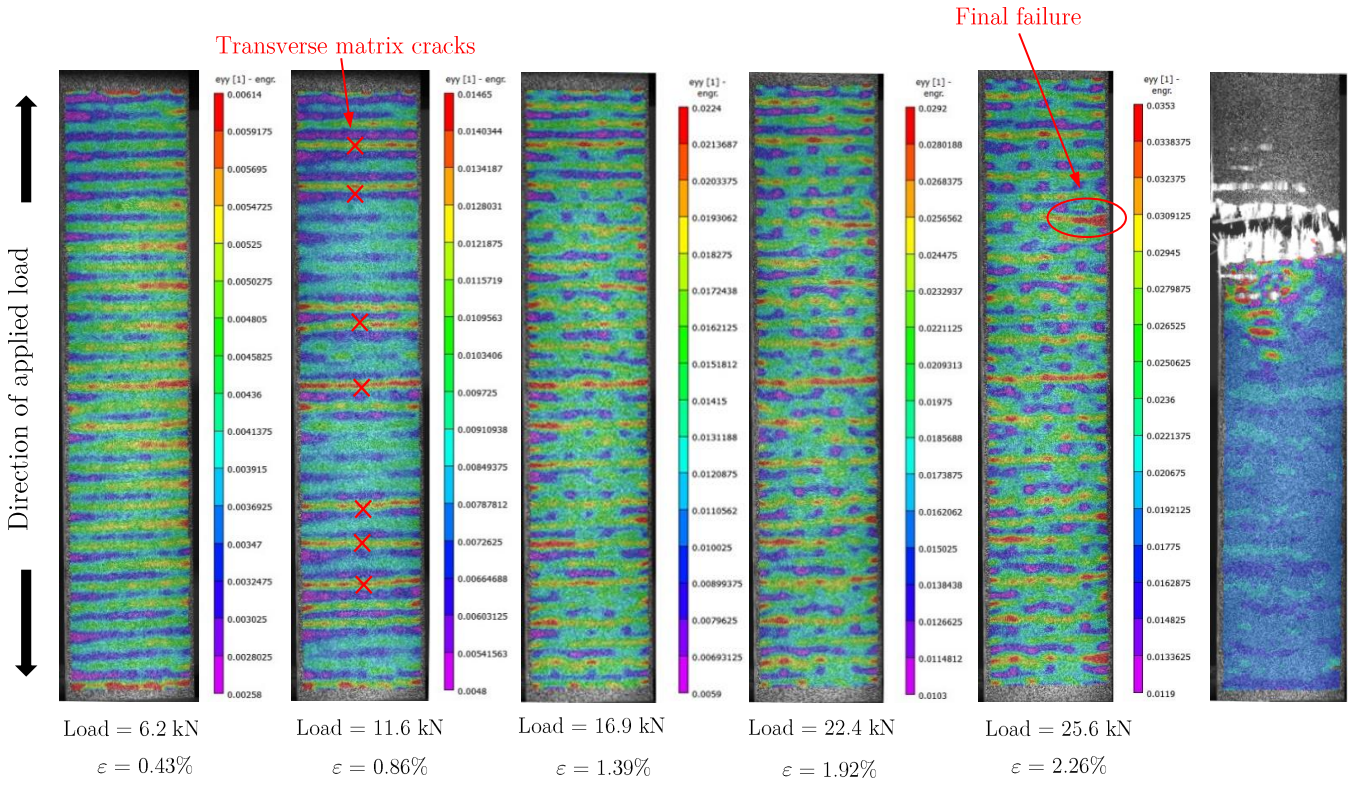


Figure 6.7: Resulting images from the DIC investigation on the plain specimen without the presence of a strain gauge, with some crosses are reported the transverse matrix cracks, with a circle the area of final failure.

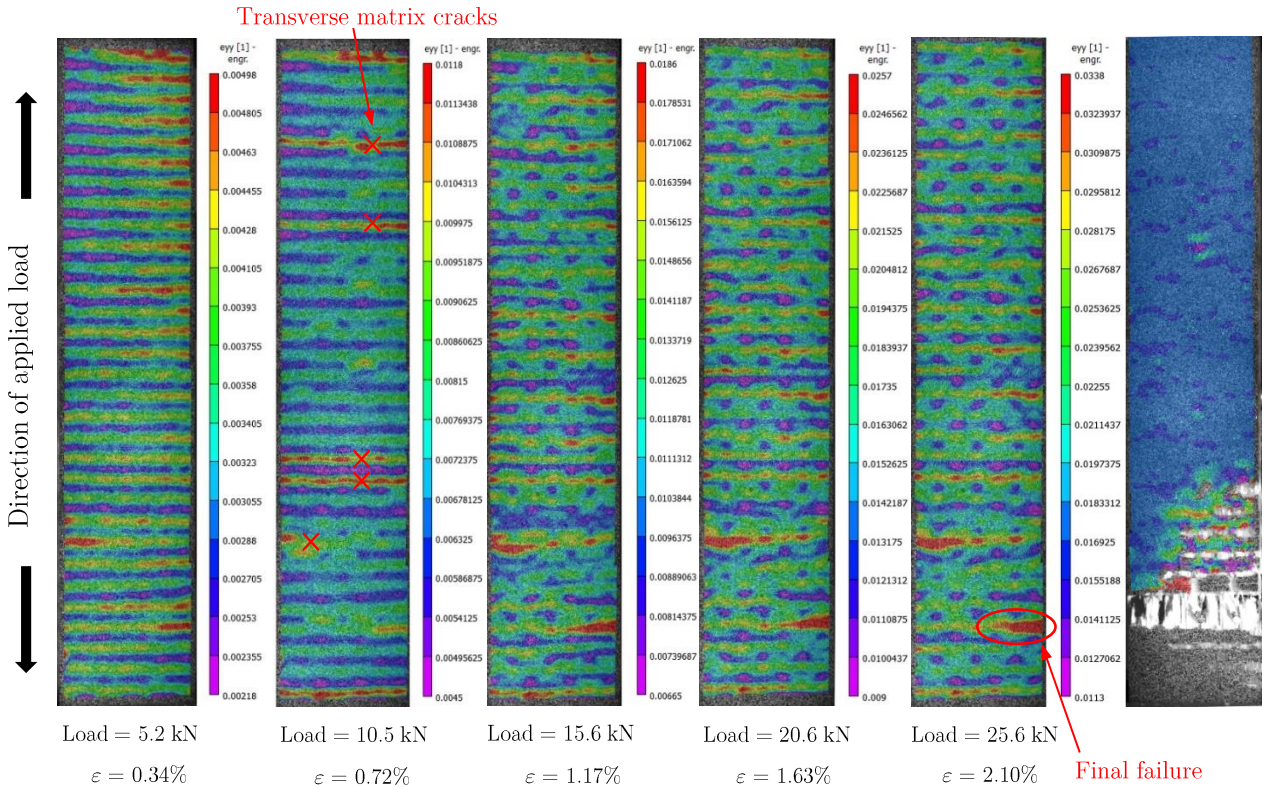
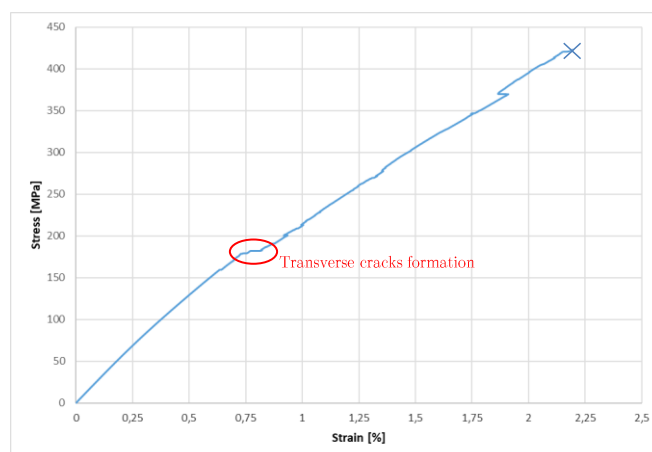


Figure 6.8: Resulting images from the DIC investigation on the plain specimen with the presence of two strain gauges, with some crosses are reported the transverse matrix cracks, with a circle the area of final failure.

In the following image (Figure 6.9) can be seen the stress-strain graph recorded during the tensile test of the second specimen with the use of DIC, using two strain gauges positioned in the area on the back, not painted with the speckle pattern. The data show a classical behaviour for this type of material as it can be seen in literature. The first part of the curve is quite linear until the values of strain equal to 0.3%-0.4%, which is represented by the first picture in Figure 6.8. After this, can be seen at about 0.6% of strain a change of slope which is related to the formation of transverse cracks in the resin regions that are depicted in the second picture, which is representative of the initial stage of this process, this is concluded roughly at 0.8% of strain. From this stage, there is a progressive reduction of stiffness related to the progressive damage in the composite. So, two thresholds can be seen for the cracks formation the first one is related to the formation of matrix cracks and their growth, the second to the formation of the final failure damage. The first stage, which is visible around 0.6% and 0.8% strain, is initiated near the so called z-crowns, as it is described by Lomov in the paper number [10]. These regions are where the z-binders arrive at their edge on the surface and overcome the weft tows laying on them. The cracks, which is supposed to be generated by the stress concentration due to the indentation produced by the z-yarns on the adjacent weft toes, then spread out in the matrix channels near them. Even transverse cracks in the weft yarns appears to form after this stage. Near the final failure, in some preferential spots, debonding generates from the previous formed cracks at the surface near the z-binders. In this second stage of the damage formation, from an edge where it is present a previous transverse matrix crack and delamination, a crack begins to open the composite until the warp fibres are broken.



*Figure 6.9: Stress-strain graph of the second plain specimen presented recorded with an axial strain gauge tested in warp direction.*

*Table 6.10: Data resulting from the test on the second plain specimen provided with two strain gauges, one longitudinal and one transversal. The measures are related to the warp direction.*

<i>Ultimate Tensile Strength [MPa]</i>	<i>Ultimate Tensile Strain [%]</i>	<i>Young's modulus [GPa]</i>	<i>Poisson's coefficient</i>
422	2.2	26.6	~-0.13

The relation between the DIC results and the transverse cracks is just supposed at this stage based on the results from the literature but there are no proves that the lines visible on the DIC are effectively cracks and, also, where they form, either in the surface or inside. So, a further analysis must be carried out to solve these questions. The method that will be adopted will be to stop the test after having passed the strain level where there is the crack formation, cut the specimen in the longitudinal direction and try to visualize the cracks using microscope images. This will be reported in §7.

### 6.4.2 2.5mm hole

Also in this case can be seen the formation of the characteristic patten, composed firstly by the formation of transverse lines, which characterize the alternation of superficial resin pockets and weft tows, then the presence of z-crowns over the composite surface is spotted. Even this time, the alternating lines which are addressed to be resin pockets and weft tows and the consecutive formation of matrix cracks are yet not fully demonstrated but only supposed at this stage.

One characteristic that can be seen testing in this case the sample with the presence of a hole is the typical strain concentration around it. In this case, contrarily to what is the experience with homogenous and isotropic materials, the strain pattern is not symmetrical on both the sides of the hole and the maximum strains are not placed at the hole edge, as it should be for example in a metal plate. This is because the internal architecture of the composite is highly non-homogenous, presenting an alternating structure of tows positioned at 90° to each other and repeated over the thickness, between them there is the presence of resin pockets and channels. The strain distribution, as was seen, is highly affected by these internal differences and, also, the strains around the hole are subjected to this. In particular, the position of the hole with respect to the weft tows is determinant because the strain flow goes preferentially inside the resin channels, leading to the formation of cracks that will cause the final failure near the hole. So, the strain distribution



around the hole is different in every case and it depends on the position of the weft tows in the specimen with respect to the hole position. As can be seen comparing the two different specimens with a  $2.5\text{mm}$  hole, the strain distribution around the hole differs because in the first case (Figure 6.10) a weft yarns pass above and below the hole and so, a strain intensification is predominant in the resin channel right at the hole edge, while in the second case (Figure 6.11) the weft yarn passes right at the hole centre and so the strain flow assumes a butterfly shape, redirecting itself in the resin channels above and below and so also the damage. It is already clear how much the fabric architecture influences the failure and the damage progression in this type of composites.

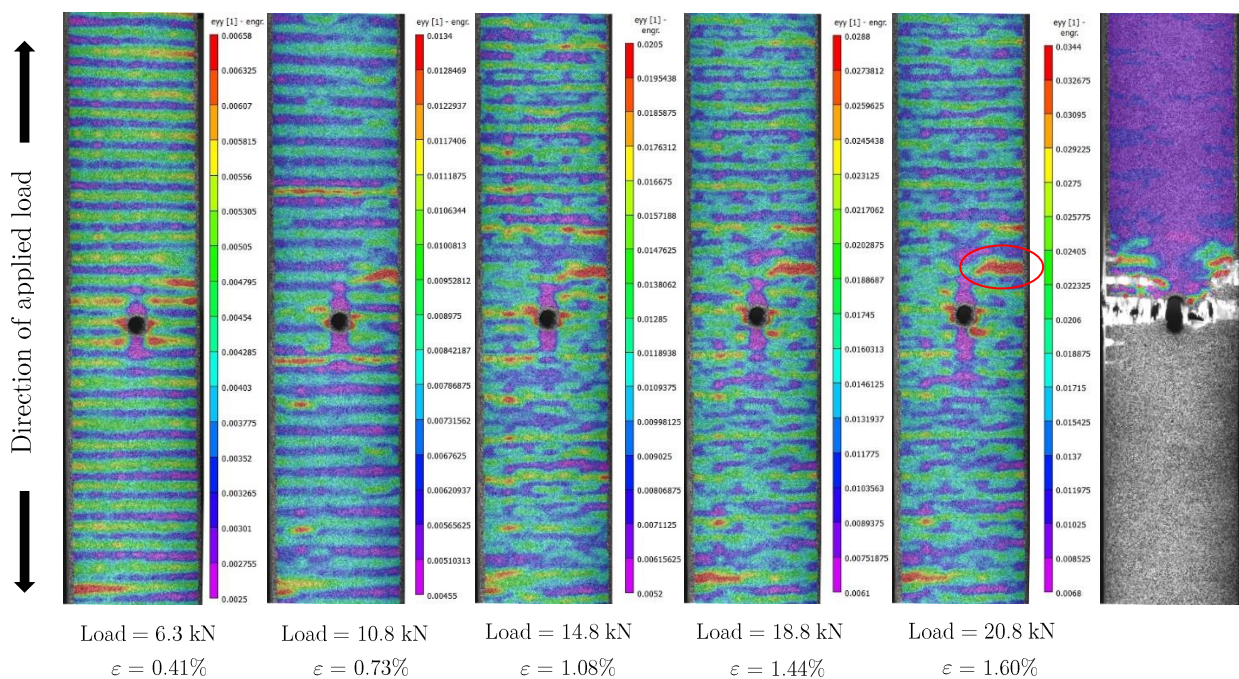


Figure 6.10: Resulting images from the DIC investigation on a specimen with a  $2.5\text{mm}$  hole, referred as specimen 2.

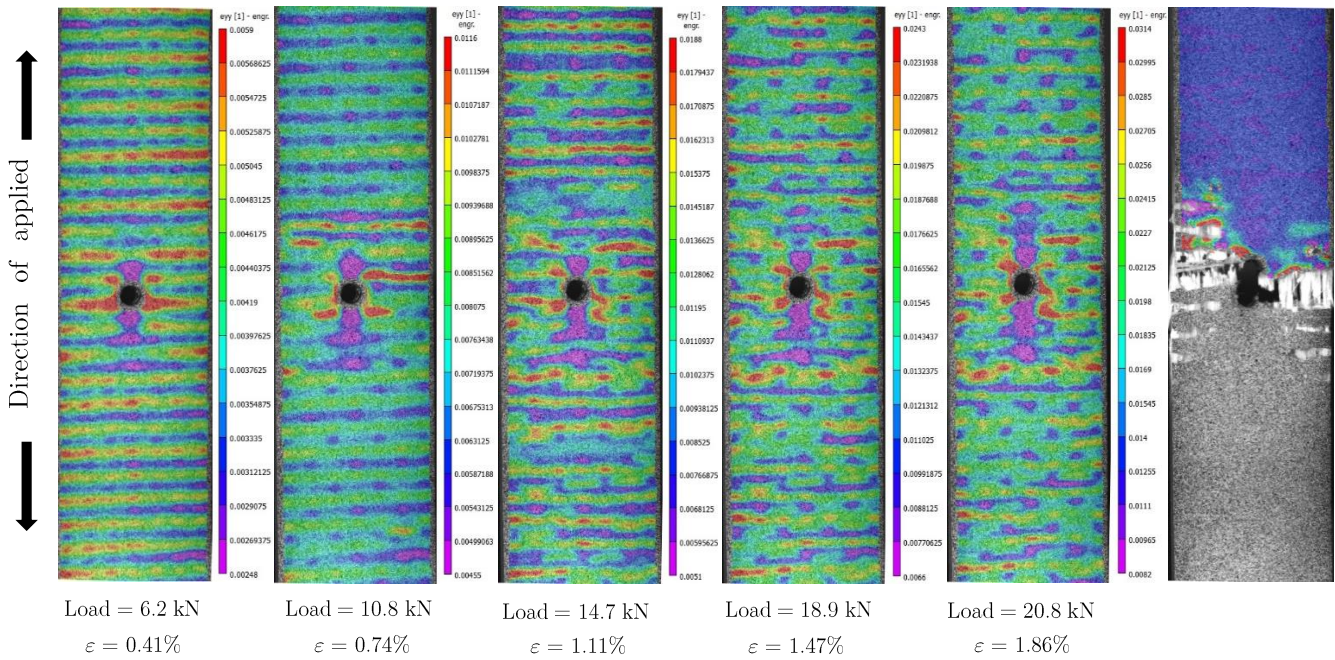


Figure 6.11: Resulting images from the DIC investigation on a specimen with a 2.5mm hole, referred to as specimen 3.

### 6.4.3 5mm hole

This case will be analysed more in detail because in a following part of the thesis will be compared the strains of the 3D woven composites with the ones present in a 2D composite and in an aluminium plate both with a 5mm hole.

An important feature which can be reached with the use of the DIC is that it can provide also punctual information together with full-field results. So, to characterize the strains around the hole and to verify if a symmetrical distribution exists, the information at some significant angles are plotted, as it is shown in Figure 6.13. After having identified the points at the edges, a strain measurement was also taken every 10°. This feature is not automated inside the software Vic-3D, to do so was performed a manual procedure to identify the angles. Must be reminded that all the considerations done for the cases before are valid also in this case for what concerns the formation of the transverse patterns, the z-crown spots and the strain intensification pattern around the hole, even if the first two are not so visible because they are hidden by the presence of the strain intensification at the hole.



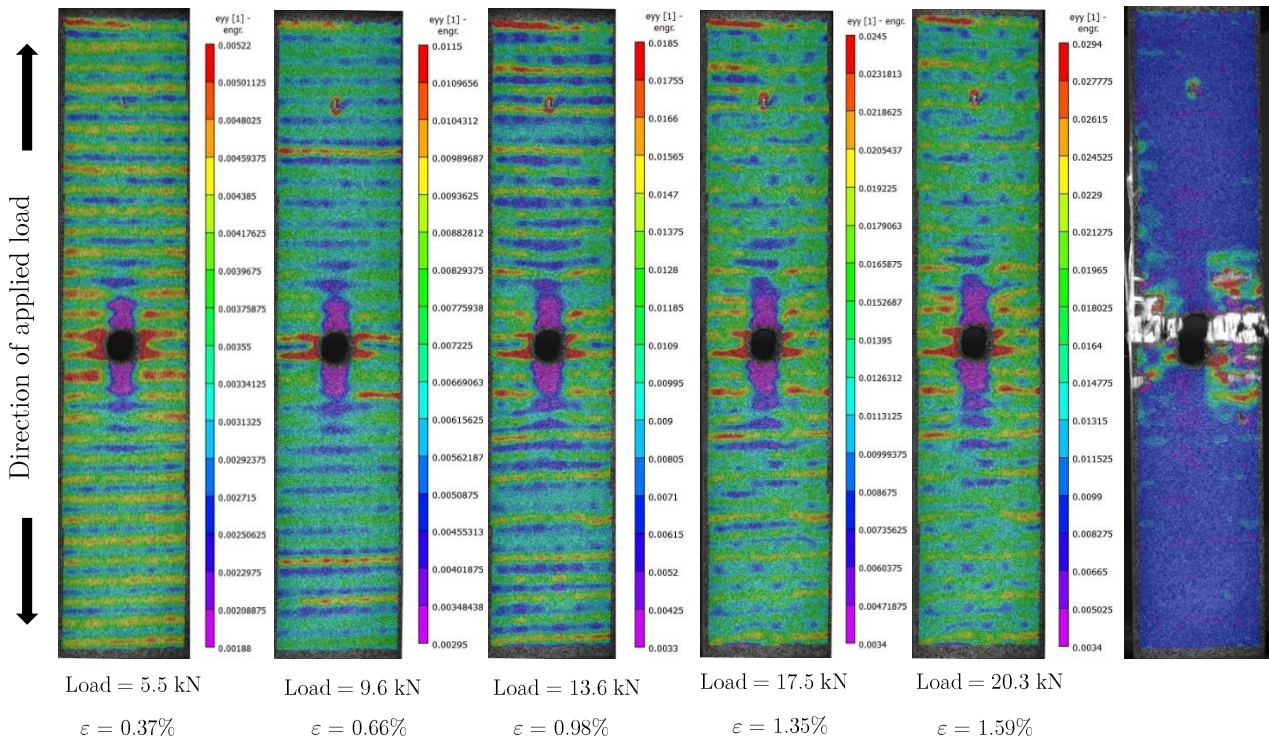


Figure 6.12: Resulting images from the DIC investigation on a specimen with a 5mm hole without the presence of a strain gauge.

In the following picture are reported the points from where the strains are extracted with their corresponding number. As can be seen, four points are taken at the hole tips and the others at some regular angles as before reported. It is so possible to relate the strain evolution with a good precision in each position, to relate this to the damage.

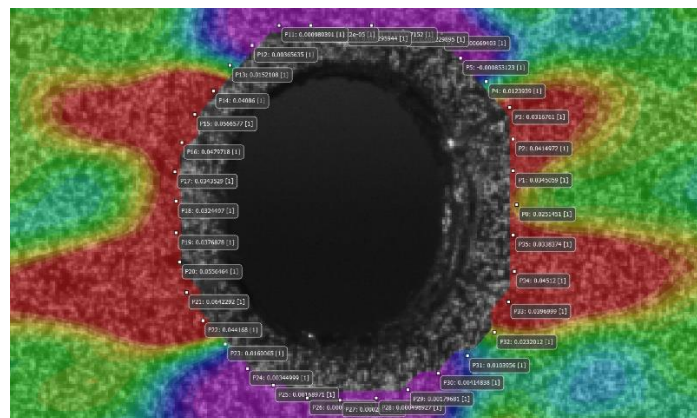


Figure 6.13: Points where the strains around the hole are taken for the VARTM laminate.

In the following graphs, the strain levels during the test until failure are reported, to do so a polar graph is created taking the strains from the points as showed in the picture before. Using this kind of representation, it is possible to visualize all at once the strain

distribution around the hole and the strain evolution during the test. It is important to mention that the curves plotted are obtained as best fit curves of the strain values every  $10^\circ$ , so the distribution plotted represents a good representation of the real one.

In the following graph can be seen that for low average strain values, which identify a condition before the damage, the strain distribution around the hole presents a degree of symmetry, while they are still influence by the presence of the resin channels since the plot presents a butterfly shape with the maximum around  $30^\circ$ . After the damage occurs, the strains start to present a different trend, especially between the right and left side of the hole. This tendency is more evident between  $30^\circ$  and  $45^\circ$ . So, the conclusion is that the damage does not occur in the same way on each side of the composite and the strain distribution is so affected by the different degree of damage in each part around the hole, while is supposed that this is guided by the presence of the resin channels.

Another important consideration that must be made is that the maximum strains are located around the  $30^\circ$  and not at  $0^\circ$  as it must be expected for a symmetric repetition of  $[0/90]$  plies in a composite, this because this type of material presents an elevated level of internal inhomogeneities, so the strains are preferentially redirected on the strain pockets between the yarns creating a different strain patter around the hole depending on its position with respect to the composite architecture. So, even if the composite presents a symmetric configuration with plies just at  $0^\circ$  and  $90^\circ$ , the resulting maximum strains are not located at the hole edge but in a different position.

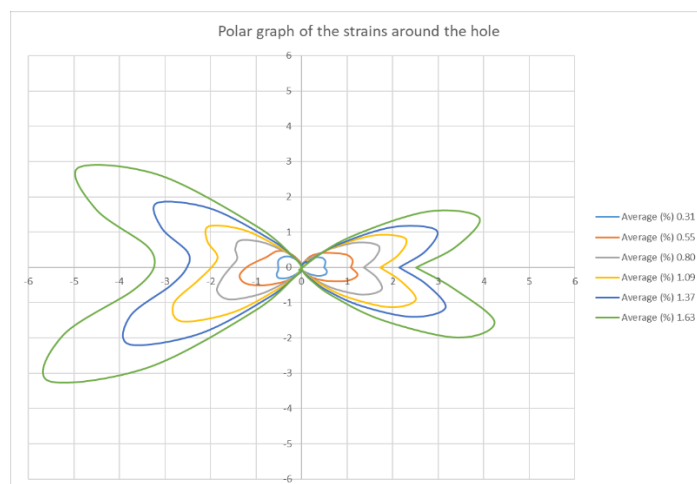


Figure 6.14: Polar graph of the strains around the hole for the first 5mm notched VARTM specimen.



In the following part will be presented the results for the second specimen tested for this hole size.

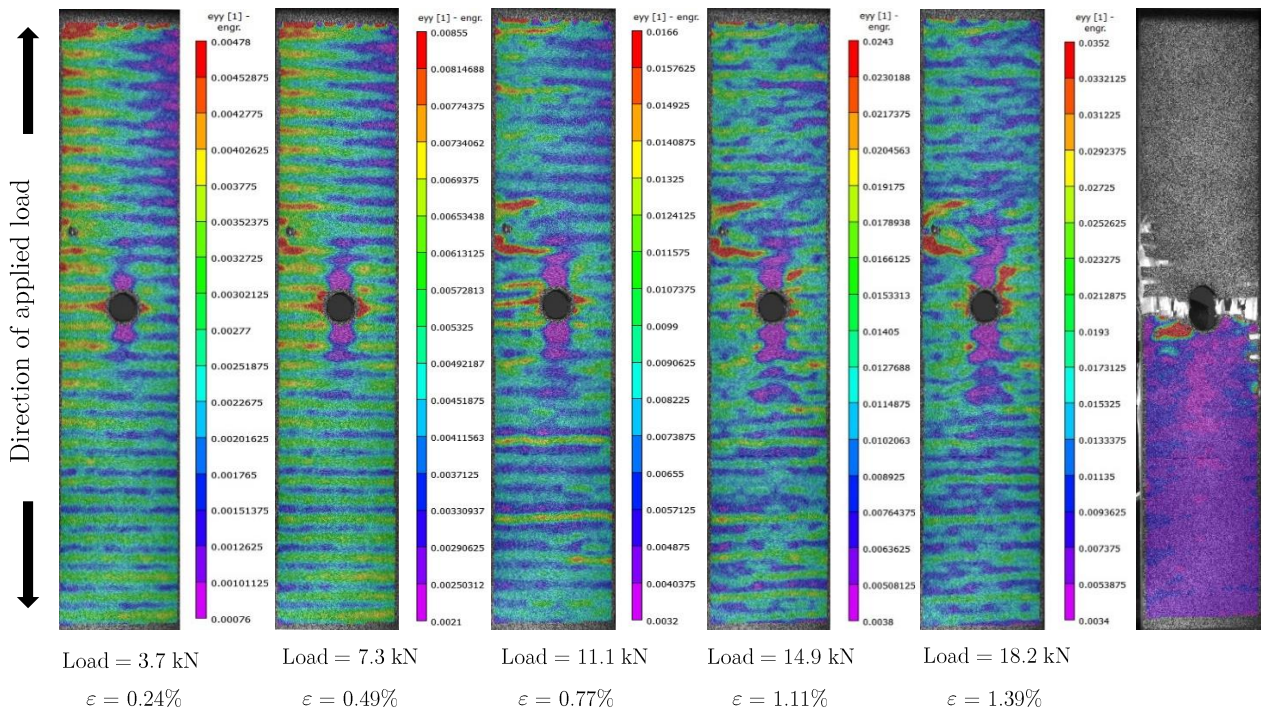


Figure 6.15: Resulting images from the DIC investigation on a specimen with a 5mm hole with the presence of a strain gauge near the hole.

Comparing the picture of the second specimen with the results of the previous, can be seen that in this case the strain distribution is completely different, with the maximum of the strains around zero degrees because of the presence of a resin channel in this area. Despite that, the strains are not only confined in this region but there is a redistribution of them also in other positions, roughly around 60°-70°, because of the presence of resin channels. This can be seen especially in the upper right part where is clearly visible the presence of a shift of the max strains from the hole edge to other resin channels, which can be part of a redistribution of the load and of the damage.

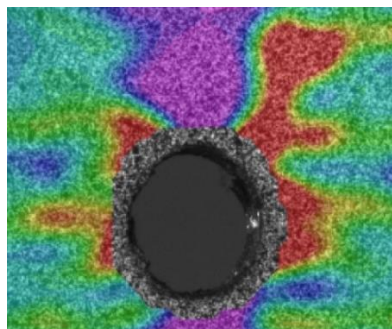
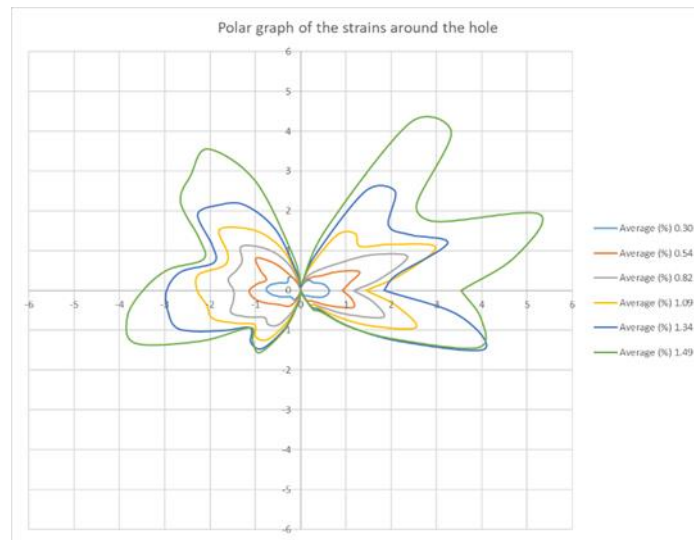


Figure 6.16: DIC result before failure for the second 5mm notched VARTM specimen.



*Figure 6.17: Polar graph of the strains around the hole for the second 5mm notched VARTM sepecimen.*

Comparing the two polar graphs is now evident how much the strain distribution is different in the two cases. In the second specimen, while at the beginning of the test the strains are centred around  $0^\circ$ , during the test they spread out at different degrees.

#### 6.4.4 10mm hole

From the tests with this hole size, which is the wider analysed in this work, can be appreciated the fact that the strain intensification pattern around the hole is extremely influenced by the presence of the resin channels. In fact, can be seen how the strains have a repetitive pattern, which is the same as the alternating distribution of resin channels and weft tows. Again, the failure does not happen at the hole edge but it is influenced by both the strain intensification produced by the hole, with a maximum at the hole edge, and by the resin channels and the defects inside the material. So, it is clear how also the final failure is affected by the resin channels and a prediction about the point where it will happen is not possible to do for the reason explained before.



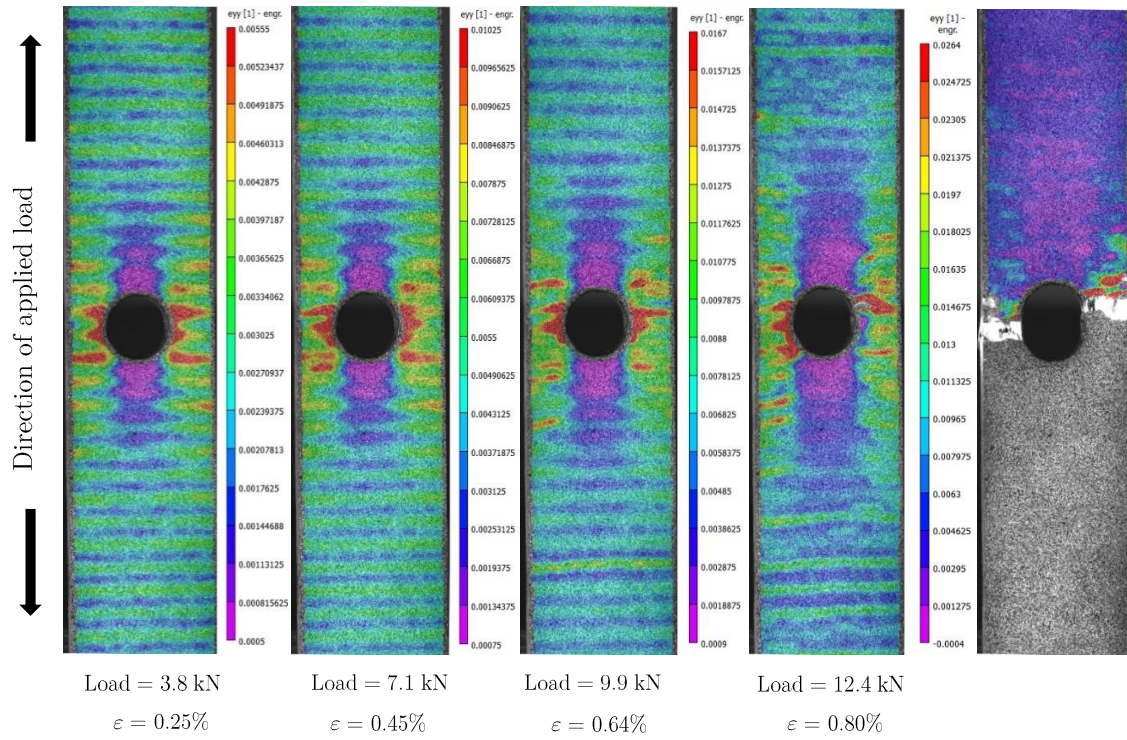


Figure 6.18: Resulting images from the DIC investigation on a specimen with a 10mm hole (Specimen 5).

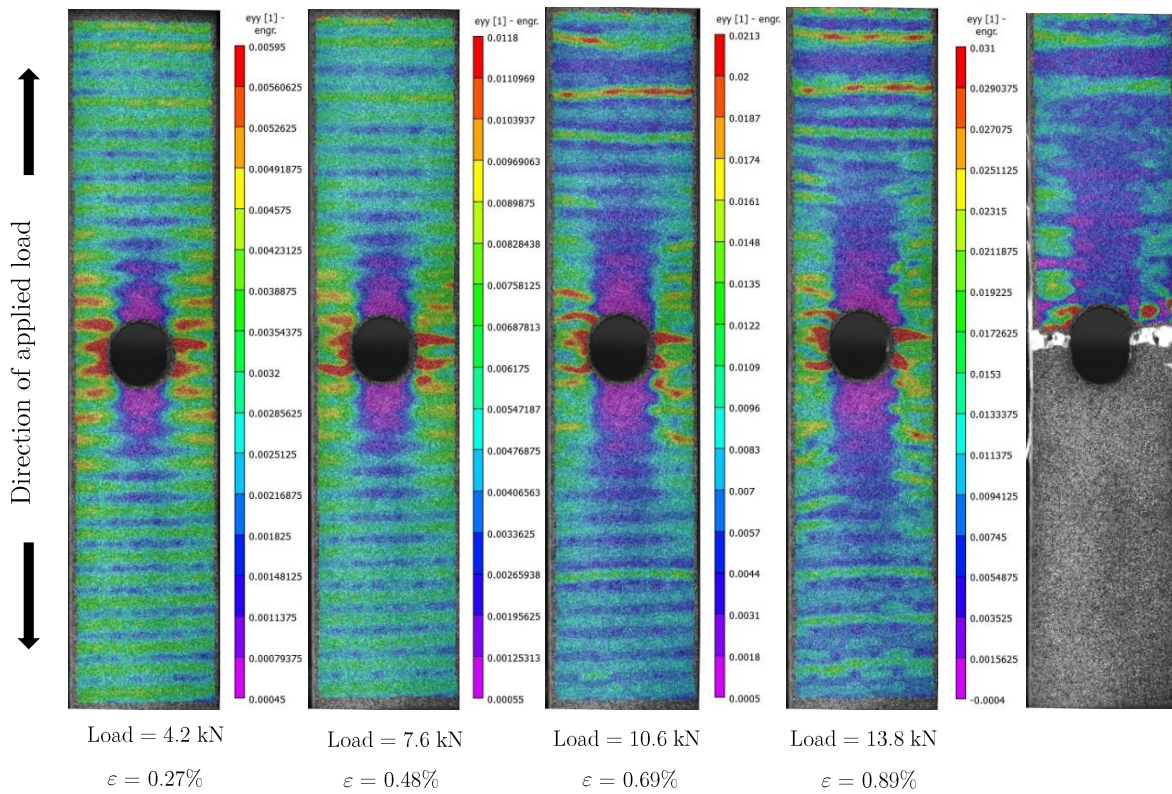


Figure 6.19: Resulting images from the DIC investigation on a specimen with a 10mm hole (Specimen 6).

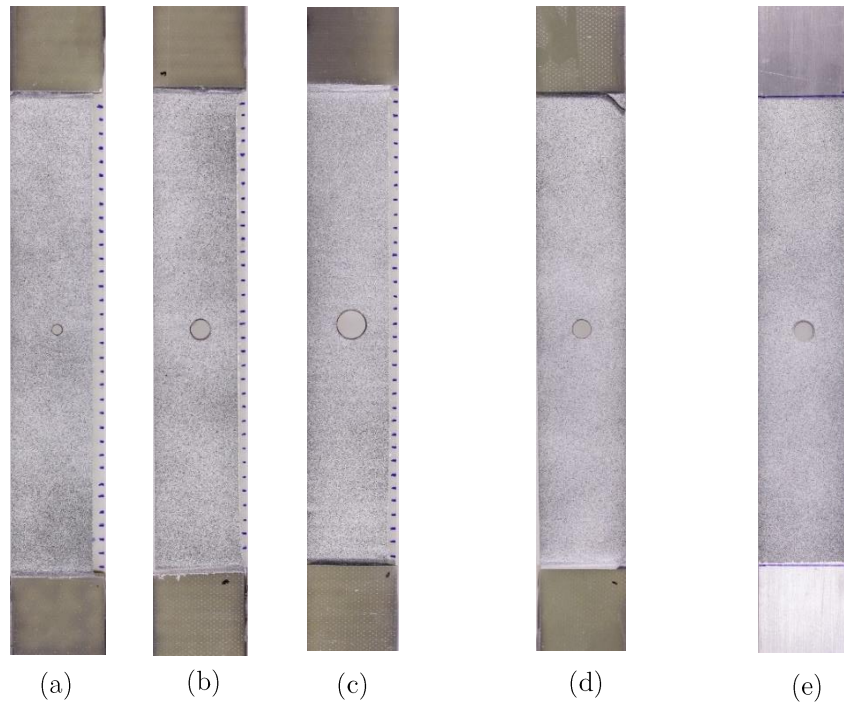
## 6.5 Strain mapping around holes using DIC

In this section, a new series of tests are presented, they have been performed on the own made laminates made with the wet lay-up technique. These tests will answer the question about the relationship between resin channels position, strain flow and final failure around the hole.

### 6.5.1 Test program and specimen preparation

In this part, several types of testing have been carried out to answer different questions. They can be summarized as follows: one specimen for each hole size analysed for the wet lay-up specimens (2.5mm, 5mm, 7.5mm hole diameter) has been tested using the DIC technique, leaving one edge without the speckle pattern because it was marked in correspondence of the weft tows, this to correlate the internal geometry with the results provided by the DIC (i.e. alternated transversal lines and strains around the hole); one 2D woven composite, precisely one stack of 8 plies of 8-harness satin fabric, was tested with a 5mm central hole to compare the strains near the hole with the results for a 3D woven composite; one aluminium specimen was tested as the 2D one to compare the DIC results around the hole with an isotropic material.

In the following images are presented the specimens tested where it is possible to see, in the first image the marks put on the free edge to correlated the weft tows with the DIC results. This procedure was chosen because it is easy and effective, since the marks will deform as the surface underneath and they are easily recognisable in the image provided by the DIC. Other possibilities that have been considered were, putting some resin drops on the external face, this solution has the problem that the drops are not easily placed in the right position. Another possibility is to glue a millimetre paper on the back with a prominent edge where the marks are put, the problem correlated with this solution is that the paper will not deform as the composite leading to some problems since the beginning of the test.



*Figure 6.20: The notched specimens tested are here shown, on the right are presented the three different types of notched specimens for the notch sensitivity analysis (a) (b) (c), on the centre are shown the 2D woven and the aluminium coupons with a 5mm central hole (d) (e).*

In this part will be discussed the strain distribution and the final failure position in 3D composites with different hole sizes, also a 2D woven composite and an aluminium plate are tested to show the different strain distribution.

### 6.5.2 3D woven composite with a 2.5mm hole

It is visible how, in the first part of the test, the strains around the hole present a symmetrical shape until an average strain of 0.3%-0.4%, so in the undamaged region. After this point it is visible that there is a strain concentration approximately around 45°, which is visible also in the DIC image before failure. Throughout the test there is also a strain concentration around 180°, on the left of the hole, which correspond to a damage formation over a weft tow. The strain level in this area before failure is quite high, confirming that cracks starts from all over the hole edge and not only from the resin gaps. Comparing the strain pattern before failure, the DIC image and the position of the resin channels, it is visible that strain concentrations are in correspondence of the resin channels. It is also visible that major cracks are formed in this region, which can so be identified as matrix cracks. So, cracks forms around the hole and then redirect themselves in the resin channels. Talking about final failure, it is visible that the cracks that lead to failure are placed in



the region between the weft tows. This is not enough to say that fibers breakage is placed right under the matrix gap between the weft tows, in fact we can just say that the warp tows failure is located near that area. Looking at the images of the whole sample, it is visible that damage development starts also from the sample edges in other locations, in any case these cracks does not lead to failure, that happens always around the hole. Talking about final failure position, major cracks happens in the positions highlighted by the highest strains in the polar graph. So, for this test it is visible a direct correlation between cracks, that will lead to final failure, and high strain in the polar graph, this will not always be possible, as it will be shown.

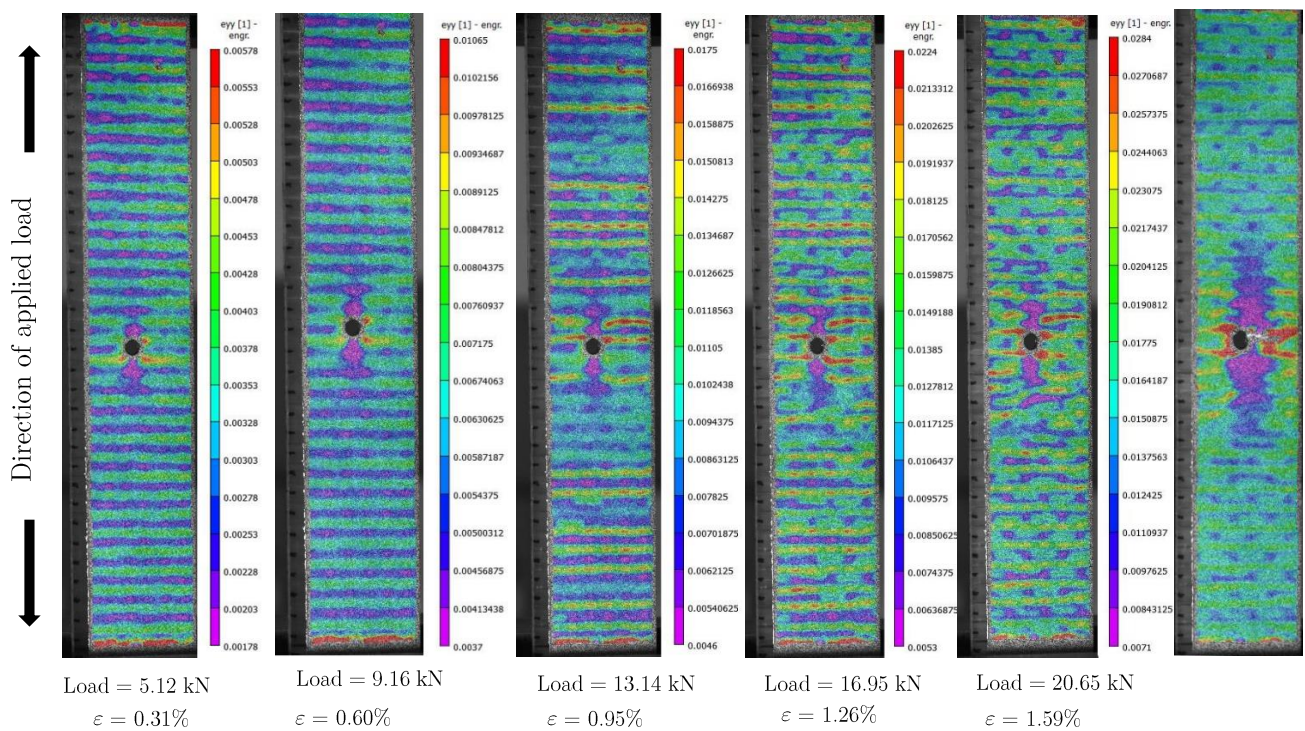
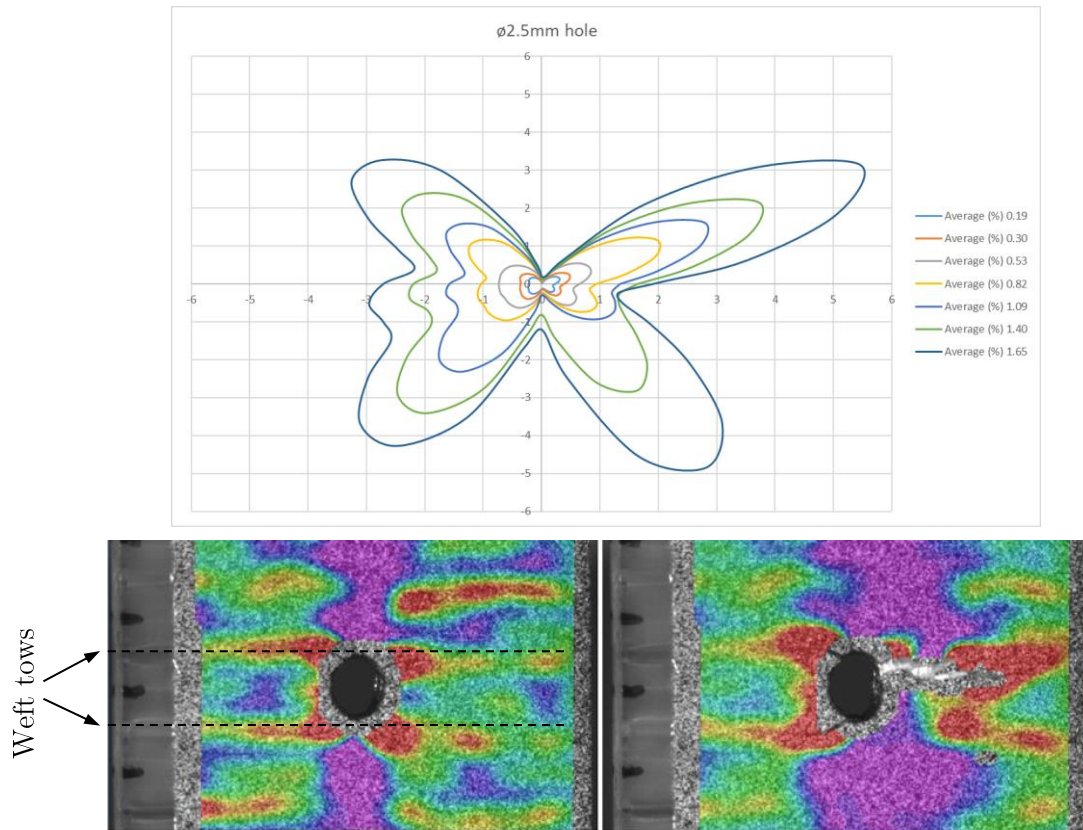


Figure 6.21: DIC resulting images on a wet lay-up 2.5mm notched specimen, can be noticed the relationship between the markers on the left of every specimen with the low strain lines pattern.



*Figure 6.22: Strains around the hole and final failure position investigation on a wet lay-up 2.5mm notched specimen. Black dashed lines represent the resin channels between weft tows, while the black marks on the specimen left edge are positioned over the weft tows.*

### 6.5.3 3D woven composite with a 5mm hole

In this second case, a test is performed on a 5mm diameter hole, it is visible from the DIC image, where is highlighted the weft tows position, that in this case are placed in a different way from the previous one. The strains are also in this case quite symmetrical until an average strain level of 0.5% on the overall specimen, with higher strains around  $0^\circ$ , as it must be expected. When the average strain increase, there is a change in the point with higher strains around the hole, which are now located around  $45^\circ$  with respect to the hole centre. This corresponds to the matrix gaps between the weft tows in the two upper ones, while the two lower ones are in correspondence of a weft tow. So, can be assumed that some cracks are formed near the z-crowns. These sites have the highest strains during all the test and a place where final failure is located is over a weft tow, in the right-bottom of the hole. In this case damage occurs one time over a resin gap and one time over a weft tow, so it is not possible to conclude that final failure always occurs inside a weft tow but, as was said, it depends on the hole position with respect to the

fabric architecture, even if there is a strain intensification in the resin channels probably due to a combination between resin cracking and strain magnification for the difference in Young's modulus. In this case, differently from the previous one, final cracks happen in the bottom-right and top-left of the hole, which are areas not with the highest strains, as it can be seen from the polar graph. This shows a different behaviour with respect to the previous sample, can be said then that the polar graph of the strains cannot exactly predict the final failure position, but it can give a rough prediction. This because damage can also occur in the other face of the sample, which is not checked by the DIC. Moreover, fibers damage can also occur inside the composite, starting from superficial cracks, so it is not possible to say exactly where the warp tows will fail starting from superficial observation, even if they can provide an indication.

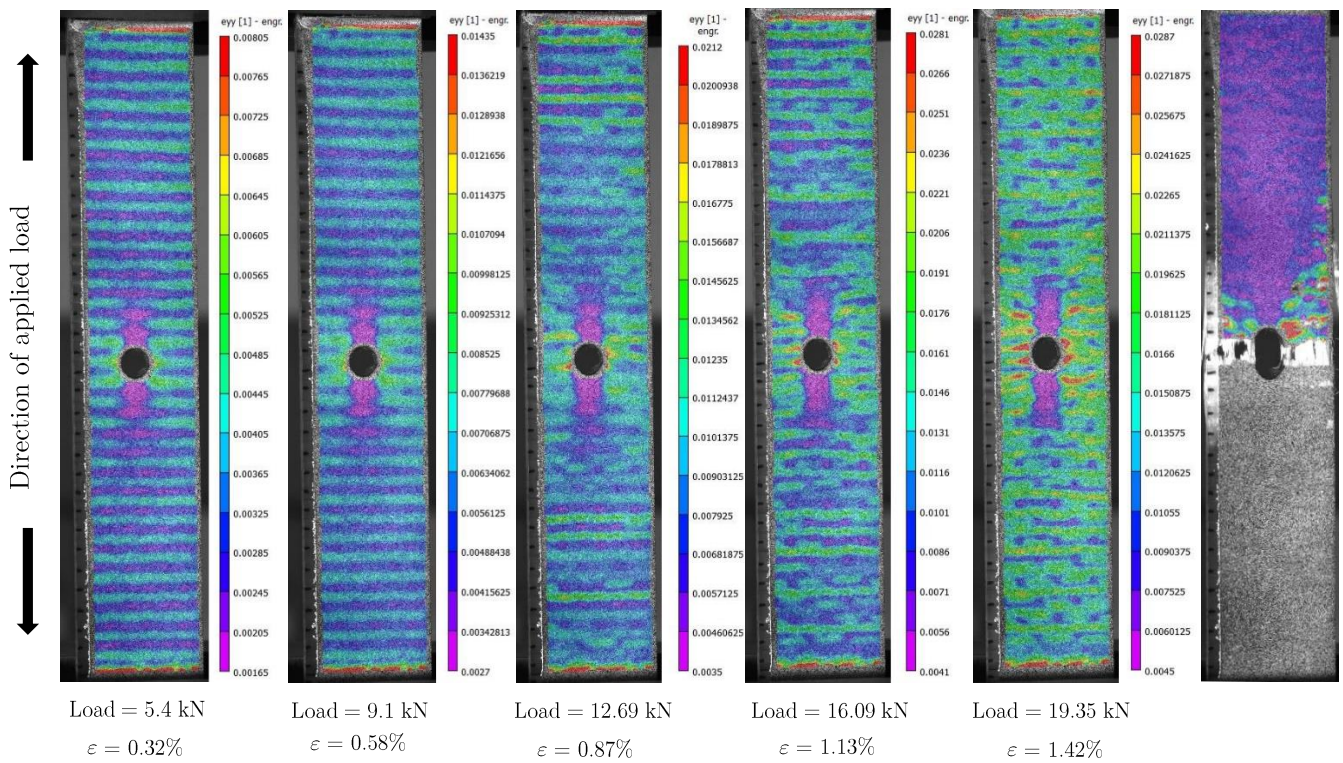
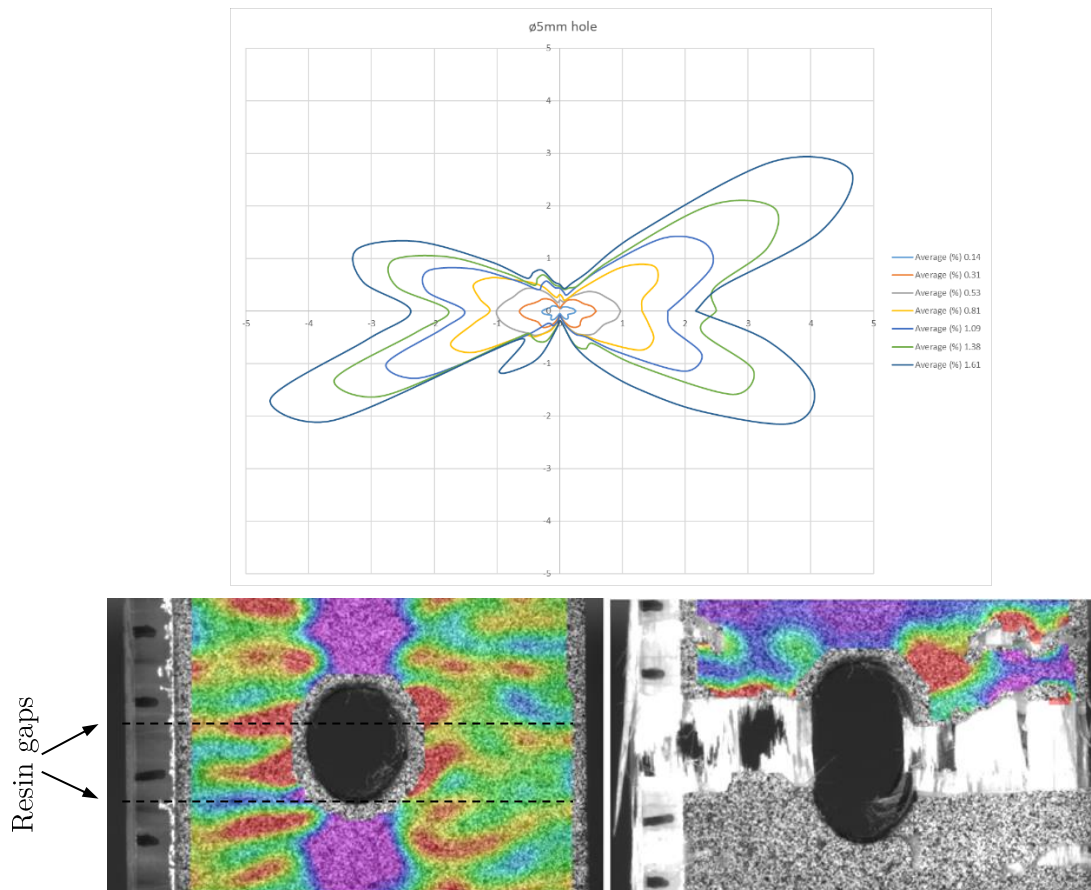


Figure 6.23: DIC resulting images on a wet lay-up 5mm notched specimen, can be noticed the relationship between the marks on the left of every specimen with the low strain lines pattern.





*Figure 6.24: Strains around the hole and final failure position investigation on a wet lay-up 5mm notched specimen. Black dashed lines represent the resin channels between weft tows, while the black marks on the specimen left edge are positioned over the weft tows.*

#### 6.5.4 3D woven composite with a 7.5mm hole

Since the hole size is quite bigger than a single weft tow in this case, there are always two resin channels along the hole. So, the typical strain pattern is visible since the beginning of the test due to the Strain Magnification in the resin channels. Differently from the other cases, the damage development is limited to the hole, while for a 2.5mm hole it is also visible the formation of damage on the specimen edges. With such a wide hole, the notch sensitivity is here higher and the strains remain centred around the hole due to the fact that the specimen fails at very low strain. It is also clear that final failure happens this time between two weft tows. Must be said again that warp tows failure can also happen in another place and not exactly under the fracture surface. The precise point where the failure happens is not possible to be known from the fracture surface, because of the energy release that alters the architecture and because of fibers sliding. In any case, it is interesting to notice that major cracks develop inside the resin channels and looking

## Notch sensitivity investigation

at the comparison at late stage damage in Figure 6.26, it is also possible to see that failure cracks develop from these resin gaps.

Even in this case, final failure happens in two spot which are not the ones with the highest strains in the polar graph. The considerations, made in the previous case, are also applicable in this one, talking about damage in the other surface not checked by the DIC and cracks development inside the composite, which can change plane, leading to warp fibers failure in other positions.

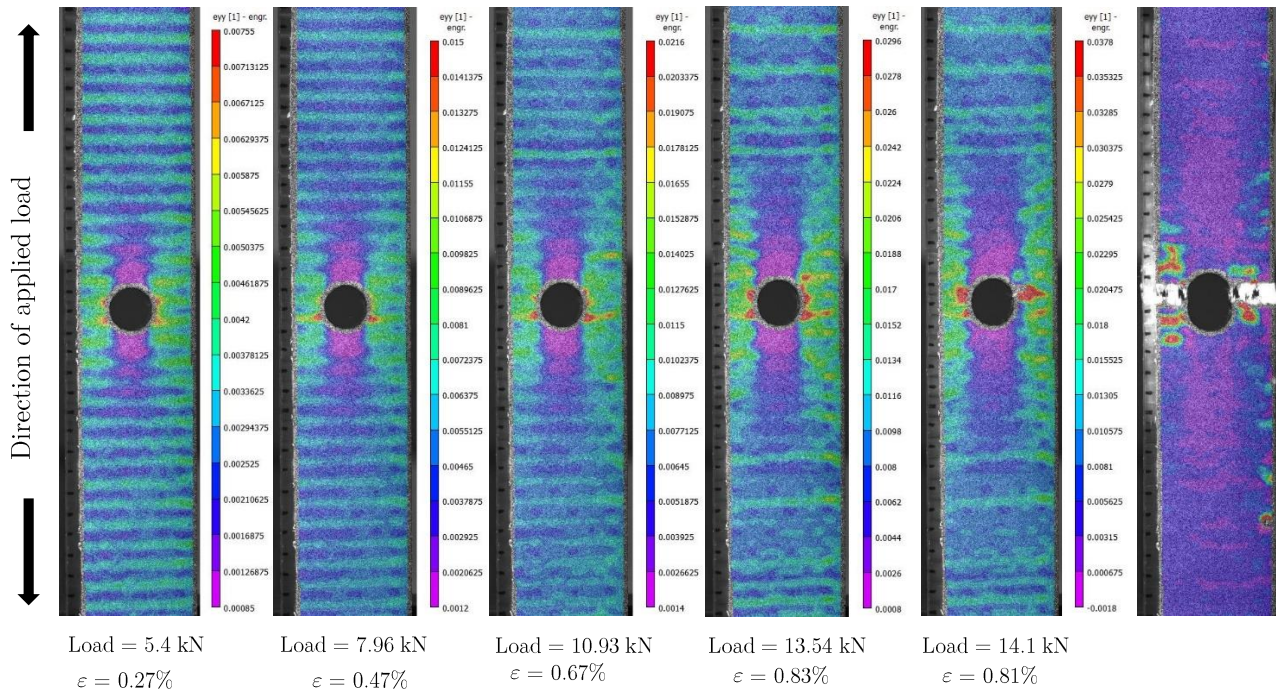


Figure 6.25: DIC resulting images on a wet lay-up 7.5mm notched specimen.

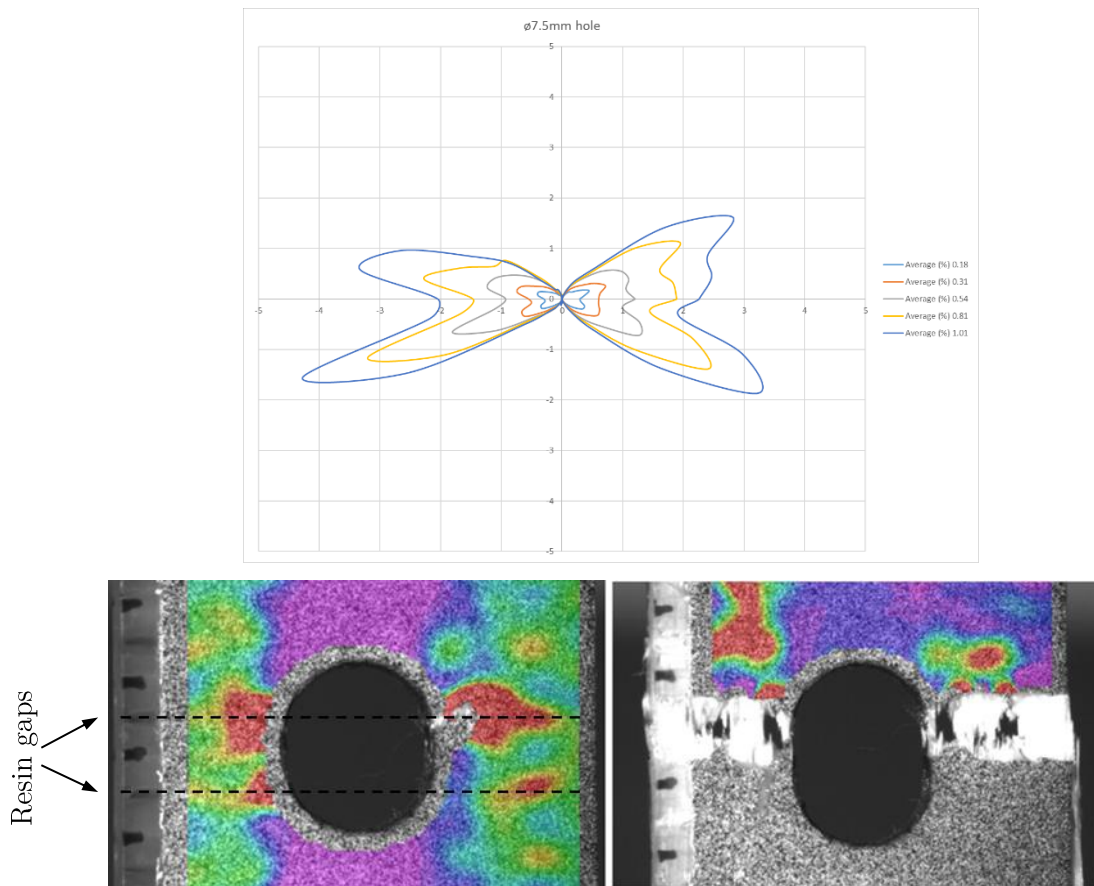


Figure 6.26: Strains around the hole and final failure position investigation on a wet lay-up 7.5mm notched specimen. Black dashed lines represent the resin channels between weft tows, while the black marks on the specimen left edge are positioned over the weft tows.

## 6.6 Comparison of 3D composite strain mapping with a 2D composite and an aluminium specimen

### 6.6.1 2D composite specimen with a 5mm hole

In this section, a balanced 8-harness satin weave laminate is tested with a 5mm central notch. The average thickness for the laminate is 2.20mm and knowing that each ply is around 0.27mm thick, it is possible to deduce the number of plies, that is 8. In this case, the material is not as thick as the 3D woven, but is quite similar, using this type of material would not be possible to have the same thickness as before because only some discrete values are possible, considering also the need to have a symmetric laminate. The laminate is made by a stack of  $0^\circ, 90^\circ_{2s}$  plies, with  $0^\circ$  on the outer surface. As described in §1.2.1, the structure of this material is made by a series of yarns at  $90^\circ$  where the fibers in one direction pass over seven fibers of the other direction and under one, and then

again over seven and so on. So, also in this case the position of the hole with respect to the internal structure can affect the resulting strains, on the other hand every tow is  $500\mu\text{m}$  wide, which is much less than the one for the 3D composite, for the latter every tow is several  $\text{mm}$  wide. In this case, the fact that the fabric architecture could influence the damage around the hole was ignored.

Looking at the 2D woven composite during the whole test, it is visible that strain intensification and damage are localised just around the hole, while in a 3D composite with the same hole size, matrix cracks and strain intensification in the resin gaps happen also far from the hole. Damage it is not visible on the sample surface a part before failure, where it is visible the formation of matrix cracks and what it seems to be a localized delamination. From the polar graph, it is possible to see that the strains are symmetrical until the last stages, which is different from the behaviour that we have seen for the 3D ones. High strains are present for  $0^\circ$  and  $180^\circ$  as it is to be expected for a balanced laminate but it is also possible to see that for values around  $45^\circ$ ,  $135^\circ$ ,  $225^\circ$  and  $315^\circ$ , the strains are still high. Looking at the polar graph, it is possible to see final failure happens near the hole edge, roughly around  $25^\circ$  from the longitudinal line passing through the centre, this behaviour is probably influence by the fabric architecture and by shear. It is noticeable that, in this case, maximum strains around the hole and final failure position are overlapping. Also in this case, the strains around the hole are symmetrical as during all the other stages. Final failure surface presents quite a smooth surface with a small presence of fibers pull off.

Must be pointed out that in this full field measurement it is not possible to see the periodic strain concentration at the yarn crimping locations, in the cross-over positions, a result of this type can be seen in [20], where a 5-harness satin weave is analysed. The difference between high strains in the crimping locations and on the other specimen surface is lower than the one between the notched regions and the specimen surface, so the scale used in the next image it is not suited to properly highlight this difference, this is the reason why it is not possible to see the low strains in the crimping locations and high strains in the matrix regions. For the same reason. It would also be not possible to see the damage formation on the plain surface, in any case damage in this specimen is located only around the hole. For the same reason, it is not possible to appreciate the damage that id present inside the composite at the edges of the weft yarns and at the resin spaces on the surface.



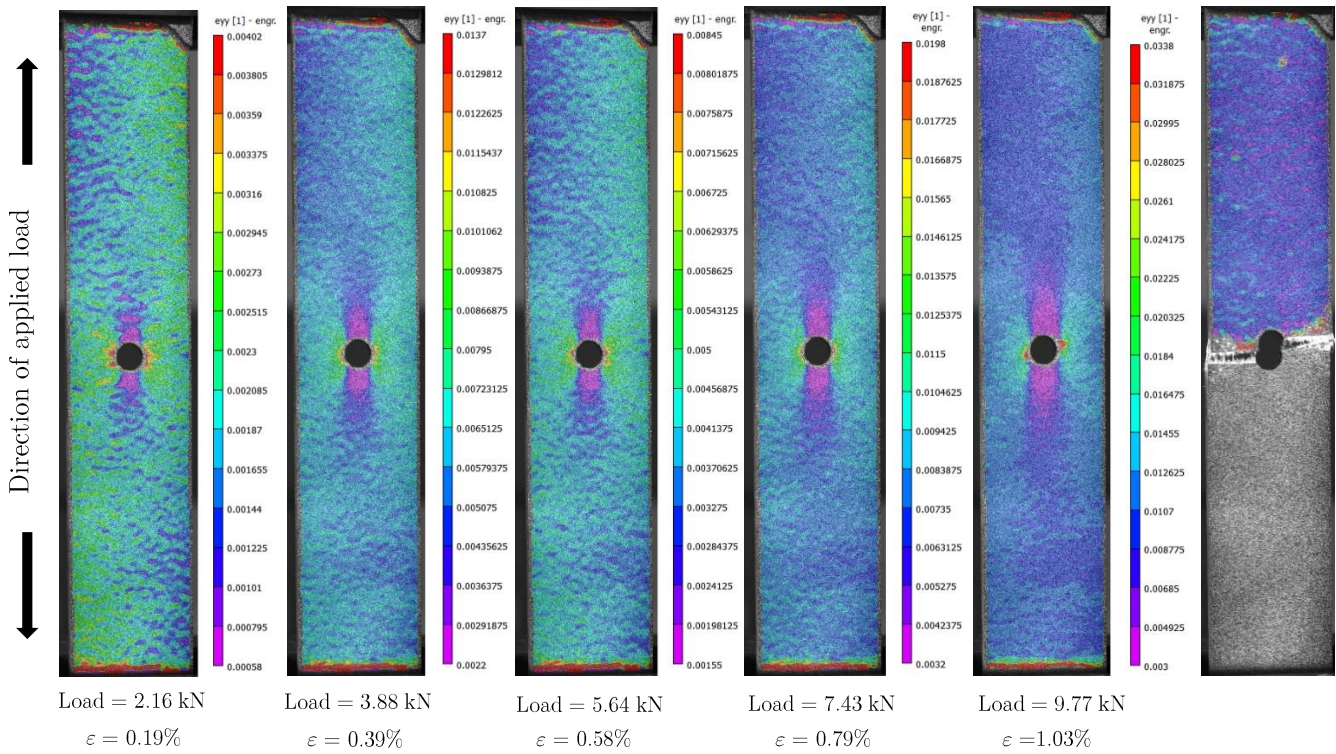


Figure 6.27: DIC resulting images on a 8-harness satin weave 2D composite with a 5mm hole .

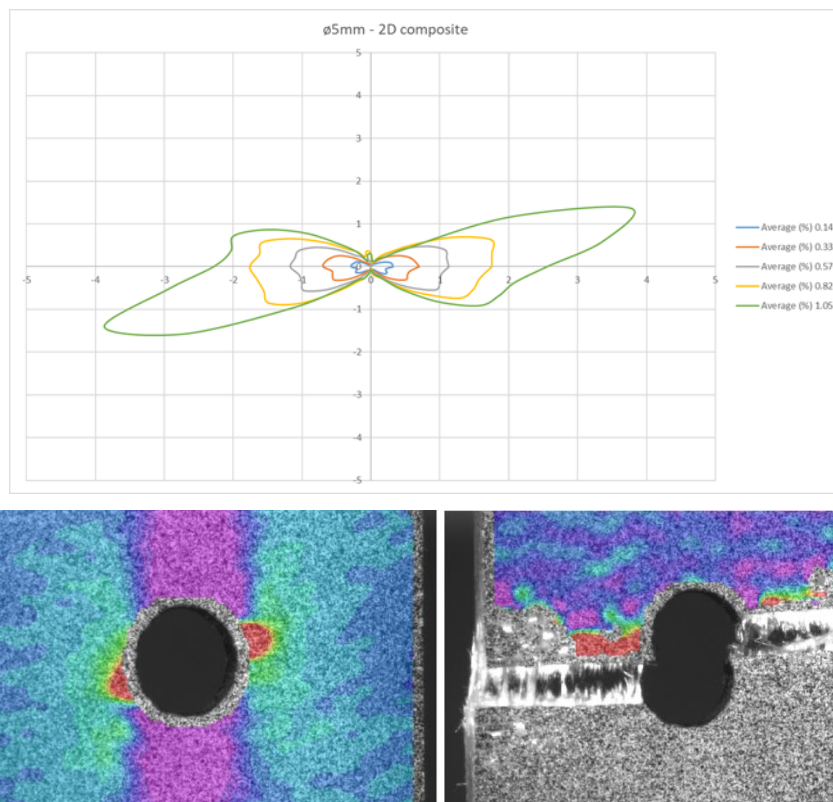


Figure 6.28: Strains around the hole and final failure position investigation on a 8-harness satin weave 2D composite with a 5mm notch.

To verify the results given by the DIC and compare them with a finite element model, an analysis using the commercial software Ansys was performed. In this case, the geometry used is the same as the one used for the real specimen, without considering any degree of symmetry since we are dealing with composites materials, so even if the layup is symmetrical and balanced, it is better to consider the whole specimen. So, a rectangular area of  $25 \times 230 \text{ mm}$  was modelled with a central hole of  $\phi = 5 \text{ mm}$ . The element type used is a *Shell281* (8-node with linear shape function), while the lay-up used is the same as the manufactured 8-harness satin weave, which is  $[0/90/0/90]_s$  symmetric lay-up made of 8 layers, each of them  $0.27 \text{ mm}$  thick. The material properties used are similar as the ones that can be found in the paper by Kyriazoglou and Guild [28]. They are listed in the table below.

*Table 6.11: List of the material properties used in the FE program [28].*

$E_x$ [GPa]	21.5
$E_y$ [GPa]	21.5
$E_z$ [GPa]	8.55
$G_{xy}$ [GPa]	3.7
$G_{xz}$ [GPa]	3.5
$G_{yz}$ [GPa]	3.5
$\nu_{xy}$	0.185
$\nu_{xz}$	0.0305
$\nu_{yz}$	0.075

The area was divided in smaller areas, particularly around the hole, to be meshed with a mapped mesh, as can be seen in the picture below. The final mesh used is here depicted. The load applied is a uniform pressure to the upper lines, this pressure was found dividing the load, recorded by the machine, that was applied at this moment by the specimen width. So, a pressure of  $-67.6 \text{ MPa}$  was applied, while the total load acting on the specimen was  $1648.2 \text{ N}$ . The opposite line at the bottom was constrained blocking all its degrees of freedom. This low level of stresses inside the material was chosen because the composite in this stage should have very low damage, almost absent, so the strain distribution plotted using the FE software, which does not take into account the presence of the damage, should give similar results to the one experimentally found using the DIC.

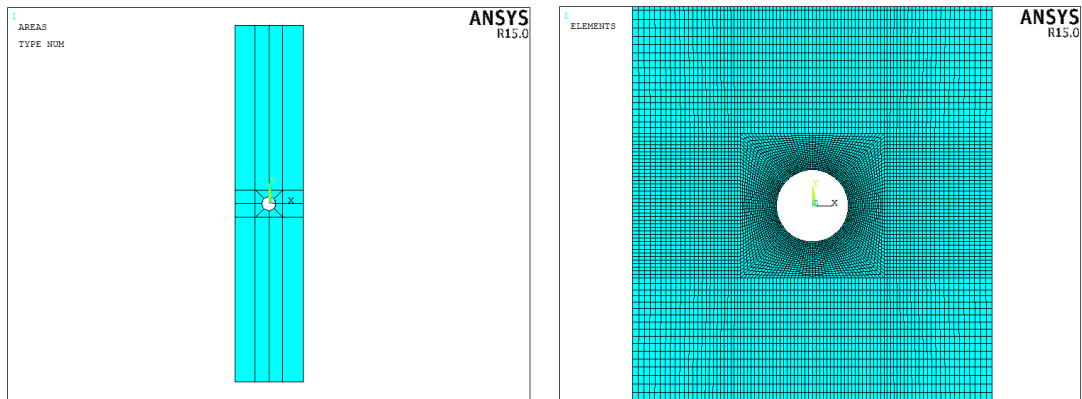


Figure 6.29: On the left it is depicted the areas division utilized, on the right can be seen a detail of the mesh around the hole.

Using the mechanical properties reported above, a similar overall average strain is found, 0.144%, and the strain pattern is very similar between the two results, this is plotted in the next figure. The peak strain is centred at the hole's tip because the laminate presents a symmetric and balanced lay-up, for the same reason there are not out-of-plane displacements caused by the coupling effect of in-plane stress and bending curvature.

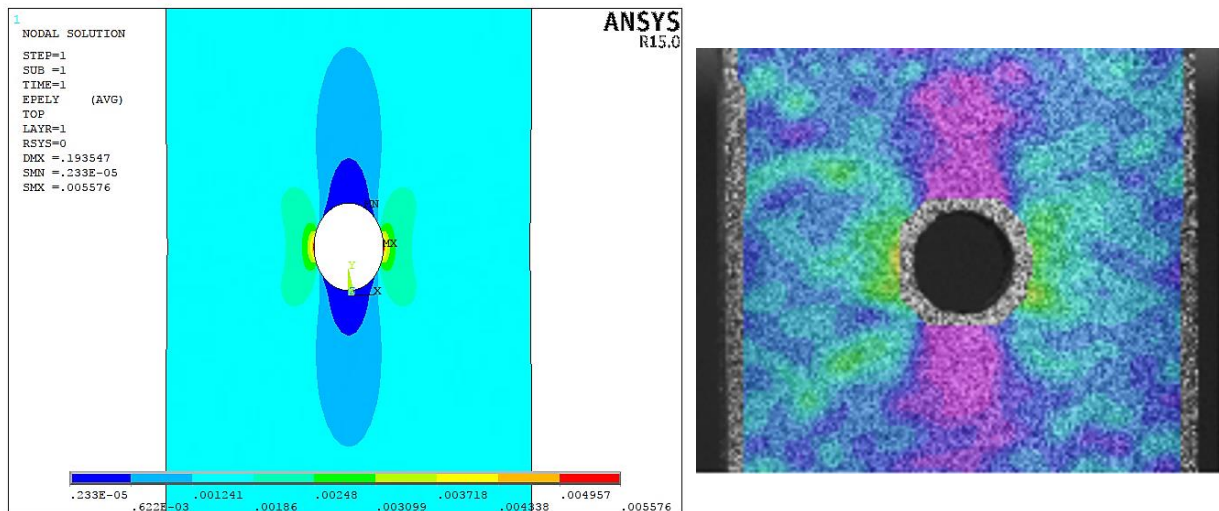
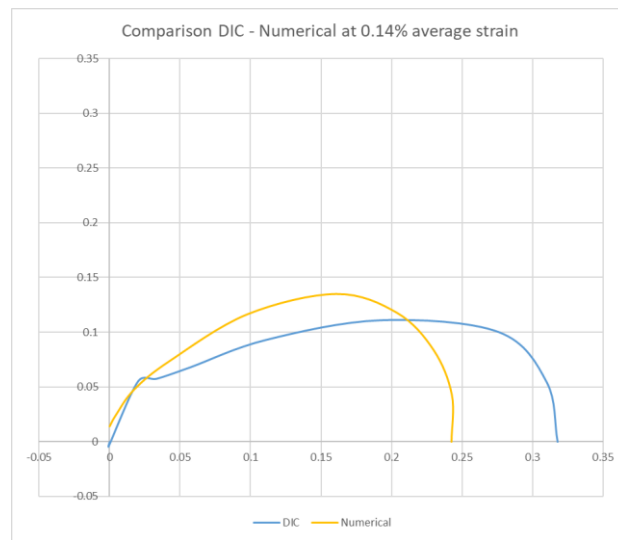


Figure 6.30: Strain pattern comparison for the 2D 8-harness satin weave modeled using a finite element model and analysed using DIC at an average strain level of 0.14%.

Even if the strain distribution is similar, the polar graph reveals that the strains around the hole have slightly different values, this can be seen in Figure 6.31, where are compared the strains in the first quarter, extracting the strain values every  $10^\circ$ , between  $0^\circ$  and  $90^\circ$ . This difference can be partially explained with the not accurate extracting method, since in both cases, with the DIC and with the FE model, it was performed by hand, so some

inaccuracies in the extracting point placing are something to consider. Must be remembered that the DIC values are taken at a distance from the hole, caused because the strains are calculated at the centre of a squared subset window. So, the same was done in FE model, considering the same ratio between extracting point and hole diameter as in the DIC pictures. The main source of discrepancy between the two results can be assumed to be the formation of damage in the real 2D woven composite. As can be found in paper [10], damage is generated at an earlier stage in 2D composites than in 3D composites and considering the strain intensification around the hole, can be said that the level for the damage initiation is already reached. This should explain the different value that is found at  $0^\circ$ , with a higher value for the DIC result probably caused by the effect mentioned before.



*Figure 6.31: Polar plot of the strain in Y direction (direction of loading) measured using DIC and a numerical model in the quarter of graph between  $0^\circ$ - $90^\circ$ .*



## 6.6.2 Aluminium specimen with a 5mm hole

To compare the behaviour of composite materials with the one of a homogenous isotropic material, an aluminium specimen was tested with a 5mm central hole. In Figure 6.32, the outcome of the test is plotted, until plastic deformation around the hole is reached. At an average strain level around 0.2%, the points around the hole have already reached the failure threshold, this is due to the effect of the stress intensification around the hole and only under the strain level of 0.07% the points are in the elastic region. Looking at the strain distribution on the whole specimen, it is visible that the strain pattern is not homogenous far from the hole. This behaviour is caused by the low level of strain that is not easily identify by the software, while at higher strain levels the parts far from the hole are depicted with a homogenous colour. Looking at the strain distribution, the strains are quite symmetrical with a high maximum at the hole edges. Final failure then happens starting from the hole tips and proceeding at 45° in shear, as the plastic surface in a cylindrical sample where the fracture surface is inclined at 45°.

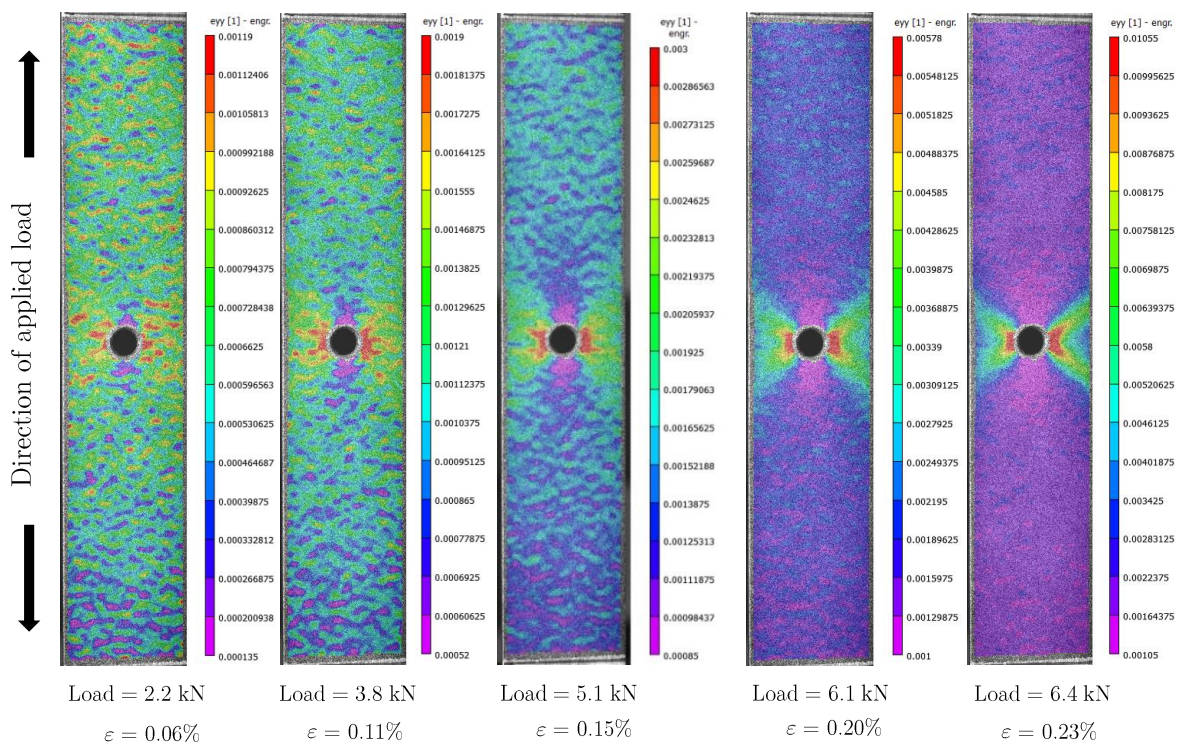
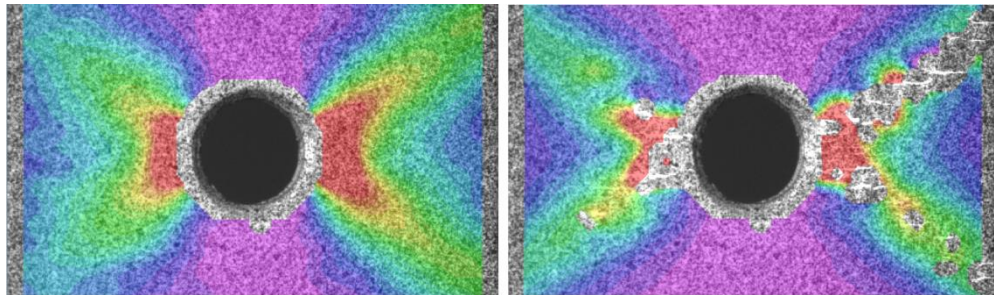
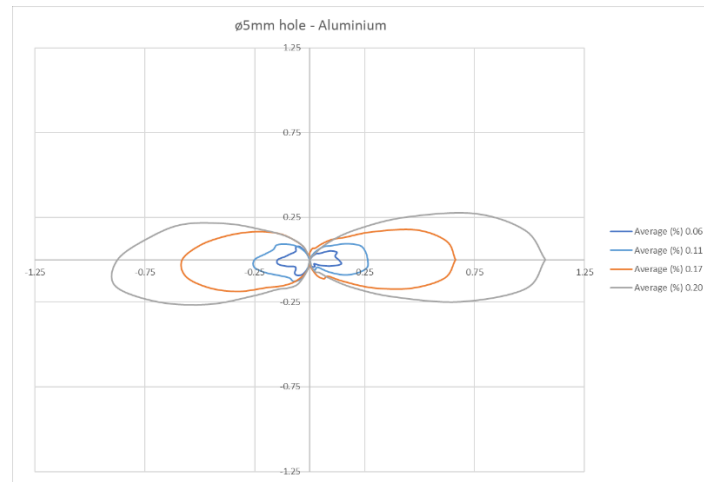


Figure 6.32: Strain distribution in a notched aluminium specimen with a 5mm hole in the elastic region, in the last pictures the specimen has already reached the plasticity around the hole.

## Notch sensitivity investigation



**Figure 6.33:** Strains around the hole and final failure position investigation on a aluminium specimen with a 5mm central notch.

The strain distribution calculated using the DIC on the 5 mm notched aluminium specimen is here compared with the one calculated using the finite element software Ansys. A plain model is here presented, using the element type *Plane182*, choosing the option *plain stress with thickness* and imposing the specimen's thickness, which is 1.94 mm, together with the option *Simple enhanced strain*. The material properties used are here reported:

**Table 6.12:** Material properties implemented in the finite element model for the aluminium specimen.

$E$ [GPa]	70
$\nu$	0.34

The geometry used is the same as the specimen under analysis, but this time only a quarter of the geometry is analysed because symmetry conditions can be used in this case. The geometry used has so the following measures: 65 x 12.5 mm, with a 5 mm notch. The load applied is the stress calculated from the load values stored by the machine and divided by the specimen's area. The model is constrained applying symmetry boundary conditions to the bottom and left lines. To conduct an analysis in the elastic region, the

load that was acting at an average strain level of 0.06 % was applied, that was equal to 45 MPa and was applied on the upper line. The mesh used is reported in the next image:



Figure 6.34: Mesh used during the calculation and areas division.

It was possible to appreciate that the average strain, far from the hole have the same value as the one calculated with the DIC. The strain pattern otherwise is not the same, as can be noted in Figure 6.35. This is probably the consequence of the low strains inside the material, so it is possible that the software graphically plots some values that are not correct.

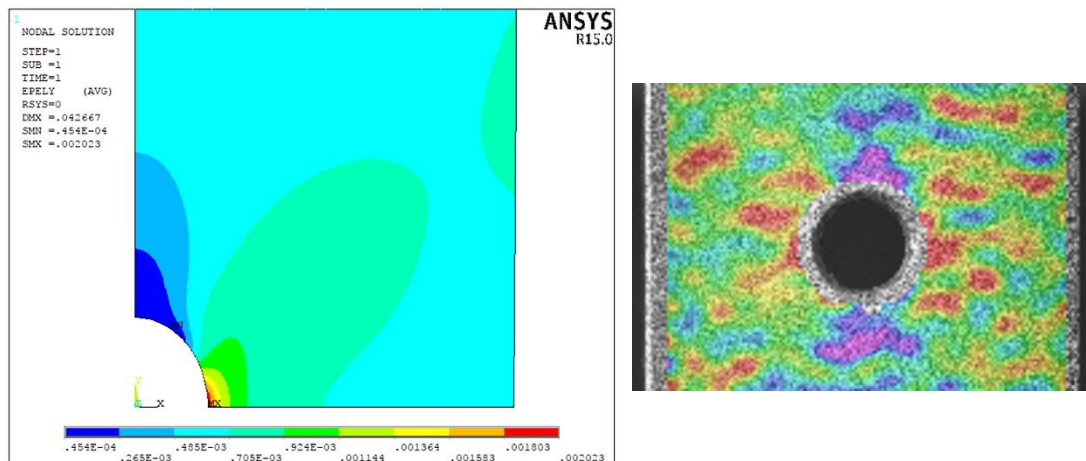
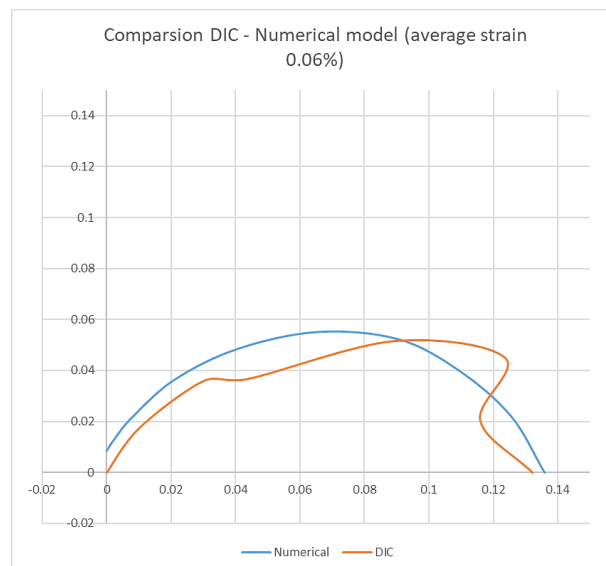


Figure 6.35: Comparison of the strain pattern calculated with the finite element software and with the use of the DIC when the whole specimen is in the elastic region at an average strain level of 0.06%.

On the other hand, must be said that plotting the strains around the hole using a polar graph, it is possible to see that the strain calculated with the two methods are actually very close. To extract the strains from the numerical model, must be remembered that the strain plotted using the DIC are not the ones at the hole edge but at a distance related

to the subset size chosen, this limitation is related to the calculation process used by the DIC software that calculates the strains at the centre of a squared window, so measures at a distance lower than half the window side cannot be performed. Taking the strains every  $10^\circ$  keeping the same offset from the edge as in the DIC, it is possible to compare the two results. Similar values at the holes tip are visible, but a quite odd distribution is present for the DIC results. This can be caused by the DIC results or by the extraction points. Must be remembered that in both the cases, numerical and DIC, the points from where to take the results have been manually placed, so errors are caused by this procedure, which is inherently not very accurate. In any case, can be said that considering an aluminium specimen, damage is not formed until plasticity is reached, so differently from composite materials the results given by the FE model and by the DIC are almost overlapping. Through this investigation, was verified that the DIC provides reliable results both for punctual and average measures, as was verified using the strain gauges.



*Figure 6.36: Polar plot of the strain in Y direction (direction of loading) measured using DIC and a numerical model in the quarter of graph between  $0^\circ$ - $90^\circ$ .*

## 6.7 Concluding remarks

In this chapter, the notch sensitivity curves for 3D woven composites manufactured with the VARTM technique and the wet lay-up are presented. The result is a significant notch insensitivity behaviour, very close to the line of the notch insensitivity. Was also found that there is not a clear effect related to the manufacturing technique, even if the number of samples broken is not sufficient to derive a statistical analysis. The results of these

tests, made starting from a 3D-96 fabric, were also compared with the results obtained testing a thinner 3D-78 fabric. The results are overlapping, letting us know that a thickness effect is not clearly evident. Comparing the notch sensitivity behaviour of a 3D composite with the one of a 2D woven, using a normalized graph of notched strength to failure for different hole sizes, was found that 2D composites have lower notch insensitivity than 3D composites. The data are disposed on a line parallel to the notch insensitivity one but with lower strength to failure values than for 3D woven composites. This is an interesting result because the 2D laminate under analysis presents a matrix dominated behaviour, while the 3D non-crimp woven composite it is supposed to be more fibre dominated than the previous one. So, the composite architecture represents the factor that differentiates the two results, giving a more matrix dominated behaviour probably caused by the presence of the resin channels and pockets between the yarns. The presence of these resin rich regions causes the development of matrix cracks inside them, but at a higher strain level compared to 2D composites, as shown by Lomov et al. [10]. It is also possible to see that 2D composites have a significant lower strain to failure compared with 3D ones, probably because of the presence of extensive delamination, which is not present in 3D composites because of the z-binders. In 3D composites are more relevant matrix cracks between the yarns instead of cracks inside them, which are more frequent in 2D ones, and micro-delamination at yarns-matrix interfaces.

Different tests until failure were analysed using the DIC technique, was found that the DIC is capable to observe the formation of transverse matrix cracks in the 3D composite and the formation of final failure in plain specimens. Looking at the damage formation around the hole, with the DIC it is noticeable how the strains around the hole are influenced by the fabric architecture, in fact was seen as high strains are formed inside the resin gaps between the weft tows and high strains are redistributed starting from the hole to other regions near the hole thanks to the resin channels. Final failure surface always happens from the resin gaps, even if strain intensification happens also over a weft tow. Comparing the strain distribution around the hole in a 3D woven composite and in a 2D, it is visible how the strains in the first case have a different behaviour for every same due to the effect mentioned before, while in a 2D composite the strains are symmetrical and with maximum strains at the hole edge. The same symmetrical and repetitive behaviour can be seen testing an aluminium sample with a 5mm hole. In this case, the strains are localized in particular around the edges, while in 3D composite materials the strains are

more distributed. From this analysis is still not possible to confirm if failure in 3D composites happens where the maximum strains are localised around the hole, in any case must be reminded that there is also the effect of the resin channels that affect this measure. Using the DIC is possible to have an idea of where the final failure will happen, even if it is not possible to know the exact position, whereas in 2D composites and in metals it is always possible to know the failure position because high strains are located just at the hole edges.

Comparing the DIC results with some Finite Element models for the 2D woven composite and the aluminium specimen, it was proven that the DIC gives reliable results also for punctual measurements together with full-field measurements. So, it can be said that the DIC is a reliable method to calculate the strains and the stresses, giving the advantage to consider what really happens inside the material, so accounting also the defects or the damage development that is not easily modelled with an FE software.

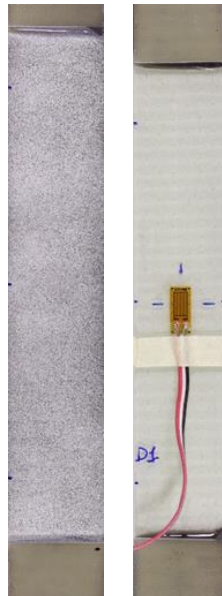


# Chapter 7

## Damage evolution investigation

### 7.1 Introduction

Two plain specimens were tested stopping the test before failure at two significant thresholds for the damage, both the two with the use of DIC to correlate these results with the internal damage, using microscopy images. One specimen was stopped at 0.7% strain, where there is the formation of transverse cracks in the resin rich regions between the weft tows. another one was stopped before failure at 2.0% strain, this to be sure not to incur in failure, which happens between 2.4-2.7%. A longitudinal strain gauge was put on one face while on the other the full-field strains were recorded. This to have a live track about the average strain inside the material to stop the test when a precise strain level is reached, this can be done with the strain gauges but not with the DIC because it is necessary a second step of post-processing.



*Figure 7.1: In this picture, are visible both the faces of the plain specimens tested for the damage investigation, the presence of the strain gauge is to monitor the average strain during the test to trigger the stop.*



Other two tests were done on notched specimens with a 5mm hole to compare the damage that occurs near strain intensification with the results provided by the DIC and with the damage development in a plain specimen. To have a slower machine displacement, in order to make easier to stop the machine at the right moment, the machine displacement was set this time to be 0.5mm/s. The DIC sampling rate was set also this time to be 1 pic/6 s, so this time we will have one picture from the DIC every 0.05mm instead every 0.1mm like the previous cases.

## 7.2 Damage investigation at 0.7% strain in a plain specimen

As was said previously, the composite undergoes to what it seems to be the formation of matrix cracks inside the resin gaps between the weft tows at a strain level around 0.7%. To prove that the red line visible in the DIC images at this strain level actually represents a matrix crack, a test was topped at this strain level and some microscopic images have been taken to see where the damage is formed. In this type of materials, it is important to be aware and identify the presence of cracks because when they start to develop, they reduce the mechanical properties of the composite, which means that the Young's modulus of the composite will start to go down and this is something that in certain applications must be avoided. Moreover, the presence of this type of damage leads to the formation of other damages, for example micro-delamination, extensive delamination and fiber fracture, so can be said the matrix cracks are the direct precursors of matrix/fibers local debonding. This is generated by the stress concentration at the crack tip that can also lead to fibers fracture. As can be seen in Figure 7.3, the test was stopped when the strain gauge positioned on the other surface of the specimen pointed out a strain equal to 0.7%, while in the other surface DIC images were taken. The sample surface was divided in two areas to make easier the following cutting. In Figure 7.2 (b) it is possible to see sudden formation of a matrix crack, it is visible that the crack formation is very fast and it spreads along all the specimen's width. In the first image in (b), the pattern is repetitive, while in the second one there is the formation of a region of high strains with a clearer distribution of low strains adjacent to it. As can be seen in Figure 7.3, the test was stopped at the point where a high acoustic emission was pointed out in the work by Lomov et al. [5]. In the graph are visible three different thresholds, the first one, referred as  $\epsilon_{min}$ , corresponds to the point when some damaging events start to occur, while  $\epsilon_1$  represents the point where

a significant quantity of events occur.  $\epsilon_2$  is the proper threshold where matrix cracks happened very fast and when they spread along the whole width, causing also local debonding. The strain levels when this cracking occurs is higher than the ones present in 2D composites, due to the fact that in this material the level of crimping is much lower than in 2D woven. The specimen was cut in the longitudinal direction and the internal surface was analysed using an optical microscope. The results of this study are exposed in the following part.

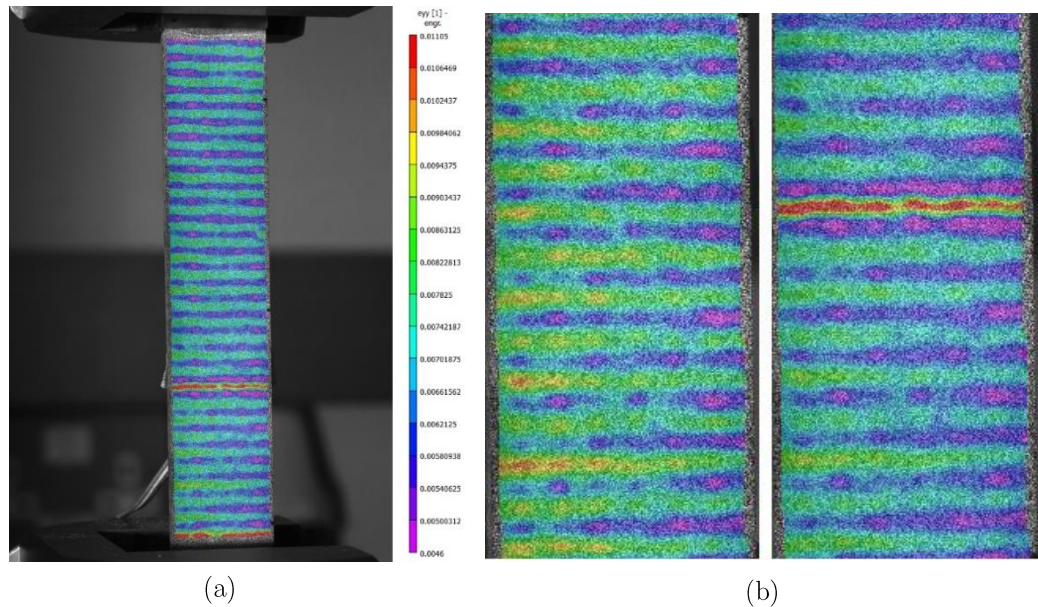


Figure 7.2: Red line formation on a DIC image (a), representing the sudden formation of a matrix cracks as it can be seen in, where two consecutive DIC images, taken at 0.05mm distance, are shown (b).

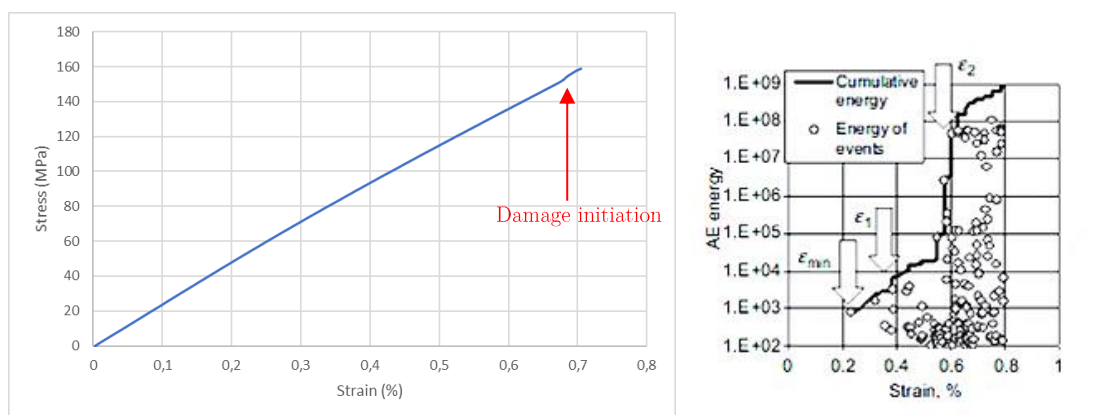
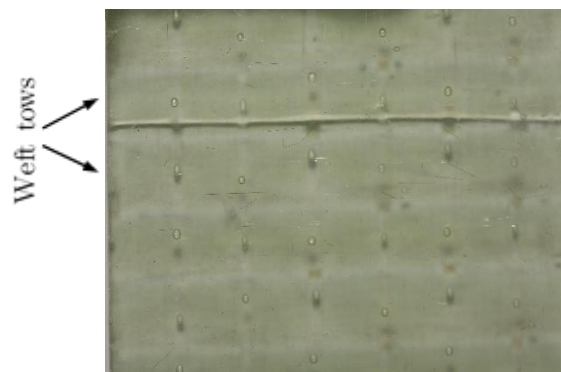


Figure 7.3: Stress-strain curve for this test, it is possible to notice the point where the test was stopped, which is the point  $\epsilon_2$  in the right image, taken from [5], representing the damage acoustic emission measurement on a 3D specimen.

As it can be seen from the pictures in Figure 7.5, cracks forms only in the resin gaps between the weft tows, these can also propagate inside the composite, starting from the surface, changing plane and passing by the warp tows. This can be seen in the figure (a), where the same crack is visible at the surface and then cracking a weft tow in the inner part of the composite. In figure (b) otherwise, it is possible to see just a crack in the matrix that does not extend in the weft tow underneath. The crack in the second image is the one spotted by the DIC, while the other one is a crack formed in the other surface of the composite and so it was not spotted by the DIC. Was so proved that the red lines that are seen in the DIC are really matrix cracks opened to the outside. In [10] was said that these cracks start from the z-crowns and in the initial stage they remain located near these spots, they are not captured by the DIC. These cracks then increase they length to the whole width and reaching also the weft yarns underneath, new cracks also appear in this phase, which is the one analysed at 0.7% strain. Keeping this in mind, it is possible to say that probably the crack in figure (a) formed before and then develop while the second one in figure (b) developed at the strain level under analysis, as it is visible from the DIC images in Figure 7.2.

In the next picture, it is possible to see a matrix cracks formed in a resin gap between two weft tows as it is visible to the naked eye when a test is stopped at 0.7% strain. Can be added that this crack extends for the full specimen width at this strain. This crack is the same that can be seen in the DIC image.



*Figure 7.4: Photography of a transverse matrix crack at 0.7% strain.*

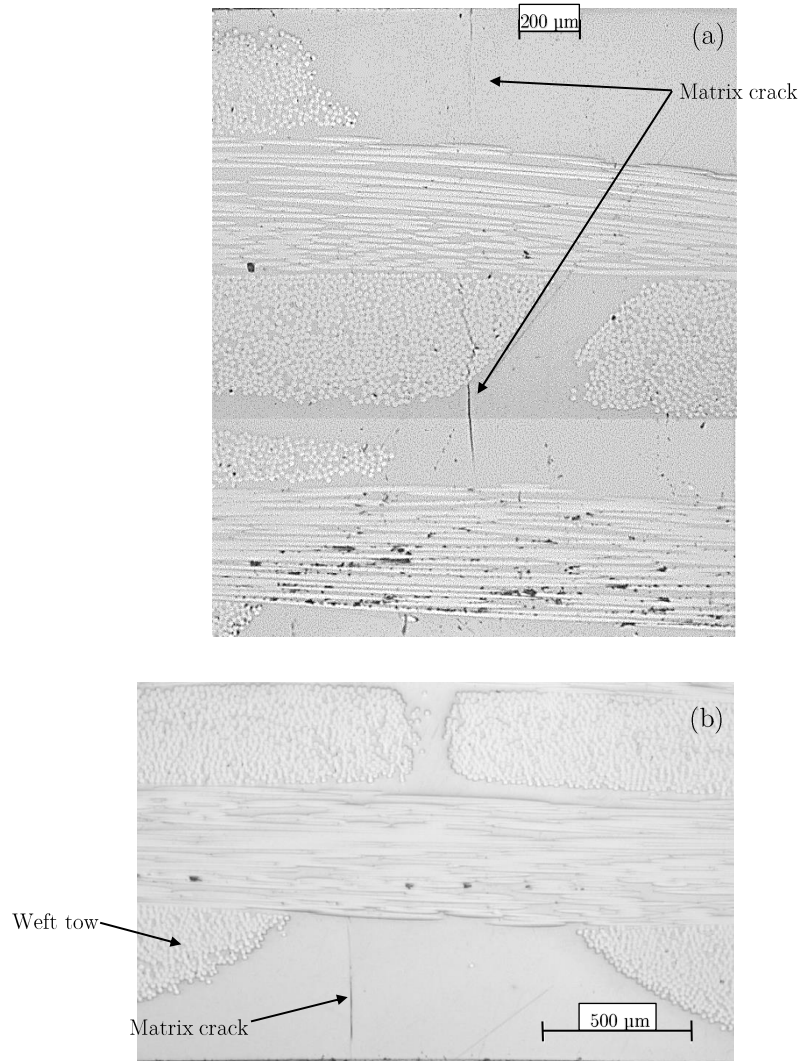
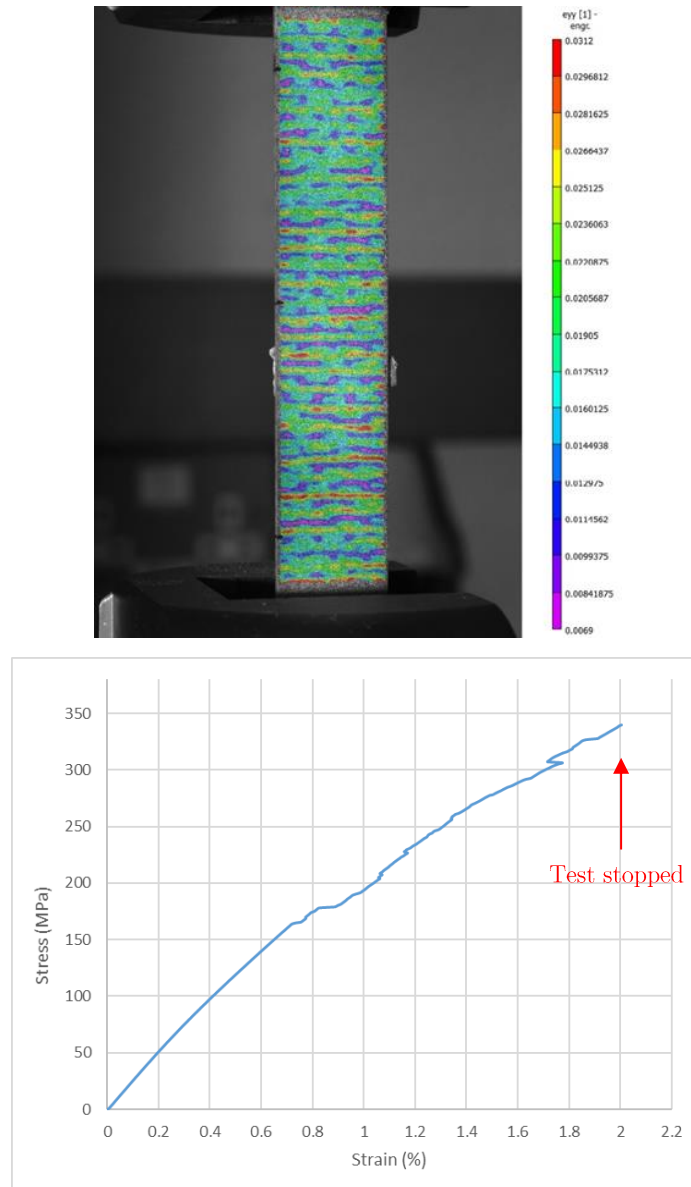


Figure 7.5: Matrix cracks inside the resin gaps between weft tows, images taken at 0.7% strain.

### 7.3 Damage investigation before failure in a plain specimen

A test like the one described before was stopped before failure, at 2.0% strain and 22kN of load, as can be seen in the stress-strain in Figure 7.6. This test was done to characterize the damage development inside the composite until failure and to understand if there is a relation between DIC images and damage inside the composite. Looking at the DIC image it is not possible to see a clear damage pattern, on the contrary it is possible to appreciate the presence of z-crowns with low strains, as described in §5, and an extensive damage along all the composite surface. Different samples were analysed using the optical and scanning electron microscope, taking them from the lower half of the specimen, indicated by the black marks on the specimen's left edge, as can be appreciated from the DIC

image. Some interesting conclusions about damage development have been obtained from the microscopies, which will help to understand the damage development around the hole and its relationship with the DIC. On the other hand, it was not possible to relate the microscopies to some characteristic damage during this phase, the conclusion was then that, the DIC is able just to grasp the extensive formation of matrix cracks on the composite surface.



*Figure 7.6: DIC image of the composite at 2.0% average strain level and stress-strain plot of the interrupted test under analysis.*

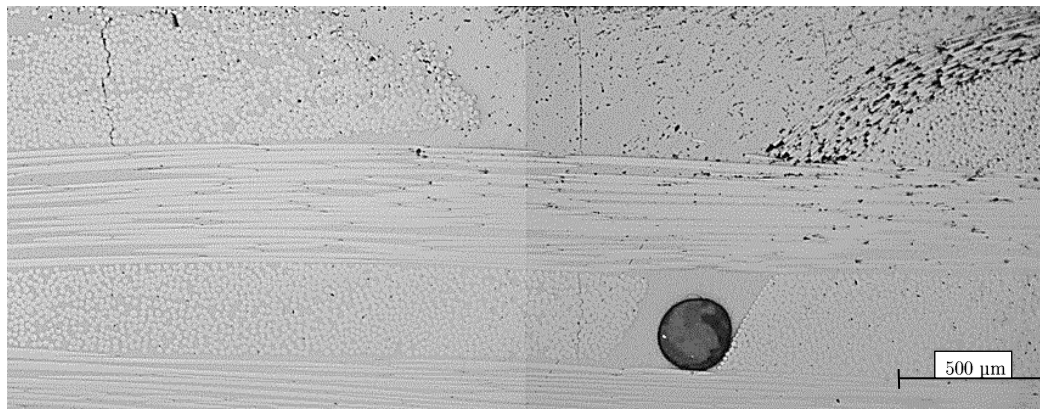
In the next image, it possible to appreciate the great crack density at this stage of the test, where all the specimen surface is saturated with transverse cracks in the resin channels and inside the weft tows starting from the z-crowns.



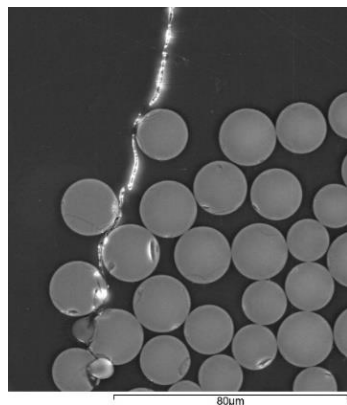
*Figure 7.7: Photography of the damage that is visible in a specimen tested before failure*

In the next images, it is possible to see that, in this stage of the test, matrix cracks start from the resin reach regions, they extend also to the weft tows underneath and are present together with cracks inside the superficial weft tows, visible in Figure 7.8 (a). These cracks inside the weft tows passes near the fibers, deviating and creating debonding between fibers and matrix, as can be seen in (b). These are created by the mismatch in the longitudinal modulus between fibers and resin when the load is applied along  $0^\circ$  plies, creating a stress concentration which is again explained by the Strain Magnification theory. One of the preferential spots for damage formation is inside the weft tows under the z-crowns, in this regions cracks forms due to the compressive-shear action of the z-binders during tensile loading, an example of this can be seen in (c). All these kinds of damage are contemporarily present at the same time along the specimen. In the following part, the interaction between matrix cracks, z-crowns and warp tows will be analysed.

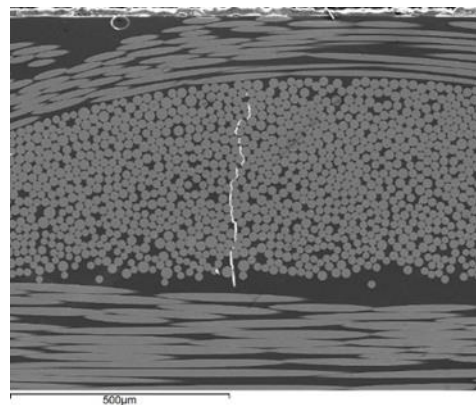




(a)



(b)



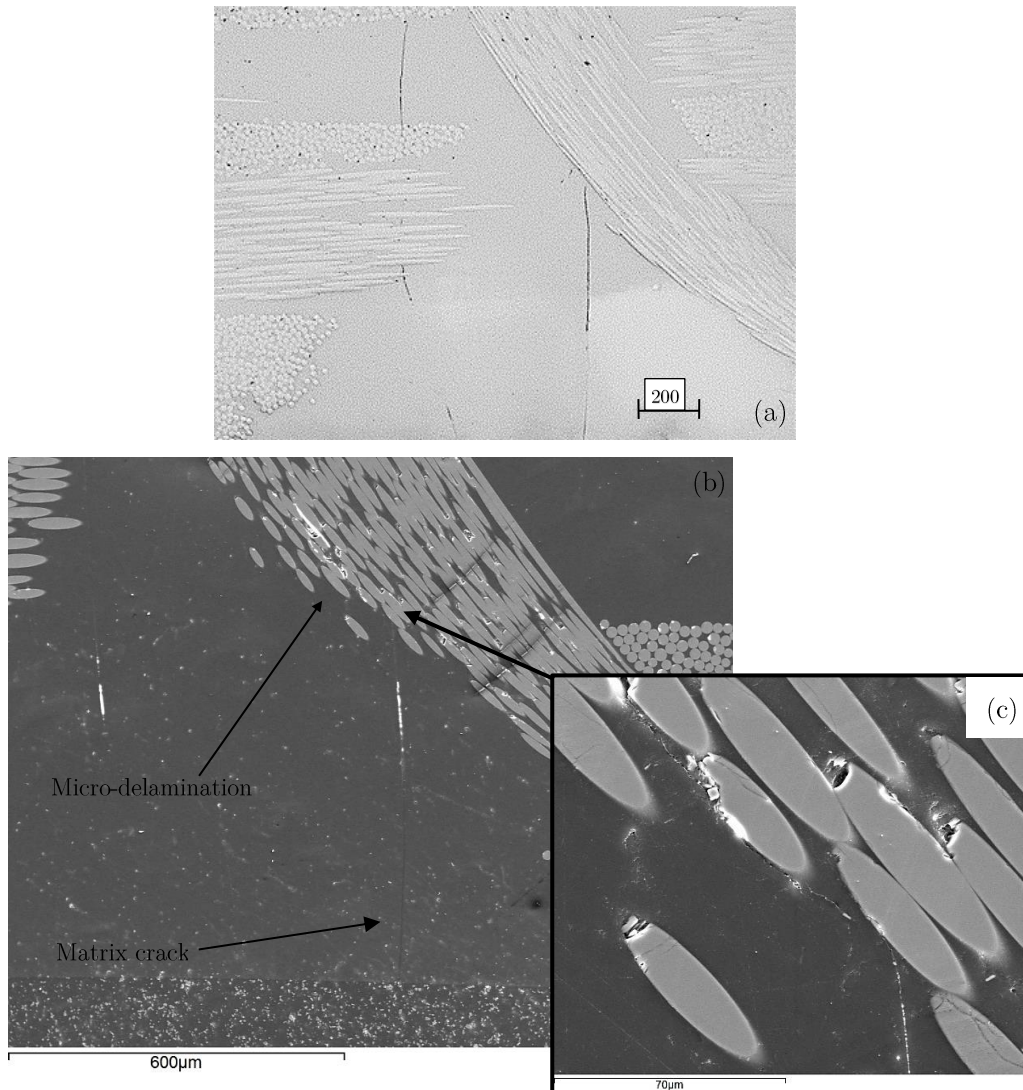
(c)

*Figure 7.8: (a) Optical microscopy showing a crack inside a weft tow, (b) SEM microscopy depicting a matrix crack that provokes a local-debonding between fibres and the resin and SEM microscopy showing again a crack starting from a z-crown (c).*

In Figure 7.9 are depicted different pictures of the same area, in the optical microscopy it is easy to see the formation of a matrix crack from the surface that arrives in proximity of a z-binder, in the next SEM image is possible to appreciate that the crack turns near the binder and initiate a delamination between these fibers and the matrix. This is due to the shear stress that arises from the interaction between transverse cracks and z-binders, [33]. This is visible more in detail in the higher magnification image. This behaviour is caused by the fact that the crack cannot pass the fibers directed orthogonally with respect to the crack and so the latter must deviate creating a local delamination. In the last, image it is also possible to see that the stress concentration at the crack edge brings the fibres to failure. Moreover, it is visible a fibers displacement in shear that causes the fibers to move one over the other, generating damage. Looking again at the first image, can be appreciate the fact that matrix crack can pass through the weft tows, while they cannot pass through the warp tows and z-binders. To surpass these fibers, a crack can pass them

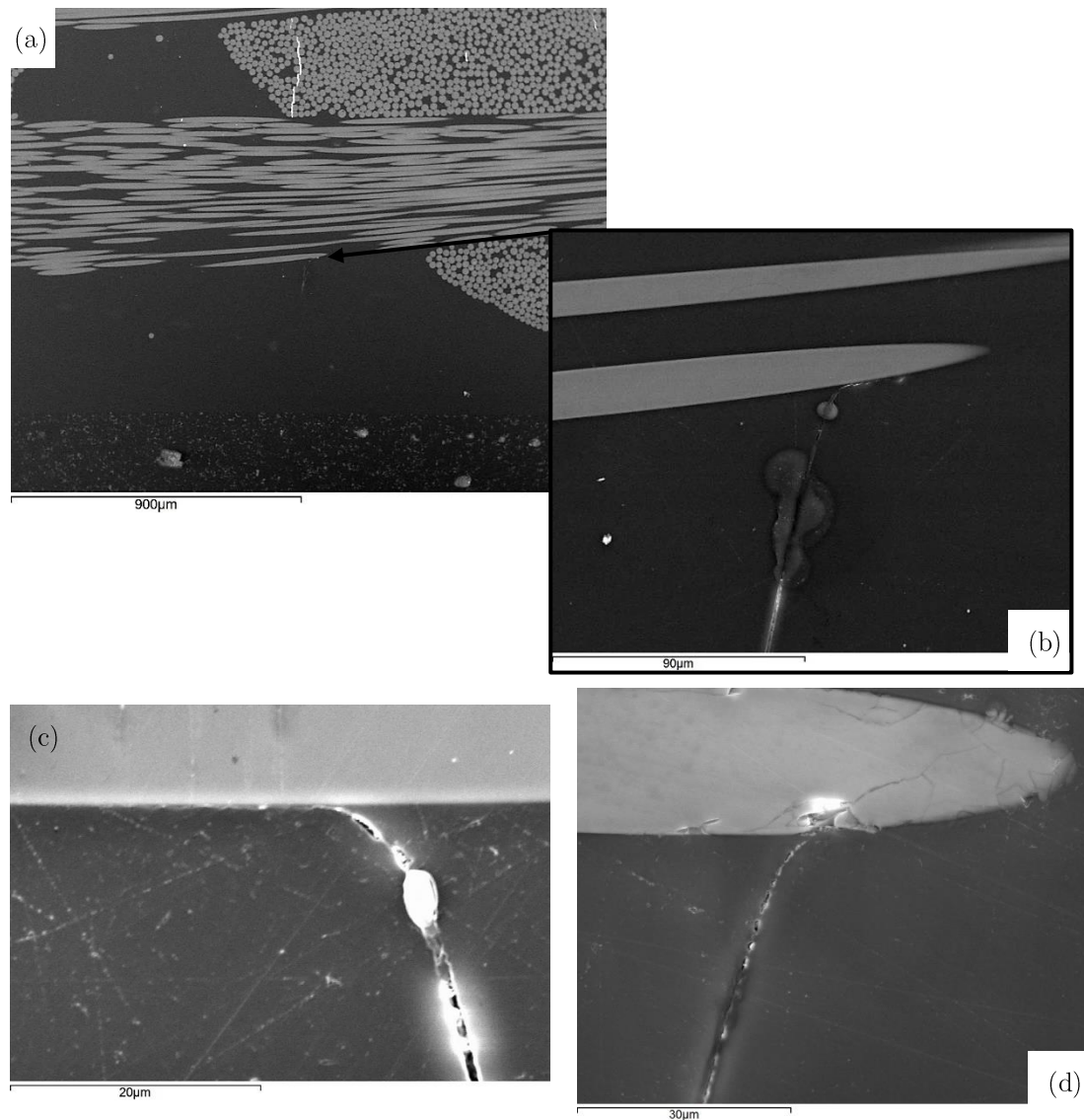


by changing plane or generate a stress intensification such that the fibers would break, as in the last stages of a static test.



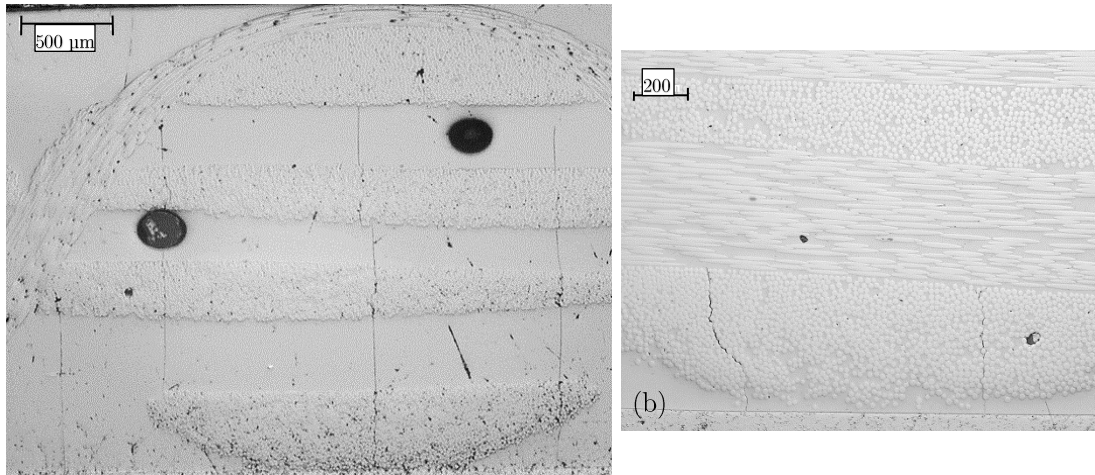
*Figure 7.9: (a) optical microscopy showing cracks in a resin gap between weft tows, (b) SEM microscopy of the same area and (c) SEM microscopy where is visible a detail of (b).*

A matrix crack can also generate a delamination in the warp tows, as was described before for the z-binder. In this case, when a matrix crack comes near a warp tow, it generates a local delamination of the loaded fibers, as can be appreciate in the next two images with a higher magnification. Even in this case can be see that the same crack can go on through the weft tow fibers, while it is blocked by a warp tow.



*Figure 7.10: (a) SEM microscopy showing a transverse resin crack approaching a warp tow, (b) a detail of (a) of the local debonding induced, (c) SEM microscopy of a debond between warp fiber and resin caused by a transverse crack and (d) SEM microscopy depicting the principle of fiber failure.*

In the next picture (Figure 7.11), it is possible to notice an interesting fact, cracks develop in the resin pockets between the weft tows but also starting near the z-crowns. From these locations, they spread inside the composite, passing through the inner weft tows and deviating from the warp tows to the adjacent resin channels. At the end of a quasi-static test, it is then possible to see a dense cracks distribution all over the specimen, not confined to on region preferentially. This behaviour will be seen also for the crack development around a hole and it will permit to derive some conclusions from the comparison with the DIC results.



*Figure 7.11: Matrix cracks inside a weft to (a) and another example of it a more enlarged pic (b). Cracks are present not only in the resin gap but also inside a weft tow, as here depicted.*

Concluding, the types of damage that is possible to see in a quasi-static tensile test are similar to the ones visible in a fatigue test, as shown in Novello's (2014) and Baiocchi's (2013) works. These types of damage are: matrix cracks generating from the resin gaps surface or near the z-crowns, micro-delaminations when a matrix cracks approach a z-binder or in a single weft tow fiber when a matrix crack proceed inside a weft tow, fiber fracture in the warp tow edges caused by the resin cracks mentioned before. Interestingly, the position of fiber fracture is the same for fatigue and quasi-static tests and this will be discussed in the following parts of this chapter. A difference between the damage that occurs in fatigue tests and the one visible in quasi-static tests, is that in the first one there is the presence of extensive delaminations, for example at the interface between warp and weft tows generated by a matrix crack. These delaminations are probably caused by the characteristic of the test, which corresponds to repetitive loads, which can open these damages that are not present in a quasi-static test.

## 7.4 Damage investigation around a 5mm hole before failure

In this paragraph, the results from a damage investigation around a 5mm hole will be discussed. Two specimens are analysed, stopping the test when an extensive damage around the hole is visible, so approximately before final failure. DIC images are recorded on one side while the other is kept clean. After the test, samples are cut from the areas near the hole, as shown in Figure 7.12, to analyse the damage formation near the hole



and compare the microscopies with the DIC results in order to better understand the notch insensitivity behaviour of 3D composites.

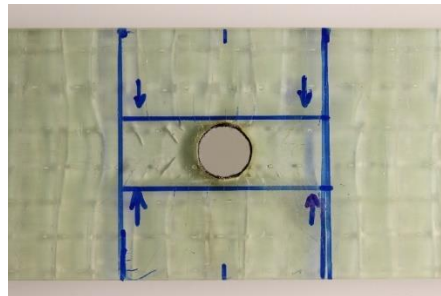


Figure 7.12: Cutting lines showing the width of the specimen for the microscopy, the arrows indicate the direction of observation.

### 7.4.1 Specimen 1

This test was stopped at 14.84 kN, which corresponds to 227.6 MPa in this specimen. The next image shows the DIC results before that the test was stopped. It is visible that major cracks are formed inside the resin gaps, which are highlighted by the high strain strips. Other cracks start around the whole hole, in the areas with higher stress and strain concentration.

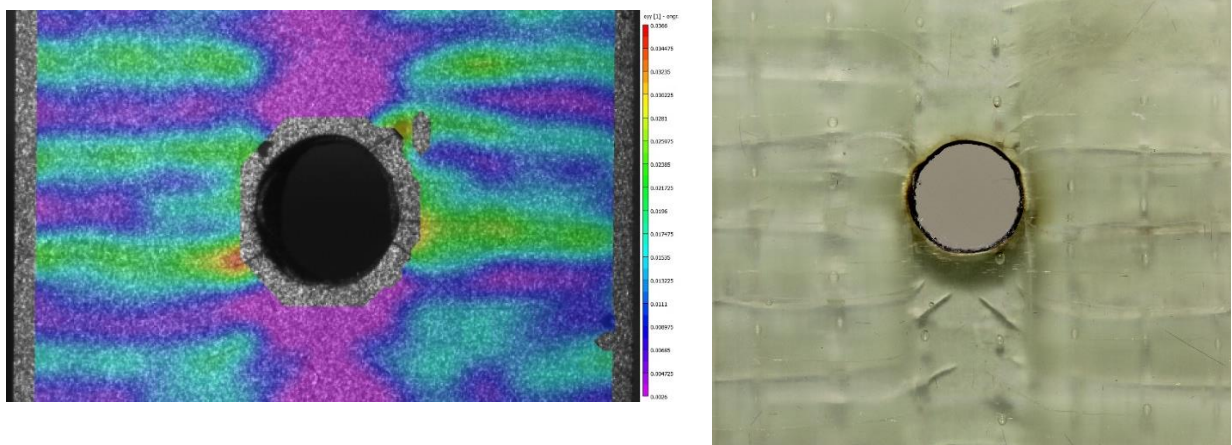
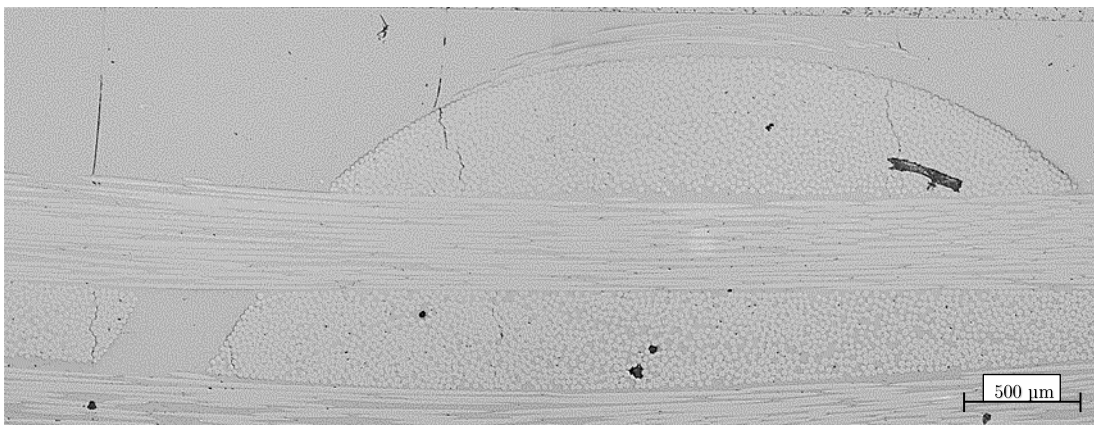


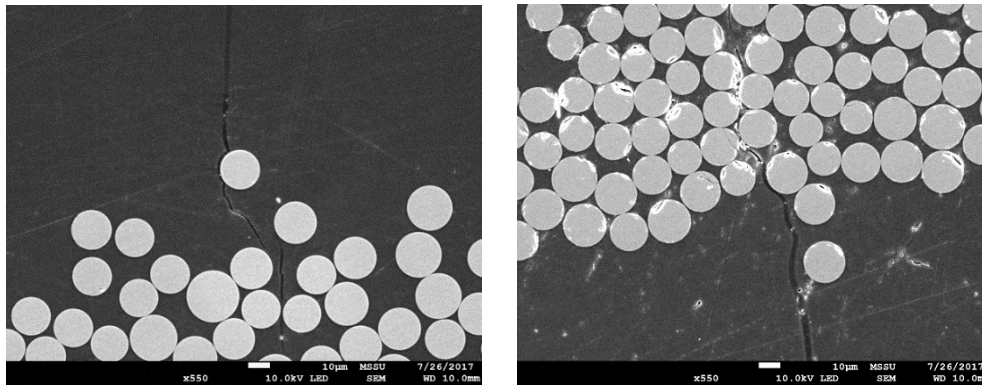
Figure 7.13: DIC results before failure obtained from the test on Specimen 1 (left) and specimen photography after the test (right).

As was said in the previous paragraph for the damage development before failure, cracks do not only start from the resin gaps between the weft tows but they originate also near the z-crowns, so it is possible to see an extensive presence of cracks near the hole before failure. The next image, taken from the same specimen seen in the DIC image before,

shows the crack formation on the whole specimen width, even for a notched specimen. So, in a notched specimen it is possible to see the same crack pattern as in a plain specimen before failure. Cracks are then not only confined in the resin gaps, so the presence of the high strains lines present in the DIC image is probably caused by a coupled effect of low modulus and crack formation in the resin gaps. It seems the not completely possible to relate the presence of cracks with the high strain lines, even if it gives a rough information, as it is visible. Looking at the SEM images in Figure 7.15, it is possible to have a better look of a crack progression inside a weft tow. A crack, passing through the fibers, can generate a micro-debonding from the matrix passing around one of them.



*Figure 7.14: Optical microscopy of a notched specimen before failure.*

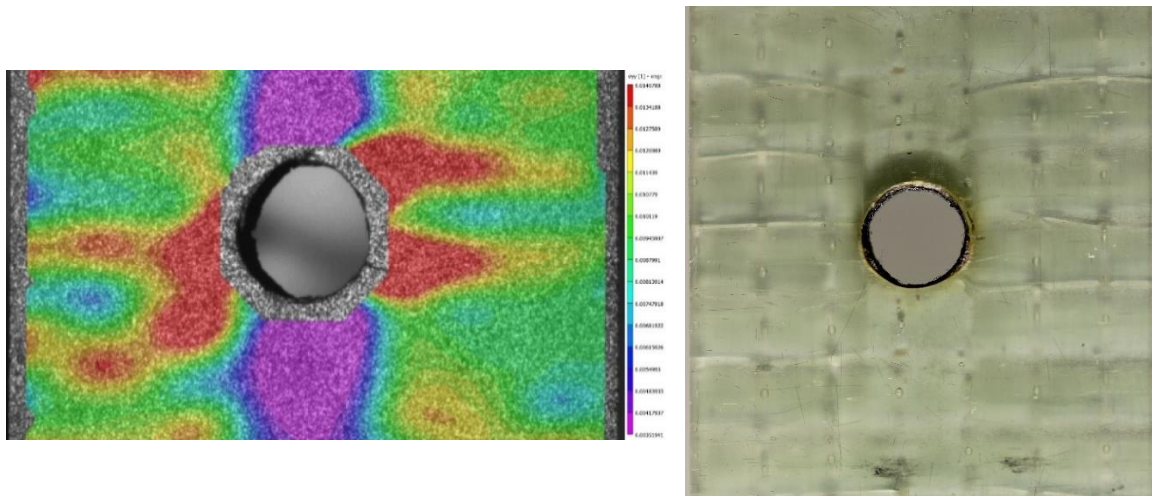


*Figure 7.15: SEM microscopies of a notched specimen, can be seen the crack progression inside a weft tow causing local debonding.*

## 7.4.2 Specimen 2

This second test was conducted as the first one, stopping the test when an extensive damage was visible around the hole, confirmed by the acoustic emission. The test was then stopped at 12.17kN and 187.8 MPa, in this case. Also in this case it is easy to see

that high strains are spotted in the resin pockets between weft tows, where well visible cracks are also present. Looking at the microscopies, it is possible to see, as in the previous specimen, that cracks generates not only in the matrix gaps but also inside the weft tows starting from the z-crowns. So, the same considerations done for specimen one can be made in this case, concerning the coupling effect of resin low modulus and crack formation that generates the high strain strips in the resin channels. In this specimen was possible to appreciate the formation of fibre cracks, which was not visible in all the previous specimens. This is just a matter of luck in finding the right plane where to take the microscopies.



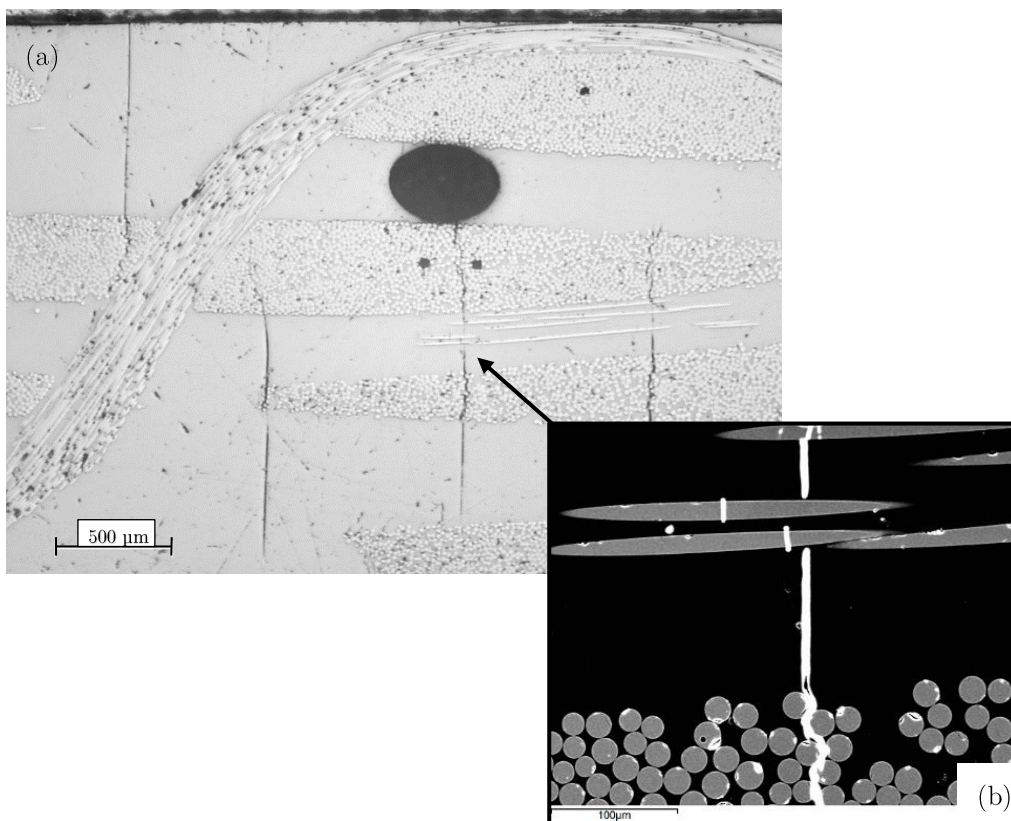
*Figure 7.16: DIC results before failure obtained from the test on Specimen 2 (left) and photography of the test stopped before failure (right).*

Looking at the next image, can be seen that fibre cracks generate inside the weft tows and not between them. Warp tows fiber cracks develop at their edges, due to the stress concentration generated where a crack has to turn in order to pass the warp tows. In this case, we are looking at a warp tow edge because only a few fibres are visible, so this is the beginning or the end of a tow. This behaviour is visible in both the next figures, especially in the second one, a crack, starting from the bottom, goes through the first weft tow, while it is not visible at the centre of the next warp tow, passing again through a weft tow, then it generates fiber failure at the edge of a warp tow, proceeding again after this. As was stated in [35], warp fibre failure is caused by a matrix crack that arise from a z-crow, close the position of maximum thickness of the weft tow. As was mentioned before, they are produced by the combined action of a matrix crack that is present in the resin channel between contiguous warp tows and the matrix crack passing through the weft tow. The stress intensification at the warp tow edge causes the fibres breakage.



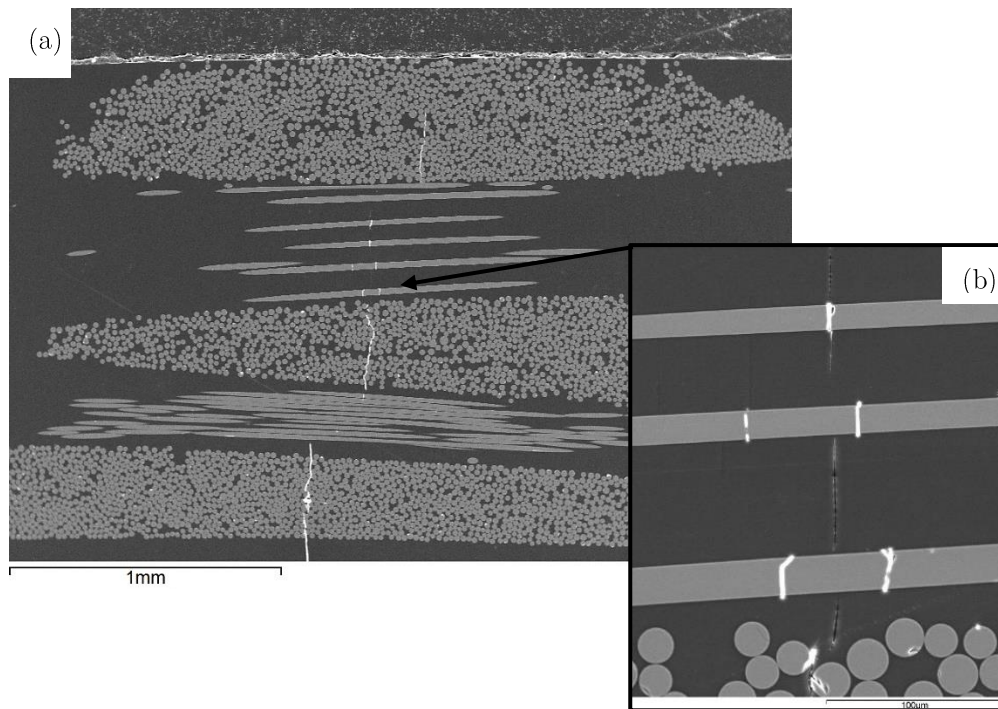
Fiber cracks do not proceed in a straight line with the matrix crack but they can happen in a slightly shifted position, this can be noted in particular in the second image (Figure 7.17), this can make us think to a failure in bending of the fibers.

The fiber failure position inside a weft tow is different from the position of maximum strains spotted by the DIC, even in the late stages right before failure. If this assumption is confirmed, which seems so considering that this result is visible also in other works, can be said that the DIC is not able to spot the precise location of the final failure, since the position of high strains is positioned in the resin channels while fibers failure happens inside the weft tows. On the other hand, must be said that the regions where final failure happens are usually close to the ones highlighted by high strains, so a relation between final failure and DIC results can be seen even if it does not provide punctual information about final failure position, but about the area where it will happen.



*Figure 7.17: Matrix cracks inside a weft tow seen in an optical microscopy (a) and a detail of warp fibers cracks in a SEM microscopy starting fiber failure in a warp tow (b).*





*Figure 7.18: Detail of a transverse crack passing through weft tows and causing fibre failure (a) and in SEM microscopy of the failure (b).*

## 7.5 Concluding remarks

In the first part of this chapter, was proven that the DIC can spot the formation of transverse matrix cracks at the strain level of 0.7%, these cracks represent the prelude for the formation of other type of damage, such as micro-delaminations, cracks inside the weft tows and at the end final failure. This precise level for crack formation was also described in other works as a threshold with the first formation of consistent acoustic emissions. So, if it is required to avoid the damage formation in a composite, with this technique it is possible to control this process. Stopping the test at 2.0% strain, was possible to see that it is not possible to directly correlate the damage position, seen from the microscopy, with the results provided by the DIC. On the contrary, with the use of the DIC it is possible to see the positions where it will be more likely that final damage will occur, which is near the area with high strains in the resin channels. Talking about final failure damage, was see that the crack formation it is not restricted just to the resin rich regions, but there is an extensive presence of cracks inside the yarns, starting from the z-crowns near the weft tows. So, damage it is visible also inside the weft tows, which cannot be seen by the DIC. At this stage, cracks generate micro-delaminations in the z-

binders and at the warp tows, depending on the type of fibre mat. These micro-delaminations represents local debonding between resin and fibers, they are not as extended as the delaminations that can be seen in fatigue, because of the different type of loading, but, as a rule, the types of damage visible in static tests are also visible in fatigue.

From the tests on the notched specimens, was seen that the same type of damage occurring in plain specimens tested until failure, it is then possible to understand that damage does not only occur in the resin rich regions, even if the results from the DIC show major cracks in these areas with the presence of strain intensification. This effect is probably caused by the combined presence of the hole and the resin channels, which creates this strain intensification. So, even if the presence of major cracks is visible from the DIC pictures, together with strain intensification, damage it is not only limited to these regions. Moreover, from the second specimen was visible that fibre failure happens inside the weft yarns, in a position not seen from the DIC, caused by the stress concentration of a matrix crack that must turn around a warp tow to surpass it, leading to failure at a warp tow edge. In conclusion, even if the DIC is capable to see the areas near where high displacement are located, it is not possible to have punctual information about final failure position, because this analysis is limited to the surface and affected by the strain magnification effect of the resin channels.



# Chapter 8

## Conclusions and further work

In this work, a 3D-96 composite was manufactured using the wet lay-up technique. This type of material presents an enhanced inhomogeneity because of the presence of thick bundles of fibres with resin gaps in between. For this reason, a characterization of the fabric architecture was necessary and it was done by using the optical microscope. Because of the structure of this composite, Digital Image Correlation can be profitably used on it. Throughout this work was proven that DIC is a reliable method to measure the strains and its results are comparable to the ones provided by traditional strain gauges, with the plus of giving full field measurements and accurate punctual information. At the beginning of the work, the relation between fabric architecture and DIC results was investigated to explain the superficial strain pattern, then the results from DIC were used to create a virtual strain gauge averaging the strains over an area, taking as a reference the composite unit-cell size. This was done to find the smallest virtual strain gauge capable of giving reliable information, was found that one unit-cell size virtual strain gauge provides sufficiently accurate results, similar to the average strain over the whole specimen. Considering smaller averaging areas, the results present an increasing scatter caused by inherently inhomogeneity of the fabric architecture.

Various tests on plain specimens were done to verify the material behaviour with the use of DIC and to obtain its mechanical properties, from these tests was clear that DIC can spot the formation of a transverse lines pattern caused by the alternating presence of weft tows and resin gaps between them. DIC can also describe the formation of a spotted pattern at high strains, caused by the superficial z-crowns which represents areas of higher stiffness with respect to the adjacent weft tows and resin gaps. Together with experimental measures, a theoretical model was utilised to compare the results, was then possible to say that the strain distribution that arises between weft tows and resin gaps can be described with the Strain Magnification Factor theory, modified to address a two-

dimensional problem. At the end, the experimental results have been compared with the calculations using the SMF theory (which also implies some experimental measurements) and a correction factor have been applied to the theory to make it overlap with the experimental results.

As was previously said, for the own made laminates, a fibre volume fraction calculation was performed together with a characterisation of the mechanical properties. Was verified that the results obtained are comparable to the ones that can be found in literature, proving the goodness of the work and the reliability of the obtained results.

As was also stated in other works, throughout this work was proven that 3D composites present an enhanced notch insensitivity, this for various manufacturing methods and various thicknesses. Their results are better than 2D laminates and this could be explained with a more matrix dominated behaviour. This is interesting because 3D composites are made of non-interlacing layers of yarns at  $0^\circ$  and  $90^\circ$ , so they are comparable to 2D composites, but with a reinforcement in z-direction. As a hypothesis, the notch insensitivity can be caused by the presence of resin rich regions and channels, which distribute the strains and permit the development of extensive matrix cracks, together with localized delaminations, all these mechanisms reduce the stress intensification near the hole.

3D-96 composites undergo to the formation of transverse matrix cracks in the resin gaps between weft tows at 0.7% average strain. DIC is useful to verify the formation of this type of damage, in this case cracks start from the specimen edge at the surface, spreading then for all the width and inside the composite, going also through the weft tows underneath. On the contrary, DIC is not useful to describe the damage in the late stages of the quasi-static tests, this because it is not possible to see the formation of a characteristic damage pattern, while the formation of transverse cracks is clearly visible. Must be remembered that the DIC is able to describe what happens just at the surface, so internal damage, for example fibre failure, is not visible with this technique. Final failure zone is defined by high strain in the resin channels, this is visible in the plain specimens where failure position is always predictable. On the contrary, in notched specimens this is not possible because strain intensification is amplified by the presence of the hole, so high strains are quite similar all around the hole and it is not possible to find the exact failure position in advance.

To analyse the strains around the hole, polar graphs have been plotted for different hole sizes and diverse types of material. Was visible the correlation between high strains and resin channels, but was not possible to locate final failure position in notched specimens based on the highest strains in the loading direction. This because it is not possible to find with a sufficient precision the fibre failure position, which is internal and it present a statistical nature. With the presence of a hole, the strain intensification has two sources, caused by the difference in stiffness of resin channels and weft tows, and because of the presence of the hole. In plain specimens, on the contrary, it is easier to spot the presence of strain intensification in a location caused by some previous defects, which will lead to the formation of cracks usually starting from an edge, because of the edge effect, and at the end to final failure. Polar graphs for 3D composites were compared with the ones of 2D woven composite and light alloy, was visible how different they are because of the macroscopic inhomogeneity of 3D composite. DIC results for the 2D composite and the metal plate were also compared with numerical analyses, proving again that the DIC gives comparable results with other methods.

From microscopy images was possible to characterise damage progression in plain specimens under quasi-static tensile loading, was found that this presents the same stages as in fatigue but without the presence of extensive delaminations. On the contrary, only micro-delaminations localized near the z-binders, at their interface with weft tows and between weft tows and warp tows are present. Warp tows failure is located near the centre of a weft tow, at the edge of the warp tow, caused by a crack that originates near the z-crown. Differently from what was initially believed, fibre failure does not happen under a resin gap between weft tows, but inside them because of the stress intensification that here is believed to be higher. The same type of damage is present both in plain and notched specimens, thus can be said that strain intensification in resin channels is a premonitory signal of where final failure will happen, but it is not possible to say in which weft tow failure will happen. With the presence of a hole, strain intensification in resin channels becomes significant in all the resin channels near it and so it is no more possible to say near which resin channel the composite will fail.

Concluding, notch insensitivity can be explained with the presence of resin channels that lower the strain intensification near the hole, shifting the behaviour to a more matrix dominated one. This is visible in the microscopies where the same type of damage is visible in plain specimens and in notched ones near the hole, so a higher crack density

near the hole is not visible and a strain redistribution can be hypothesized. Another point that turns in favour of 3D composites is the absence of extensive delaminations between the plies. This would concentrate near the hole and it would cause a premature end of life caused by the reduced stiffness, in 3D composites this is not present and so a source of stress concentration is avoided.

As further work, the realization of a 3D finite element model would be necessary to explain and compare the superficial strain results, particularly for transverse lines formation. This would be very useful because the architecture of this type of material and its behaviour can be accurately reproduced using a 3D model, incorporating the presence of z-binders and all the yarns composing the 3D structure. During the whole work, tests were conducted in warp direction, so a future detailed study could involve the same study done here but involving tests in weft direction. This will help to better understand the parameters that influence the notch insensitivity behaviour. A complete statistical investigation of the notch sensitivity, both in warp and weft direction, would be useful to accurately describe the material, since in this work not enough tests were made. Another topic that can be improved is the damage characterization, stopping and cutting specimens at other strain levels will permit to have a better description of damage progression and its mechanism.





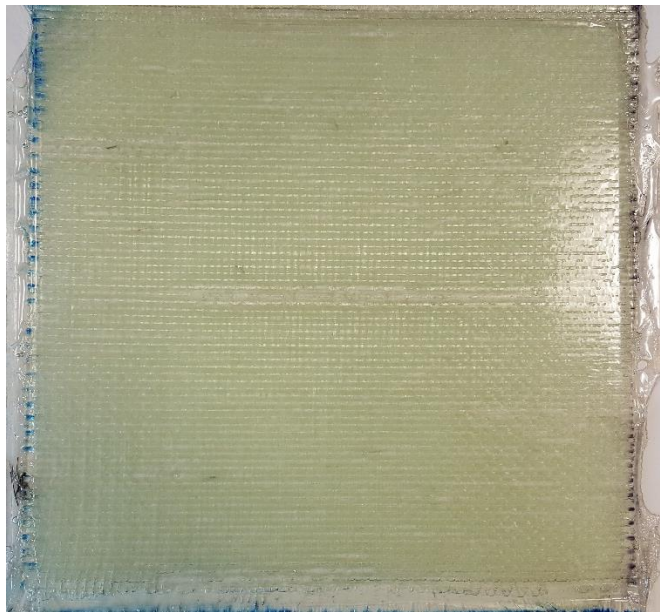


# Appendix 1

## Wet lay-up manufacturing progress

Several attempts were made to produce a good laminate, in the following paragraph some of the attempts are described, trying to explain the reasons that produced the result and the improvements that can be taken to avoid the defects found.

1. In this attempt, the same amount of resin needed for a laminate made of 2D woven plies with the same final thickness was used, more precisely: 100g of epoxy, 60g of hardener and 4g of curing agent. Another difference was the use of a glass plate and a layer of Melinex over the fabric during the infusion inside the vacuum chamber. The result can be seen in Figure A1.1, it is easy to understand that the quantity of resin is not enough to impregnate all the 3D fabric, which requires more resin. The result of this is the presence of open channels both at the top and at the bottom, which is the result of the lack of resin, and a lot of scratches inside the tows, which can be due to the unperfect wetting of the fibres inside the yarns. Concluding, from this first attempt was learnt that the quantity of resin should be approximately double than the one used for 2D woven composites.



*Figure A1.1: Picture of the first laminate produced.*

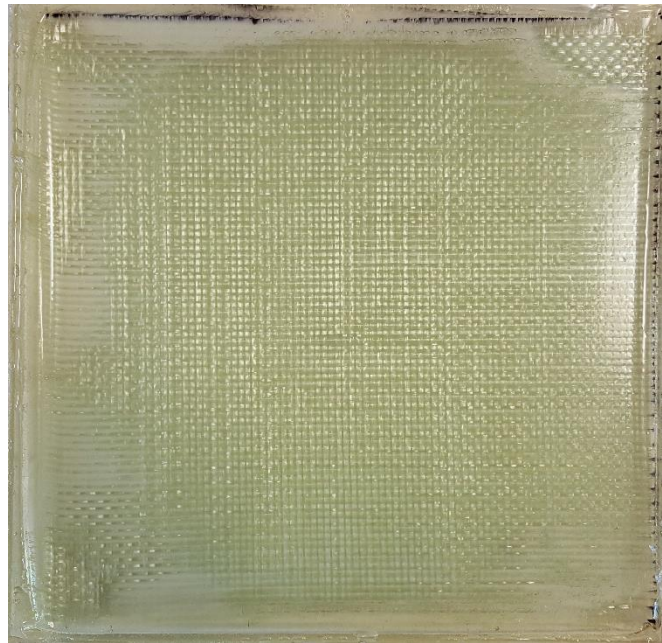
2. In a second attempt, the quantity of resin used was roughly double than the previous and equal to the one recommended. The resin was poured trying to homogenously distribute it all over the surface. Must be reported that, in this attempt, the vacuum box had some problems of leakage which supposedly caused a higher pressure inside the chamber and, as a consequence, more difficulties to remove the air trapped inside the dry fabric. The result was a laminate quite well impregnated but with some voids inside caused by the micro-bubbles of air trapped and some open channels. So, from this attempt was understood that to seal properly the vacuum box the arrows drawn on it should be aligned, which was not done previously, moreover another check should be done to detect some residual leaks and seal them with some plastic sealant.



*Figure A1.2 : Picture of the second laminate produced.*

3. In the third attempt a slightly different path was followed, the amount of resin was the right one, but the plastic layer and the glass plate were not placed over the fabric during the infusion inside the vacuum box. The main different part in the procedure was conducted during the pouring of the resin, this time the resin was poured in one spot at the centre, letting it spread out during the period inside the vacuum box. The set-up of the vacuum box this time was correctly made, so there were no problems for the point of view of the leakages. The composite was left inside the vacuum box for an hour and fifteen minutes and the initial temperature of the glass and metal plate was 100 °C. The result was a panel with some un-wetted fabrics at the edges of the laminate, caused by the fact that the resin was completely poured in one spot. The main defect visible is that most of the yarns seems to have not been wetted by the resin and this produces the presence of what seems scratches and a white colour

inside the yarns, which corresponds to a lack of resin inside them. The improvements that can be made from this attempt are, trying to distribute the resin all-over the fabric or even under it to remove the air trapped inside the dry fabric and get rid of the open holes at the surface, since was seen that pouring the resin in one spot gives worse results than the ones reached in the previous attempts. Moreover, a hotter glass and metal plates can be used to have a less viscous resin for a longer time, which should improve the wetting. Another thing that can improve the wetting of the fibres and the impregnation of the fabric is to let it a longer time inside the vacuum box.

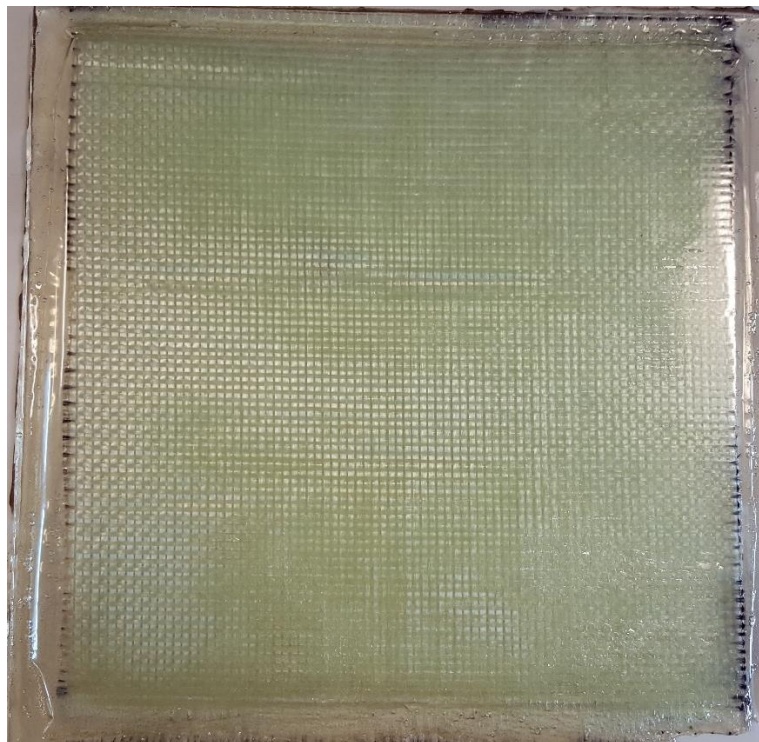


*Figure A1.3: Picture of the third laminate produced.*

*Note:* The problem with the infusion of 3D composites is that, since they are a one-layer fabric, it is more difficult to remove the air trapped inside them, so a different technique must be used to try to get rid of all the voids caused by the air stuck between the yarns. Thus, it shall be tried to mechanically distribute the resin before the infusion to facilitate the penetration of the resin, which is what is done for 2D woven composites, where it is easier to take out the air bubbles and impregnate the fabric because each layer has a small thickness and the mechanical procedure can be done for every layer, even in the ones which will be inside the final laminate after the curing.

4. In the fourth attempt, several changes have been made trying to improve the result. The resin was poured directly inside the vacuum chamber, so the metal and the glass plates were positioned inside it before the sustaining structure with the Melinex. After this, some resin was poured at the bottom, approximately a quarter of the

entire amount and the rest was poured at the top of the fabric, trying to distribute it very carefully. The temperature of the oven where the plates were kept was increased from 100 °C to 130 °C, this to have a thinner resin for a longer time, which permits to keep the composite inside the vacuum chamber for a longer time, approximately for one hour and a half or two hours. The result is a laminate with a nice finishing on the upper part, but with a lot of voids and open bubbles without resin at the bottom. This could be due to the fact that the high temperature generated by the plates had interacted with the resin poured at the bottom or with the Melinex, generating the bubbles that does not permitted the resin to infuse completely the fabric.



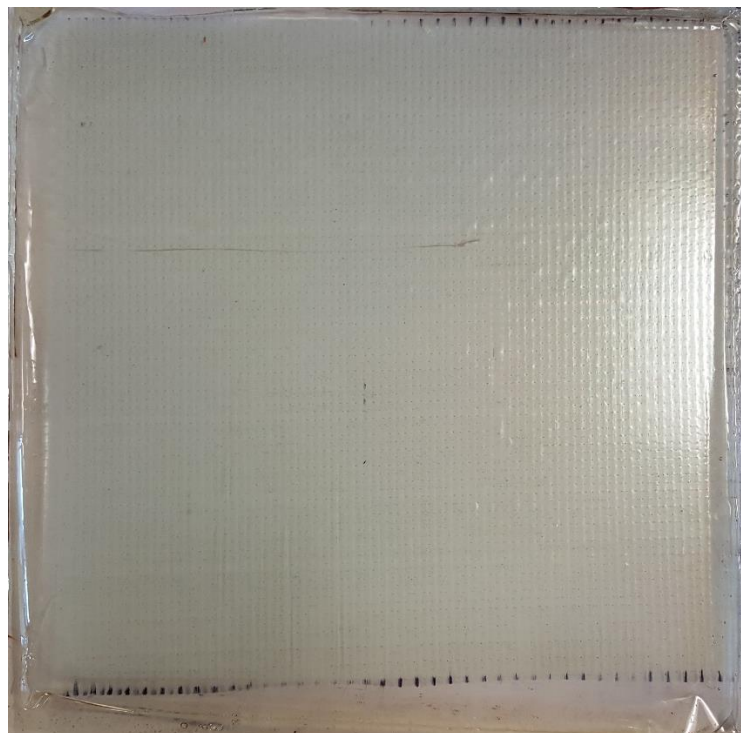
*Figure A1.4: Picture of the fourth laminate produced.*

So, the choice for the procedure was to use the procedure from the second attempt, using a temperature of the plates of 100 °C and trying to distribute the resin in the best feasible way. This passage is very important because inhomogeneities in the distribution of the resin leads to an excess of resin in one part of the laminates, which will end to be accumulated outside of the fabric, leading to other areas with voids due to the lack of resin inside the fabric. Another thing that will be changed is pouring the resin at the bottom of the laminate which did not give the expected results, since the intent was to close the voids at the lower part of the laminate. The temperature of the plates is again lowered at 100 °C because was not seen a beneficial effect of this and the resin may start curing at



some parts due to the elevated temperature. Moreover, even if the temperature was raised to 130 °C, after one hour and a half the resin was quite thick leading to a difficult procedure for the extraction of the bubbles trapped inside. At the end, the temperature will be lowered again at 100 °C at the infusion time to one hour or one hour and a quarter.

5. In this attempt, two metal plates were used to heat up the vacuum box and their temperature was set at 100 °C, because, as was said, a higher temperature would cause the resin to start curing. The composite was let inside the vacuum box for 1 hour and fifteen minutes. No weight or glass plate was placed over the lamina during the infusion process. The resin was poured as much homogeneously as possible all over the cloth directly inside the vacuum chamber and no resin was placed under the cloth, but it was poured only over it. The main thing that was changed this time was the release of the valve after the infusion process to make the air enter again inside the chamber. This time the operation was carried out very slowly, approximately twelve minutes was necessary to complete this operation. This was identified as the main cause for the presence of voids and air trapped inside the composite, because it was done too fast.



*Figure A1.5: Picture of the fourth laminate produced.*





# Appendix 2

## Quasi-static tensile tests

In this Appendix are presented the stress strain curve obtained from strain gauging measurements on 3D-96 plain specimens tested until failure to derive the mechanical parameters of the material, which are Young's modulus, Poisson's ratio, strength to failure and strain to failure, these have been listed in Chapter 6.

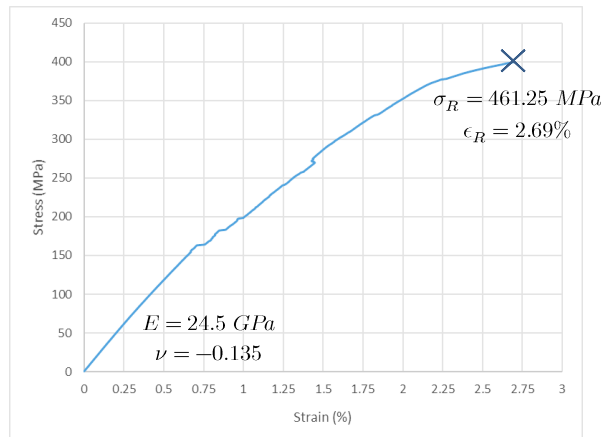


Figure A2.1: Quasi-static tensile test number 1 for the mechanical properties characterization.

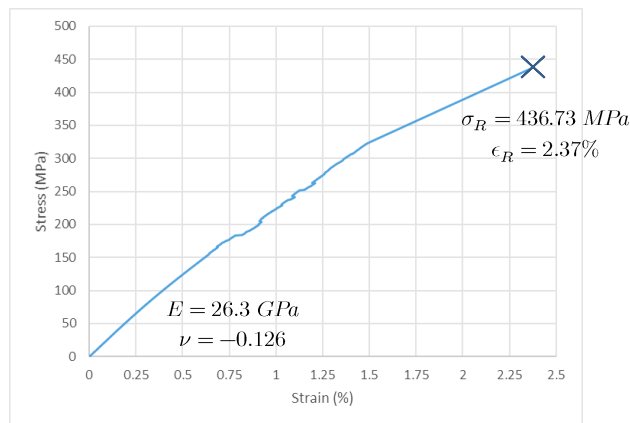


Figure A2.2: Quasi-static tensile test number 2 for the mechanical properties characterization.

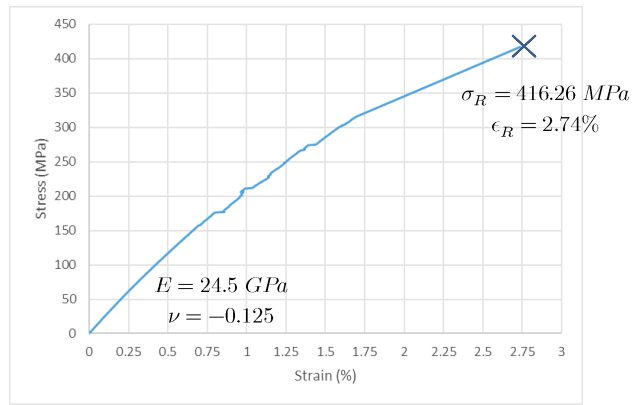


Figure A2.3: Quasi-static tensile test number 3 for the mechanical properties characterization.

# Appendix 3

## Fibre density and tow area measures

In this Appendix, the microscopies used to calculate the number of fibres inside an area for the fibre volume fraction measurement are reported. Then, the weft tows area measurements are depicted, these have been used to calculate the equivalent area in the analytical model for the Strain Magnification Factor, presented in Chapter 5.

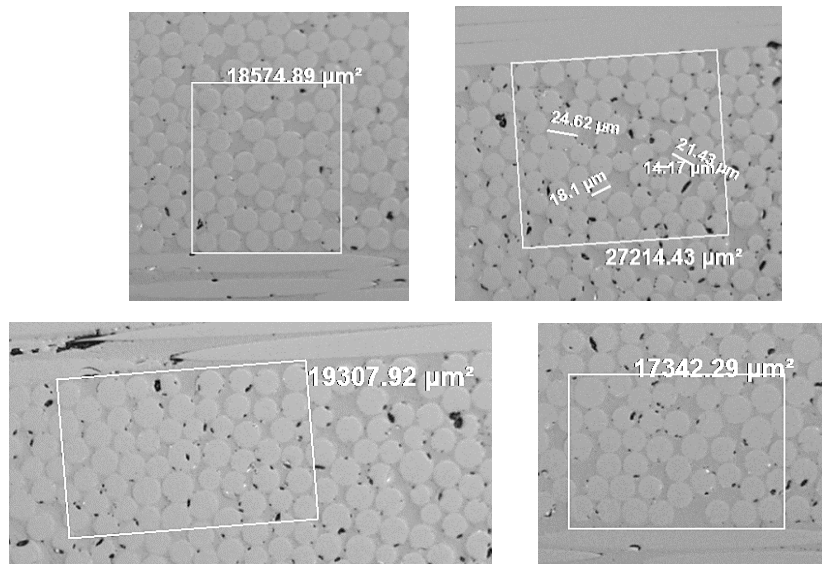


Fig A3.1: Areas for fiber volume fraction calculation (details in §5.4).

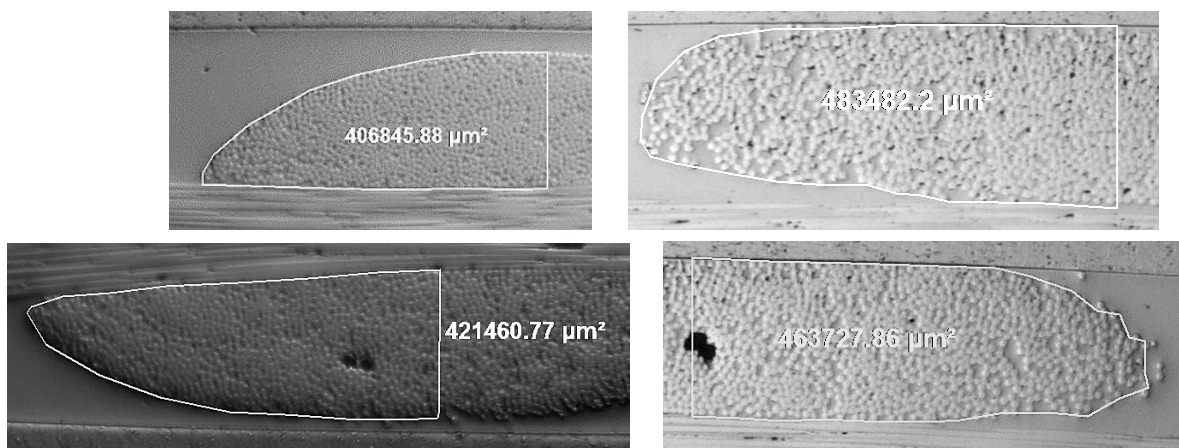


Figure A3.2: Tow areas to calculate the length of the idealized squared area in the Strain Magnification model (details in §5.4).



# Appendix 4

## Numerical plane simulation to verify the SMF idealized model

To verify the accuracy of the idealized model for the Strain Magnification Factor (SMF) calculation, a plane numerical model is introduced. The geometry used is the taken from a general weft tow profile, the model was done using the same shape but not the same measures, since the only thing that counts is the ratio between them. So, a unit-cell was modelled, as can be seen in the next picture on the left, this because this geometry is the smallest repetitive unit inside the composite. The type of element used is *Plane182*, since a plane analysis is done, using the options *plane strain* and *simple enhanced strain*. The modulus assigned to the tows was the same obtained in the previous section, while for the Poisson's ration the value used in [27] was adopted. Talking about the resin, typical values for an epoxy resin were set. The parameters used are reported in the next table.

*Table A4.1: Elasti properties used during the modeling.*

<i>Epoxy resin</i>	<i>E [GPa]</i>	<i>4</i>
	<i>ν</i>	<i>0.4</i>
<i>Resin impregnated fibre</i>	<i>E<sub>t</sub></i>	<i>12</i>
	<i>ν [GPa]</i>	<i>0.3</i>

The measures used are the same in ratio, as the ones presented for *Area1*, which is the one visible in Figure 5.10, but scaled to millimetres. So, the height of the model is  $h = 528mm$ , the tow maximum length is  $1364 mm$  and the semi-length of the unit-cell is  $3800 mm$ , keeping the ratio between the parts. The constraints applied are, zero displacement in Y direction to the entire bottom line, symmetry conditions to the left contour line, while the applied load is a uniform pressure in traction of  $1 MPa$  to the right line. The elements used, after a convergence analysis, have the following measures,  $20 mm$  as element size for the elements inside the tow and  $10 mm$  for the elements in the resin, meshed using free meshing, that was assured to give reliable results. A detail of the mesh is presents in the picture below.

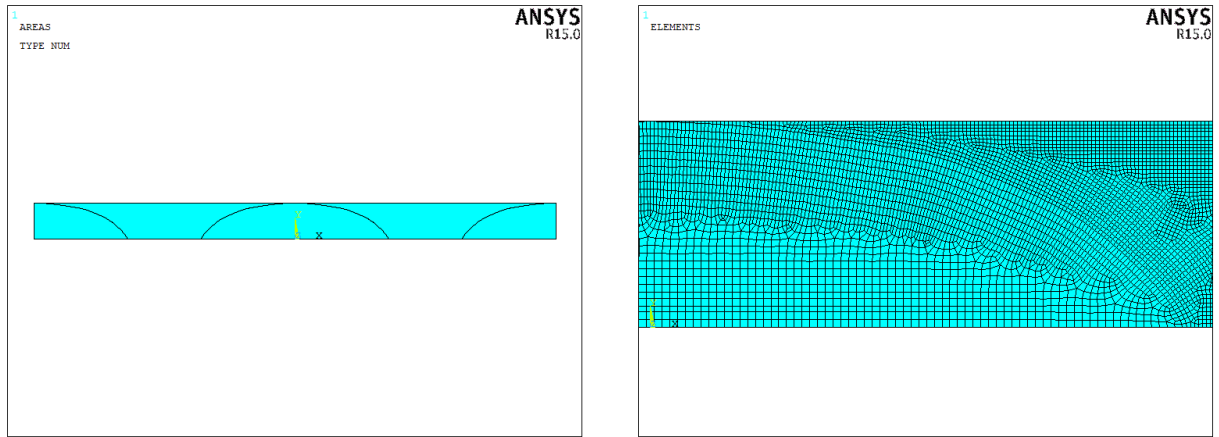


Figure A4.1 : On the left the areas with which are modeled the geometry of a unit-cell as the idealized geometry of the Strain Magnification Factor calculation, on the right a detail of the used mesh.

The results obtained are not significant considering their absolute value, but the ratios between them are significant, since the strain distribution is affected just by the geometry. So, the plot of the strains below is significant just for the distribution but not for the absolute values plotted. In any case, this calculation is useful to plot the superficial strains to calculate the ratio between the mean value and the peak one to calculate the Strain Magnification Factor.

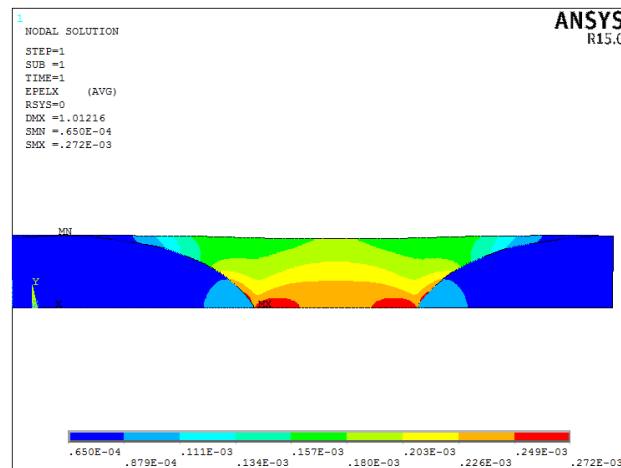
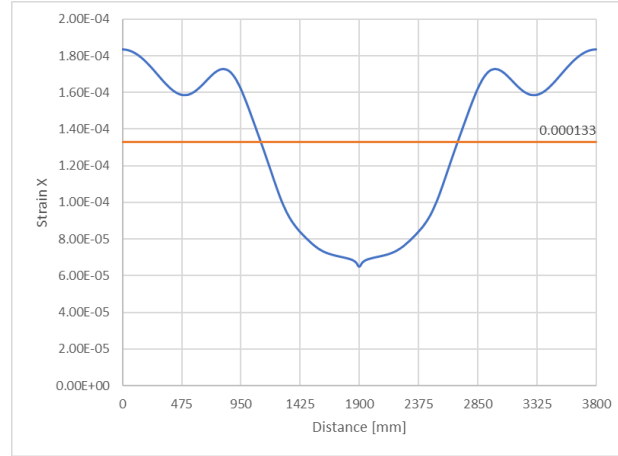


Figure A4.2: Plot of the strain field in X direction, which is the direction of the applied load.

The plot of the superficial strains, calculated using the plot path operation, is here reported. Can be noted that its shape, although having a sinusoidal distribution, is different from the one experimentally calculated. It has a local peak at the midway between the tow's edge and the resin gap. This difference is not easily explainable, since is used a similar geometry to the one presented in the real fabric and visible in the mi-



croscopies. Must be here pointed out that comparing this simulation with the experimental results is not correct since the model here used is not representative of the whole composite behaviour, in fact the presence of the z-binders and of the warp tows is not accounted and this surely influence the strain distribution.



*Figure A4.3: Plot of the superficial strains in X direction, which is the direction of the applied load.*

Dividing the peak strain for the mean value is then obtained the Strain Magnification Factor, the result is comparable to the one obtained for the idealized model considering that, in this case, a continuous distribution is accounted. The value found is:

$$SMF_{numerical} = 1.38$$

This result let us know that the values obtained using the formula of the Strain Magnification model are correct. This model is not representative of the strain distribution on the whole composite since here the presence of the warp tows and of the z-binders is ignored. It is also not modelled the layers structure, so a comprehensive model must be used to compare the numerical results with the experimental ones.



# References

- [1] X. Chen, L. W. Taylor, and L. Tsai, "An overview on fabrication of three-dimensional woven textile preforms for composites", *Textile Research Journal*, vol. 81, no. 9, pp. 932-944, 2011.
- [2] M. H. Mohamed and A. E. Bogdanovich, "Comparative analysis of different 3D weaving processes, machines and products", *Proceedings of 17th International Conference on Composite Materials (ICCM-17)*, Edinburgh, UK, 27-31 July 2009.
- [3] L. Tong, A.P. Mouritz and M.K. Bannister, "3D Fibre Reinforced Polymer Composites", *Elevier*, Oxford UK, 2002.
- [4] A. P. Mouritz, M. K. Bannister, P. J. Falzon, and K. H. Leong, "Review of applications for advanced three-dimensional fibre textile composites", vol. 30, pp. 1445-1461, 1999.
- [5] S. V Lomov, A. E. Bogdanovich, D. S. Ivanov, D. Mungalov, M. Karahan, and I. Verpoest, "Composites: Part A, A comparative study of tensile properties of non-crimp 3D orthogonal weave and multi-layer plain weave E-glass composites. Part 1: Materials, methods and principal results", *Compos. Part A*, vol. 40, no. 8, pp. 1134-1143, 2009.
- [6] A. E. Bogdanovich, "Advancements in manufacturing and applications of 3-D woven preforms and composites", 16<sup>th</sup> international conference on composite materials (ICCM-16), July 8-13, 2007, Kyoto, Japan.
- [7] M. H. Mohamed and M. M. Salama, "High speed three-dimensional weaving method and machine", *United States Patent*, vol. 1, no. 12, 2001.
- [8] A. P. Mouritz, "Composites: Part A, Tensile fatigue properties of a 3D orthogonal woven composite", vol. 39, pp. 1018-1024, 2008.
- [9] V. Carvelli, G. Gramellini, S. V Lomov, A. E. Bogdanovich, D. D. Mungalov, and I. Verpoest, "Fatigue behavior of non-crimp 3D orthogonal weave and multi-layer plain weave E-glass reinforced composites", *Compos. Sci. Technol.*, vol. 70, no. 14, pp. 2068-2076, 2010.
- [10] D. S. Ivanov, S. V Lomov, A. E. Bogdanovich, M. Karahan, and I. Verpoest, "Composites: Part A, A comparative study of tensile properties of non-crimp 3D orthogonal weave and multi-layer plain weave E-glass composites. Part 2: Comprehensive experimental results", *Compos. Part A*, vol. 40, no. 8, pp. 1144-1157, 2009.

- [11] R. Muñoz, V. Martínez, F. Sket, C. González, and J. Llorca, “*Composites: Part A, Mechanical behavior and failure micromechanisms of hybrid 3D woven composites in tension*”, vol. 59, pp. 93–104, 2014.
- [12] S. Dai, P. R. Cunningham, S. Marshall, and C. Silva, “*Open hole quasi-static and fatigue characterisation of 3D woven composites*”, *Compos. Struct.*, vol. 131, pp. 765–774, 2015.
- [13] L. Qin, Z. Zhang, X. Li, Y. Wang, H. Miao, and L. He, “*Full-field analysis of notch effects of 3D carbon/carbon composites*”, vol. 48, no. 9, pp. 3454–3460, 2013.
- [14] S. Yoneyama, “*Basic principle of digital image correlation for in-plane displacement and strain measurement*”, *Adv. Compos. Mater.*, vol. 3046, no. March, pp. 1–19, 2017.
- [15] N. J. Saiger, “*Effects of Graphitisation on the Mechanical Properties of Cast Iron Water Mains – An Investigation into the use of Digital Image Correlation for Strain Measurement*”, Mechanical Engineering MEng Project Report, University of Surrey, 2015.
- [16] M. A. Sutton, J. Orteu and H. W. Schreier, “*Image Correlation for Shape, Motion and Deformation Measurements*”, Springer, New York NY, 2009.
- [17] University of South Carolina - Correlated Solutions inc., “*Digital Image Correlation: Overview of Principles and Software 2D Image Correlation Fundamentals*”, SEM workshop, 2009.
- [18] Correlated Solutions inc., “*Vic-3D testing guide*”, 2007.
- [19] H. M. S. Belmonte, C. I. C. Manger, S. L. Ogin, and P. A. Smith, “*Characterisation and modelling of the notched tensile fracture of woven quasi-isotropic GFRP laminates*”, vol. 61, 2001.
- [20] S. Daggumati *et al.*, “*Local strain in a 5-harness satin weave composite under static tension: Part I – Experimental analysis*”, vol. 71, pp. 1171–1179, 2011.
- [21] T. C. Chu, W. F. Ranson, M. A. Sutton, and W. H. Peters, “*Applications of Digital Image-Correlation Techniques to Experimental Mechanics*”, no. September, pp. 232–244, 1985.
- [22] L. Baiocchi, “*Late Fatigue Damage Development in a 3-D Woven E-glass/Epoxy Composite*”, M.Sc. Thesis Mechanical Engineering, Università di Padova, 2013.
- [23] E. Novello, “*Thermomechanical and microscopy investigation of fatigue damage development in a 3D E-glass/epoxy woven composite*”, M.Sc. Thesis Mechanical Engineering, Università di Padova, 2014.

- [24] K. Farik, “*Effect of hole size on failure of notched 3D composite in the warp direction*”, BEng Mechanical Engineering project report, University of Surrey, 2015.
- [25] S.L. Ogin, P. Brøndsted, J. Zangenberg, “*Composite materials: constituents, architecture, and generic damage*”, in R. Talreja, J. Varna, “*Modeling Damage, Fatigue and Failure of Composite Materials*”, Chapter 1, Elsevier, 2016.
- [26] L. Lee, S. Rudov-Clark, A.P. Mouritz, M.K. Bannister, I. Herszberg, “*Effect of weaving damage on the tensile properties of three-dimensional woven composites*”, *Composite Structures* vol. 57, pp. 405–413, 2002.
- [27] S. Topal, L. Baiocchi, A. D. Crocombe, S. L. Ogin et al., “*Late-stage fatigue damage in a 3D orthogonal non-crimp woven composite: An experimental and numerical study*”, *Composites Part A*, vol. 79, pp. 155-163, 2015.
- [28] C. Kyriazoglou, F.J. Guild, “*Quantifying the effect of homogeneous and localized damage mechanisms on the damping properties of damaged GFRP and CFRP continuous and woven composite laminates - an FEA approach*”, *Composites: Part A*, vol. 36, pp. 367–379, 2005.
- [29] C. A. Conway, “*3D reinforcement of composite materials*”, B.Sc. Thesis Materials Engineering, Politecnico di Torino, 2011.
- [30] M. Karahan, S. V. Lomov, A. E. Bogdanovich, D. Mungalov, I. Verpoest, “*Internal geometry evaluation of non-crimp 3D orthogonal woven carbon fabric composite*”, *Compos. Part A*, vol. 41, pp. 1301-1311, 2010.
- [31] S. Daggumati, E. Voet, W. Van Paepegem, J. Degrieck, J. Xub, S.V. Lomov, I. Verpoest, “*Local strain in a 5-harness satin weave composite under static tension: Part I – Experimental analysis*”, *Composites science and Technology*, vol. 71, pp. 1171-1179, 2011.
- [32] L. Gorbatikh, S.V. Lomov, “*Damage accumulation in textile composites*”, in R. Talreja, J. Varna, “*Modeling Damage, Fatigue and Failure of Composite Materials*”, Chapter 3, Elsevier, 2016.
- [33] 3TEX inc., 2017, Available at <http://www.3tex.com/>.
- [34] L. Baiocchi, T.F. Capell, S.A. McDonald, S.L. Ogin, P. Potluri, M. Quaresimin, P.A. Smith, P.J. Withers, A. Bogdanovich, “*Late-stage Fatigue Damage Development in a glass/epoxy non-crimp 3D orthogonal woven fabric composite*”, 16th European Conference on Composite Materials, Seville, Spain, 22-26 June 2014.



# Acknowledgments

Firstly, I would like to thank my Supervisors, Professor Marino Quaresimin for giving me the opportunity to make this experience of producing the dissertation in another country on such an interesting topic that is composite materials and Professor Stephen Ogin for his continuous support, his kindness, patience and encouragement.

I thought goes also to all my exchange friends, Surrey students and especially to my office mates, doctorates, technicians and all the people in the Mechanical Engineering department at the University of Surrey for making my experience wonderful, for all their help and for making me feel always welcome, it was such an enriching experience and without them this would not have been the same.

A special thank goes to my parents for their unconditioned support, without them this journey through University till this point would not have been possible, and to my family for always making me feel important.

Thanks goes also to all my close friends, who are my second family, for being by my side since so long and to my friends in the Mechanical Engineering course who shared with me and helped me through this journey of joys and sorrow.